

An Ageing Stockpile: Atomistic Simulation of Helium Behaviour in Plutonium Dioxide

by

ELANOR ROSE MURRAY

A thesis submitted to
The University of Birmingham
for the degree of
DOCTOR OF PHILOSOPHY

School of Chemistry
College of Engineering and Physical Sciences
University of Birmingham
September 2022

UNIVERSITY OF
BIRMINGHAM

University of Birmingham Research Archive

e-theses repository

This unpublished thesis/dissertation is copyright of the author and/or third parties. The intellectual property rights of the author or third parties in respect of this work are as defined by The Copyright Designs and Patents Act 1988 or as modified by any successor legislation.

Any use made of information contained in this thesis/dissertation must be in accordance with that legislation and must be properly acknowledged. Further distribution or reproduction in any format is prohibited without the permission of the copyright holder.

Dedication

In memory of my school chemistry teacher Debbie Murray. Thank you for putting joy into science and giving me the best advice I've ever received,
"There's no need to be so stressed - take an Orange Wednesday and enjoy yourself!"

Acknowledgements

The completion of this thesis would not have been possible without Prof. Pete Slater, thank you for taking me on and of course for introducing me to Dr Pooja Goddard, you have both been fantastic! I am extremely grateful to to Dr Ying Zhou for being relentlessly helpful and patient and always just an email away. My sincere thanks also go to Prof. Roger Smith for his insightful questions and for always pushing this research further. You've all been a dream team.

I'd like to express my gratitude to the NDA for funding this research, to the TRANSCEND consortium for providing an excellent community of knowledge and ample opportunities to present and discuss this research, and to the University of Birmingham's blueBEAR HPC service. I extend my sincere thanks to Dr Helen Steele and Dr Rick Short for their invaluable guidance. I'd like to thank Dr Mark Read for introducing me to computational chemistry and establishing this project, Dr Rob Jackson for his continuing support, and Dr Robin Orr for helpful discussions.

I would be remiss not to thank everyone who has ever responded to a frantic message when error messages got the better of me, in particular Sam Moxon, Helen Abbott, and Will Neilson. Thank you to everyone who has shared food, drinks, and joy with me during this work, especially the friends I've made from Floor 5 despite me mainly working from home(!). Many thanks go to Dr Antony Nearchou for always helping me with uni admin stuff and being a sympathetic ear.

Thanks must also go to the everyone who supported me through my masters programme and gave me the confidence to pursue this PhD, especially Dr Tzany Wheldon and the friends I made in Dorset. I am grateful to have lived with such welcoming and encouraging people during that time, thank you to Ed, Liv, Max, Rhys, Rach and Simone. Thank you also to my Bradford lasses!

My university journey wasn't always the most straightforward and I'd like to thank everyone who uplifted me along the way. Special thanks go to Zoë, Alex, Rob, Harry, Aaron and Jack - thank you for staying with me throughout, being ridiculous, and never letting me give in on myself; I'm so incredibly proud of us all!

None of this would have been possible without my family. Unlimited thanks go to my Mum, Dad, and brother (Wendy, Peter and Sam). You are all the absolute best and my constant sources of inspiration. Thank you to Robin for being by my side throughout this work, and always humouring me when I was excited about ′the dots on my screen!′ I'm looking forward to relaxing with you all soon (you can hold me to the relaxing part!). Finally, to my Grandmas Peggy and Mal, thank you for being such examples in resilience and humour; you've been with me throughout.

Abstract

Until the UK Government arrives at a decision regarding the final treatment and disposition of plutonium, the NDA remain responsible for the safe and secure storage of the PuO_2 stockpile currently in inert steel cans at Sellafield. Radiogenic helium gas generation naturally occurs in the ageing of PuO_2 due to the spontaneous alpha decay of Pu isotopes, creating self-radiation damage to the lattice. The risk of helium gas pressurisation is a safety concern for long-term storage of PuO_2; hence, fundamental understanding of helium behaviour, including its incorporation, diffusion, and clustering, is needed. Atomistic simulation techniques are ideally suited to provide fundamental insight into helium behaviour in PuO_2.

Initial defect calculations from atomistic simulations of bulk PuO_2 were performed, identifying the Schottky trio and oxygen Frenkel pair as favourable defects. The (111) surface was predicted to have the lowest surface energy and therefore dominate the PuO_2 growth morphology. Intrinsic defects were simulated for the (100), (110) and (111) surfaces. It was found that there is an energetic drive for plutonium Frenkel pairs to form at the surface rather than the bulk of PuO_2.

Atomistic simulations using interatomic potentials were performed to model helium incorporation in bulk PuO_2. In defect-free PuO_2 the octahedral interstitial site was determined to be the most energetically favourable site for helium. When defects were present, the plutonium vacancy had a negative helium incorporation energy, indicating it may act as a trap for helium atoms. Helium clustering around plutonium vacancies and Schottky trios was observed. However, Pu vacancies and Pu Frenkel pairs are energetically unstable and so may not be available for helium accommodation.

Molecular dynamics and energy barrier searching methods were employed to investigate the diffusion and clustering of helium in PuO_2. The results show that in perfect PuO_2, interstitial He is not mobile over nanosecond time scales at temperatures below $\sim$ 1500 K, with the lowest energy diffusion barrier being 2.4 eV.

When oxygen vacancies are present the He diffusion barrier drops to 0.6 eV, enabling helium diffusion at lower temperatures. The dominant He diffusion mechanism is shown to be oxygen vacancy assisted inter-site hopping rather than the direct path between adjacent interstitial sites. Thus, oxygen vacancies are key to the diffusion of helium; such vacancies are generated either via self-radiation damage, or thermally at high temperatures.

Unlike oxygen vacancies, plutonium vacancies act as helium traps. In molecular dynamics simulations it was observed that helium occupying a Pu vacancy can easily be ejected via Frenkel pair recombination. As such, plutonium vacancies must be stabilised to nucleate helium clusters, such as in Schottky trios. High temperature molecular dynamics simulations show that helium can diffuse via oxygen vacancies into clusters with the majority of helium clusters which form over nanosecond time scales having a He:Vacancy ratio below 1:1. Further static calculations show that a $\sim$ 3.5:1 He:Vacancy ratio is the largest possible for an energetically stable helium cluster. Schottky defects are found to act as seed points for He cluster growth and high local concentrations of He can create such defects, which then pin the growing He cluster.

Table of Contents

Dedication i

Acknowledgements ii

Abstract iii

Publications x

Figures xi

Tables xxiv

Abbreviations xxvii

1 Introduction 1

1.1 Nuclear Fuel Cycle . . . 1

1.1.1 Nuclear Reactor . . . 2

1.1.2 Spent Fuel Reprocessing . . . 4

1.2 PuO_2 Stockpile . . . 6

1.2.1 Reuse . . . 7

1.2.2 Immobilisation . . . 8

1.2.3 Interim Storage - Gas Generation . . . 9

1.3 Plutonium Dioxide . . . 11

1.4 Research Aims . . . 12

1.5 Thesis Structure . . . 13

2 Methodology 14

2.1 Force Field Methods . . . 15

2.1.1 The Long Range Interaction . . . 16

2.1.2 The Short Range Interaction . . . 18

2.1.3 Empirical Fitting 18
2.1.4 Modelling Ionic Polarisation 19
2.2 Energy Minimisation 20
2.2.1 Potential Energy Surface 20
2.2.2 First-Order Solvers 21
2.2.3 Second-Order Solvers 22
2.2.4 Dynamic Relaxation 23
2.2.5 Nudged Elastic Band 23
2.3 Static Bulk Simulation Methodology 24
2.3.1 Symmetry Optimisation 24
2.3.2 Bulk Properties 25
2.3.3 Modelling Defects 26
2.3.4 Defect Visualisation Methodology 28
2.3.5 Defect Notation 29
2.4 Static Surface Simulation Methodology 29
2.4.1 Pure Surfaces 29
2.4.2 Morphology 31
2.4.3 Defective Surfaces 31
2.5 Molecular Dynamics 32
2.5.1 Equations of Motion 33
2.5.2 Periodic Boundary Conditions 34
2.5.3 Ensembles 35
2.5.4 Mean Square Displacement 36
2.5.5 Summary 37

3 Bulk Plutonium Dioxide **39**
3.1 Literature Review 39
3.2 Review of Interatomic Potentials 41
3.2.1 Interatomic Potentials for PuO_2 42
3.2.2 Results and Discussion 46
3.2.3 Summary 50
3.3 Mott-Littleton Region Optimisation 51
3.3.1 Methodology 51
3.3.2 Results 51
3.4 Isolated Defect Incorporation 54
3.4.1 Point Defects 54
3.4.2 Intrinsic Defects 58

3.5 Cluster Defect Incorporation . . . 59
3.6 Binding Energies . . . 63
3.6.1 Discussion . . . 64
3.7 Conclusions . . . 67

4 Surfaces of Plutonium Dioxide **69**
4.1 Literature Review . . . 69
4.2 Pure Surfaces . . . 71
4.2.1 The (100) Surface . . . 73
4.2.2 The (110) Surface . . . 74
4.2.3 The (111) Surface . . . 75
4.2.4 Morphology . . . 76
4.3 Defective Surfaces . . . 77
4.3.1 Isolated Surface Defects . . . 77
4.3.2 Intrinsic Defects . . . 79
4.4 Conclusions . . . 82

5 Static Helium Incorporation **83**
5.1 Literature Review . . . 83
5.2 Dremov Potential . . . 85
5.2.1 Fitting Procedure . . . 87
5.2.2 δ-Pu—He . . . 88
5.2.3 α-Pu—He . . . 91
5.2.4 He—He . . . 94
5.2.5 Summary . . . 97
5.3 Helium Potential Evaluation . . . 97
5.3.1 Grimes Potential . . . 97
5.3.2 Aziz Potential . . . 97
5.3.3 Dremov Potential . . . 98
5.3.4 Evaluation . . . 98
5.4 Helium Incorporation in Pure PuO_2 . . . 100
5.4.1 Single Helium . . . 100
5.4.2 Two Helium Atoms . . . 102
5.4.3 Helium Build-Up . . . 104
5.5 Helium in Defective PuO_2 . . . 105
5.5.1 Single Helium . . . 105
5.5.2 Helium Build-Up . . . 108

5.6 Conclusions . . . 118

6 Molecular Dynamics of Plutonium Dioxide 120
6.1 Literature Review . . . 120
6.2 Potential Evaluation . . . 122
6.2.1 Lattice Parameter . . . 122
6.2.2 Defect Calculations . . . 124
6.3 Diffusion in PuO_2 . . . 124
6.4 Diffusion in Defective PuO_2 . . . 132
6.5 Conclusions . . . 137

7 Helium Diffusion 139
7.1 Literature Review . . . 139
7.2 Helium Potential . . . 141
7.2.1 Helium Incorporation . . . 143
7.3 Migration Pathways . . . 145
7.4 Helium Diffusion . . . 147
7.4.1 Literature Comparison . . . 150
7.4.2 Helium Concentration . . . 152
7.4.3 Migration Pathways Analysis . . . 159
7.5 Defect Inclusion . . . 161
7.5.1 Schottky Trios . . . 161
7.5.2 Frenkel Pairs . . . 165
7.5.3 Helium Input Position . . . 167
7.6 Conclusions . . . 179

8 Helium Clustering 180
8.1 Literature Review . . . 180
8.2 Energy Minimisation . . . 182
8.2.1 Procedure . . . 182
8.2.2 Example: He_3V_3 . . . 184
8.2.3 Results . . . 186
8.2.4 Trapping Energies . . . 188
8.3 Energy barriers . . . 190
8.3.1 Nearest Neighbour Position . . . 190
8.3.2 Example: 1 He joins a He_6V_{12} cluster . . . 192
8.3.3 Example: 1 He leaves a $He_{17}V_{12}$ cluster . . . 194

8.3.4 Results . . . 195
8.4 Molecular Dynamics, Schottky Void . . . 199
8.4.1 0.5% Helium . . . 200
8.4.2 1% Helium . . . 201
8.4.3 2% Helium . . . 202
8.4.4 4% Helium . . . 206
8.4.5 7.7% Helium . . . 208
8.4.6 14.3% Helium . . . 212
8.5 Molecular Dynamics, Defect-Free PuO_2 . . . 215
8.5.1 Configurations . . . 215
8.5.2 Cluster Analysis . . . 218
8.5.3 Comparison . . . 226
8.6 Conclusions . . . 229

9 Conclusions **230**
9.1 Future Work . . . 233

Appendix A **235**

Appendix B **263**

References **266**

Publications

E. Murray , N. Palmer , W. Neilson , R. Jackson , M. Read , H. Steele and R. Orr. *Atomistic Simulation of Helium Incorporation in PuO_2. Proceedings of the WM Symposia*, 2022, **22512**

E. Murray, Y. Zhou, P. Slater, R. Smith, P. Goddard, H. Steele. *Atomistic Simulation of Helium Diffusion and Clustering in Plutonium Dioxide. Phys. Chem. Chem. Phys.*, 2022, **24**, 20709-20720

Figures

1.1 Schematic displaying the nuclear fuel cycle, the front end of the cycle is in blue and the back end of the cycle is in orange. 2
1.2 Schematic displaying the process of electricity generation from heating water to generate steam which turns a turbine. 3
1.3 Schematic displaying an example fission of $^{235}_{92}$U. 4
1.4 Schematic displaying the PUREX process which is used to separate plutonium and uranium from irradiated nuclear fuel. In the three cylinders the top is the organic phase and the bottom the aqueous phase. 5
1.5 Options under consideration by the UK government for the disposition of plutonium. From [3]. 7
1.6 Cutaway diagram of a multiple barrier containment Magnox PuO_2 storage can. From [40]. 10
1.7 Figure displaying the observed unit cell of PuO_2. From [55]. 11
1.8 Figure displaying plutonium decay and the generation of defects. Adapted from [45]. 12

2.1 Graph displaying range of computational chemistry methods over the time and size scales they occupy. 14
2.2 Graph displaying the potential energy, V, against the interatomic distance, r, showing the breakdown into long and short range components. 16
2.3 Schematic displaying the separation of the potential into real and reciprocal space via the Ewald summation method. 17
2.4 The shell model. 19
2.5 Local and global minimums. 20
2.6 Representation of finding the minimum energy site from start site x_0 via steepest decent (purple line) and conjugate gradient (green line) methods. 22

2.7 Visualisation of the regions used in Mott-Littleton methodology. From [55]. 27
2.8 Schematic representation of a surface [93]. 30
2.9 Schematic representation of a modelling a defect on a surface. 32
2.10 Schematic representation of periodic boundary conditions. Purple spheres represent atoms. 35
2.11 Schematic of the molecular dynamics simulation procedure employed in this thesis. 38

3.1 Graph displaying the point defect energy and number of ions in the region against radius for O^{2-} vacancy used in order to optimise the Mott-Littleton regions. 53
3.2 Region I centred on a plutonium vacancy after relaxation. O atoms are red, Pu are blue. 55
3.3 Plutonium vacancy visualisation. LHS: before relaxation, RHS: after relaxation. O atoms are red, Pu are blue. 56
3.4 Oxygen vacancy visualisation. LHS: before relaxation, RHS: after relaxation. O atoms are red, Pu are blue. 56
3.5 Plutonium interstitial with regions of lattice distortion labelled ′a′ and ′b′. LHS: before relaxation, RHS: after relaxation. O atoms are red, Pu are blue. 57
3.6 Oxygen interstitial visualisation. LHS: before relaxation, RHS: after relaxation. O atoms are red, Pu are blue. 57
3.7 Plutonium Frenkel Pair visualisation. LHS: before relaxation, RHS: after relaxation. 60
3.8 Visualisation of an oxygen Frenkel pair. 60
3.9 Oxygen Frenkel Pair defect with lattice distortion regions labelled. LHS: before relaxation, RHS: after relaxation. Circled regions ′a′ and ′b′ indicate regions of oxygen ion distortion. 61
3.10 Visualisation of the Schottky trio configurations. From [55]. 62
3.11 Schottky trio defect. LHS: before relaxation, RHS: after relaxation. . 63
3.12 Plutonium Frenkel pair visualisation after relaxation. 65
3.13 Defect energies of unbound and bound intrinsic defects in PuO_2. . . . 66
3.14 Defect energies of OFP, PuFP and Schottky trios PuO_2 from avaliable literature studies. Authors are Read [49], Tiwary [133], Cooper [122], Wang [121], Lu [119], Freyss [130], Tian [131], Nakamura [120] and Neilson [132]. 67

4.1 Bar Chart displaying the surface energies for the $\{n10\}$, $\{n11\}$ and $\{nn1\}$ surfaces (n=1,2,3), both before and after relaxation. 72
4.2 The (100) surface, LHS before relaxation, RHS after relaxation. . . . 74
4.3 The (110) surface, LHS before relaxation, RHS after relaxation. . . . 75
4.4 The (111) surface, LHS before relaxation, RHS after relaxation. . . . 76
4.5 Wulff construction for PuO_2. 76
4.6 Defect segregation energies at varying depths for different defects on each low index surface: (a) oxygen vacancy (b) plutonium vacancy (c) oxygen interstitial (d) plutonium interstitial. 78
4.7 The (100) surface with ions labelled numerically and interstitial sites labelled alphabetically. 79
4.8 The (110) surface with ions labelled numerically and interstitial sites labelled alphabetically. 80
4.9 The (111) surface with ions labelled numerically and interstitial sites labelled alphabetically. 80

5.2 Screenshot displaying MATLAB code used for the fitting procedure. . 87
5.3 Function fitting to the δ-Pu—He using (a) Lennard-Jones, (b) Morse, (c) Buckingham and (d) Born-Mayer. 89
5.4 Function fitting to the α-Pu—He using (a) Lennard-Jones, (b) Morse, (c) Buckingham and (d) Born-Mayer. 92
5.5 Function fitting to the He—He using (a) Lennard-Jones, (b) Morse, (c) Buckingham and (d) Born-Mayer. 95
5.6 Visualisations from the study of helium potentials to examine if the helium atom migrated to a plutonium vacancy upon atomic relaxation. Displaying (a) input configuration, and (b) output configurations of all potential combinations. 99
5.7 PuO_2 unit cell with Helium interstitial in the OIS, the most energetically stable site in defect-free PuO_2. 101
5.8 Energy profile map of the incorporation energy of helium at lattice sites in PuO_2. The colour bar corresponds to the magnitude of the defect energy with red being high and blue being low. The lattice was divided into five planes in the z-axis. 102
5.9 Two He atoms initially in edge-centred positions form a dumbbell configuration around the OIS upon atomic relaxation. 103

5.10 Mechanisms for helium dumbbell formation. In (a) helium atoms migrate from separate OISs, in (b) one helium joins another in an OIS. Figure from [156], oxygen atoms are red, plutonium atoms are blue. 104
5.11 Energy barrier between two configurations when two He atoms move from different OISs and form a dumbbell. (a) Two He atoms move simultaneously to the nearest empty OIS, and (b) one He moves to the other He trapped at an OIS. 104
5.12 Defect energy of He interstitials in separate OIS as a function of the number of He atoms. There is a linear increase in defect energy as the number of He atoms in the lattice increases. 105
5.13 Energy profile map of a helium atom at various locations surrounding an oxygen vacancy at (0.25,0.25,0.25). 107
5.14 Energy profile map of a helium atom at various locations surrounding an plutonium vacancy at (0.5,0.5,0.5). 108
5.15 Defect energies of three configurations of two helium atoms and an oxygen vacancy. 109
5.16 Six helium atoms in OISs surrounding a V_{Pu} (a) and a V_O (b), before and after relaxation. 111
5.17 Defect energies of six configurations of two helium atoms and a Schottky trio defect. 112
5.18 Relaxed He configurations surrounding a Schottky trio. 113
5.19 Graphic displaying two He atoms in a dumbbell configuration at an OIS by an oxygen Frenkel pair and the relaxation pathway: (a) displays the initial configuration, (b) displays the migration pathways, and (c) displays the relaxed configurations. 115
5.20 Graphic displaying OFP3 configuration. Figure (a) displays OFP before and after relaxation, the Frenkel pair recombines. Figure (b) has a He atom accommodating the oxygen vacancy site which prevents the recombination of the OFP. 116
5.21 Normalised incorporation energy of He at various defect sites for up to 12 He atoms. 117
5.22 Successive energy of incorporation of Helium at defect sites. Black dashed line at 1.06 eV is the incorporation energy of He at an isolated OIS for comparison. 118

6.1 Lattice parameter as a function of temperature for three different interatomic potentials in comparison to experimental data of PuO_2. . 123
6.2 MSD versus time for oxygen at 2500 K in PuO_2. The red line indicates the linear line of best fit, with the fit details displayed. 125
6.3 Oxygen MSD in PuO_2 at three temperatures. 126
6.4 Plutonium MSD in PuO_2 at three temperatures. 127
6.5 The volume variation of the simulation cell, and the Pu and O mean squared displacements as a function of time at 1200 K. 128
6.6 Oxygen and plutonium diffusivity as a function of temperature in PuO_2. The yellow region indicates no diffusive behaviour. 129
6.7 Oxygen diffusivity as a function of temperature in PuO_2 by this work and available data [a][121], [b][122], [c][169], [d][174], [e][175], [f][184]. 131
6.8 Number of vacancies within the system as a function of simulation time for three temperatures: 2700 K, 2800 K, and 2900 K. 132
6.9 Number of clusters before and after energy minimisation (performed at 0 K) for three configurations of lattices containing 0.5, 2 and 4% Schottky trios. 133
6.10 Oxygen diffusivity as a function of temperature in PuO_2 with increasing concentrations of Schottky defects. The yellow highlight indicates lnD values that correspond to no diffusion. 134
6.11 Plutonium diffusivity as a function of temperature in PuO_2 with increasing concentrations of Schottky defects. The yellow highlight indicates lnD values that correspond to no diffusion. 135
6.12 Trajectories of oxygen and plutonium ions in PuO_2 with a 2% Schottky concentration at 1700 K (only six O trajectories are displayed). . 137

7.1 Helium incorporation energies at sites in AO_2 where A is an actinide. Results of this work and other authors for PuO_2 ([a][154], [b][130], [c][131], [d][132]), ThO_2 ([e][155]) and UO_2 ([f][163]). 145
7.2 Relative energy barriers for different helium migration pathways between two interstitial sites in PuO_2 from NEB calculations. A direct OIS-OIS hop (green squares) has the highest energy barrier, migrating via an V_O (blue circles) has a much lower energy barrier and via a V_{Pu} (pink triangles) there is a negative energy at the plutonium vacancy site. 146

7.3 Diffusivity as a function of temperature for He, O and Pu in PuO_2. 0.5% He concentration, simulation evolved for 4 ns at every 100 K between 1000-3000 K. Three regions are highlighted, R1, R2 and R3, and are discussed in the text. 147
7.4 MSD of Pu, O and He in an 8x8x8 supercell at 1200, 2000 and 2800 K.149
7.5 Visualisation of helium atoms, plutonium vacancies and oxygen vacancies after 4 ns. The lattice was initially defect-free with 0.5% He input in OIS, molecular dynamics was run with temperatures of (a) 2000 K and (b) 2800 K. 150
7.6 Diffusivity as a function of temperature for all available literature data of helium diffusion experimentally in PuO_2 (Ronchi [200], Pipon [199]) and UO_2 (Roudil [188], Garcia [191], Talip [189], Belle [195], Trocellier [194], Guilbert [190], Martin [193], Sung [196], Nakajima [198], Rufeh [197]. And computational data of UO_2 (Govers [203], Liu [201], Yakub [202] and Nakajima [198]). 151
7.7 Three mechanisms of helium generation in nuclear fuel samples for experimental analysis. Adapted from [187]. 152
7.8 Percentage volume expansion as a function of the helium concentration in PuO_2, UO_2 and Pu. [a][156] [b][45]. Experiments show a typical volume expansion of 1% after large irradiation doses (Helen Steele, private communication) indicating a maximum He concentration of 5%. 153
7.9 The variation of helium diffusivity in PuO_2 as a function of temperature for four different helium concentrations (0.5, 2, 4 and 10 %). In the highlighted region no diffusive behaviour is exhibited. At 1750 K, the diffusivity starts to increase with increasing temperature. The high temperature diffusivity plateau region begins at lower temps for higher He concentrations. 154
7.10 Visualisation of helium atoms (yellow) and oxygen and plutonium vacancies (blue and pink respectively) after 1 ns in PuO_2 at 2000 K (LHS) and 2500 K (RHS) at three different helium concentrations. For clarity, oxygen and plutonium ions are not displayed. It can be seen that at higher helium concentrations (10%), helium clustering occurs at lower temperatures. 155

7.11 Bar chart displaying the percentage of helium atoms which occupy large clusters in lattices containing 0.5, 2, 4 and 10% helium over a range of temperatures. 156
7.12 Bar and line chart showing the percentage helium clustered (left-axis bar chart) and the helium diffusivity (right-axis line chart) for lattices with different helium concentrations over a range of temperatures. . . 158
7.13 Trajectory of He atoms in initially defect-free PuO_2 at 2100 K (a) displays the trajectory of all He atoms during 1 ns, it is evident there is inter-site hopping (b) displays a snapshot of a He inter-site hop from the area circled in green in (a). The time period in (b) is 514-517 ps and illustrates that part of a He atoms trajectory. It can be seen that at 515 ps an oxygen vacancy is generated in the vicinity of the He and the He uses this to migrate to a neighbouring OIS. 159
7.14 Configurations of helium atoms (yellow) alongside oxygen vacancies (blue) and plutonium vacancies (pink) after 1 ns at 1200 K (LHS) and 2400 K (RHS). 160
7.15 Helium MSD as a function of time over a range of temperatures for a PuO_2 lattice with 2% Schottky trios and a 2% helium concentration. 162
7.16 Helium diffusivity as a function of temperature for four different Schottky defect concentrations in PuO_2. The helium concentration was 2% with all helium atoms initially randomly inserted into OIS. In the lower temperature range when oxygen vacancies would not be being thermally generated, the higher Schottky concentrations have higher He diffusivity. The highlighted region indicates no diffusive behaviour. 163
7.17 Oxygen diffusion coefficients as a function of temperature in PuO_2 at four different Schottky defect concentrations. The yellow highlight indicates data points when no diffusive behaviour was exhibited. . . . 165
7.18 Diffusivity of helium in PuO_2 with the lattice containing different concentrations of randomly distributed oxygen Frenkel pairs. The yellow highlighted region indicates no diffusive behaviour. 166
7.19 Diffusivity of helium in PuO_2 with the lattice containing different concentrations of randomly distributed plutonium Frenkel pairs. . . . 167

7.20 Helium diffusivity in a PuO_2 lattice with a 2% concentration of Schottky trio defects. The helium atoms were input in OIS, V_O and V_{Pu} in separate simulations for comparison. The lines of best fit for the Arrhenius behaviour calculations are also plotted. 168
7.21 Trajectory of helium atoms in PuO_2 with a 2% Schottky defect concentration at 2250 K over 1 ns. (a) Displays the trajectory when the helium started in V_O sites (blue lines) and (b) when the helium atoms started in V_{Pu} sites (pink lines). There is much less inter-site hopping when helium atoms are input at plutonium vacancies. 169
7.22 Helium diffusivity in a PuO_2 lattice with a 0.5% concentration of plutonium Frenkel pairs. The helium atoms were input in OIS and PuFPs in separate simulations for comparison. 170
7.23 Visualisation from MD simulation of a PuO_2 lattice with 0.5% He and 0.5% PuFPs, with the He input in the V_{Pu} sites at 2250 K. (a) Displays the input configuration, the PuFPs can be seen with helium atoms occupying the vacancy sites. (b) Displays the configuration after 1 ns, the majority of the PuFPs have recombined with helium atoms now in interstitial sites. 171
7.24 Visualisation from molecular dynamics simulation of a PuO_2 lattice with 0.5% He and 0.5% PuFPs, with the He input in the V_{Pu} sites at 1250 K at 2 ps. Pu and O atoms have been removed for clarity. . . . 172
7.25 Helium diffusivity in a PuO_2 lattice with a 0.5% concentration of plutonium vacancies. The helium atoms were input in OIS and V_{Pu} in separate simulations for comparison. The yellow highlighted region indicates no diffusive behaviour. 173
7.26 Trajectory of helium atoms in PuO_2 with 0.5% plutonium vacancies at 2250 K. The simulation is split into two time periods. The top row illustrates the trajectory when He is input at V_{Pu} sites and the bottom row when He is input at OISs. 0-300 ps shows He in OIS with high mobility. 300-700 ps shows He occupying V_{Pu} sites. 174
7.27 Helium diffusivity in a PuO_2 lattice with a 0.5% concentration of oxygen Frenkel pairs. The helium atoms were input in OIS and V_O in separate simulations for comparison. The yellow highlighted region indications no diffusive behaviour. 175

7.28 Visualisation from MD simulation of a PuO_2 lattice with 0.5% He and 0.5% oxygen vacancies, with the He input in the V_O sites. (a) Displays the input configuration, the OFP can be seen with helium atoms occupying the vacancy sites. (b) Displays the configuration after 1 ps, some helium atoms now occupy OIS, but the OFPs have not recombined. 176
7.29 Helium diffusivity in a PuO_2 lattice with a 0.5% concentration of oxygen vacancies. The helium atoms were input in OIS and V_O in separate simulations for comparison. 177
7.30 Helium MSD in a PuO_2 lattice with a 0.5% concentration of oxygen vacancies at 2250 K. The helium atoms were input in OIS and V_O in separate simulations for comparison. 178

8.1 Examples of naming conventions of He:Vacancy clusters. (a) Displays examples of He:Vacancy clusters which all have a 2:3 ratio, but are based on 1, 2 and 4 Schottky trio defects. (b) Displays three possible configurations of the He_2V_3 cluster. 183
8.2 Flow chart detailing methodology followed for helium cluster energy minimisation calculations. 184
8.3 Example schematic of the energy minimisation procedure outlined in Figure 8.2. Each subfigure is discussed in the text. 185
8.4 Plots of the incorporation energies of multiple configurations of helium in clusters containing 1, 2 and 4 Schottky trios. 187
8.5 Incorporation energies and the minimum energy configurations for four different He_3V_6 input configurations (A, B, C and D). The output configurations are displayed colour coordinated with the bar chart energy for each configuration. 188
8.6 Trapping energies of He atoms at Schottky void sites as a function of a cluster's He:Vacancy ratio. A more negative trapping energy means a more energetically favourable site for helium to occupy. Three seed locations for the clusters were considered, made of 1, 2 and 4 Schottky defect clusters. 189

8.7 Energy to incorporate successive He atoms at Schottky void sites as a function of the cluster's He:Vacancy ratio. The orange straight line at 1.7 eV is the energy to incorporate He at an isolated OIS. When the incorporation energy is greater than this line it is less favourable for an additional He to join the cluster than to exist in isolation occupying an OIS. 190
8.8 Schematic displaying the nearest neighbour positions surrounding a He_2V_6 cluster with a helium atom occupying the 5th nearest neighbour position (5N). 191
8.9 Graph displaying the energy barrier for one helium atom to join a He_nV_3 cluster (where $n = 2, 4, 6$) from 1-6 nearest neighbour positions (N). 192
8.10 Energy barrier calculation for a helium atom joining a He_6V_{12} cluster. (a) Displays the relative energies at each image from the calculation. (b) Displays the migration pathway for a helium atom. The helium configurations from images 1, 6 and 9 are highlighted and discussed in the text. Each helium atom is labelled according to its corresponding image. 193
8.11 Energy barrier calculation for a helium atom leaving a $He_{17}V_{12}$ cluster. (a) Displays the relative energies at each image from the calculation. (b) Displays the migration pathway for a helium atom. The helium configurations from images 2 and 5 are highlighted and discussed in the text. Each helium atom is labelled according to its corresponding image. 195
8.12 Energy barriers for a helium joining (purple squares) or leaving (green circles) a cluster with various He:Vacancy ratios. 197
8.13 Difference in energy barriers for a He interstitial to join and leave a cluster as a function of a cluster's He:Vacancy ratio. When the energy difference becomes negative, it requires more energy for helium to join the cluster than to leave it, so the maximum energetically favourable He:Vacancy ratio is at this point. Three Schottky seed location sizes were considered (1, 2 and 4 Schottkies) and the average maximum stable He:Vacancy ratio was $\sim$ 3:1. 198
8.14 PuO_2 lattice with three Schottky trios clustered in the centre. The vacancies are displayed in black, Pu atoms in pink and O atoms in blue. 199

8.15 Legend of the colours of Pu vacancies (pink), O vacancies (blue), and He interstitials (yellow). 200
8.16 Lattice containing 0.5% helium and a cluster of three Schottky trios in the centre. (a) Displays the input configuration. (b), (c) and (d) are the configurations after molecular dynamics was run at 750, 1500 and 2250 K respectively. 200
8.17 Lattice containing 1% helium and a cluster of three Schottky trios in the centre. (a) Displays the input configuration. (b), (c) and (d) are the configurations after molecular dynamics was run at 750, 1500 and 2250 K respectively. 201
8.18 Configuration of helium atoms and oxygen and plutonium vacancies after a 5 ns simulation at 2250 K with initial input of 1% helium atoms in OISs. 202
8.19 Lattice containing 2% helium and a cluster of three Schottky trios in the centre. (a) Displays the input configuration. (b), (c) and (d) are the configurations after molecular dynamics was run at 750, 1500 and 2250 K respectively. 203
8.20 Helium migration to a cluster of three Schottky trios during a 1 ns simulation at 1500 K. (a) Displays the trajectories (orange) of all four helium atoms which migrate into the vacancies, they are labelled in order of migration time. (b), (c), (d) and (e) display detail of how the migration occurred and are discussed in the text. 205
8.21 Lattice containing 4% helium and a cluster of three Schottky trios in the centre. (a) Displays the input configuration. (b), (c) and (d) are the configurations after molecular dynamics was run at 750, 1500 and 2250 K respectively. 206
8.22 PuO_2 supercell with 4% He concentration. Initially three Schottky trios were input in the centre of the lattice with the He atoms randomly occupying OISs. Cluster formation is shown at different times and He:Vacancy ratios labelled. 207
8.23 Lattice containing 7.7% helium and a cluster of three Schottky trios in the centre. (a) Displays the input configuration. (b), (c) and (d) are the configurations after molecular dynamics was run at 750, 1500 and 2250 K respectively. 208

8.24 Lattice containing 7.7% helium and a cluster of three Schottky trios in the centre, (a) and (c) display the helium atoms clustered at 750 and 1500 K respectively, (b) and (d) display the initial position of the helium atoms which join the cluster and their trajectories (orange) for 750 and 1500 K respectively. 209
8.25 Lattice containing 7.7% helium after molecular dynamics has been run for 1 ns at 2250 K. Only helium atoms are displayed. Cluster analysis has been performed and the helium atoms coloured according to which cluster they occupy. 12 clusters are labelled. 211
8.26 Lattice containing 14.3% helium and a cluster of three Schottky trios in the centre. (a) Displays the input configuration, (b), (c) and (d) are the configurations after molecular dynamics was run at 750, 1500 and 2250 K respectively. 212
8.27 Lattice containing 14.3% helium and a cluster of three Schottky trios in the centre, only the helium atoms and vacancies clustered are displayed. The simulation was run for 1 ns at 1500 K. (a) Displays the cluster. (b) Displays the helium atoms initial positions and the migration pathways taken to the cluster (orange). 213
8.28 Lattice containing 14.3% helium after molecular dynamics has been run for 1 ns at 2250 K. Only helium atoms are displayed. Cluster analysis has been performed and the helium atoms coloured according to which cluster they occupy. The 12 largest clusters are labelled. . . 214
8.29 Legend of the colours of Pu vacancies (pink), O vacancies (blue), and He interstitials (yellow). 215
8.30 Lattice containing 0.5% helium evolved at 2250 K for 5 ns. 215
8.31 Lattice containing 1% helium evolved at 2250 K for 5 ns. 216
8.32 Lattice containing 2% helium evolved at 2250 K for 5 ns. 216
8.33 Lattice containing 4% helium evolved at 2250 K for 5 ns. 217
8.34 Lattice containing 7.7% helium evolved at 2250 K for 5 ns. 217
8.35 Lattice containing 14.3% helium evolved at 2250 K for 5 ns. 218

8.36 The number of helium clusters (left y-axis, red) and the number of vacancies (right y-axis, blue) as a function of time. The simulation was of PuO_2 at 2250 K with a 4% He concentration. As the number of vacancies increases, the number of clusters decreases, as more helium atoms are joining clusters so the overall number decreases as there are fewer, bigger helium clusters. After 3000 ps a stable state of the number of He clusters and lattice vacancies is established. 220
8.37 Histogram of the He:Vacancy ratio of large ($\geq$9 He) clusters formed after (a) 1 ns and (b) 5 ns for different helium concentrations in PuO_2 with 2% Schottky concentration. (a) After 1 ns at the mode He:Vacancy ratio was 0.7:1. (b) After the system was evolved for 5 ns, large clusters had formed for all helium concentrations. The mode He:Vacancy ratio was 0.5:1. The number of clusters is significantly reduced as smaller clusters have merged together. 221
8.38 Configuration of a He_2V_3 cluster formed after 5 ns at 2400 K. 222
8.39 Bar and line chart showing the percentage of helium atoms occupying a cluster (left-axis bar chart) and the helium diffusivity (right-axis line chart) over a range of temperatures. 223
8.40 Scatter plot with three y-axes detailing the evolution of the largest He cluster as a function of time. The left y-axis (dark grey) plots the No. of He atoms and the right y-axis (grey) plots the No. of vacancies in the largest cluster. The far right y-axis (pink) plots the He:Vacancy ratio for the largest cluster. 224
8.41 Box plot of the He:Vacancy ratio of the largest cluster at each temperature in which clustering was observed during 5 ns. Dashed orange line through y=1. The mean values are displayed. 225
8.42 Bar chart displaying the number of helium clusters formed after 1 ns in initially defect-free PuO_2 (green) and a lattice containing three Schottky trios (pink) at 2250 K. 226
8.43 Bar chart displaying the number of helium clusters formed after 5 ns in initially defect-free PuO_2 (green) and a lattice containing three Schottky trios (pink) at 2250 K. 227
8.44 Bar chart displaying the number of plutonium vacancies in a PuO_2 lattice containing 0.5% helium after 5 ns at a range of temperatures. . 228

1 MSD of Pu, O and He in an 10x10x10 supercell at 1200, 2000 and 2800 K including the initial 1 ns equilibriation period. 264

2 MSD of Pu, O and He in an 12x12x12 supercell at 1200, 2000 and 2800 K including the initial 1 ns equilibriation period. 265

Tables

3.1 Names of the combinations of potentials used in this work 42
3.2 Parameters of the Read potential 43
3.3 Parameters of the Arima1 potential 44
3.4 Parameters of the Arima2 potential 44
3.5 Parameters of the Yu potential 45
3.6 Observed values of PuO_2 structural properties 46
3.7 Results of structural properties of PuO_2 47
3.8 Observed values of PuO_2 mechanical properties 48
3.9 Results of mechanical properties of PuO_2 49
3.10 Observed values of PuO_2 optical properties 50
3.11 Results of optical properties of PuO_2 50
3.12 Mott-Littleton region optimisation for four defects in PuO_2 52
3.13 Point defect coordinates 54
3.14 Defect formation energies for isolated defects 54
3.15 Defect formation energy for unbound defects 58
3.16 Calculated oxygen Frenkel pair defect formation energies for the two configurations considered 61
3.17 Schottky Trio defect coordinates for cluster calculations 62
3.18 Calculated Schottky trio defect formation energies 63
3.19 Intrinsic defect formation energies 64

4.1 Calculated and reported energies of low index PuO_2 surfaces 73
4.2 Isolated defect energies on PuO_2 surfaces 77
4.3 Intrinsic Defects on the (100), (110) and (111) Surfaces. Energies in eV/Defect 81

5.1 Dremov *et al.* [44] parameters for the exp-6 potential 86
5.2 Fitting Results for δ-Pu—He 90

5.3 Fitting Results α-Pu—He . . . 93
5.4 Fitting Results He—He . . . 96
5.5 Parameters of the Grimes potential [158] . . . 97
5.6 Parameters of the Aziz He—He potential [161] . . . 98
5.7 Parameters of the Dremov potential fitted to a Buckingham potential 98
5.8 Incorporation energies of He at different vacancies in AO_2. Where A is an actinide . . . 106

6.1 Lattice parameter as a function of the PuO_2 supercell size for 1 ns simulations at 1000 K . . . 122
6.2 Intrinsic defect energies in PuO_2 calculated in LAMMPS . . . 124
6.3 The three Shottky concentrations considered and the number of constituent Pu and O vacancies . . . 132
6.4 Parameters calculated from Arrhenius behaviour exhibited by oxygen in PuO_2 in the mid and high temperature regimes (R2 and R3) . . . 136

7.1 Parameters of the Aziz potential to describe the He—He interaction [161] . . . 143
7.2 Incorporation energy of helium occupying an OIS for increasingly large supercells . . . 144
7.3 Parameters calculated from Arrhenius behaviour exhibited by helium in PuO_2 with various Schottky concentrations . . . 163
7.4 Parameters calculated from Arrhenius behaviour exhibited by helium in PuO_2 with a 2% Schottky concentration with different helium input sites . . . 168

8.1 Coordinates of the nearest neighbour octahedral interstitial sites moving further outwards . . . 191
8.2 Helium concentrations considered and the number of helium atoms they correspond to . . . 199
8.3 Detailing the number of helium atoms and vacancies in each cluster displayed in Figure 8.25 and the He:Vacancy ratio calculated for each 211
8.4 Detailing the number of helium atoms and vacancies in each cluster displayed in Figure 8.28 and the He:Vacancy ratio calculated for each 214
8.5 The number of large helium clusters ($\geq$ 9 He) formed after 1 ns and 5 ns in PuO_2 at 2250 K and the number of helium atoms in the largest clusters . . . 219

Abbreviations

μVT Grand canonical ensemble.

BFGS Broydon-Fletcher-Goldfarb-Shanno.

CHAOS Computer Simulation HADES on Surfaces.

DFT Density Functional Theory.

DNC Did Not Converge.

EAM Embedded-Atom Method.

GDF Geological Disposal Facility.

GGA Generalised Gradient Approximation.

GGA+U Generalised Gradient Approximation with the Hubbard U correction.

GULP General Utility Lattice Program.

HIP Hot Isostatic Pressing.

HLW High Level Waste.

HPC High Performance Computing.

ILW Intermediate Level Waste.

LAMMPS Large-scale Atomic/Molecular Massively Parallel Simulator.

LDA+U Local Density Approximation with the Hubbard U correction.

LEED Low Energy Electron Diffraction.

LJ Lennard-Jones.

LSDA+U Local Spin Density Approximation with the Hubbard U correction.

LWR Light Water Reactors.

MD Molecular Dynamics.

METADISE Minimum Energy Techniques Applied to Dislocations, Interface and Surface Energies.

MOX Mixed Oxide.

MSD Mean Square Displacement.

NDA Nuclear Decommissioning Authority.

NEB Nudged Elastic Band.

NPT Isothermal-isobaric ensemble.

NVE Micro-canonical ensemble.

NVT Canonical ensemble.

OFP Oxygen Frenkel Pair.

OIS Octahedral Interstitial Site.

PBE+U Perdew-Burke-Ernzerhof with the Hubbard U correction.

PPPM particle-particle-particle-mesh.

PuFP Plutonium Frenkel Pair.

PUREX Plutonium URanium EXtraction.

TEM Transmission Electron Microscopy.

$\mathbf{V_O}$ oxygen vacancy.

$\mathbf{V_{Pu}}$ plutonium vacancy.

VASP Vienna Ab initio Simulation Package.

XRD X-Ray Diffraction.

YSZ Yttria-Stabilized Zirconia.

ZBL Ziegler-Biersack-Littmark.

Chapter 1

Introduction

Nuclear power is set to play an essential role in the supply of reliable low-carbon energy for achieving urgent climate change mitigation [1]. The UK is committed to the use of nuclear power to achieve its target of net-zero carbon emissions by 2050 [2]. At present, the UK has the largest stockpile of civil separated plutonium in the world, with approximately 140 tonnes stored as PuO_2 powder at Sellafield in Cumbria [3]. This plutonium is a by-product of the nuclear fission of uranium from legacy reactors. The UK Government is developing a long-term solution for this material, with one option being re-use as Mixed Oxide (MOX) fuel in future reactors to supply new low-carbon energy. However the implementation of the long-term solution will take decades, requiring the continued safe and secure storage of PuO_2 powder within inert nested steel storage cans [3]–[5].

A key concern for the continued storage of the PuO_2 is the pressurisation of the canisters, with radiogenic helium gas generation being a potential mechanism. Helium could diffuse to form large bubbles and at some point be released from the lattice. Through the use of computational simulations, this research aims to provide a deeper understanding of helium behaviour in PuO_2. Whilst there is operational experience in the safe and secure storage of PuO_2 [6], there remains a need to scientifically underpin long-term storage through better understanding of the fundamental chemical and physical processes occurring within the storage cans [3].

1.1 Nuclear Fuel Cycle

Nuclear power stations currently provide approximately 20% of the UK's electricity supply [7]. UK policy aims to reduce greenhouse gas emissions by 80% by 2050 [8]. As nuclear power stations provide a low-carbon source of electricity, nuclear fuel will

continue to play an essential role in the UK energy supply [9].

A schematic of the nuclear fuel cycle is displayed in Figure 1.1. The fuel cycle can be split into two sections: the front and back end. The front end consists of the fuel mining and fabrication process for new fuel. The back end of the cycle consists of how the spent fuel is treated, stored and the future options of the fuel. A nuclear fuel cycle can either be an open or closed fuel cycle. In an open fuel cycle the spent fuel is disposed of; in a closed fuel cycle the spent fuel is reprocessed for use in future reactors.

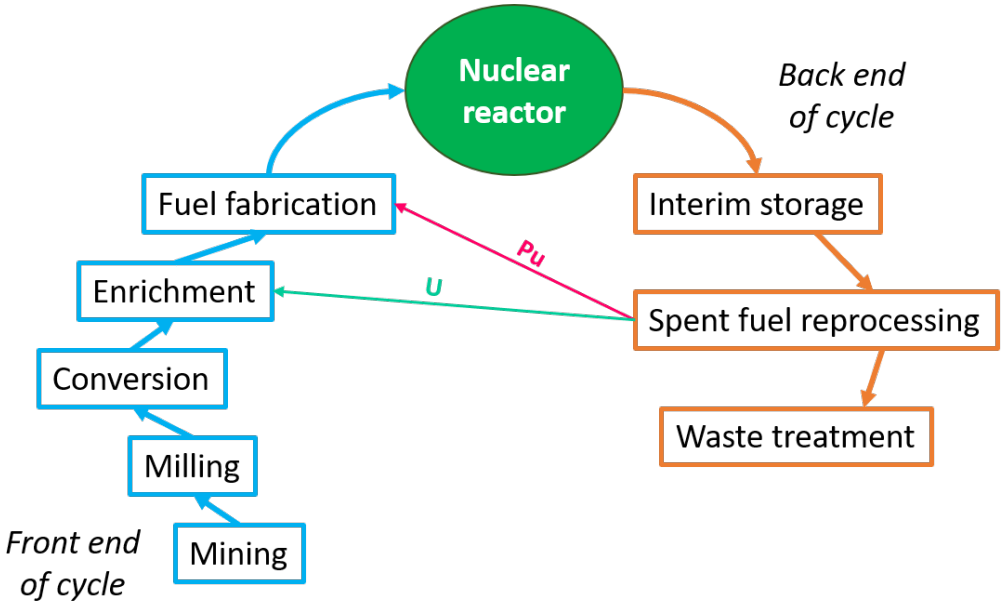


Figure 1.1: Schematic displaying the nuclear fuel cycle, the front end of the cycle is in blue and the back end of the cycle is in orange.

The pink arrow in Figure 1.1 indicates the recycling of reprocessed plutonium from spent fuel to be used in future reactors. At present, the UK is yet to implement this stage in the fuel cycle and as such has generated a stockpile of reprocessed civil PuO_2. It is the ageing of this stockpile that is the focus of this research. The following sections will detail how the plutonium was generated and the necessary considerations for the future of the UK's plutonium inventory.

1.1.1 *Nuclear Reactor*

A nuclear power plant works in a similar way to any typical coal fired power plant, in that water is heated to generate steam which turns a turbine as displayed by Figure 1.2. The spinning turbine is coupled to an electromagnet which spins inside

a coil of copper wire. Due to Faraday's law, electricity is produced. This electricity is stepped up at a transformer and fed to the grid to supply energy [1].

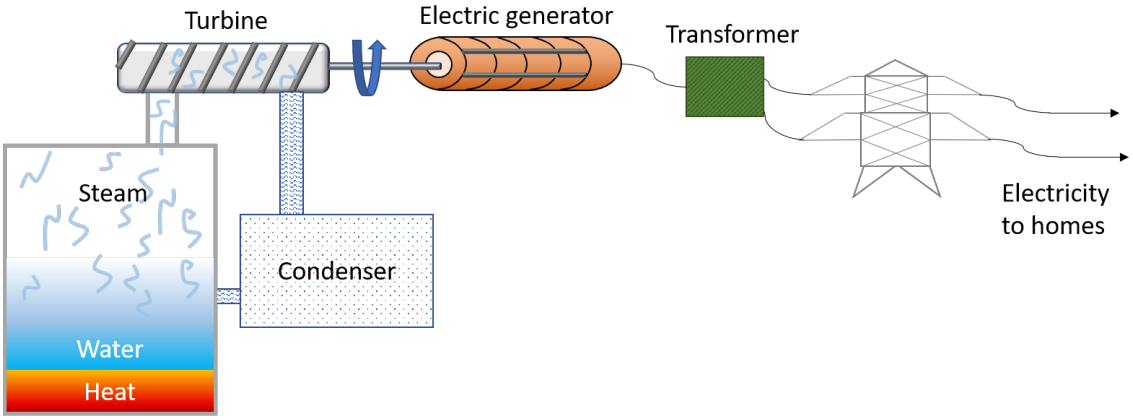


Figure 1.2: Schematic displaying the process of electricity generation from heating water to generate steam which turns a turbine.

In the case of a nuclear power plant, it is nuclear fission which generates the heat to heat water. Unlike coal fired plants, no CO_2 gas is generated, making nuclear power a clean (low-carbon) energy [1] [2].

Nuclear power plants use fuel that is typically either natural uranium composed of 0.7% ^{235}U or enriched uranium composed of 2-3% ^{235}U, with the rest being ^{238}U for both. ^{235}U is fissile (fissions with neutrons of all energies) while ^{238}U is fissionable (fission can be induced but only by neutrons of high enough incident energy) [10]. When a low-energy neutron is absorbed by an atom of ^{235}U, the atom fissions into two nuclei, releasing energy.

Nuclear fission is a nuclear reaction in which the nucleus of an atom splits into smaller parts. Figure 1.3 displays an example of the fission process. A slow neutron (n) is absorbed by a nucleus resulting in an unstable nucleus, (in this case ${}^{1}_{0}n + {}^{235}_{92}\mathrm{U} \rightarrow {}^{236}_{92}\mathrm{U}$). The unstable nucleus then fissions, and a large amount of energy is released with the unstable nucleus splitting into smaller nuclei and free neutrons (collectively called fission products) [11].

In the example displayed in Figure 1.3, the daughter nuclei are ${}^{92}_{36}\mathrm{Kr}$ and ${}^{141}_{56}\mathrm{Ba}$; three neutrons are also released. This fission can be written as ${}^{236}_{92}\mathrm{U} \rightarrow {}^{92}_{36}\mathrm{Kr} + {}^{141}_{56}\mathrm{Ba} + 3{}^{1}_{0}n$. From this it can be seen that the total number of nucleons (protons and neutrons) is conserved ($92 + 141 + 3 = 236$). However, the total mass of the fission products can be shown to be slightly less than the mass of the starting nucleus. This 'missing' mass is the key to nuclear power. The 'missing' mass ($\sim 0.1\%$ of initial mass) has been converted into energy in accordance with $E = mc^2$.

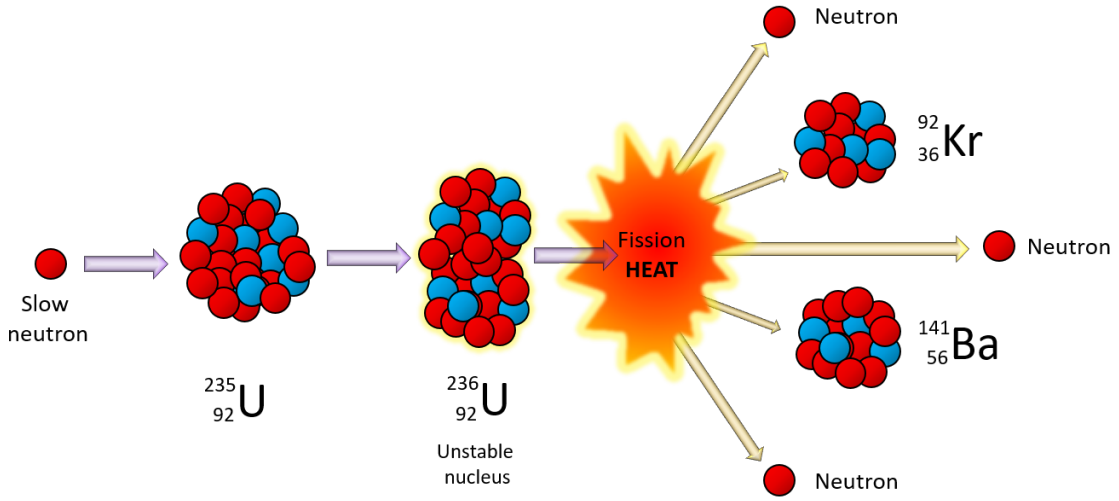


Figure 1.3: Schematic displaying an example fission of $^{235}_{92}$U.

The energy is the binding energy, which is the energy required per nucleon to separate a nucleus. As the fission products generated are more stable, it requires more energy to split them apart. Thus, their binding energies are higher. The difference in the binding energies of the original nucleus and the fission products is equivalent to the 'missing' mass via the Einstein relation [12].

One of the ejected neutrons may become captured by another $^{235}_{92}$U nucleus, and as such a chain reaction can be generated. A stable chain reaction is what powers a nuclear facility. The other neutrons may be absorbed by ^{238}U, which subsequently decays to ^{239}Pu [13]. Therefore, irradiated nuclear fuel contains a mixture of fission products, including plutonium and uranium [14].

There are many types of nuclear reactors worldwide, the UK's legacy fleet contains Magnox and Advanced-Gas cooled Reactors (AGRs) [15] [16]. Current plans are underway for building the next generation of nuclear power in the UK, with small modular reactors being developed [7].

1.1.2 *Spent Fuel Reprocessing*

Before reprocessing, irradiated fuel is kept in interim storage to enable short lived fission products to decay [3] [17].

Reprocessing is important for numerous reasons, including recovery of useful constituents of fuel for reuse, and for waste management. Reprocessing enables the reduction of the volume of fission products by concentration, which in turn results in lower volumes of High Level Waste (HLW).

In the UK, the Plutonium URanium EXtraction (PUREX) process has been

used to separate plutonium and uranium from the remaining fission products in irradiated nuclear fuel [10] [18]. Figure 1.4 displays a schematic of the PUREX process. PUREX is a multi step solvent extraction process which works via extracting a metal ion from an aqueous phase to an immiscible organic phase [19].

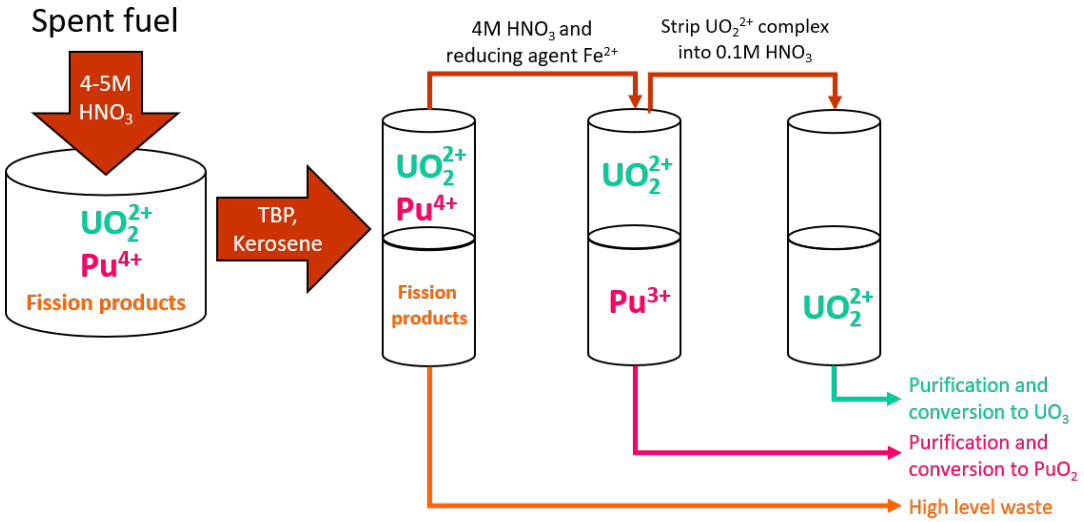


Figure 1.4: Schematic displaying the PUREX process which is used to separate plutonium and uranium from irradiated nuclear fuel. In the three cylinders the top is the organic phase and the bottom the aqueous phase.

The first step in the process is the acid dissolution of the spent fuel using nitric acid. From this the uranium will form $[UO_2(NO_3)_2(H_2O)_2]$ and the plutonium $[Pu(NO_3)_4]$, along with fission products. The first solvent extraction is to remove the fission products into the aqueous phase [19] [20].

The acid dissolutioned spent fuel is mixed with Tri-n-Butyl Phosphate (TBP) and kerosene which extracts the uranyl and plutonium species into the organic phase as $[UO_2(NO_3)_2(TBP)_2]$ and $[Pu(NO_3)_4(TBP)_2]$ complexes. From this the fission products are removed to be stored as HLW.

The second solvent extraction occurs after the organic phase is mixed with a reducing agent (Fe^{2+}) and nitric acid leading to:

$$Pu^{4+} + Fe^{2+} \rightleftharpoons Pu^{3+} + Fe^{3+} \tag{1.1}$$

$$UO_2^{2+} + Fe^{2+} \rightarrow \text{no reaction.} \tag{1.2}$$

The Pu is then in the aqueous phase as it has reduced to Pu^{3+} which does not form complexes with nitrate and is therefore non extractable. The plutonium is then purified and converted into PuO_2.

The final step is to strip the $[UO_2(NO_3)_2(TBP)_2]$ complex into 0.1 M HNO_3 leaving UO_2^{2+} in the aqueous phase. The uranium is purified and converted into UO_3.

Both of the UK's spent fuel reprocessing programs have now ended with THORP (Thermal Oxide Reprocessing Plant) closing in 2018 [3] and the Magnox reprocessing facility completing its work in 2022 [21]. As was displayed in Figure 1.1, in a closed loop system the uranium and plutonium would then undergo enrichment and fuel fabrication respectively. However, this stage has not yet been reached in the UK for the reprocessed plutonium. Rather, the separated plutonium is stored in powder form as PuO_2 in inert steel cans which are kept in reinforced concrete buildings above ground at Sellafield [22]. The legacy and future of this separated and stored plutonium will now be discussed.

1.2 PuO_2 Stockpile

The UK has the largest civil separated plutonium stockpile in the world at approximately 140 tonnes [3], accounting for 38% of global civil separated plutonium [22]. The continued indefinite long-term storage of plutonium creates a burden of security risks and proliferation sensitivities [3] [23]. The decision on the future of the stockpile is influenced by political, economic and strategic factors as well as by technical considerations [24]. The Nuclear Decommissioning Authority (NDA) has been reviewing the Pu management options since 2004 and advising the UK government on it's choice [22]. There are three stages in the current guidance: consolidation, safe and secure storage and disposition.

In 2022, the first stage of the management plan, consolidation, was completed [25]. This process consisted of transferring the Dounreay Pu inventory to be consolidated at Sellafield. As discussed by Hyatt [5] the key benefits of consolidation are to the sites from which the inventory has been removed, as it enables accelerated decommissioning of those sites and reduces security requirements. The consolidated inventory can also be managed more efficiently with concentrated skills capabilities and facilities [3].

To ensure the safe and secure storage of plutonium, a process of repacking and retreating has been implemented by the NDA [3]. The plutonium will then be stored in a suite of modern stores with enhanced resilience measures to ensure the safe storage of Pu until such a time that the long-term solution of disposition can be implemented [25].

The final stage, disposition, is still in development. Research and development is ongoing to determine the best long-term solution to put separated plutonium 'beyond reach' [3]. Figure 1.5 displays the two options currently under consideration.

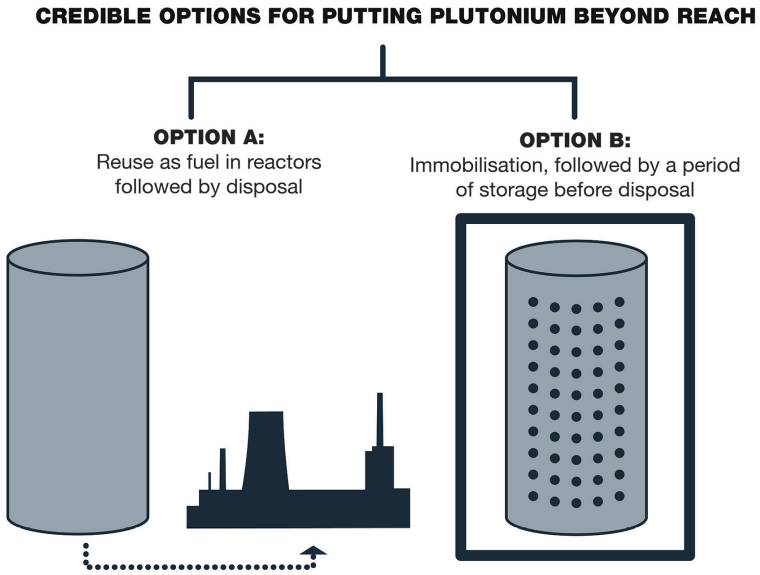


Figure 1.5: Options under consideration by the UK government for the disposition of plutonium. From [3].

The current options considered by the UK government for the long-term future of plutonium are [3]: reuse as fuel in reactors followed by disposal in a Geological Disposal Facility (GDF), or immobilisation, followed by a period of storage before disposal in a GDF. However, regardless of which option is chosen, a proportion of the stockpile (approx. 5%) is deemed unsuitable for use in future fuel, so will require immobilisation and disposal [4].

1.2.1 *Reuse*

A key advantage of the reuse strategy is that it enables the plutonium stockpile to be fully utilised as the energy resource it is [26]. It simultaneously reduces proliferation risk whilst also increasing the sustainability of nuclear power. Furthermore, the use of plutonium in the nuclear fuel supply reduces the production of more plutonium, as it limits the use of new uranium fuels.

The use of reprocessed plutonium nuclear fuel is currently under consideration for three nuclear reactor types:

1. Light Water Reactors (LWR)
2. CANDU Reactors

3. Fast Reactors

The first two options rely on the production of MOX fuel which is a blend of plutonium and uranium oxides. The reuse of plutonium as MOX fuel has been achieved in commercial LWRs in France and Japan [4] [5]. Research is in progress to demonstrate the fabrication of MOX fuel pellets from UK plutonium [3]. As discussed by Hyatt [5], the UK Pu has unique powder characteristics, isotopic composition and significant ^{241}Am ingrowth, from the decay of ^{241}Pu during storage. Morrison *et al.* [27] [28] has performed detailed neutronics studies, which provide confidence that MOX fuels manufactured from the UK Pu stockpile could perform satisfactorily in LWRs. The use of MOX fuel in CANDU reactors (termed the CANMOX solution) and the production of CANMOX fuel has not been demonstrated on an industrial scale.

Despite the technical viability of MOX, the commercial manufacture of MOX fuels from separated UK Pu has not yet been convincingly demonstrated. Moreover, at the present time no UK reactor operator has expressed interest in MOX, as the supply of uranium is predicted to be sufficient to meet future demand. As such, the economic driver for plutonium reuse as MOX fuel is weak [5], [29].

Fast reactors would irradiate a plutonium alloy fuel rather than MOX. This technology is at a low level of technical maturity and a major research and development programme is still required [3] [30].

1.2.2 *Immobilisation*

Approximately 5% of the Pu stockpile will be unsuitable for reuse in future reactors [3]. Therefore, this percentage of material will require immobilisation regardless of the disposition strategy chosen. As such it is essential that a robust immobilisation method is developed. Currently there are three immobilisation options under development:

i) Hot Isostatic Pressing (HIP) to produce a monolithic ceramic product

ii) Pressing and sintering process similar to MOX manufacturing to produce pellets

iii) Encapsulation in cement-based matrices as used in the UK for Intermediate Level Waste (ILW)

In both options i) and ii), plutonium would be immobilised as a ceramic product [31]. Zirconolite ceramics are currently being considered for use as a potential host

phase to immobilise plutonium with both experimental [32] and computational [33] [34] studies being performed.

As discussed by Bingham *et al.* [35], in nuclear research, surrogate species are often used. This is due to the radiotoxicity of Pu and the specialist research facilities required to study it. Much research uses cerium due to its similar ionic size [32] [34]. Alternatively, computational studies can be performed such as those by Dimosthenous *et al.* [33]. Computational studies can also be used to evaluate the efficacy of the surrogate species. The planning and development of pilot tests using plutonium-active products for the HIP process is underway to demonstrate the viability of the technology [3].

Due to the volume of waste anticipated, at present it is suggested that option (iii) is non-viable [3].

1.2.3 *Interim Storage - Gas Generation*

At the present time the NDA states that there is insufficient understanding of either option to move to implementation confidently [3]. Until such a time that the disposition route is decided, the plutonium will remain in safe and secure indefinite long-term storage at Sellafield. Therefore, it is essential to have a thorough understanding of the ageing phenomena of plutonium to inform the decision as the stockpile ages [4], [36]–[39].

The storage of the stockpile is as calcined PuO_2 powder contained within a series of nested stainless steel or aluminium cans. The outer can is welded to maintain storage integrity as displayed by Figure 1.6. Some legacy cans require urgent repacking due to deterioration of the cans and contamination with packing materials such as PVC. Under certain circumstances, the calcined powders have been observed to cause gas generation within the cans, resulting in pressurisation of the storage package. This pressurisation comprises one of the most serious fault scenarios that must be considered in the safety cases for the long-term storage of actinides [40] [41].

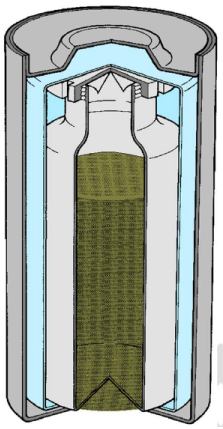


Figure 1.6: Cutaway diagram of a multiple barrier containment Magnox PuO_2 storage can. From [40].

There are a number of fundamental mechanisms that could lead to pressurisation, and all must be understood. The five key mechanisms suggested are:

1. Decomposition of polymeric packing material within the cans
2. Helium accumulation from α-decay
3. Desorption of entrained/adsorbed water as steam from the hygroscopic PuO_2 powders
4. Radiolysis of the same adsorbed water to generate, inter alia, H_2 gas
5. Generation of H_2 gas by chemical reaction of PuO_2 with H_2O, producing a postulated PuO_{2+x} phase – essentially an (electrochemical) corrosion reaction

Due to the recent and future repackaging practises, mechanism 1 is no longer of high concern. This is because new packaging practises avoid the use of PVC packing material in Pu storage. As discussed by Webb *et al.* [42], work is underway thermally treating chlorine contaminated PuO_2 at Sellafield.

Developing an understanding of the behaviour of helium in PuO_2 is the focus of this research. Despite the importance of mechanism 2, studies of helium diffusion and clustering in PuO_2 remain scarce [43]. Often, comparison is drawn from studies of helium in related nuclear fuel materials such as metallic Pu, UO_2 and MOX fuel [44] [45]. From comparison with these materials it has been predicted that helium atoms are likely to cluster at lattice vacancies and these clusters could act as precursors to helium bubbles. Understanding the stability of the bubbles and the diffusive behaviour of helium is key to determining if radiogenic helium accumulation leads to pressurisation of stored PuO_2.

Mechanisms 3-5 all involve PuO_2/H_2O interactions and are complex, inter-connected and poorly understood [40], [46], [47]. Experimental studies of the surface chemistry of water adsorbed on PuO_2 surrogates such as those of Laventine *et al.* [48] are ongoing, with an aim to help predict conditions that may lead to gas generation during long-term Pu storage.

The physico-chemical state and amount of the water ad-/absorbed at the surface, will be determined not only by the PuO_2 crystal faces presented at the surface of the powders, but also radiation damage to the surface and bulk defect structure. Such radiation damage will also affect the susceptibility of the PuO_2 to corrosion – potentially by mechanism 5. However this corrosion is more likely to be by hydroxyl radicals/hydrogen peroxide generated by the radiolysis of water at or close to the plutonium dioxide surface [40].

1.3 Plutonium Dioxide

An assessment report of plutonium fuel by the Nuclear Energy Agency in 1989 [24] stated that separated stored plutonium becomes progressively more difficult to handle as time passes. However, the ageing mechanisms associated with the storage of PuO_2 are poorly understood [49] [50]. The difficulty of handling plutonium due to its radiotoxicity is a key reason for the lack of experimental data [45], [51], [52]. Additionally, as mentioned by S.S. Hecker *et. al* [53] and T.H. Allen *et. al* [54], due to the relatively recent discovery of Pu in the 1940s, and only minuscule amounts being present in nature, there is a lack of natural data on how plutonium ages.

Plutonium dioxide has the fluorite structure with space group $Fm\bar{3}m$ and is a ceramic substance [24]. Figure 1.7 displays the observed unit cell of PuO_2.

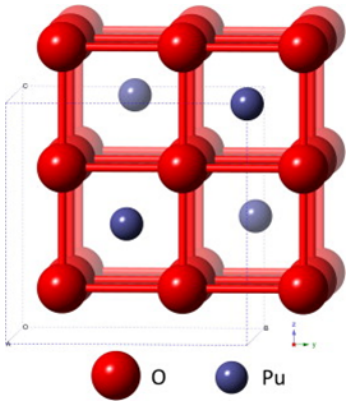


Figure 1.7: Figure displaying the observed unit cell of PuO_2. From [55].

Plutonium is vulnerable to ageing as it is a radioactive element [45] [56]. ^{239}Pu

decays principally by α-decay, emitting an alpha particle and a recoil uranium nucleus. The alpha particles pick up electrons along their path and become helium atoms [13] [57]. As displayed by Figure 1.8, the daughter nuclei travel through the lattice in opposite directions and towards the end of their path may initiate a collision cascade where they transfer their energy and momentum to the electrons and atoms of the material [45] [58]. From collisions, plutonium atoms can be displaced, creating numerous vacancies. A displaced plutonium atom will ultimately come to rest at an interstitial site, becoming a self-interstitial. Therefore, each displacement creates a Frenkel pair consisting of a vacancy and a self-interstitial [45]. Each decay event creates many Frenkel pairs as illustrated by Figure 1.8. Kinetic properties of point defects govern radiation tolerance, fission product accommodation, fission gas release and micro-structural evolution in-pile, so a comprehensive understanding of defect behaviour is crucial to understanding the ageing of plutonium [59]–[61].

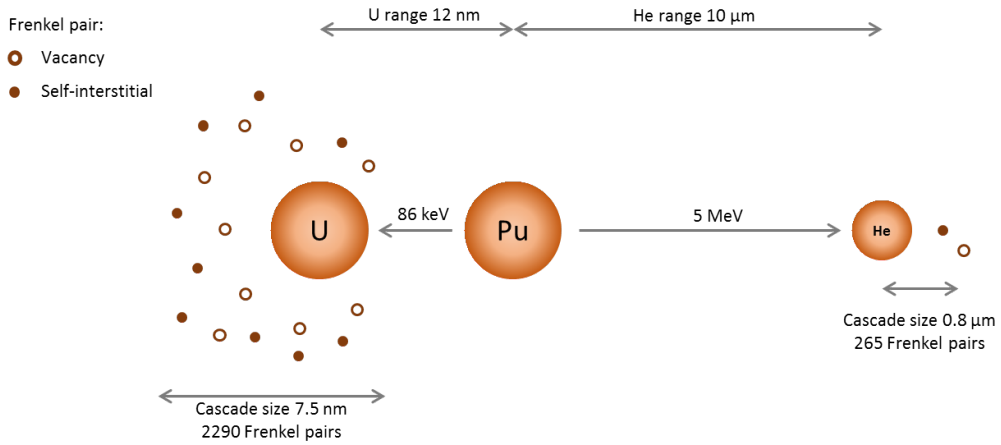


Figure 1.8: Figure displaying plutonium decay and the generation of defects. Adapted from [45].

Due to the radiotoxicity of PuO_2, computational studies are ideally suited to study the defect chemistry of PuO_2 [62]. Atomistic simulations have been deemed suitable for nuclear applications as they are concerned with the atoms rather than the electrons and sub-atomic particles [63] [64]. Through modelling the atomic behaviour of PuO_2, energetically favourable defects can be predicted. Helium incorporation in such defects can then be studied.

1.4 Research Aims

As discussed, a key concern for the continued storage of the PuO_2 canisters is pressurisation, with radiogenic helium gas generation being a potential mechanism. He-

lium could diffuse to form bubbles which could then be released from the lattice and into the canister head space. The aim of this research is to deepen the understanding of helium behaviour in the ageing PuO_2 stockpile. It is imperative for the nuclear industry that this knowledge gap is addressed to enable the scientific underpinning of the stockpile management options and ensure the continued safe storage of PuO_2.

This research uses atomistic simulation based on classical potentials with an aim of elucidating helium behaviour in PuO_2. Atomistic simulation techniques using interatomic potentials are employed to study the defect behaviour of PuO_2 both in the bulk and at the surface. From the development of a model of PuO_2 defect chemistry, available trap sites for helium are predicted. From these trap sites, helium clusters are built up and optimum bubble sizes determined. Molecular dynamics simulations are also used to identify helium diffusion mechanisms and study helium clustering over a range of temperatures.

1.5 Thesis Structure

Chapter 2 contains the theory and methodology of the work presented in this thesis. The first three results chapters detail static computational simulation results. Chapter 3 provides an evaluation of available interatomic potentials for modelling PuO_2. The best performing is then implemented to model the defect chemistry of bulk PuO_2. Next, the chosen potential is used in Chapter 4 to model the surfaces of PuO_2. In Chapter 5 the incorporation of helium into the bulk of PuO_2 is discussed, with a potential fitted to a standard form.

The final three results chapters detail molecular dynamics simulation results. Chapter 6 provides evaluation of interatomic potentials suitability in molecular dynamics simulations for bulk PuO_2. In Chapter 7, helium diffusion in PuO_2 is discussed. Chapter 8 presents the results of simulations investigating helium clustering behaviour.

Chapter 2

Methodology

This chapter will describe the computational methods used throughout this research. As displayed by Figure 2.1, there are many possibilities for computational simulations spanning a vast range of size domains and time scales. As such, it is essential to choose the appropriate techniques for the specific research at hand.

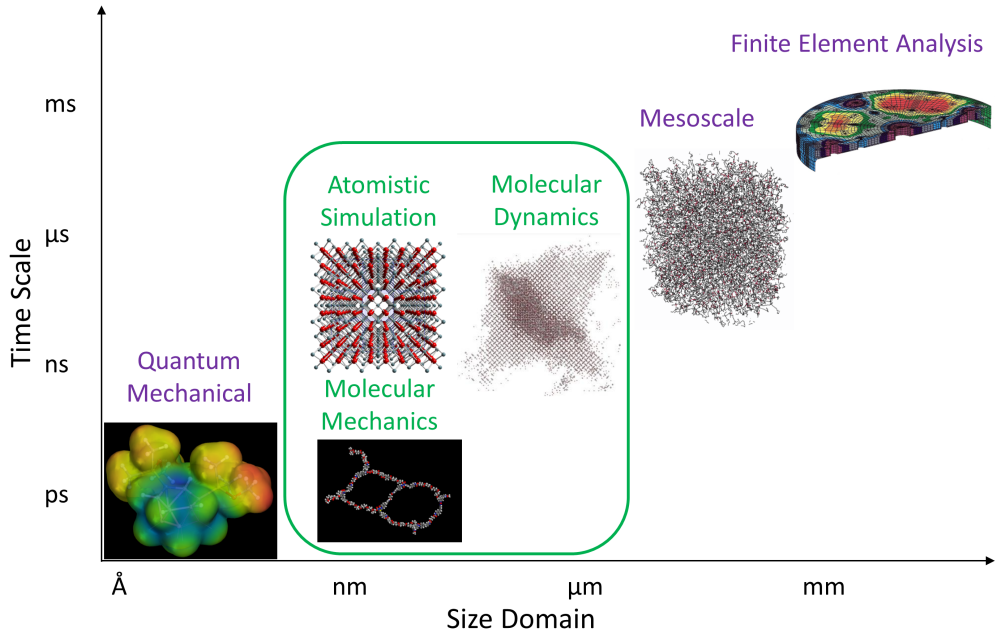


Figure 2.1: Graph displaying range of computational chemistry methods over the time and size scales they occupy.

The realm of computational chemistry can be split into two streams: *Ab initio* and semi-/empirical modelling. *Ab initio* methods are entirely theoretical; they attempt to solve the Schrödinger equation. The only values input in *ab initio* computational methodology are the values of fundamental constants, the atomic numbers

of the atoms present, and their geometry. Density Functional Theory (DFT) is the most commonly employed *ab initio* method [65]. Empirical or semi-empirical methods are named as such because they employ experimental results, from accurate models of related materials, to approximate some elements of the underlying theory. In this work atomistic simulations have been deemed the most suitable to model plutonium, as they primarily model the atoms rather than the electrons and sub-atomic particles [63]. It is the defects at an atomic level within the PuO_2 lattice that are of primary interest when investigating the ageing of plutonium.

The simulations detailed in this work were performed using the University of Birmingham's blueBEAR High Performance Computing (HPC) facilities.

2.1 Force Field Methods

All of the results presented in this thesis were generated from the study of systems in which the interactions between atoms was described by force fields. In the force field method effective interatomic potentials, V, (in analytical or numerical form) describe the variation in the energy of the molecule or solid as a function of the nuclear coordinates of the number of atoms present, N [55]. A potential describes the effects of valence electron interactions, without the electrons being explicitly described [66]. The total potential is generally broken down into pair, three-body, four-body and higher order terms [67],

$$V(r_1...r_N) = \sum_{i,j=1} v^{(2)}(r_{ij}) + \sum_{i,j,k=1} v^{(3)}(\mathbf{r}_i, \mathbf{r}_j, \mathbf{r}_k) + \sum_{i,j,k,l=1} v^{(4)}(\mathbf{r}_i, \mathbf{r}_j, \mathbf{r}_k, \mathbf{r}_l) + ... \quad (2.1)$$

V is often approximated by the leading pair potential term, $v^{(2)}$, which only depends on the distance, r, between atoms i and j.

An interatomic potential must have a repulsive component to ensure the Pauli repulsion at short distances between atoms is observed, this is defined by a short-range potential ϕ. An interatomic potential may also have an attractive component, defined by the Coulomb interaction. Thus an interatomic potential can be written as,

$$V(r_1...r_N) \approx v^{(2)}(r_{ij}) = V_{Coulomb} + \phi(r_{ij}) \quad (2.2)$$

with,

$$V_{Coulomb} = \frac{q_i q_j}{4\pi\epsilon_0 r_{ij}}. \tag{2.3}$$

q_i and q_j are the effective charges of atoms i and j, respectively and ϵ_0 is the permittivity of free space [67].

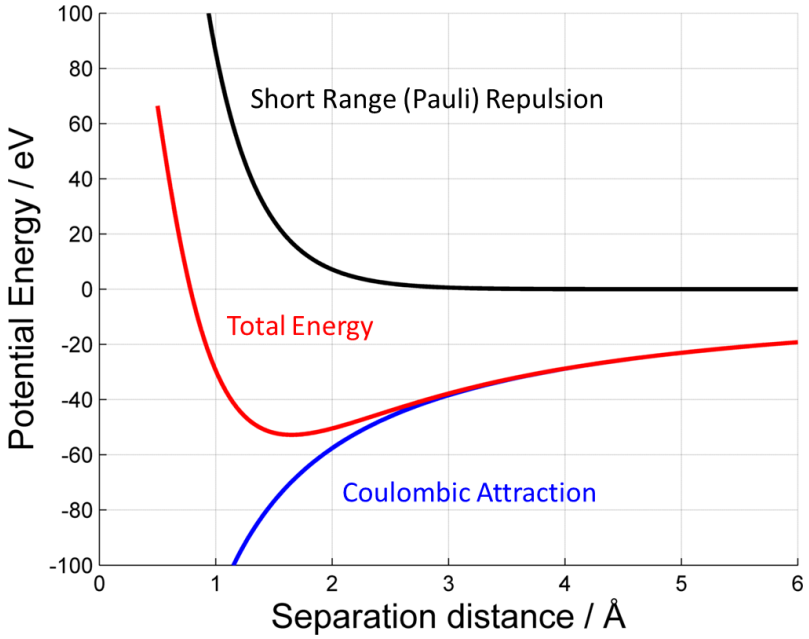


Figure 2.2: Graph displaying the potential energy, V, against the interatomic distance, r, showing the breakdown into long and short range components.

Figure 2.2, displays the breakdown of the potential energy into long and short range components. The long range component corresponds to the Coulomb interaction and the short range component corresponds to ϕ. An appropriate form of ϕ for a particular system must be chosen; it must describe both the Pauli repulsion at short distances, and the dispersive interaction at long range [68].

2.1.1 *The Long Range Interaction*

To evaluate the lattice energy the sum of the Coulomb interactions across the ions must be calculated. As the magnitude of the Coulomb potential energy decreases as a function of $\frac{1}{r_{ij}}$, it converges very slowly. In addition, as the interaction of an ion with anything but its nearest neighbours involves only Coulomb interactions, the energy density of the sum increases with distance, resulting in an infinite sum. Thus, the Ewald summation is often used to calculate the Coulomb interaction as it enables faster convergence and therefore is less computationally demanding.

In the Ewald summation, a basic cell containing $\frac{N}{2}$ positive and negative charges in some spatial arrangement is considered as a single crystallographic element surrounded by an infinite number of identical copies of itself [69] [70]. The whole system is then neutral and contains an infinite number of charges situated at points $\mathbf{r}_{j+}$ and $\mathbf{r}_{j-}$, respectively. The total potential at the position of some ion i residing in the basic cell is calculated as the finite difference of two infinite diverging series,

$$\phi(\mathbf{r}_i) = q \sum_{j+=1}^{\infty} \frac{1}{|\mathbf{r}_i - \mathbf{r}_{j+}|} - q \sum_{j-=1}^{\infty} \frac{1}{|\mathbf{r}_i - \mathbf{r}_{j-}|}. \tag{2.4}$$

Rather than evaluating the sum over the point charges for the potential, the charges can be rewritten as delta-like charge densities

$$\rho(\mathbf{r}) = q \sum_{j+=1}^{\infty} \delta\left(\mathbf{r} - \mathbf{r}_{j+}\right) - q \sum_{j-=1}^{\infty} \delta\left(\mathbf{r} - \mathbf{r}_{j-}\right) \tag{2.5}$$

and these expressions expanded in a Fourier series whose terms determine the Fourier components, $\phi(k)$, of the electrostatic potential. However, this again leads to convergence issues as the Fourier transform of a delta-function requires infinite terms [69].

The solution is to separate the potential into two parts; one in real space and the other in reciprocal space. The real space component consists of the point charges with an additional Gaussian charge distribution of the same magnitude, but opposite charge, superimposed on. The result of this is to prevent neighbouring ions interacting and as such it is rapidly convergent in real space [70]. The reciprocal component is made up of the same point charges but with Gaussians centred on the ions, and it decays quickly in reciprocal space [71]. Figure 2.6 displays a visual representation of this method.

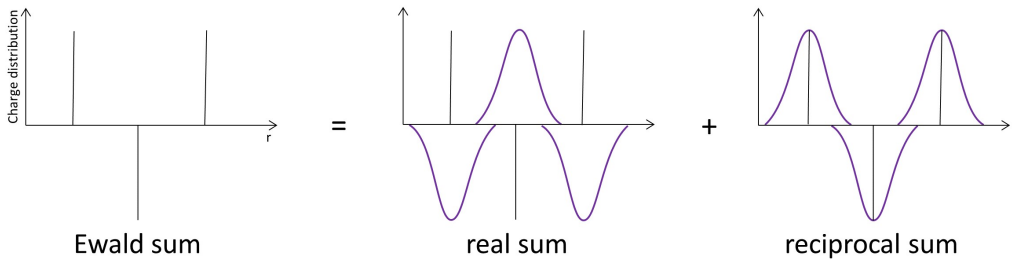


Figure 2.3: Schematic displaying the separation of the potential into real and reciprocal space via the Ewald summation method.

The calculation of the Ewald sum is constrained by cut-off radii in both real and reciprocal space. By the use of suitable constraints, an optimal convergence of both series can be achieved.

An alternative method of ensuring convergence of the long range term is the particle-particle-particle-mesh (PPPM) solver from Hockney [72], which is an adaptation of the Ewald method. In this method the charges of the atoms are mapped onto a 3D mesh, and 3D fast Fourier transform algorithms are then used to solve Poisson's equation on the mesh. The electric fields are interpolated on the mesh and point back to the atoms [73]. The computational cost of traditional Ewald summation scales as $N^{\frac{3}{2}}$, where N is the number of atoms in the system. Due to the fast Fourier transforms, the PPPM solver scales as $NlogN$, and so is a faster choice and is consequently implemented in the molecular dynamics simulations in this work.

2.1.2 *The Short Range Interaction*

A number of standard analytical functions are available for ϕ, with common pair potentials including the Lennard-Jones potential and the Morse potential. The Ziegler-Biersack-Littmark (ZBL) potential is often used for short-ranged interactions [74]. A commonly used many-body potential is the Embedded-Atom Method (EAM).

To choose the appropriate potential, the accuracy, transferability and computational speed of the potential must be considered [60], [62]. As the power and accessibility of computers increased through the 1960s, efficient algorithms for minimising functions of many variables were developed [75]. These developments enabled many forms of the potential to be evaluated at reasonable computational expense.

Specific potentials will be described and evaluated when setting up simulations, and are discussed in detail later in this work.

2.1.3 *Empirical Fitting*

The material specificity for a potential is provided by the associated parameters for each of the terms in the chosen analytical form. Developing potentials for a particular material requires determining a set of parameters [66]. To determine the parameters, empirical fitting procedures are often used [55].

Empirical fitting consists of adjusting the potential parameter values via a least squares fitting procedure, in order to reproduce crystal structural data as accurately as possible [67]. Experimental data are required for this method. However, for PuO_2,

previously published theoretical predictions of properties are also used due to the limited availability of experimental data [49], [63].

2.1.4 *Modelling Ionic Polarisation*

The polarisability of an ion is its ability to form instantaneous dipoles and is of importance in understanding a molecules internal structure. The shell model of Dick and Overhauser [76] was used to model the polarisability of individual ions in static calculations.

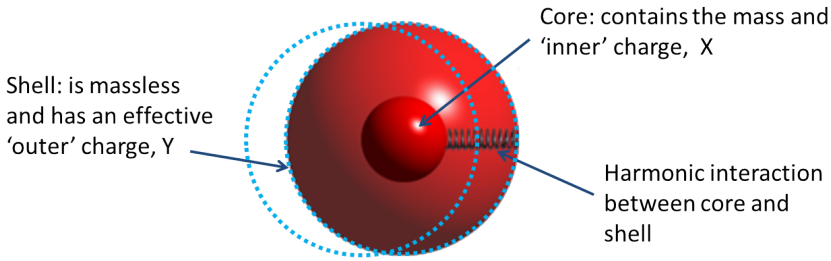


Figure 2.4: The shell model.

As displayed by Figure 2.4, in the shell model a massless shell of charge, Y, simulates the outer valence electron cloud of an ion. The core of charge X, simulates the nucleus and inner electrons. The total charge of the ion is therefore $X + Y$ and is equal to the oxidation state of the ion [76], [77]. The interaction between the core and the shell is harmonic, as defined by,

$$V_i(r_i) = \frac{1}{2} k_i d_i^2, \tag{2.6}$$

where k is the spring constant of the interaction and d is the relative displacement of the core and shell of ion i. The polarisability for a free-ion is given by,

$$\alpha_i = \frac{Y_i^2}{k_i}. \tag{2.7}$$

When the shell model is employed in atomistic simulations, the required parameters are Y, X, and k. These parameters are often derived by empirical fitting [49], [77].

However, the implementation of the shell model in a Molecular Dynamics (MD) simulation is not straightforward, as it results in massless entities [78]. To handle the massless entities either an energy minimisation is performed on the shells after each timestep to update their positions [79], or nominal small masses are assigned to the shells [80]. Both methods add computational demands and are omitted from

the MD code used throughout this work, with rigid-ions used instead.

2.2 Energy Minimisation

Energy minimisation methodology has been used throughout this work. The choice of which algorithm to use for geometry optimisation depends on many factors such as the storage and computing requirements. A range of energy minimisation methods will now be detailed.

2.2.1 *Potential Energy Surface*

The potential energy, $E(x)$, is a function of atomic positions (and lattice parameters). As such, there should be a set of positions which produces the lowest energy - the ideal configuration of the atoms. All possible atomic positions can be displayed as a potential energy landscape. The potential energy surface of a structure is therefore the potential energy as a function of the positions of the atoms.

Optimisation is the process of finding the point that minimises a function; a stationary point. A local minimum of a function is a point at which the function value is less than or equal to the value at nearby points, but may be greater than at a distant point as displayed by Figure 2.5. A global minimum is the point at which the value of the function is less than or equal to the value at all other possible points. Points surrounding a local minimum are higher in energy but a local minima is not the actual lowest energy site.

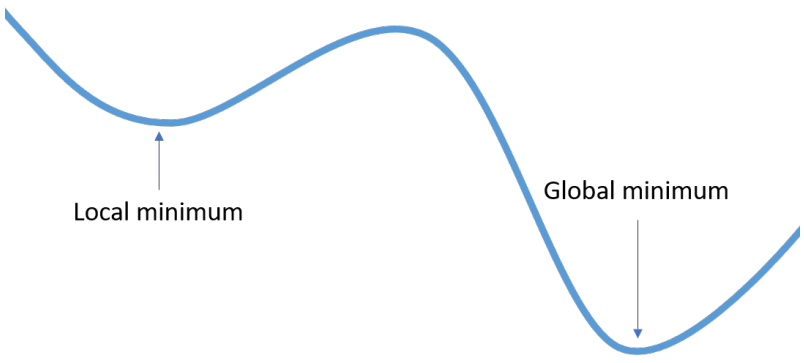


Figure 2.5: Local and global minimums.

A frequent problem with geometrical optimisation is that optimisation processes go downhill. Thus, they find the local minimum to their position and not necessarily the global minimum.

2.2.2 *First-Order Solvers*

The first derivative can be used to find minima of a potential energy surface. The sign of the first derivative indicates the direction to the minimum. The magnitude indicates the steepness. Therefore, to search for minima the derivative at some point can be taken and then some distance moved in the direction indicated. The simplest choice of direction is taken in the steepest descents method, which is outlined below:

1. Generate derivatives at first point and follow the steepest line
2. Find minimum along this
3. At minimum calculate new derivatives and follow the steepest line
4. Find minimum along this
5. Repeat cycle until true minimum found

At the minimum all non-zero derivatives will be orthogonal to the direction which has just been minimised along. This process can be quite slow, but it is robust.

The problem with the steepest descent method is that whilst the new direction is orthogonal to the previous direction, it is not orthogonal to any others. Thus, later minimisation directions can undo the effect of earlier ones and so the method is very inefficient in dealing with long, narrow valleys unless it happens to go straight down them.

It is therefore desirable to choose a set of directions where a minimisation along any one will not interfere with the others. These directions will span the solution space and are referred to as conjugate directions [81]

$$v_k = -g_k + \gamma_k v_{k-1}, \tag{2.8}$$

where v_k is the new direction, g_k is the derivative at position k, v_{k-1} is the direction of the previous step and γ_k is the weighting of the previous step calculated by,

$$\gamma_k = \frac{g_k \dot{g}_k}{g_{k-1} \dot{g}_{k-1}}. \tag{2.9}$$

The use of conjugate directions for energy minimisation is called the conjugate gradient method and is outlined below [82]:

1. Generate derivatives at first point and follow the steepest line

2. Find minimum along this

3. At minimum calculate new derivatives and conjugate directions

4. Find minimum along this

5. Repeat steps 3 and 4 until the true minimum is found

The conjugate gradient method is much more robust than the steepest decent method.

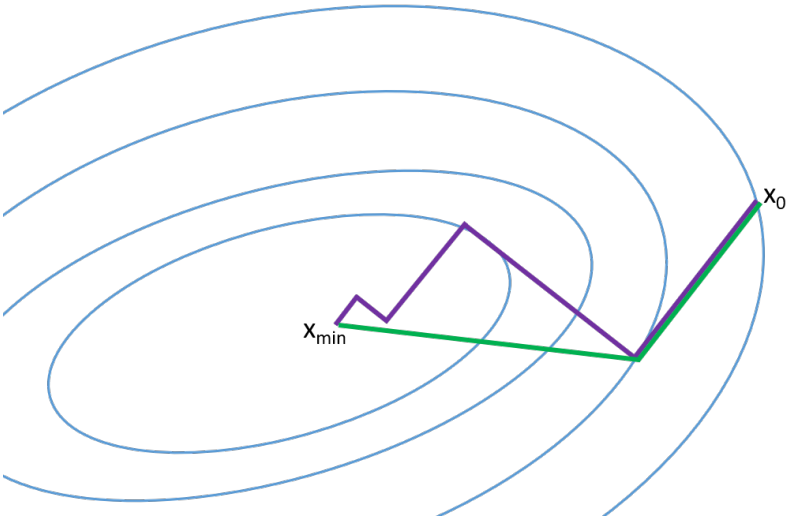


Figure 2.6: Representation of finding the minimum energy site from start site x_0 via steepest decent (purple line) and conjugate gradient (green line) methods.

Figure 2.6 displays both the steepest decent and conjugate gradient methods. It can be seen that the conjugate gradients method is much more efficient.

2.2.3 *Second-Order Solvers*

In second-order methods, rather than just using the first derivative (the gradient) to search for minima, the second derivative is also used. The second derivative calculates the Hessian which details how the curvature of the surface is changes. The Newton-Raphson method is a second order solver [83]

$$x_{min} = x_k - \frac{f'(x_k)}{f''(x_k)}, \tag{2.10}$$

where x_{min} is the minimum position, x_k is the current position and $f'(x)$ and $f''(x)$ are the first and second derivatives respectively, given as Hessians. The method is

very powerful and can find the minimum extremely quickly, but it is very computationally expensive. As such, Quasi-Newton approximations are used which update the Hessian with numeric approximations each step and only recalculate when necessary.

One such approximation used in this work is the Broydon-Fletcher-Goldfarb-Shanno (BFGS). This is used for unconstrained and nonlinear optimisation problems. In BFGS the exact Hessian is calculated initially, and is then updated over a number of steps or cycles [83]. The exact Hessian is only calculated when certain criteria have been met, such as when the energy change in a cycle exceeds certain thresholds.

2.2.4 *Dynamic Relaxation*

This optimisation methodology performs dynamics on a system which only allows for downhill movement on the potential energy landscape. The acceleration is calculated from the specified atomic force fields. The Fast Inertial Relaxation Engine (FIRE) [84] calculates the acceleration via

$$\boldsymbol{v}'(t) = \frac{\boldsymbol{F}(\boldsymbol{r}(t))}{m} - \gamma(t)\big|\boldsymbol{v}(t)\big|\big[\hat{\boldsymbol{v}}(t) - \hat{\boldsymbol{F}}(\boldsymbol{r}(t))\big], \tag{2.11}$$

where r is position, v, velocity, F, force, m, mass, and γ is a scalar function of time. The hats represent unit vectors. The power, P, is calculated via $P = F\dot{v}$. The velocity is reset if the force and velocity are in opposite directions. Combining this equation with an adaptive time-stepping technique results in a simple and efficient solver. The time-stepping technique used is the Velocity-Verlet detailed later in Section 2.5.1. The method does not use Hessians and so is less computationally expensive.

2.2.5 *Nudged Elastic Band*

Nudged Elastic Band (NEB) optimisation procedures are performed to determine the minimum energy path between two points [85]. In NEB calculations both the initial and final states of the system must be known. Along the minimum energy path there will be a saddle point, which is the maximum energy along the reaction path. From the identification of the saddle point, the migration pathway energy barrier can be calculated. The energy barrier is calculated via the difference in energy of the initial configuration and energy of the saddle point.

The NEB method works by first creating a set of images between the initial and

final states. These images are connected by springs to keep the images evenly spaced and stop them falling into the end minima. The total force on each image is

$$\boldsymbol{F}_i^T = \boldsymbol{F}_i^{\perp} + \boldsymbol{F}_i^{\parallel}, \tag{2.12}$$

where the perpendicular force is the gradient of the potential that pulls the system towards the minimum energy path and the force parallel to the trajectory is the spring force. Energy minimisation is performed on each image to minimise the total force until the images converge to the minimum energy path, at which point the tangential force on each image is the same.

In this work a second stage is added to the NEB calculation, known as the climbing image modification [73] [85]. In the second stage, the image with the highest energy is selected and the inter-image forces on it are converted into a force that drives the atom coordinates to the saddle point of the barrier via a barrier-climbing calculation. The other images rearrange themselves along the minimum energy path due to the spring forces, so they remain roughly equally spaced. Both of the stages in NEB are energy minimisation procedures and are performed via the damped dynamics method detailed previously in Section 2.2.4. Throughout this work the number of images for each NEB calculation was 12.

2.3 Static Bulk Simulation Methodology

The General Utility Lattice Program (GULP) was used for static bulk simulations [86]. This code focuses on the use of analytical solutions to develop the understanding of the lattice dynamics of a system. Force fields are used within GULP to model the relationship between atoms. Energy minimisation is used to calculate relaxed atomic coordinates and from this many crystal properties are calculated. Additionally, defects can be modelled, enabling the calculation of defect energies.

2.3.1 *Symmetry Optimisation*

The energy minimisation methodology used in GULP is the Newton-Raphson BFGS modified method (Section 2.2.3). During an energy minimisation all the ionic interactions are calculated and each ion subsequently moves a distance proportional to the force acting on each ion in the direction of the net field. A constant pressure energy minimisation is also performed which is a symmetry-adapted technique of energy minimisation [86].

In the GULP code, symmetry is utilised to accelerate structural optimisation. The rate of convergence can be correlated to the number of independent variables in a system. As symmetry lowers the number of independent geometric variables, it can lead to reducing the number of steps required in an optimisation.

The asymmetric unit of a space group is the part of the crystallographic unit cell which can be used to generate the complete unit cell via the symmetry of the space group. Utilising the asymmetric unit can increase the efficiency of a calculation. For example, when symmetry is present in a two-body potential model, rather than looping over all of the pairs of atoms to compute energy, only the interactions between the asymmetric unit and the other atoms require calculation. Thus, the computational memory required for an optimisation is significantly reduced and the processing of the algorithm is faster.

2.3.2 *Bulk Properties*

Once the optimised structure for a material has been determined, it is possible to calculate many physical properties based on the curvature of the energy surface about the minimum (the second-derivative matrix). Via comparison of the calculated bulk properties with experimental values, the accuracy of the model can be evaluated. Some of the calculable properties shall now be discussed.

Elastic constants, C_{ij}, describe the mechanical hardness of the material with respect to deformation. This is calculated by the second derivative of the energy density with respect to strain. The elastic constant tensor is a 6x6 symmetric matrix, so contains 21 potentially independent matrix elements. However for a cubic material the number of independent matrix elements is reduced significantly due to symmetry; for a cubic material the only unique elements are C_{11}, C_{12} and C_{44}.

Stress, σ, is the way a force interacts with the area over which it is applied. There are three main types of stress: normal σ_n, shear σ_t, and bulk σ_b. Strain, ϵ, is the result of stress, calculated by the change in a dimension over an original dimension. Thus, strain is independent of the size of the solid. There are three strains (normal ϵ_n, shear ϵ_t and bulk ϵ_b) corresponding to the three stresses.

A solid can be characterised by an elastic modulus which relates strain to stress. Three elastic moduli are calculated:

- Bulk Modulus ($K = \frac{\sigma_b}{\epsilon_b}$), measures the substances resistance to uniform compression. Defined as the ratio of the infinitesimal pressure increase to the resulting relative decrease of the volume

- Shear Modulus ($G = \frac{\sigma_t}{\epsilon_t}$), defined as the ratio of shear stress to the sheer strain
- Young's Modulus ($E = \frac{\sigma_n}{\epsilon_n}$), defined as the ratio of uniaxial stress over the uniaxial strain in the range of stress in which Hooke's law holds. It is a measure of the stiffness of a material

Poisson's ratio, ν, measures the change in a material perpendicular to the uniaxial stress. It is defined as the ratio of lateral to longitudinal strain under a uniform, uniaxial stress.

Optical properties can also be calculated. These include the static and high frequency dielectric constants (relative permittivities), which measure the optical response of a solid to an applied electric field [87]. The dielectric constants are given by 3x3 tensors.

2.3.3 *Modelling Defects*

To find defect energies the potential, ϕ, of a defective static lattice is minimised with respect to the displacements and moments of the surrounding ions [75]. The Mott-Littleton methodology was employed in this work to perform defect calculations. In the Mott-Littleton methodology, minimising ϕ is simplified by dividing the defective lattice into two regions (Region I and Region II), as displayed by Figure 2.7. Region I contains the defect and a certain number of immediate neighbours. Region II is further subdivided into Region IIa, which is the outer spherical shell of ions, and Region IIb, which contains the rest of the crystal lattice extending to infinity [75], [86], [88].

As Region I contains the defect and neighbouring ions, ions in this region are assumed to be strongly perturbed by the defect. Therefore, ions in this region are explicitly relaxed with respect to their positions [86]. Ions in Region IIb are assumed to be weakly perturbed by the defect as the defect forces are relatively weak at a greater distance, and so can be described as a dielectric continuum approximation. Region IIa acts as the interface region, to ensure a smooth convergence between the explicitly summed and continuum regions [89].

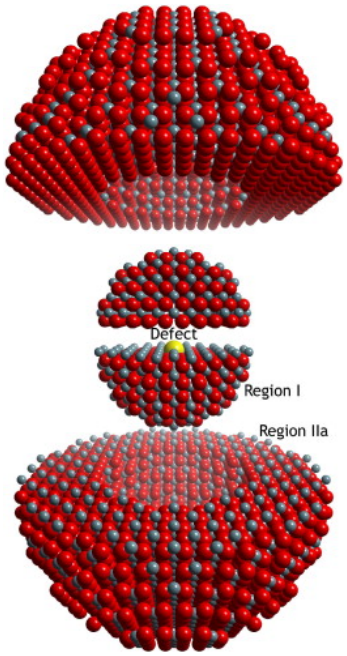


Figure 2.7: Visualisation of the regions used in Mott-Littleton methodology. From [55].

The total energy of the two region system, E_{tot}, is calculated by,

$$E_{tot}(x,\xi) = E_{11}(x) + E_{12}(x,\xi) + E_{22}(\xi), \tag{2.13}$$

where E_{11} is the energy of Region I as a function of Cartesian coordinates (x), E_{22} is the energy of Region II as a function of Cartesian coordinates of displacement (ξ) and E_{12} is the energy of the interaction of regions I and II as a function of x and ξ [63]. At this point regions IIa and IIb are not distinguished.

By assuming the forces acting on Region II are small, the response of the atoms here will be purely harmonic,

$$E_{22}(\xi) = \frac{1}{2}\xi^T H_{22}\xi, \tag{2.14}$$

where H_{22} is the Hessian matrix for Region II. Next, we apply the condition that displacements in Region II will be at equilibrium, resulting in a condition of,

$$\left(\frac{\delta E_{tot}(x,\xi)}{\delta\xi}\right)_x = \left(\frac{\delta E_{12}(x,\xi)}{\delta\xi}\right)_x + H_{22}\xi = 0. \tag{2.15}$$

By combining Equations 2.14 and 2.15, we can eliminate the energy of Region II

from E_{tot} (Equation 2.13),

$$E_{tot}(x,\xi) = E_{11}(x) + E_{12}(x,\xi) - \frac{1}{2}\Big(\frac{\delta E_{12}(x,\xi)}{\delta \xi}\Big)_x \xi, \tag{2.16}$$

thus greatly simplifying the calculation [63].

The defect energy is then calculated from the difference in energy of the perfect Regions I and II, E^p_{tot}, and the defective case, E^d_{tot}

$$E_{defect}(x,\xi) = E^d_{tot}(x,\xi) - E^p_{tot}(x,\xi). \tag{2.17}$$

This enables a cancellation of the terms, so the individual contributions need not be calculated, just the total energies. As a consequence of this method, the optimised energy with respect to the Cartesian coordinates of Region I must be calculated by force balance rather than energy minimisation. Generally, the point at which the forces tend to zero varies little from the minimum in internal energy. So, during a defect energy optimisation, the energy is minimised via a conventional Newton-Raphson procedure. Once the gradient norm is less than a certain tolerance, and Region I is within the harmonic region, then (without the use of a line search) the harmonic displacements according to the Hessian and gradients are applied until the forces fall below the tolerance [63].

Via the Mott-Littleton scheme GULP enables vacancies, interstitials and impurities to be modelled. The defect energy is output, with lower defect energies of formation being more thermodynamically favourable. Therefore, defects with low defect energies are more likely to be present in the lattice.

2.3.4 *Defect Visualisation Methodology*

After defect calculations were performed, it was of use to visualise the defect and surrounding lattice. In order to do this a script was generated to interrogate the GULP output file, extract the coordinates of the input and relaxed ions, and then generate the respective input files for visualisation by CrystalMaker® [90]. Therefore, an image of the lattice both before and after relaxation could be generated. This enabled comparison between the two images to investigate how the defects are accommodated by lattice distortion.

The images were made with the defect at the centre, and the rest of the lattice would surround the lattice radially at a size set when reading the file. When the image radius was greater than the Region I radius, all the ions simulated explicitly

would be displayed in the visualisation. Using a reduced radius, e.g. 5.5 Å, enabled a clear visual representation of the lattice relaxation around the defect site.

Tools in CrystalMaker® were used to calculate and display the bond lengths, from the ion Cartesian coordinates determined by GULP.

2.3.5 *Defect Notation*

Kröger Vink notation can be used to represent defect reactions [91]. M_S^C represents the general notation, where:

- M is the species of interest. $M = V$ for a vacancy, and X for an atom or ion of element of symbol X
- C is the effective charge relative to lattice. $C = X$ when uncharged, $\bullet$ when positive, and / when negative
- S is the site in the lattice. $S = i$ for interstitial, and X for lattice position of an atom or ion of element of symbol X

For example, $V_O^{\bullet\bullet}$ represents an oxygen vacancy, with a double effective positive charge.

2.4 Static Surface Simulation Methodology

The Minimum Energy Techniques Applied to Dislocations, Interface and Surface Energies (METADISE) code, developed by Parker *et al.* [92], was used throughout this work to simulate surfaces. It is a lattice statistics methodology.

2.4.1 *Pure Surfaces*

Miller indices (hkl) define a crystallographic surface, they are prescriptive of a specific plane in the unit cell. To model a surface, the unit cell is cleaved along the desired (hkl) plane, and repeated periodically in two dimensions, as displayed by Figure 2.8. A two region approach is employed in METADISE to simulate the surface and calculate the surface energy via energy minimisation.

As depicted by Figure 2.8, Region 1 represents the initial surface layers which are allowed to relax fully and Region 2 represents the bulk, in which the atoms are fixed [94]. The regions consist of stacks of planes parallel to the surface. The total energy of the crystal is the sum of the lattice energies of the two regions [92],

$$E_{tot} = E_1 + E_2. \tag{2.18}$$

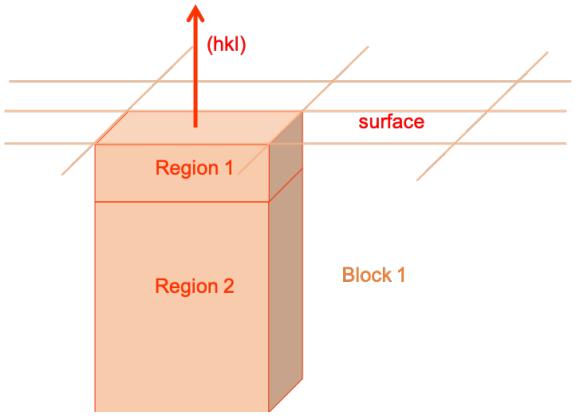


Figure 2.8: Schematic representation of a surface [93].

Where E_1 and E_2 are the energies of the ions in Region 1 and Region 2 respectively. The total energy can be broken down further to include an expression for the boundary interaction energy between the two regions,

$$E_{tot} = E_{11} + E_{12} + E_{21} + E_{22}. \tag{2.19}$$

It should be noted that the energy of interaction of Region 1 with Region 2 appears twice as $E_{12} = E_{21}$. Additionally, the energy of interaction of Region 2 with itself, E_{22}, is constant and so can be ignored. As such the surface energy, E_s, is calculated from the interactions both in and with Region 1. Finally, the bulk energy, E_b, can be calculated as E_{22}. During the energy minimisation procedure, an adaptation to the Ewald summation method is used, known as the Parry method [95].

The specific surface energy, γ, is defined as the energy per unit area needed to transform a bulk region into a surface region,

$$\gamma = \frac{E_\mathrm{s} - \frac{1}{2}E_\mathrm{b}}{A}, \tag{2.20}$$

where A is the surface area. The factor of a half arises because the bulk calculation contains double the number of ions as the surface. The surface with the lowest positive surface energy is the most energetically stable surface. A lower surface energy indicates a lower mode of cleavage energy requirement. Therefore, the surfaces with low surface energies dominate the growth morphology of a crystal [96].

The attachment energy, E_{att}, is defined as the energy released when a growth slice is added to a growing crystal [97]. The d spacing is the separation between the layers of ions. Both E_{att} and d spacing values were calculated for each pure surface

simulated using METADISE.

2.4.2 *Morphology*

From the surface simulations, the calculated surface energies were used to predict the equilibrium morphology. The morphology of a crystal describes its topology. A Wulff construction is used to generate the equilibrium morphology [98]. Wulff's theory states that the equilibrium crystal shape is obtained when there is minimal total surface energy for a fixed volume [98].

In the Wulff construction, a normal vector, $\boldsymbol{h_i}$, to the corresponding surface is drawn from the crystallite centre for all relevant surfaces. The magnitude of the vector is proportional to the surface energy via,

$$\boldsymbol{h_i} = \lambda\gamma_i, \tag{2.21}$$

where λ is the constant of proportionality. Tangents to these vectors are determined and the inner envelope of these gives the equilibrium crystal shape.

The Wulff construction does not consider kinetic factors such as growth rate. To predict the crystal growth morphology, the modulus of the surface attachment energies is used. The use of the surface attachment energy rather than the surface energy ensures that the surfaces with the least exothermic attachment energies dominate the growth morphology.

2.4.3 *Defective Surfaces*

The Computer Simulation HADES on Surfaces (CHAOS) code, which is embedded into METADISE, is used to simulate defective surfaces [99]. The defect formation energy is calculated via a two region approach, as depicted by Figure 2.9. CHAOS Regions I and IIa are centred on the defect, and both are within Region 1 of the surface. The ions within Region I and IIa are relaxed explicitly, with those outside approximated using Mott-Littleton methods as detailed in Section 2.3.3. When a defect is simulated deeper into the crystal, these regions become more spherical, resulting in fully spherical regions for a bulk defect as depicted by Figure 2.7. The sizes of Region I and IIa used throughout this work were 9 Å and 35 Å respectively [93].

For charged surface defects, a corrective energy term is required. This is because charged defects on the surface can lead to a shift in the defect energy due to the electrostatic potential [99]. Therefore the defect energies were normalised by the

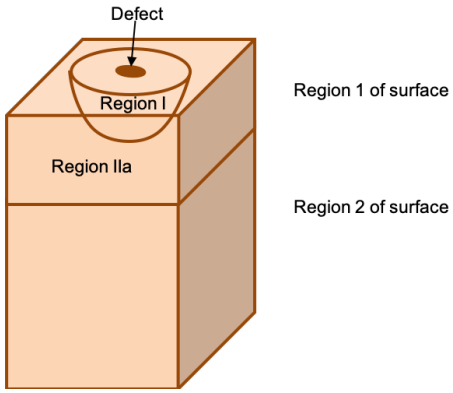


Figure 2.9: Schematic representation of a modelling a defect on a surface.

addition of an energy correction term, E_{Corr} [93].

The corrective term was calculated by comparison of the defect formation energy calculated in the bulk (via GULP) with the defect formation energy of the defect deep in Region 2 of the surface,

$$E_{Corr} = E^{F}_{D,Bulk} - E^{F,Reg2}_{D,Surf}. \tag{2.22}$$

The final defect formation energy was then calculated by addition of this corrective term to the defect formation energy in Region 1,

$$E^{F,Corr}_{D,Surf} = E^{F,Reg1}_{D,Surf} + E_{Corr}. \tag{2.23}$$

In order to investigate the energetic preference of a defect to form either at the surface, or in the bulk, segregation energies were calculated. The segregation energy is defined as the difference in the defect formation energy at the surface to that in the bulk lattice,

$$E^{Seg}_{D} = E^{F,Reg1}_{D,Surf} - E^{F}_{D,Bulk}. \tag{2.24}$$

If a segregation energy is negative, there is a thermodynamic drive for a defect to form at the surface rather than in the bulk [94].

2.5 Molecular Dynamics

The Large-scale Atomic/Molecular Massively Parallel Simulator (LAMMPS) code [73] was used for all molecular dynamics simulations included in this work. The Open Visualization Tool (OVITO) [100] was employed to visualise and analyse the output files. The PPPM solver was used for computation of the Coulomb long range

force throughout the MD simulations.

2.5.1 *Equations of Motion*

The force on a particular particle is calculated as the derivative of the interatomic potential.

For a system of N particles which have positions $\boldsymbol{r}_i$ (i=1,...N), the force acting on particle i can be calculated via the first-derivative of the interatomic potential,

$$\boldsymbol{F}_i = -\frac{\partial V(\boldsymbol{r}_1, ...\boldsymbol{r}_N)}{\partial \boldsymbol{r}_i}. \tag{2.25}$$

If each particle has mass m_i, then from Newton's second law ($\boldsymbol{F} = m\boldsymbol{a}$) and knowing acceleration, $\boldsymbol{a}$, is the derivative of velocity, $\boldsymbol{v}$, the equation of motion can be written as,

$$m_i \frac{\partial \boldsymbol{v}_i}{\partial t} = -\frac{\partial V(\boldsymbol{r}_1, ...\boldsymbol{r}_N)}{\partial \boldsymbol{r}_i}, \tag{2.26}$$

where $\boldsymbol{v}_i(t)$ is the velocity of a particle i at time t. Therefore, for a given atomic configuration, the interatomic potential can be used to determine the acceleration of the atoms at a time, t. From this it is possible to determine the atomic position and velocity at a time, $t + \Delta t$. Repeating this process generates the trajectory of an atom.

However, it is not possible to analytically solve the equation of motion, rather the equation of motion is numerically integrated over time via an integration algorithm. The integration algorithm used in this work is the Velocity-Verlet algorithm [101]. Via Taylor expansion of $\boldsymbol{r}(t + \Delta t)$ and ignoring higher order terms, we can write

$$\boldsymbol{r}(t + \Delta t) \approx \boldsymbol{r}(t) + \boldsymbol{v}(t)\Delta t + \frac{\boldsymbol{a}(t)\Delta t^2}{2}, \tag{2.27}$$

and for the reverse,

$$\boldsymbol{r}(t - \Delta t) \approx \boldsymbol{r}(t) - \boldsymbol{v}(t)\Delta t + \frac{\boldsymbol{a}(t)\Delta t^2}{2}. \tag{2.28}$$

Addition of Equations 2.27 and 2.28 gives the Verlet algorithm for position,

$$\boldsymbol{r}(t + \Delta t) = 2\boldsymbol{r}(t) + \boldsymbol{a}(t)\Delta t^2 + \boldsymbol{r}(t - \Delta t). \tag{2.29}$$

However, Equation 2.29 is not self-starting. I.e., if a simulation starts at time $t = 0$, it would be required to know the position at $t = -\Delta t$ to begin the simulation. To

improve this the Velocity-Verlet algorithm is used. This scheme is mathematically equivalent to Verlet, but it explicitly incorporates velocity:

$$\boldsymbol{r}(t+\Delta t) = \boldsymbol{r}(t) + \boldsymbol{v}(t)\Delta t + \frac{1}{2}\boldsymbol{a}(t)\Delta(t)^2. \tag{2.30}$$

The velocity can be calculated by starting from the Taylor expansion of $\boldsymbol{v}(t+\Delta t)$,

$$\boldsymbol{v}(t+\Delta t) = \boldsymbol{v}(t) + \boldsymbol{a}(t)\Delta t + \frac{\boldsymbol{b}(t)\Delta t^2}{2}, \tag{2.31}$$

where $\boldsymbol{b}(t)$ is the third derivative of $\boldsymbol{r}(t)$. Acceleration can also be written as,

$$\boldsymbol{a}(t+\Delta t) = \boldsymbol{a}(t) + \boldsymbol{b}(t)\Delta t, \tag{2.32}$$

which rearranges to,

$$\boldsymbol{b}(t) = \frac{\boldsymbol{a}(t+\Delta t) - \boldsymbol{a}(t)}{\Delta t}. \tag{2.33}$$

By substitution of Equation 2.33 into 2.31 and rearranging we get

$$\boldsymbol{v}(t+\Delta t) = \boldsymbol{v}(t) + \frac{\Delta t}{2}[\boldsymbol{a}(t) + \boldsymbol{a}(t+\Delta t)]. \tag{2.34}$$

Via $\boldsymbol{F} = m\boldsymbol{a}$, Equation 2.34 can be written as

$$\boldsymbol{v}(t+\Delta t) = \boldsymbol{v}(t) + \frac{\Delta t}{2}\Big[\frac{\boldsymbol{F}(t) + \boldsymbol{F}(t+\Delta t)}{m}\Big]. \tag{2.35}$$

Equations 2.30 and 2.35 are the Velocity-Verlet algorithms for position and velocity [101]. It is evident that $\boldsymbol{r}(t+\Delta t)$ must be defined before $\boldsymbol{v}(t+\Delta t)$. The Velocity Verlet algorithm is self-starting and minimises roundoff errors. The Velocity-Verlet algorithm is used at each timestep to calculate the atomic positions and then velocities, and thus the trajectories of the atoms within a MD simulation.

Smaller timesteps result in lower errors. Throughout this work a timestep of 1 fs was used.

2.5.2 *Periodic Boundary Conditions*

Periodic boundary conditions are used in MD to approximate a bulk system. The unit cell is replicated in three-dimensions as can be seen by Figure 2.10. The particles in the central box are conserved. As such, when a particle leaves the box through one side, it is inserted into the box at the opposite side with the same velocity.

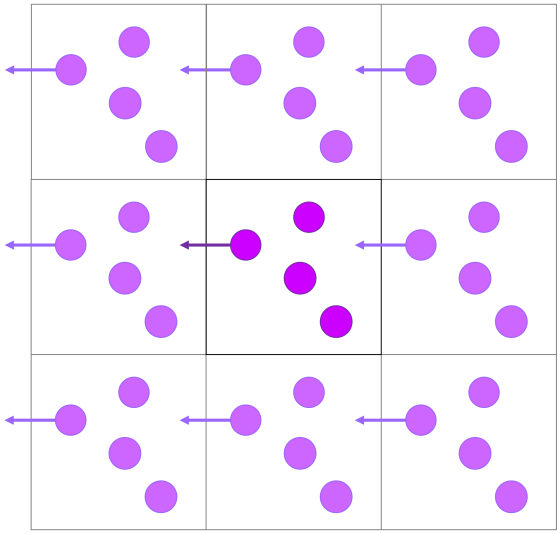


Figure 2.10: Schematic representation of periodic boundary conditions. Purple spheres represent atoms.

2.5.3 *Ensembles*

Statistical mechanics provides the link between atomic and macroscopic scales via the concept of a thermodynamic ensemble. An ensemble is a collection of particles which have different microscopic states (e.g. atomic positions) but have an identical macroscopic state (thermodynamic properties e.g. temperature) [102]. From the ergodic hypothesis, the ensemble average is equal to the time average of a property [103].

There are four ensembles commonly used in statistical thermodynamics [12]:

- The Canonical ensemble (NVT) in which the number of atoms, the volume and the temperature are fixed
- The Micro-canonical ensemble (NVE) in which the number of atoms, the volume and the total energy are fixed
- The Isothermal-isobaric ensemble (NPT) in which the number of atoms, the pressure and the temperature are fixed
- The Grand canonical ensemble (μVT) in which the chemical potential, the volume and the temperature are fixed

In this work the NPT ensemble was used. To keep the pressure and temperature constant, the Nosé-Hoover thermostat and barostat was applied [104]. Nosé-Hoover works by the coupling of a fictitious dynamic variable to the particle velocities for

thermostatting, and to the simulation domain dimensions for barostatting. The variable adjusts the particles speed until the desired temperature and pressure are reached during the equilibration period.

As pressure includes a kinetic component from particle velocities, both thermostatting and barostatting require the calculation of temperature. The average kinetic energy and the temperature of the system are related by,

$$< E_k >= \frac{3}{2} N k_B T, \tag{2.36}$$

where E_k is the kinetic energy, N is the number of particles in the system, k_B is the Boltzmann constant and T is the temperature.

2.5.4 *Mean Square Displacement*

The diffusion of particles can be likened to a random walk, there are many steps in random directions. As a result, if the displacement of the particles over a simulation was simply summed, it would result in an average displacement of zero. Therefore, the sum of the absolute displacement ignoring direction is required [105]. The Mean Square Displacement (MSD) at time t is defined as an ensemble average,

$$\text{MSD} \equiv < |x(t) - x_0|^2 >= \frac{1}{N} \sum_{i=1}^{N} |\boldsymbol{x}^{(i)}(t) - \boldsymbol{x}^{(i)}(0)|^2 \tag{2.37}$$

where N is the number of particles to be averaged, $x^{(i)}(0)$ is the reference position of a particle, i, and $x^{(i)}(t)$ is the position of particle i at time t [106].

The diffusivity, D, can then be calculated from the MSD via the relationship,

$$\text{MSD} = 6Dt. \tag{2.38}$$

The MSD was calculated during the LAMMPS simulation when the compute function was specified within the input file. This was calculated by the displacement of an atom is from its reference position which was the original position at the time the compute command was issued (the input position) [73].

A vector of four quantities is calculated at each time step by the MSD compute. A group of atoms to calculate the MSD for is specified in the input file, N is the number of atoms in the group. In this work each group contained all atoms of each element, i.e., all Pu atoms and all O atoms calculated separately. The first three elements of the vector are the squared dx, dy, and dz displacements, summed

and averaged over atoms in the group. The fourth element is the total squared displacement ($dx^2 + dy^2 + dz^2$) summed and averaged over atoms in the group. The MSD calculation includes all effects due to atoms passing through periodic boundaries [73].

2.5.5 *Summary*

Figure 2.11 displays a flow chart of the simulation process used during a molecular dynamics simulation via LAMMPS. Crystallographic data were used to determine the lattice structure. When defects were simulated the conjugate gradient energy minimisation procedure was performed prior to the running of MD. The input file consisted of the set of parameters and instructions. The atomic positions file was supplied separately as this was the starting point of each simulation.

At each time step, chosen properties such as the total energy, kinetic energy, and MSD of specific atom type were output to the LAMMPS log file, which was written to throughout the simulation. Dump files were also generated which are snapshots of atom quantities every X timesteps. The dump files were read into OVITO [100] to visually plot the atomic coordinates and inspect the trajectories. Dump files are huge files and require large amounts of memory; so there is a trade off for the frequency of output of the number of files versus the memory demands. Throughout this work X was set to 1000. The log files were analysed in ORIGIN [107] and MATLAB [108] for data post-processing, such as calculating an element's average MSD.

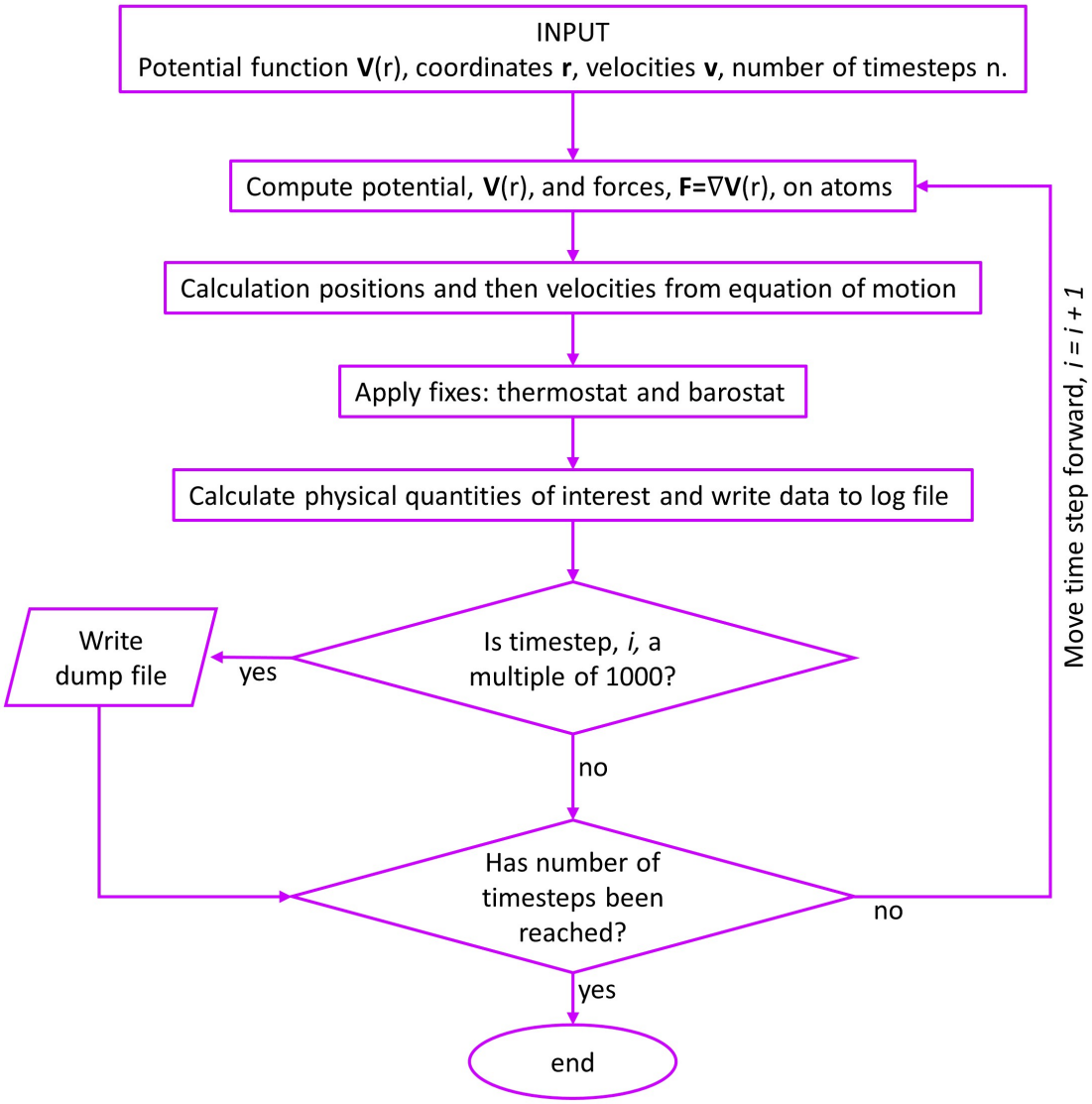


Figure 2.11: Schematic of the molecular dynamics simulation procedure employed in this thesis.

Chapter 3

Bulk Plutonium Dioxide

This chapter provides a detailed evaluation of potentials available to model the PuO_2 system. The best performing potential is then implemented to investigate the stability of intrinsic defects in bulk PuO_2.

3.1 Literature Review

A detailed understanding of PuO_2 is essential to enable the safe and secure storage of the UK's plutonium inventory. However whilst much work (both computational and experimental) has been done on UO_2, MOX fuel, and fluorite systems such as Yttria-Stabilized Zirconia (YSZ), studies of PuO_2 are limited [5], [109]. The defect chemistry of PuO_2 is challenging to study experimentally. Therefore, computational simulations provide a valuable tool in developing the scientific understanding of PuO_2.

Development of robust interatomic potentials for the simulation of PuO_2 has been a focus of many research groups. Read *et al.* [49] derived a new Pu—O potential via empirical fitting to crystal structural data and parametric fitting to additional physical properties. The Read *et al.* [49] model describes the O—O interaction via adaptation of the potential derived for oxygen interactions in UO_2 by Jackson *et al.* [89]. Alternative parameters for the Buckingham interaction between O—O were developed by Meis *et al.* [110]; their work adapted the attractive term of the potential published by Catlow [67]. Meis *et al.* [110] notes that as PuO_2 has such high symmetry, two-body terms are often sufficient to obtain a suitable model. Additionally, they detail how the Coulombic attraction is the dominant part of the potential model for the O—O interaction. By trial and error methods to replicate experimental data, Arima *et al.* [111] developed a new potential for the

Pu—O interaction which they have implemented in molecular dynamics simulations. Arima *et al.* [111] combined their potential with both the O—O potential of Meis *et al.* [110] and with an O—O potential developed by Dwivedi *et al.* [77] for ZrO_2. As ZrO_2 is also a fluorite lattice, Arima *et al.* [111] considered the interatomic potential for O—O transferable to a PuO_2 system. A Born-Mayers Higgins Pu—O potential was developed by Yu *et al.* [112], which was used in combination with the O—O potential of Meis *et al.* [110] to model oxygen self diffusion in α-Pu_2O_3. More recently, Cooper *et al.* [113] developed a new potential model for PuO_2. However, in contrast to the aforementioned pair-potentials, the Cooper potential is a many body potential which explicitly describes the short range Pu—Pu interaction.

Defects are present in PuO_2 due to collision cascades resulting from α-decays which cause atoms to be knocked from their lattice positions. However, during the local thermal spike which follows a collision cascade [114], additional re-configurations of the defect structure take place, including the recombination of Frenkel pairs [115] [116]. This re-configuration process is known as self-annealing and is often due to the mobility of vacancies at room temperature [57]. Wheeler *et al.* [57] used dialometry to investigate the volume changes of lattice damaged plutonium. Their work found that the material initially contracts due to the self-annealing of lattice damage, and that the magnitude of contraction was dependent on the age of the sample. Kato *et al.* [117] used X-Ray Diffraction (XRD) to measure the lattice parameter of MOX powder samples both before and after isothermal annealing. Three thermal recovery stages were observed; the mechanisms for which were considered to be due to the recovery of cation Frenkel defects, anion Frenkel defects and helium trapped by a vacancy.

Although comparisons with other irradiated materials would suggest that the self-irradiation of ambient temperature plutonium could lead to potentially catastrophic damage, work with plutonium over several decades at Los Alamos laboratory has shown no evidence for such damage [53]. Lattice defect structures may be insufficient to result in catastrophic damage, but with such emphasis on extended lifetimes of plutonium storage [4], it is clear that a thorough understanding of the fundamental processes behind irradiation damage and concurrent healing processes is vital [53].

The understanding of the risk of void swelling in plutonium has grown rapidly in recent years. Void swelling is due to the tendency of vacancies to diffuse through a metal and cluster to form voids which results in the net effect macroscopically of a metal swelling in size. In 2000, from simple calculation, Wolfer [45] predicted

that macroscopic swelling in plutonium due to helium bubbles was very unlikely at ambient temperature. However, in the same year, Hecker *et al.* [53] published that reliable predictions of void swelling in plutonium were not currently possible, due to a lack of knowledge of intrinsic properties such as the relaxation volumes for vacancies and interstitials. More recently in 2016, Chung *et al.* [118] employed mechanical tests on plutonium alloys to investigate the self-irradiation effects of plutonium alloys. They determined that after a self-irradiation equivalent time of almost 200 years, there were no signs of void swelling and the maximum volume expansion at ambient temperature was less than 0.25% [118]. Despite this, Chung *et al.* [118] noted that it remains necessary to investigate an integrated contribution from multiple self-irradiation induced defects in plutonium [118].

As discussed, computational methods are ideally suited to developing the understanding of the defect chemistry of PuO_2. *Ab initio* and potential based studies of intrinsic defects in PuO_2 are available in the literature. Via Local Spin Density Approximation with the Hubbard U correction (LSDA+U) calculations at 1000 K, Lu *et al.* [119] found that oxygen related defects always have much lower defect formation energies than purely plutonium related ones. They suggest this may be because the lattice distortion is greater for Pu related defects than O related defects. Nakamura *et al.* [120] used Local Density Approximation with the Hubbard U correction (LDA+U) with spin-orbit coupling methods to model PuO_2, this methodology enabled paramagnetic insulating states to be obtained. In agreement with Lu *et al.* [119], their work found O related defects to have lower defect formation energies than Pu related defects. This result has been widely acknowledged by pair potential methods in static simulations [49] and molecular dynamical simulations [121] [122].

3.2 Review of Interatomic Potentials

A review of different published interatomic potentials for PuO_2 was performed to enable the most accurate potential to be chosen. Each potential was implemented in GULP [86], and the output file analysed to evaluate the calculated values against experimental values. As stated by Catlow [67], when a potential is able to replicate experimental data, it gives confidence in the potential to become a predictive tool in further work.

Table 3.1: Names of the combinations of potentials used in this work

Name	Author	
	Pu—O	O—O
Read	Read *et al.* [49]	Jackson *et al.* [89]
Arima1	Arima *et al.* [111]	Dwivedi *et al.* [77]
Arima2	Arima *et al.* [111]	Meis *et al.* [110]
Yu	Yu *et al.* [112]	Meis *et al.* [110]

3.2.1 *Interatomic Potentials for PuO_2*

This section will list the published parameters for each potential considered. Four fully ionic models for PuO_2 were identified in the literature. Each potential assumes the plutonium and oxygen ions have full formal oxidation states of 4+ and 2-, respectively. The potentials have been named corresponding to the cation-anion (Pu—O) potential authors, as detailed in Table 3.1. The many-body potential of Cooper Rushton Grimes [113] is referred to as the Cooper potential.

3.2.1.1 Read Potential

Read *et al.* [49] developed a potential for PuO_2, built upon their work deriving a potential for UO_2 via empirical fitting. In this description the anion-anion and cation-anion potentials are described using different analytical forms based on the Born-Mayer potential.

For the cation-anion interaction, a Buckingham potential with an electrostatic interaction term was employed,

$$V_{ij} = A_{ij} \exp\Big(-\frac{r_{ij}}{\rho_{ij}}\Big) - \frac{C_{ij}}{r_{ij}^6} + \frac{q_i q_j}{r_{ij}}, \tag{3.1}$$

where q_i and q_j are the charges of the interacting ions and constitute the supplementary electrostatic interaction term. The parameters of A, ρ and C for each interaction are displayed in Table 3.2. As the C value is zero for this interaction, this potential may be referred to as a Born-Mayer-Huggins potential. To improve calculation efficiency this interaction energy function does not contribute beyond the defined cut-off of 15 Å, which is due to the rapid convergence of the short-range energy to zero [55].

For the anion-anion potential, a Buckingham four range potential (Buck4) as derived by Jackson *et al.* [89] was employed. This potential was derived for UO_2.

However, as noted by Read *et al* [49], anions within PuO_2 and UO_2 unit cells are arranged with the same symmetry, due to both compounds adopting the same cubic crystal structure. Therefore, the same description of anion-anion interactions used for UO_2 may be used for PuO_2.

The Buck4 potential is required for the anion-anion interaction to negate the unphysical attractive forces at short-range. This is done by the function discarding the attractive $-\frac{C}{r^6}$ term below a certain distance [55]. As the function is defined by intervals, only the appropriate terms of the standard Buckingham function are used over relevant interaction distances [89]. Equation 3.2 displays the potential and its defining intervals,

$$\phi^{\text{Buck4}}(r_{ij}) = \begin{cases} A_{ij}\exp(-\frac{r_{ij}}{\rho_{ij}}) & \text{if } r_{min} < r_{ij} \leq \text{cut}_1, \\ \sum_{m=0}^{5} a_m r_{ij}^m & \text{if } \text{cut}_1 < r_{ij} \leq r_{\text{minimum}}, \\ \sum_{n=0}^{3} b_n r_{ij}^n & \text{if } r_{\text{minimum}} < r_{ij} \leq \text{cut}_2, \\ -\frac{c_{ij}}{r_{ij}^6} & \text{if } \text{cut}_2 < r_{ij} \leq r_{\text{max}}. \end{cases} \tag{3.2}$$

The interval definitions are: r_{max}, the short range cut-off, r_{min}, a minima stationary point of the function, cut_1 and cut_2, which are the boundary points at which the functions and their first and second derivatives are required to be continuous [49]. The parameter values are listed in Table 3.2.

Finally, the potential includes a description of the electronic polarisation of ions, using the shell model, as described by Section 2.1.4. Values for which are also listed in Table 3.2.

Table 3.2: Parameters of the Read potential

Interaction	Short range parameters			Shell model parameters	
	A (eV)	ρ (Å)	C (eV Å^{-6})	Y ($\lvert e\rvert$)	k_2 (eV Å^{-2})
Pu—O [a]	1116.3317	0.3926	0.0	6.54	206.77
O—O [b]	11272.6	0.1363	134	−4.4	296.2
	r_{min} (Å)	cut_1 (Å)	$r_{minimum}$ (Å)	cut_2 (Å)	r_{max} (Å)
	0.0	1.2	2.1	2.6	15.0

[a] Ref. [49]
[b] Ref. [89]

3.2.1.2 Arima1 Potential

The form of the potential used for both interactions was the Born-Mayer-Huggins potential with the fully ionic model, which is identical to that described by Equation 3.1. The parameters for the anion-anion interaction (including the shell model parameters) were obtained by Dwivedi *et al.* [77] via empirical fitting.

The parameters for the cation-anion interaction were determined by trial-and-error methodology to reproduce the experimental thermal expansion behaviour and the compressibility at room temperature by Arima *et al.* [111]. For this interaction no shell model parameters were included. The parameters are listed in Table 3.3.

Table 3.3: Parameters of the Arima1 potential

Interaction	Short range parameters			Shell model parameters		r_{max} (Å)
	A (eV)	ρ (Å)	C (eV Å^{-6})	Y ($\|e\|$)	k_2 (eV Å^{-2})	
Pu—O [a]	1129.706	0.383	0.0	–	–	15.0
O—O [b]	22759.942	0.149	27.89	−2.077	27.290	15.0

[a] Ref. [111]
[b] Ref. [77]

3.2.1.3 Arima2 Potential

Work by Chu *et al.* [123] combined the Pu—O potential derived by Arima *et al.* [111] (described above in Section 3.2.1.2), with a O—O potential derived by Meis *et al.* [110]. The form of the potential used by Meis *et al.* was once again the Buckingham potential, described by Equation 3.1, with empirically fitted parameters. As before, the shell model parameters were only included for the anion-anion interaction. The parameters used in this potential are listed in Table 3.4.

Table 3.4: Parameters of the Arima2 potential

Interaction	Short range parameters			Shell model parameters		r_{max} (Å)
	A (eV)	ρ (Å)	C (eV Å^{-6})	Y ($\|e\|$)	k_2 (eV Å^{-2})	
Pu—O [a]	1129.7	0.383	0.0	–	–	10.0
O—O [b]	22764	0.149	31.984	−2.86	52.308	12.0

[a] Ref. [111]
[b] Ref. [110]

3.2.1.4 Yu Potential

Yu *et al.* [112] used the Born-Mayer-Huggins potential (Equation 3.1) and the shell model to describe PuO_2. The parameters for the Pu—O interaction were determined via the trial-and-error method to reproduce the experimental cell parameters, density, space group and high frequency dielectric constants at room temperature [112]. The parameters derived by Meis *et al.* [110] were used for the O—O interaction, but with updated shell model parameters. The parameters are displayed in Table 3.5.

Table 3.5: Parameters of the Yu potential

Interaction	Short range parameters			Shell model parameters		r_{max} (Å)
	A (eV)	ρ (Å)	C (eV Å^{-6})	Y ($\|e\|$)	k (eV Å^{-2})	
Pu—O [a]	1304.8	0.3653	0.0	–	–	10.0
O—O [b]	22764	0.149	31.984	−2.86	37.05	12.0

[a] Ref. [112]
[b] Ref. [110]

3.2.1.5 Cooper Potential

Cooper *et al.* [113] developed a consistent set of potentials for actinide dioxides, with updated parameters for PuO_2 [122]. The potential has two components: one that is pairwise, and one that is many-bodied.

$$E_i = \frac{1}{2}\sum_j \phi_{\alpha\beta}(r_{ij}) - G_\alpha \sqrt{\sum_j \sigma_\beta(r_{ij})}. \tag{3.3}$$

The pairwise interaction between atoms i and j is given by $\phi_{\alpha\beta}(r_{ij})$. This has both long range electrostatic, $\phi_{\mathrm{C}}(r_{ij})$, and short range contributions described by Buckingham, $\phi_{\mathrm{B}}(r_{ij})$, and Morse, $\phi_{\mathrm{M}}(r_{ij})$, potential forms (Equation 3.4).

$$\phi_{\alpha\beta}(r_{ij}) = \phi_{\mathrm{C}}(r_{ij}) + \phi_{\mathrm{B}}(r_{ij}) + \phi_{\mathrm{M}}(r_{ij}), \tag{3.4}$$

where

$$\phi_{\mathrm{C}}(r_{ij}) = \frac{q_\alpha q_\beta}{4\pi\epsilon_0 r_{ij}}, \tag{3.5}$$

$$\phi_{\mathrm{B}}(r_{ij}) = A_{\alpha\beta}\exp\left(\frac{-r_{ij}}{\rho_{\alpha\beta}}\right) - \frac{C_{\alpha\beta}}{r_{ij}6}, \tag{3.6}$$

$$\phi_{\mathrm{M}}(r_{ij}) = D_{\alpha\beta}[\exp(-2\gamma_{\alpha\beta}(r_{ij}-r_0)) - 2\exp(-\gamma_{\alpha\beta}(r_{ij}-r_0))]. \tag{3.7}$$

In the above $A_{\alpha\beta}$, $\rho_{\alpha\beta}$, $C_{\alpha\beta}$, $D_{\alpha\beta}$, $\gamma_{\alpha\beta}$ and r_0 are the empirical parameters.

The second term in Equation 3.3 uses the EAM to introduce a subtle many-body perturbation to the more dominant pairwise interactions.

3.2.2 *Results and Discussion*

Each potential was implemented in GULP. The output values will now be evaluated against the available data. The experimental values used were found from the available literature. For some properties no experimental data was available, so some theoretical values from *ab initio* studies are included.

3.2.2.1 Structural Properties

The structural properties evaluated were the lattice constant and ionic distances. Table 3.6 displays the observed values of these properties as found in the literature.

Table 3.6: Observed values of PuO_2 structural properties

Property	Experimental
Lattice Constant:	
a_0 (Å)	5.39819 [a]
Ionic Distances:	
Pu-Pu (Å)	3.816 [b]
Pu-O (Å)	2.337 [b]
O-O (Å)	2.698 [b]

[a] Ref. [124]
[b] Ref. [110]

The calculated values output from each simulation are displayed in Table 3.7. The percentage difference, Δ, between observed and calculated values was calculated as a means of comparison to determine which potential was the most accurate.

It can be seen from Table 3.7 that the Read potential provides excellent agreement with observed values ($\Delta < |0.01|$ %). Only the Yu potential has potential differences greater than 0.5%, therefore for structural properties this potential provides the least accurate simulation of PuO_2.

Table 3.7: Results of structural properties of PuO_2

Potential	Property	Calculated (Å)	Δ (%)
Read	a_0	5.398117	0.001
	Pu-Pu	3.817	-0.026
	Pu-O	2.338	-0.021
	O-O	2.699	-0.041
Arima1	a_0	5.380861	0.321
	Pu-Pu	3.805	0.294
	Pu-O	2.330	0.300
	O-O	2.690	0.282
Arima2	a_0	5.375371	0.423
	Pu-Pu	3.801	0.393
	Pu-O	2.328	0.402
	O-O	2.688	0.382
Yu	a_0	5.237218	2.982
	Pu-Pu	3.703	2.953
	Pu-O	2.268	2.961
	O-O	2.619	2.943
Cooper	a_0	5.379873	0.339
	Pu-Pu	3.817	-0.029
	Pu-O	2.338	-0.021
	O-O	2.699	-0.041

3.2.2.2 Mechanical Properties

The mechanical properties evaluated were the elastic constant matrices, the bulk modulus and Young's modulus. Although a value for shear modulus was calculated in the simulation, an experimental value was not available from the literature and therefore the shear modulus is not considered in the evaluation. The observed values are displayed in Table 3.8.

The calculated values output from each simulation are displayed in Table 3.9. The percentage difference, Δ, between observed and calculated values was calculated as a means of comparison to determine which potential was the most accurate.

Comparison of the mechanical property values for each potential show that the Read potential provided the closest agreement with experimental values. The Read potential was the only potential to have all values for the elastic constant matrices

Table 3.8: Observed values of PuO_2 mechanical properties

Property	Experimental
Elastic Constant Matrices:	
C_{11} (GPa)	430.6 [a]
C_{12} (GPa)	128.4 [a]
C_{44} (GPa)	67.3 [a]
Moduli:	
Bulk (GPa)	178 [b]
Shear (GPa)	-
Young's (GPa)	268.4 [c]

[a] Ref. [110]
[b] Ref. [125]
[c] Ref. [126]

below a 6% deviation. For the bulk and Young's moduli, the Read potential again has the lowest deviation from observed values. However, they are still relatively large deviations.

Table 3.9: Results of mechanical properties of PuO_2

Potential	Property	Calculated (GPa)	Δ (%)
Read	C_{11}	408.56	5.118
	C_{12}	130.21	-1.410
	C_{44}	67.30	-0.001
	Bulk Modulus	222.99	-25.275
	Young's Modulus	345.62	-28.770
Arima1	C_{11}	503.58	-16.948
	C_{12}	106.09	17.375
	C_{44}	97.95	-45.535
	Bulk Modulus	238.59	-34.039
	Young's Modulus	466.66	-73.867
Arima2	C_{11}	502.02	-16.586
	C_{12}	107.55	16.238
	C_{44}	53.59	20.377
	Bulk Modulus	239.04	-34.292
	Young's Modulus	464.07	-72.902
Yu	C_{11}	559.68	-29.977
	C_{12}	130.39	-1.550
	C_{44}	48.87	27.386
	Bulk Modulus	273.49	-53.646
	Young's Modulus	510.40	-90.164
Cooper	C_{11}	423.62	1.620
	C_{12}	125.92	1.930
	C_{44}	53.53	20.455
	Bulk Modulus	225.16	-26.492
	Young's Modulus	365.92	-36.332

3.2.2.3 Optical Properties

The optical properties evaluated were the static and high frequency dielectric constants. Table 3.10 displays the observed values found in the literature. To ensure accurate defect calculations, accurate dielectric constants are crucial. This is due to the fact that the response of a solid to a charged defect within the material depends on the inverse of the dielectric constant [86].

The calculated values output from each simulation are displayed in Table 3.11. The percentage difference, Δ, between observed and calculated values was calculated

Table 3.10: Observed values of PuO_2 optical properties

Property	Experimental
Dielectric Constants:	
Static ϵ_0	21.03 [a]
High Frequency ϵ_∞	3.0 [b]

[a] Ref. [126]
[b] Ref. [127]

as a means of comparison to determine which potential was the most accurate.

Table 3.11: Results of optical properties of PuO_2

Potential	Property	Calculated	Δ (%)
Read	ϵ_0	15.92	24.308
	ϵ_∞	3.23	-7.520
Arima1	ϵ_0	11.49	45.359
	ϵ_∞	2.34	21.940
Arima2	ϵ_0	14.55	30.799
	ϵ_∞	2.78	7.477
Yu	ϵ_0	13.868	34.056
	ϵ_∞	1.78	40.567
Cooper	ϵ_0	3.39	83.874
	ϵ_∞		

Comparison of the calculated values for each potential shows that the Read and Arima2 potentials gave similar values. The Arima2 and Yu potentials grossly overestimate the values. In contrast, the Cooper potential underestimates the static dielectric constant. Once again, the Read potential overall displays the lowest deviation from observed values.

3.2.3 *Summary*

The evaluation of calculated values compared to observed values found the Read potential to be the most accurate for structural, mechanical and optical properties. Therefore the Read potential shall be implemented in all static simulations included in this thesis [67] (Chapters 3, 4, and 5).

3.3 Mott-Littleton Region Optimisation

3.3.1 *Methodology*

To model defects the Mott-Littleton methodology was used, as detailed in Section 2.3.3. For a particular lattice system the optimum Region I and IIa radii must be chosen to ensure the model is accurate.

The larger the radius of Region I, the less approximation is made and therefore the more accurate the simulation. However, larger Region I radii result in more ions being explicitly relaxed, and therefore lead to higher computational processing requirements. Thus, the optimum radii must be chosen to ensure that for the lowest number of ions in Region I, the defect energy is sufficiently converged [86].

In order to determine the optimum region radii to use in the Mott-Littleton approximation, simulations of isolated point defects in PuO_2 were run with a range of radii. In each trial the radius of Region IIa was double that of Region I. Four different defect simulations were run independently to ensure that the radii chosen provided convergence for each defect.

3.3.2 *Results*

Table 3.12 displays the number of ions in each region and the defect energy of the trialled radii for each defect. The minimum Region I radii trialled was 9 Å as below this radius conditions for a minimum were unable to be satisfied as the region was too small. The maximum Region I radii trialled was 18 Å, as the defect energy had converged at a radii lower than this value, and the simulation took significantly longer to compute. Therefore no value was being gained for the increased computational time.

It can be seen from Table 3.12 that each defect energy begins to converge to its minimum value at approximately 13 Å. Figure 3.1 displays the results for the O^{2-} vacancy defect. It can be seen that as the Region I radius increases, the number of ions increases due to more ions being within the region. Concurrently the point defect energy decreases as it is converging to its minimum value. Both of these trends are as expected. The Region radii chosen were 14 Å and 28 Å for Region I and IIa respectively. This was due to these being the lowest radii which have minimum values of defect energy for each defect investigated. These radii were used throughout the simulations presented in this chapter.

Table 3.12: Mott-Littleton region optimisation for four defects in PuO_2

Defect: O_i''

Region Size (Å) I	IIa	No. ions Reg. I	Defect Energy (eV)
18	36	3668	-11.757
17	34	3188	-11.756
16	32	2680	-11.757
15	30	2176	-11.756
14	28	1888	-11.756
13	26	1408	-11.754
12	24	1072	-11.747
11	22	840	-11.757
10	20	588	-11.750
9	18	476	-11.725

Defect: $Pu_i^{••••}$

Region Size (Å) I	IIa	No. ions Reg. I	Defect Energy (eV)
18	36	3668	-60.015
17	34	3188	-60.006
16	32	2680	-60.010
15	30	2176	-60.002
14	28	1888	-59.985
13	26	1408	-59.972
12	24	1072	-59.963
11	22	840	-59.938
10	20	588	-59.956
9	18	476	-59.846

Defect: V_{Pu}''''

Region Size (Å) I	IIa	No. ions Reg. I	Defect Energy (eV)
17	34	3188	17.076
16	32	2680	17.080
15	30	2176	17.080
14	28	1888	17.080
13	26	1408	17.090
12	24	1072	17.088
11	22	840	17.094
10	20	588	17.110
9	18	476	17.120

Defect: $V_O^{••}$

Region Size (Å) I	IIa	No. ions Reg. I	Defect Energy (eV)
17	34	3188	80.026
16	32	2680	80.019
15	30	2176	80.031
14	28	1888	80.040
13	26	1408	80.031
12	24	1072	80.089
11	22	840	80.056
10	20	588	80.053
9	18	476	80.187

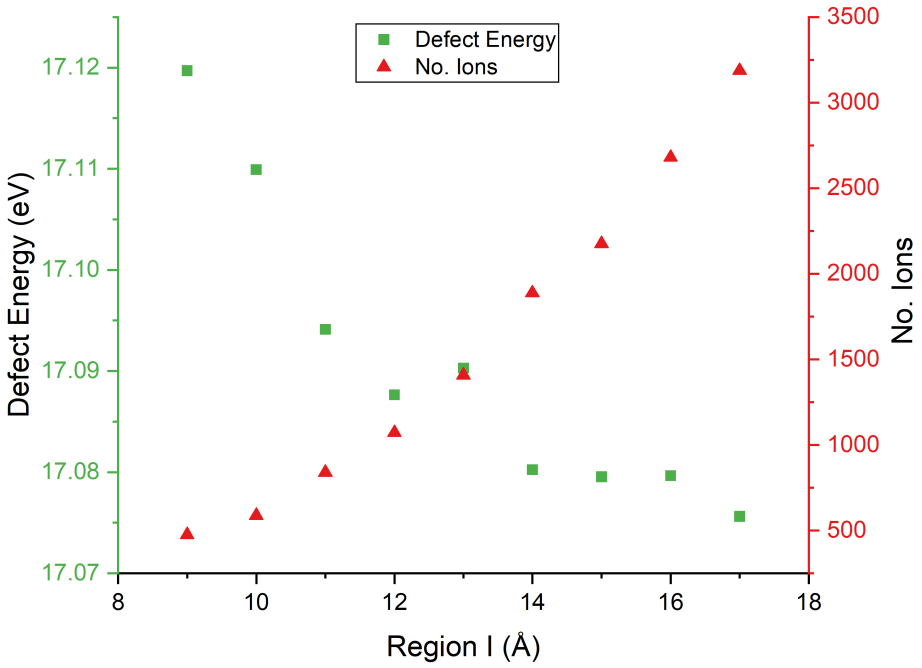


Figure 3.1: Graph displaying the point defect energy and number of ions in the region against radius for O^{2-} vacancy used in order to optimise the Mott-Littleton regions.

3.4 Isolated Defect Incorporation

3.4.1 *Point Defects*

In pure PuO_2, vacancies (where a lattice site is vacant) and interstitials (where an interstitial site is occupied) are the primary defects. Table 3.13 lists the defects along with their unit cell coordinates. As the Pu^{4+} ions are organised in a face-centred cubic array, and the oxide ions occupy tetrahedral holes, interstitial ions are located in the octahedral holes, $(\frac{1}{2}, \frac{1}{2}, \frac{1}{2})$.

Table 3.13: Point defect coordinates

Defect	Position
Pu^{4-} vacancy (V''''_{Pu})	(0, 0, 0)
O^{2+} vacancy ($V^{\bullet\bullet}_{O}$)	$(\frac{1}{4}, \frac{1}{4}, \frac{1}{4})$
Pu^{4+} interstitial ($Pu_i^{\bullet\bullet\bullet\bullet}$)	$(\frac{1}{2}, \frac{1}{2}, \frac{1}{2})$
O^{2-} interstitial (O''_i)	$(\frac{1}{2}, \frac{1}{2}, \frac{1}{2})$

To run the simulation the defect keyword was included in the GULP input file. The lattice was allowed to relax in accordance with Mott-Littleton methodology as described by Section 3.3.1.

The defect formation energies for isolated point defects are displayed in Table 3.14. These defects will not occur in isolation within the defective lattice, as charge neutrality must be preserved.

Table 3.14: Defect formation energies for isolated defects

Defect	Position	E_f (eV)
V''''_{Pu}	(0, 0, 0)	80.03
$V^{\bullet\bullet}_{O}$	$(\frac{1}{4}, \frac{1}{4}, \frac{1}{4})$	17.09
$Pu_i^{\bullet\bullet\bullet\bullet}$	$(\frac{1}{2}, \frac{1}{2}, \frac{1}{2})$	-59.97
O''_i	$(\frac{1}{2}, \frac{1}{2}, \frac{1}{2})$	-11.75

The following section will describe the lattice distortion observed in the CrystalMaker® visualisation due to the isolated point defects. Although the defects will not occur in this manner, the lattice distortion effects of intrinsic defects may be a combination of the distortion experienced for each point defect. Thus, visualising defects independently adds clarity to how intrinsic defects may distort a lattice.

3.4.1.1 Plutonium Vacancy

Figure 3.2 displays a visualisation of Region I around a plutonium vacancy after relaxation. It can be seen that the lattice distorts around the defect, but this distortion only occurs within a close proximity to the defect. This is due to the defect forces becoming weaker with distance. It is well documented that the lattice distortion is due to the point defects changing the electronic structures within the lattice [119].

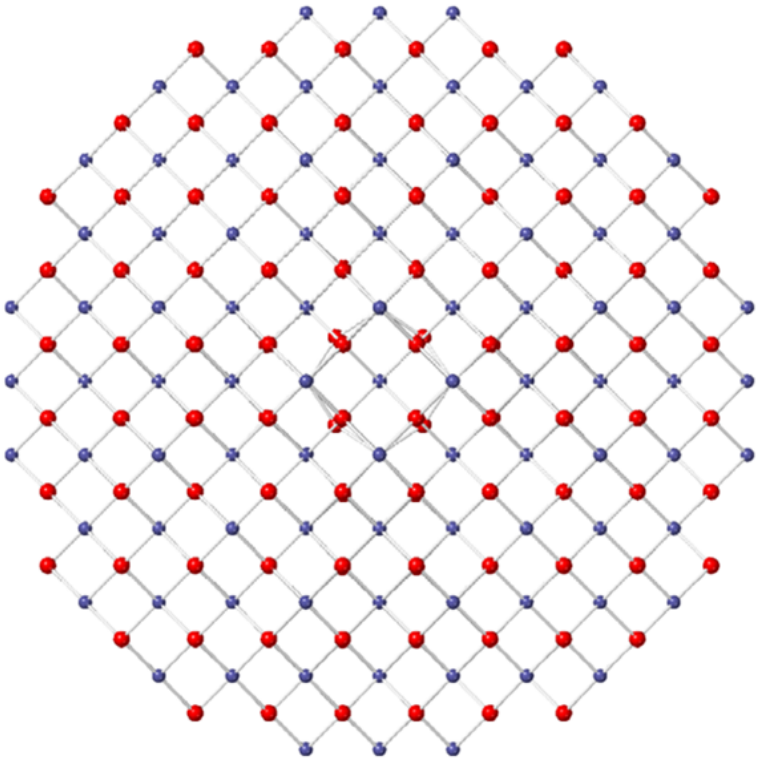


Figure 3.2: Region I centred on a plutonium vacancy after relaxation. O atoms are red, Pu are blue.

Figure 3.3 displays the lattice distortion around the plutonium vacancy. It can be see that neighbouring oxygen ions move further from the vacant site in the relaxed configuration due to the repulsive electrostatic interaction between themselves and the positive vacant site.

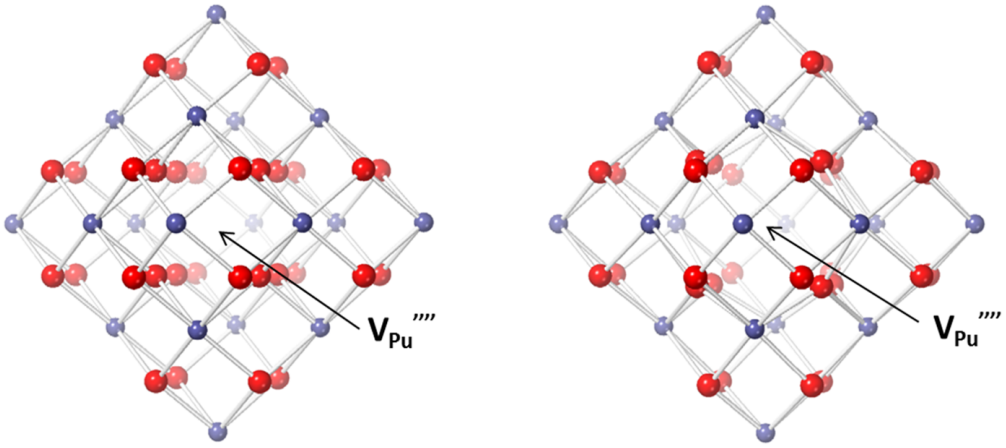


Figure 3.3: Plutonium vacancy visualisation. LHS: before relaxation, RHS: after relaxation. O atoms are red, Pu are blue.

3.4.1.2 Oxygen Vacancy

Figure 3.4 displays the visualisation of an oxygen vacancy both before and after relaxation was allowed to occur. A lattice oxygen ion has a 2- charge, so the vacant site has a 2+ charge. It can be seen that the oxygen ions in the immediate vicinity of the oxygen vacancy are closer to the vacant site in the relaxed configuration, as seen by the label 'lattice distortion' on Figure 3.4. This may be due to the electrostatic attraction between the vacant site and oxygen ions.

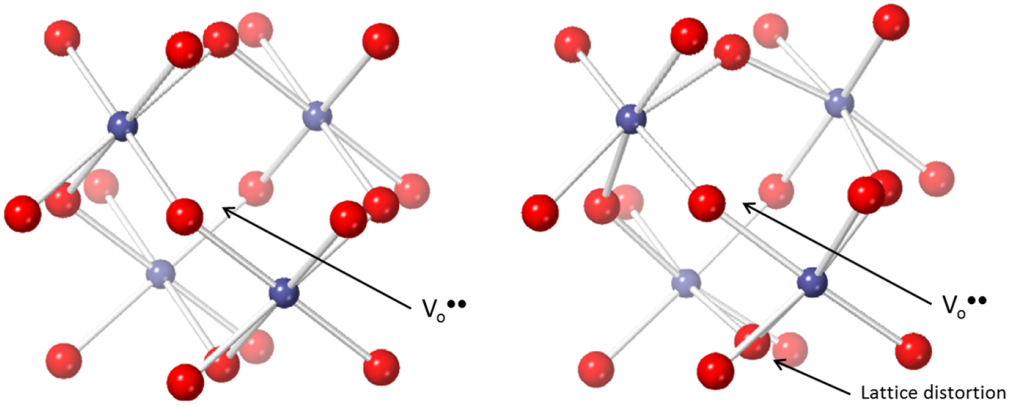


Figure 3.4: Oxygen vacancy visualisation. LHS: before relaxation, RHS: after relaxation. O atoms are red, Pu are blue.

3.4.1.3 Plutonium Interstitial

Figure 3.5 displays the visualisation of a plutonium interstitial ion within the lattice, both before and after relaxation. An interstitial plutonium ion introduces a 4+

charge to the lattice. Due to electrostatic forces, the lattice distorts to accommodate the additional charge. Lattice distortion due to electrostatic attraction (e.g. labelled ′a′ on Figure 3.5) is due to the oxygen ions being attracted to the positive plutonium ion. Lattice distortion due to electrostatic repulsion (e.g. labelled ′b′ on Figure 3.5) is due to the lattice plutonium ions being repelled away from the interstitial ion.

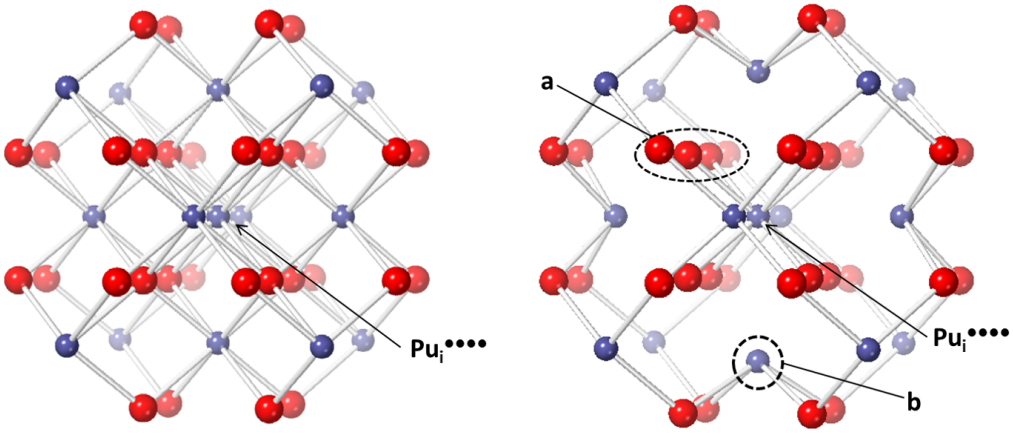


Figure 3.5: Plutonium interstitial with regions of lattice distortion labelled ′a′ and ′b′. LHS: before relaxation, RHS: after relaxation. O atoms are red, Pu are blue.

3.4.1.4 Oxygen Interstitial

Figure 3.6 displays a visualisation of an oxygen interstitial located in an octahedral hole in the lattice, both before and after the lattice is relaxed. It can be seen that lattice distortion, in the form of neighbouring oxygen atoms moving further from the oxygen interstitial, occurs around the defect site. This is due to the repulsive electrostatic interaction acting between the positively charged ions.

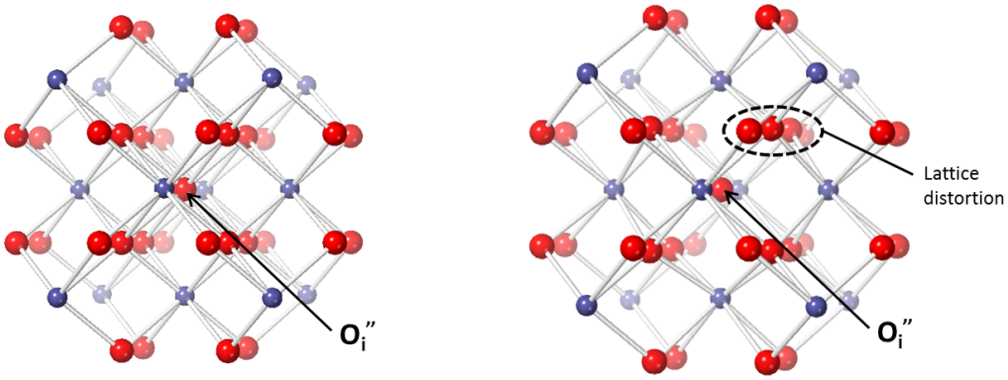


Figure 3.6: Oxygen interstitial visualisation. LHS: before relaxation, RHS: after relaxation. O atoms are red, Pu are blue.

3.4.2 *Intrinsic Defects*

In order to maintain charge neutrality of the lattice, point defects occur in combination. The three intrinsic defects considered were: Oxygen Frenkel Pair (OFP), Plutonium Frenkel Pair (PuFP) and the Schottky trio.

The energies from the separate point defect formation energy calculations were combined into the formation reactions, on the assumption that the defects are ′unbound′, i.e. they do not interact. The point defects were considered to be sufficiently far apart, dissolved in the bulk, or isolated. This assumption was valid since the charge of the defect is screened at distance within an ionic lattice by the constituent ions. The formation reactions are as follows,

$$\mathrm{Pu}_{\mathrm{Pu}}^{\mathrm{x}} + 2\mathrm{O}_{\mathrm{O}}^{\mathrm{x}} \leftrightarrow \mathrm{V}_{\mathrm{Pu}}^{''''} + 2\mathrm{V}_{\mathrm{O}}^{\bullet\bullet} + \mathrm{PuO}_{2(\mathrm{surface})}, \tag{3.8}$$

$$\mathrm{O}_{\mathrm{O}}^{\mathrm{x}} \leftrightarrow \mathrm{V}_{\mathrm{O}}^{\bullet\bullet} + \mathrm{O}_{i}^{''}, \tag{3.9}$$

$$\mathrm{Pu}_{\mathrm{Pu}}^{\mathrm{x}} \leftrightarrow \mathrm{V}_{\mathrm{Pu}}^{''''} + \mathrm{Pu}_{i}^{\bullet\bullet\bullet\bullet}. \tag{3.10}$$

Equation 3.8 is the formation reaction for the Schottky trio, and Equations 3.9 and 3.10 are the formation reactions for an oxygen or plutonium Frenkel pair, respectively. Therefore, a vacancy in combination with an interstitial was used to calculate Frenkel defect reaction energy, and vacancies and the lattice formation energy, E_f were used to calculate the Schottky defect reaction energy. The calculated formation energy (in eV) is divided by the number of defects in the equation to give the formation energy per defect. Table 3.15 displays the results.

Table 3.15: Defect formation energy for unbound defects

Defect	E_f (eV/Defect)
Schottky	3.55
PuFP	10.03
OFP	2.67

It can be seen from Table 3.15 that for unbound intrinsic defects, the oxygen Frenkel pair has the lowest defect formation energy. Therefore, considering purely unbound defects, the oxygen Frenkel pair defect is predicted to be the most dominant in the lattice as it is the most thermodynamically favourable. This result was also found by Read *et. al* [49].

3.5 Cluster Defect Incorporation

The calculation of intrinsic defect formation energies by combining isolated defect energies as described by Section 3.4.2 assumes the infinite dilution of the defects. Thus, the binding energy associated with the aggregation of point defects is omitted [128]. To simulate bound defects, cluster calculations were performed.

3.5.0.1 Cluster Defect Formation Reactions

Defect clusters were simulated by defining all the required vacancies or interstitials in one calculation, which determined the total energy for the cluster of defects. A cluster is charge neutral overall. For example, an oxygen Frenkel pair cluster would consist of, $\{V_O^{\bullet\bullet} : O_i^{''}\}^x$. The formation reactions for the bound intrinsic defects are assumed reversible at 0 K and are as follows,

$$Pu_{Pu}^x + 2O_O^x \leftrightarrow \{V_{Pu}^{''''} : 2V_O^{\bullet\bullet}\}^x + PuO_{2(surface)}, \tag{3.11}$$

$$O_O^x \leftrightarrow \{V_O^{\bullet\bullet} : O_i^{''}\}^x, \tag{3.12}$$

$$Pu_{Pu}^x \leftrightarrow \{V_{Pu}^{''''} : Pu_i^{\bullet\bullet\bullet\bullet}\}^x. \tag{3.13}$$

Equation 3.11 is the formation reaction for the bound Schottky trio, and Equation 3.12 and 3.13 are the formation reactions for the bound oxygen and plutonium Frenkel pairs, respectively.

3.5.0.2 Plutonium Frenkel Pair Cluster Calculation

Only one configuration of the plutonium Frenkel pair was simulated. The defect formation energy was calculated to be 7.87 eV/Defect. Figure 3.7 displays the visualisation of the plutonium Frenkel pair in the lattice both before and after relaxation. It can be observed that lattice distortion occurs around both the vacancy and the interstitial plutonium sites. As was found for the isolated point plutonium vacancy defect (Figure 3.3), the surrounding oxygen ions are repelled by the negative charge of the defect and in the relaxed configuration have moved away from it. The plutonium ions adjacent to the plutonium interstitial move away from the interstitial in the relaxed structure, again likely due to electrostatic repulsion.

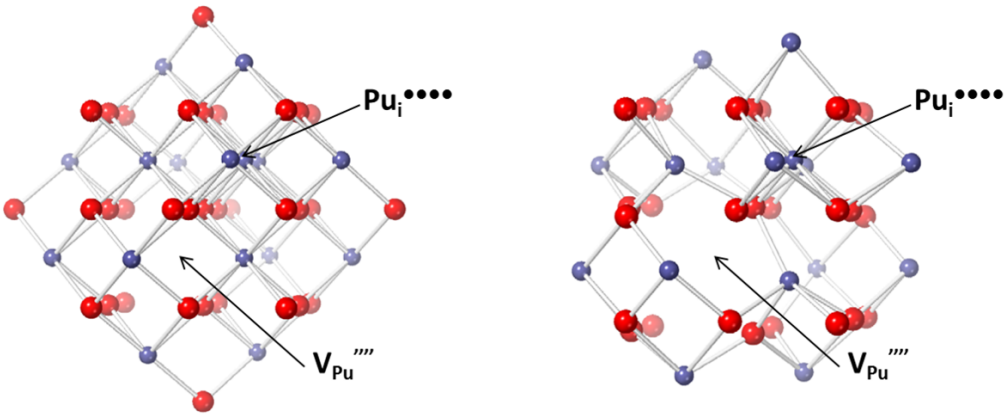


Figure 3.7: Plutonium Frenkel Pair visualisation. LHS: before relaxation, RHS: after relaxation.

3.5.0.3 Oxygen Frenkel Pair

Two configurations of OFPs were considered. Work by Read *et. al* [49] found that in OFP cluster simulations, when the oxygen vacancy is close to the oxygen interstitial, recombination occurs during the geometry optimisation procedure. To prevent this the oxygen interstitial was constrained by separation of the oxygen interstitial and vacancy by a lattice plutonium ion. Figure 3.8 displays an oxygen Frenkel pair separated by a lattice plutonium ion.

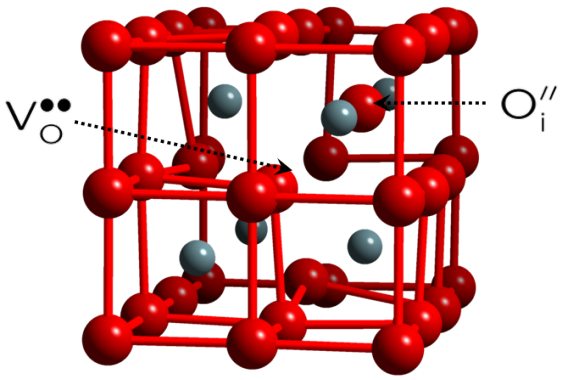


Figure 3.8: Visualisation of an oxygen Frenkel pair.

Two geometries for the oxygen Frenkel pair were considered (OFP1 and OFP2). Both OFP geometries were run to find which gave the lowest defect formation energy, and therefore which was the most energetically favourable and and such, likely to form. Table 3.16 displays their coordinates and the calculated defect formation energies for each geometry.

It can be seen from Table 3.16 that configuration OFP1 has the lower defect

Table 3.16: Calculated oxygen Frenkel pair defect formation energies for the two configurations considered

Defect	Coordinates $V_O^{\bullet\bullet}$	O_i''	Formation energy (eV/Defect)	Binding energy (eV/Defect)
OFP1	$(-\frac{1}{4}, -\frac{1}{4}, -\frac{1}{4})$	$(\frac{1}{2}, \frac{1}{2}, \frac{1}{2})$	2.069	-0.599
OFP2	$(-\frac{1}{4}, -\frac{1}{4}, \frac{1}{4})$	$(\frac{1}{2}, \frac{1}{2}, \frac{1}{2})$	2.116	-0.552

formation energy. Therefore this configuration is more likely to occur within the lattice as it is more thermodynamically favourable. So future cluster calculations of oxygen Frenkel pair defects will be the OFP1 configuration.

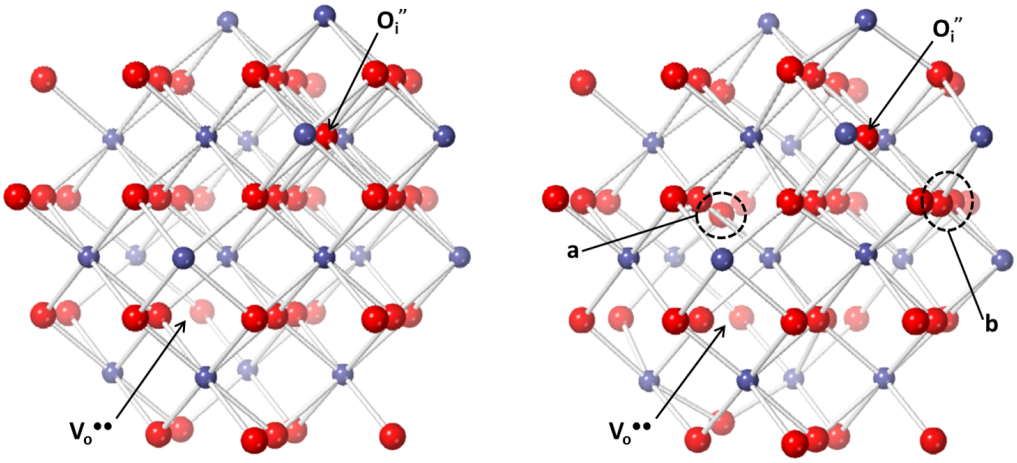


Figure 3.9: Oxygen Frenkel Pair defect with lattice distortion regions labelled. LHS: before relaxation, RHS: after relaxation. Circled regions ′a′ and ′b′ indicate regions of oxygen ion distortion.

Figure 3.9, displays the visualisation of an oxygen Frenkel pair defect in the lattice (OFP1 configuration). Comparison of the lattice before and after relaxation indicates regions of lattice distortion. Although the Frenkel pair overall is charge neutral, the vacancy and interstitial are independently charged. Label ′a′ indicates distortion induced by the electrostatic attraction from the vacant site. Label ′b′ indicates distortion induced by the electrostatic repulsion between the oxygen ions and the oxygen interstitial. However, comparison with the distortion induced by the constituent isolated point defects (displayed by Figures 3.4 and 3.6) indicates that the distortion induced by the Frenkel pair is lesser surrounding each constituent defect than when the defects are in isolation. This could be due to the charge neutrality of the defect.

3.5.0.4 Schottky Trio

As the Schottky trio consists of three defects, there are multiple possible geometries for the cluster defect. Three distinct configurations were considered. The plutonium vacancy and first oxygen vacancy were held at the same coordinates for each geometry, with the second oxygen vacancy (required to preserve charge neutrality) located at three different equivalent positions as displayed by Figure 3.10.

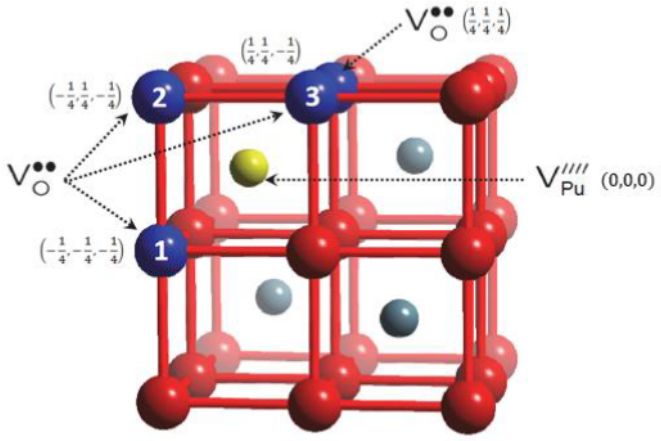


Figure 3.10: Visualisation of the Schottky trio configurations. From [55].

Table 3.17 displays the coordinates of the Schottky Trio geometries considered.

Table 3.17: Schottky Trio defect coordinates for cluster calculations

Defect	$V_{Pu}^{////}$	First $V_O^{\bullet\bullet}$	Second $V_O^{\bullet\bullet}$
Sch.1	(0,0,0)	$(\frac{1}{4},\frac{1}{4},\frac{1}{4})$	$(-\frac{1}{4}, -\frac{1}{4}, -\frac{1}{4})$
Sch.2	(0,0,0)	$(\frac{1}{4},\frac{1}{4},\frac{1}{4})$	$(-\frac{1}{4}, \frac{1}{4}, -\frac{1}{4})$
Sch.3	(0,0,0)	$(\frac{1}{4},\frac{1}{4},\frac{1}{4})$	$(-\frac{1}{4}, \frac{1}{4}, \frac{1}{4})$

All three geometries were run to establish which configuration gave the lowest defect energy and therefore is the most favourable and most likely configuration.

Table 3.18 displays the calculated Schottky trio defect formation energies for the three geometries considered. It can be seen that configuration $'$Sch.1$'$ has the lowest formation energy. Therefore this configuration is predicted to be the most thermodynamically favourable configuration. Future cluster calculations of Schottky trios will be of Sch.1 configuration.

Figure 3.11 displays the visualisation of the Schottky trio defect in PuO_2. Comparison of the initial and relaxed structures indicate the lattice distortion which takes

Table 3.18: Calculated Schottky trio defect formation energies

Type of defect	Second $V_O^{\bullet\bullet}$ position	Formation energy (eV/Defect)	Binding energy (eV/Defect)
Sch.1	$(-\frac{1}{4}, -\frac{1}{4}, -\frac{1}{4})$	1.929	-1.616
Sch.2	$(-\frac{1}{4}, \frac{1}{4}, -\frac{1}{4})$	1.931	-1.614
Sch.3	$(-\frac{1}{4}, \frac{1}{4}, \frac{1}{4})$	2.114	-1.432

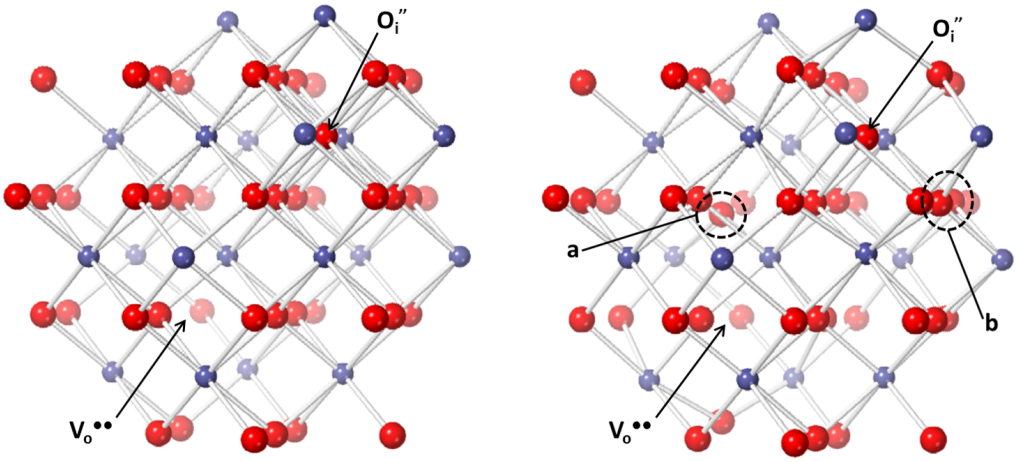


Figure 3.11: Schottky trio defect. LHS: before relaxation, RHS: after relaxation.

place to accommodate for the defect. It can be seen that the negatively charged oxygen ions surrounding the negatively charged vacant plutonium site have distorted to move away from the vacancy site. The oxygen ions surrounding the positive vacant oxygen site have clustered closer together due to electrostatic attraction.

3.6 Binding Energies

The difference in energy between the defects 'bound' in a cluster and those at infinite dilution (unbound) is equal to the binding energy, E^B. The binding energy may be calculated by finding the difference in energy between a cluster defect energy and the sum of the composite point defect energies at infinite dilution. The equations used to calculate the binding energies are as follows,

$$E^B_{\text{Schottky}} = \left[V''''_{\text{Pu}} : 2V^{\bullet\bullet}_{\text{O}}\right]^{\text{x}} - \left(V''''_{\text{Pu}} + 2V^{\bullet\bullet}_{\text{O}}\right), \tag{3.14}$$

$$E^B_{\text{OFP}} = \left[V^{\bullet\bullet}_{\text{O}} : O''_i\right]^{\text{x}} - \left(V^{\bullet\bullet}_{\text{O}} + O''_i\right), \tag{3.15}$$

$$E^B_{\text{PuFP}} = \left[V''''_{\text{Pu}} : Pu^{\bullet\bullet\bullet\bullet}_i\right]^{\text{x}} - \left(V''''_{\text{Pu}} + Pu^{\bullet\bullet\bullet\bullet}_i\right). \tag{3.16}$$

Equation 3.14 is used to calculate the binding energy of a Schottky trio, and Equations 3.15 and 3.16 are used to calculate the binding energy of an oxygen or plutonium Frenkel pair, respectively.

Table 3.19 displays the results of the bound and unbound defect formation energies, alongside the calculated binding energy for each defect. All of the calculated binding energies are negative, indicating that they correspond to bound defects.

Table 3.19: Intrinsic defect formation energies

Type of defect	Defect formation energy		E^B
	Unbound (eV/Defect)	Bound (eV/Defect)	(eV/Defect)
Schottky trio	3.545	1.929	-1.616
PuFP	10.029	7.868	-2.161
OFP	2.668	2.069	-0.599

3.6.1 *Discussion*

From the cluster calculations simulating bound defects it was found that the plutonium Frenkel pair has the highest defect formation energy. Therefore PuFPs are the least thermodynamically favourable defects and so are the least likely to form in PuO_2. This may be due to the high charge on this defect and hence the relaxed lattice displays distortion over an extended area (as displayed by Figure 3.12). Work by Lu *et al.* [119] found the displacement of atoms for plutonium related defects to be larger than those of oxygen related defects, suggesting that lattice distortion is larger for plutonium related defects, leading to higher defect formation energies. Similarly in Yttria-Stabilized Zirconia (YSZ), the cation Frenkel pair has been found to have the highest defect formation energy [129], leading to the Schottky defects being the energetically stable source of cation defects.

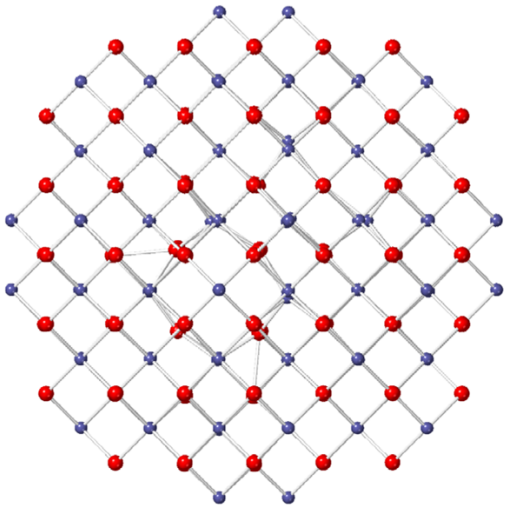


Figure 3.12: Plutonium Frenkel pair visualisation after relaxation.

It is of interest that in the unbound defect calculations at infinite dilution, the oxygen Frenkel pair had the lowest defect formation energy. Whilst the cluster calculations of bound defects determined the Schottky trio to have the lowest defect formation energy, as displayed by Figure 3.13. However, the difference in formation energy between these two defects is negligible (< 0.1 eV/Defect). Therefore, it is predicted that both the Schottky trio and oxygen Frenkel pair are likely to occur within the PuO_2 lattice.

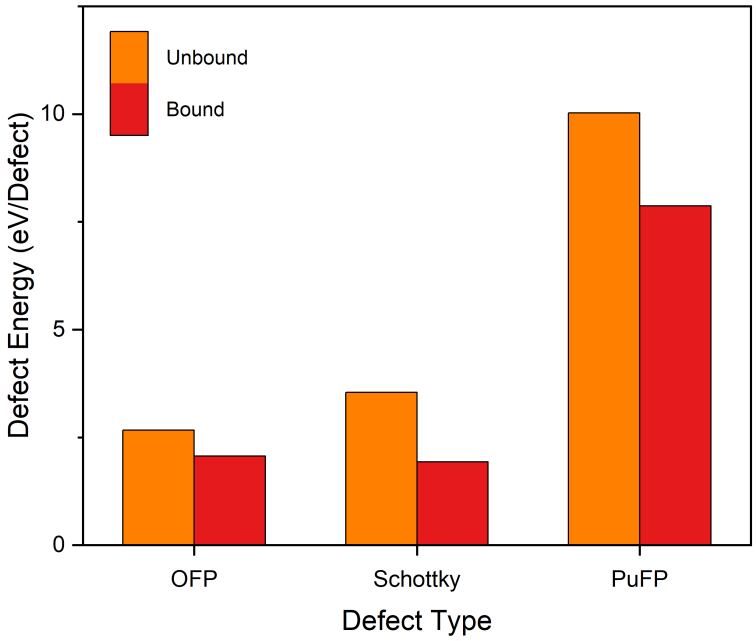


Figure 3.13: Defect energies of unbound and bound intrinsic defects in PuO_2.

Figure 3.14 displays reported defect formation energy values found from literature. These studies were conducted by *ab initio* ([119], [120], [130]–[132]) and potential ([49], [121], [122], [133]) methods. The same trend as found by this work was found in all studies; PuFPs have the highest formation energy per defect. Many of the authors suggested that this was due to the increased volume of distortion created by a PuFP, as was also found was this work. In YSZ, which also has a fluorite structure, the cation Frenkel pair has also been found to have the highest defect formation energy [129]. All authors except Read *et al.* [49] and Wang *et al.* [121] found the order of defect stability in PuO_2 to be OFP < Schottky < PuFP. Instead, Read *et al.* [49] and Wang *et al.* [121] found OFP and Schottky defects to have very similar defect energies, which was also found by Dong *et al.* [129] for YSZ. The defect formation sequence found in this work, is the same as that of the reported literature for PuO_2. It is predicted that oxygen atoms are more likely to be involved in defect formation than plutonium atoms.

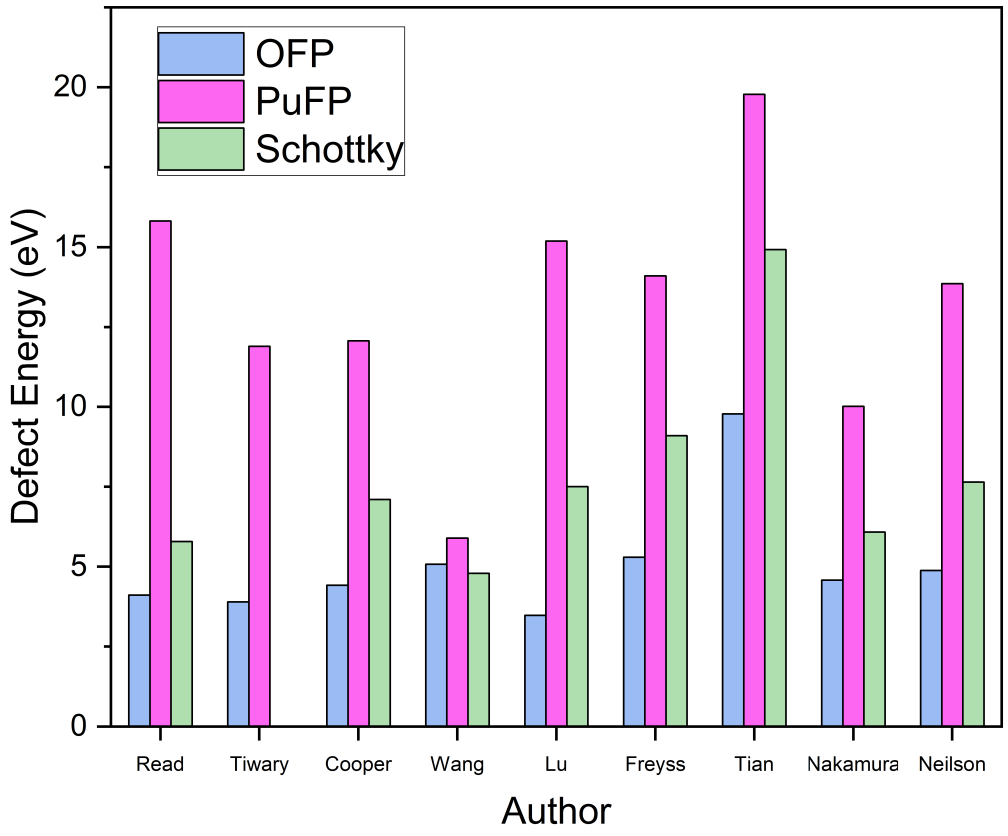


Figure 3.14: Defect energies of OFP, PuFP and Schottky trios PuO_2 from avaliable literature studies. Authors are Read [49], Tiwary [133], Cooper [122], Wang [121], Lu [119], Freyss [130], Tian [131], Nakamura [120] and Neilson [132].

3.7 Conclusions

It was identified that for static simulations of PuO_2, the Read potential is the most suitable due to it having the lowest potential difference between computed values and experimental values from the literature. The optimum Mott-Littleton Region I and IIa radii were determined to be 14 and 28 Å, respectively. From implementation of the Read potential for defect simulations using the Mott-Littleton methodology, the most thermodynamically favourable intrinsic defects were found to be the Schottky trio and oxygen Frenkel pair. It is therefore predicted that these are the most likely to form within PuO_2 which is in agreement with the available literature. The plutonium Frenkel pair was found to be the least thermodynamically favourable intrinsic defect, and is therefore predicted to be the least likely to form within

PuO_2. This finding is in agreement with other fluorite systems in which the cation Frenkel pair has the highest defect energy, such as in UO_2 [55] and YSZ [129].

Chapter 4

Surfaces of Plutonium Dioxide

In the following chapter the surface energies of PuO_2 are calculated to predict the equilibrium growth morphology. Then intrinsic defects are included at surface sites to establish if there is an energetic drive for defects to form at the surface rather than in the bulk.

4.1 Literature Review

Due to the fact that PuO_2 is frequently stored as a powder and so has high surface areas [3] understanding its surface structure is crucial. Despite this, experimental studies investigating the surface structure of PuO_2 are scarce. Computational methods can be used to calculate the relative surface energies. At equilibrium, a lower surface energy implies a greater expression of that surface [134]. Therefore, through identifying low energy surfaces, the morphology of PuO_2 powder can be predicted [98].

Throughout the literature there is agreement that the (111) surface is the most stable for many actinide dioxides [96]. In 1979 Tasker [135] developed a computational study of UO_2 surfaces, their study identified that the (111) surface was the most stable. Since then, this trend has been found throughout other fluorite lattices [136] with PuO_2 being no exception. Jomard *et al.* [51] used *ab initio* calculations to address the influence of electronic correlations on the surface stability of PuO_2. Via Perdew-Burke-Ernzerhof with the Hubbard U correction (PBE+U) methods they found the equilibrium PuO_2 crystal exhibits (111) facets only [51]. Via Generalised Gradient Approximation with the Hubbard U correction (GGA+U) methods, Sun *et al.* [137] studied PuO_2 surfaces at 300 K and 600 K and in agreement with the 0 K calculations of Jomard *et al.* [51], they found that the (111) surface was dominant.

A nanoparticle with all (111) crystallographic planes forms an octahedral shape. Via DFT simulations, Moxon *et al.* [138] found that octahedral PuO_2 nanoparticle vertices may be truncated by (100) planes. Their work found that this truncation was prominent at low temperatures (< 600 K). At higher temperatures (> 600 K) they found only (111) planes were present, corresponding to an octahedral with sharp vertices [138]. The distinction between the truncated and sharp edged octahedra was also studied by Nekrasov *et al.* [139]. Their work used molecular dynamics to investigate the equilibrium shapes of PuO_2 nanoparticles. They found that octahedral morphologies with sharp vertices correspond to metastable states of the crystal lattice [139]. In contrast to the findings of Moxon *et al.* [138], Nekrasov *et al.* [139] found the truncated octahedral morphology to be the most common nanoparticle formed at 1700 K. The difference in findings may be due to the work of Nekrasov *et al.* [139] being under constant pressure (an NPT simulation) conditions whereas Moxon *et al.* [138] considered varying pressures.

Whilst there have been a number of studies of defective UO_2 surface systems as discussed by Wellington *et al*. [140], studies of defective PuO_2 surface systems are scarce. Similarly to in the bulk of PuO_2, defects resulting from radiation damage are likely to govern key behaviours at the surface of the material. For example, the susceptibility of PuO_2 to corrosion and fission product diffusion [53]. As such, the incorporation of defects at PuO_2 surfaces is a topic of high scientific importance.

The surface of PuO_2 will play a significant role in all suggested storage canister pressurisation mechanisms detailed in Section 1.2.3. Mechanisms such as the radiolysis of water and generation of H_2 by a postulated chemical reaction of PuO_2 with H_2O are predicted to be surface phenomena [46]. Wellington *et al.* [140] used DFT methods to investigate oxygen vacancy formation and water adsorption on UO_2 and PuO_2 surfaces. They found oxygen vacancy formation energies on UO_2 surfaces to be significantly larger than for PuO_2. Tan *et al.* [141] studied defect configurations on the (100) surface of UO_2 via potential methods and found that oxygen vacancies stabilise the (100) surface. Oxygen vacancy formation on surfaces is an important factor as when oxygen vacancies are present, dissociative adsorption of water can occur.

The surface state of PuO_2 has been predicted by Pegg *et al.* [142] to be a crucial parameter in governing hydrogen accumulation. Radiolysis methods have been used by Venault *et al.* [143] to study PuO_2 surfaces with a focus on the behaviour of hydrogen. They found a steady state of hydrogen content was reached when the relative humidity was kept constant, suggesting the existence of both hydrogen

generation and consumption at the surface of PuO_2. This finding highlights the importance of PuO_2 surfaces in hydrogen behaviour.

A study by Stanek *et al.* [144] found that the release of fission products can be inhibited or enhanced by the specific arrangements of PuO_2 surface ions. Similarly in UO_2, Williams *et al.* [145] found that grain boundary structures affect the diffusion of oxygen, with it being enhanced by all grain boundary structures. From this, it is concluded that an understanding of the defect behaviour at PuO_2 surfaces is required to aid in the investigation of helium behaviour in PuO_2.

Venault *et al.* [143] emphasised the importance of studying PuO_2 surface chemistry via non-intrusive techniques to study mechanisms occurring at the surface. Due to the difficulty of experimentally studying PuO_2, computational modelling can provide a solution to the investigation of surface chemistry as shown by the work of Pegg *et al.* [142].

4.2 Pure Surfaces

PuO_2 surfaces were simulated using METADISE with the interatomic potential model the same as that detailed in Chapter 3. The $\{n10\}$, $\{n11\}$ and $\{nn1\}$ surfaces were simulated for n = 1,2,3. Figure 4.1 displays the surface energies (E_{surf}) for each simulation, both before and after relaxation (E_{surf}^{unrel} and E_{surf}^{rel} respectively). For each index the surface energy follows the $\{nn1\} < \{n11\} < \{n10\}$ trend. The (111) surface was found to have the lowest surface energy (1.32 Jm^{-2}) and therefore is predicted to be the the most energetically stable. Additionally, the energetic stability generally decreases with increasing n.

Table 4.1 displays the calculated energies and d spacings of the low index surfaces, in addition to calculated and experimental values from the literature [51], [124], [141]. Notably, the surface energies calculated using ionic potentials by Tan *et al.* [141] are extremely close to values predicted by this work. The small differences could be attributed to the use of a different Pu—O potential by Tan *et al.* [141]. However, the values calculated by Jomard *et al.* [51] via PBE+U methods are almost half that calculated by this work and Tan *et al.* [141]. This could be because DFT methods model the electronic structure of the ions in greater detail. Watson [146] also found surface energies of CeO_2 obtained by VASP calculations to be roughly half that of those calculated by ionic potentials [147].

The (111) surface was predicted to have the highest attachment energy (E_{att}). Again, this suggests that the (111) surface is likely to dominate the growth mor-

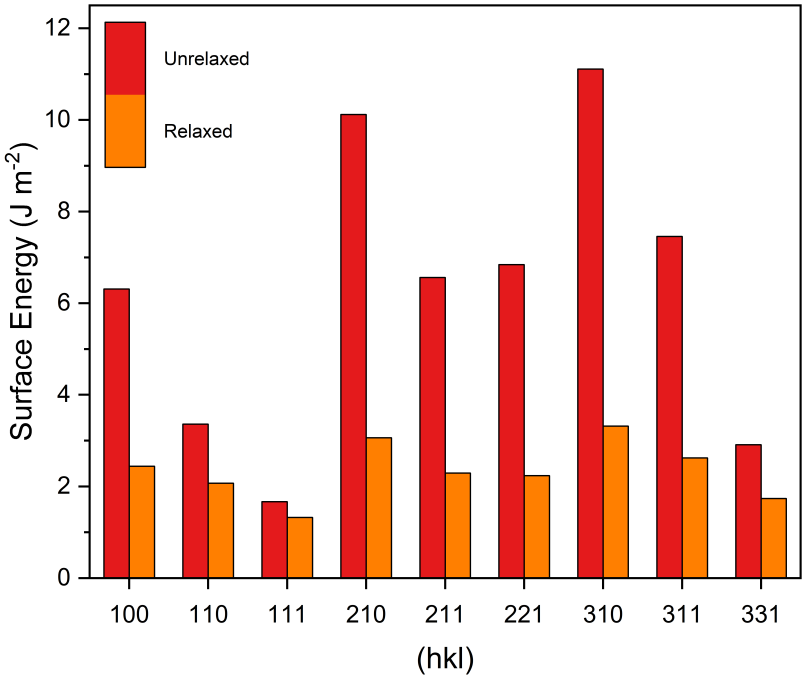


Figure 4.1: Bar Chart displaying the surface energies for the $\{n10\}$, $\{n11\}$ and $\{nn1\}$ surfaces (n=1,2,3), both before and after relaxation.

phology, as the relative growth rate of a face increases with increasing E_{att} [148].

As can be seen by Table 4.1, the calculated d spacings provide excellent agreement with reported crystallographic values [124]. The accuracy of the d spacings gives confirmation that the potentials evaluated for GULP are transferable to METADISE for surface simulations. Additionally, it gives confidence in the use of the potentials in METADISE to be a predictive tool, when modelling defective surfaces.

The (111) surface was also found to be the most stable for other binary fluorite structures such as UO_2 [96], [134], [135] and CeO_2 [136], [146], [147]. From their study of UO_2 surfaces, Williams *et al.* [145] notes that there appears to be a correlation between the surface energy and the coordination of uranium surface atoms, with the most stable surfaces having the highest surface uranium coordination. The results presented in this work are in agreement, as the (111) surface has the highest surface plutonium coordination.

Table 4.1: Calculated and reported energies of low index PuO_2 surfaces

Property	(hkl) (100)	(110)	(111)
E_{surf}^{unrel} (eV)	6.28	3.27	1.63
E_{surf}^{rel} (eV)			
This work	2.44	2.07	1.32
PBE+U [a]	1.69	1.13	0.72
Ionic [b]	2.92	2.20	1.39
E_{att} (eV/PuO_2)	-2.86	-2.10	-1.28
d spacing (Å)			
This work	5.3981	3.8170	3.1166
XRD [c]	5.3982	3.8171	3.1166
Area (Å^2)	29.14	41.21	50.47

[a] Ref. [51]
[b] Ref. [141]
[c] Ref. [124]

4.2.1 *The (100) Surface*

Figure 4.2 displays the structure of the (100) PuO_2 surface. The surface energy calculated for the (100) surface was 2.44 Jm^{-2}. This was the highest surface energy calculated, thus this surface is predicted to be the least energetically stable. By examining the structure of the surface, it is evident that it is a Tasker type III surface as it consists of alternating charged layers of ions with a polar oxygen termination [135]. The dipole of this surface was quenched by removal of 50% of the surface oxygen ions to Region 2. The percentage relaxation of the surface is -61.13%.

Comparing the structure of the (100) surface before and after relaxation (Figure 4.2 RHS and LHS respectively), the distortion of the relaxed surface is visible. Rumpling can be seen on the second layer of the oxygen ions. This distortion is less visible at deeper layers and appears bulk-like. Upon relaxation the Pu-O bond lengths for the top layer reduce from 2.337 Å to 2.101 Å. The bond length does not remain constant upon relaxation until lattice depths of $\sim$ 16 Å from the surface. Similarly from the literature, Low Energy Electron Diffraction (LEED) studies of the UO_2 (100) surface by Taylor *et al.* [149] found faceting to occur. Diffraction patterns of UO_2 indicated structural changes, suggesting that the (100) surface

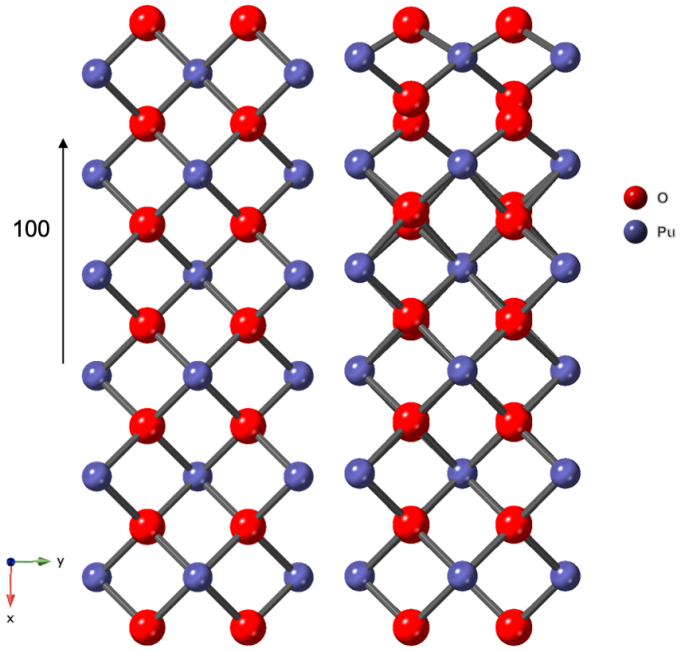


Figure 4.2: The (100) surface, LHS before relaxation, RHS after relaxation.

may be stabilised by defects such as steps and ledges, in order to form regions of oppositely charged surfaces [149]. It is suggested that such defect structures may be present in PuO_2 (100) surfaces to stabilise it.

It would be of interest to simulate highly defective (100) surfaces to see if the defects stabilise the surface to the extent that they appear in the morphology. Work by Tan *et al.* [134] focused on the simulating defect configurations on the UO_2 (100) dipolar surface. Despite generating extensive models including the surface trench configuration proposed from LEED studies of UO_2 by Muggelberg *et al.* [150], the (100) surface energy calculated by Tan *et al.* [134] was never stabilised enough to appear in the morphology.

4.2.2 *The (110) Surface*

Figure 4.3 displays the (110) PuO_2 surface. The surface energy calculated for this surface was 2.07 Jm^{-2}. It is a Tasker type I surface [135]. A percentage surface relaxation of -36.65% was predicted. From Figure 4.3 no obvious distortion to the crystal in the relaxed structure can be seen. However, inspection of the bond lengths and ionic distances in CrystalMaker® found that the top layer Pu-O bond lengths reduce from 2.337 Å to 2.274 Å. It was also found that there is a slight contraction of the d spacing for the top layer (3.757 Å rather than 3.817 Å). Similar contractions were found by Sun *et al.* [137]. These contractions are much less pronounced than

that of the (100) surface. The bond lengths return to bulk values at depths of $\sim$ 8 Å from the surface; half the depth that the distortions reached in the (100) surface. This corresponds with the percentage surface relaxation difference of the (110) surface being roughly half that of the (100) surface.

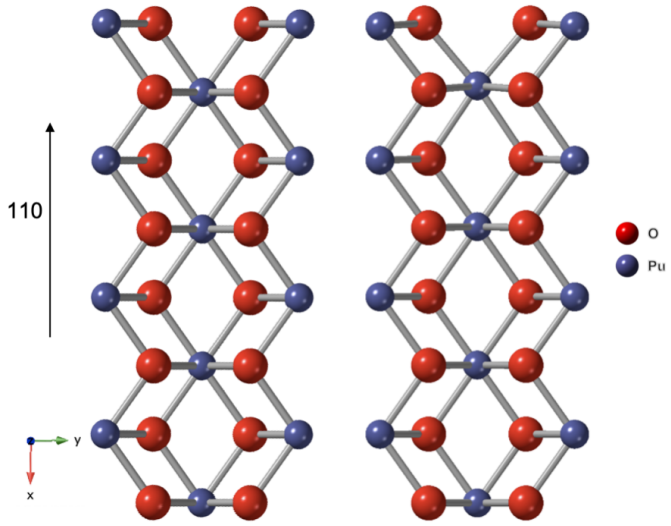


Figure 4.3: The (110) surface, LHS before relaxation, RHS after relaxation.

4.2.3 *The (111) Surface*

Figure 4.4 displays the structure of the (111) PuO_2 surface. The surface energy calculated for this surface was 1.32 Jm^{-2}. As this was the lowest surface energy calculated, it is predicted that this surface is the most energetically stable and therefore will be most likely to grow. The surface is a Tasker type II surface, as it is cleaved so as to not create a dipole moment [96] [135]. The predicted percentage relaxation was -18.67%, the lowest of the n=1 surfaces. This is reflected in the limited contraction of the Pu-O bond lengths; 2.308 Å on the top layer of the relaxed structure. The bond lengths return to bulk values at depths of $\sim$ 5 Å from the surface, so the distortion is minimal.

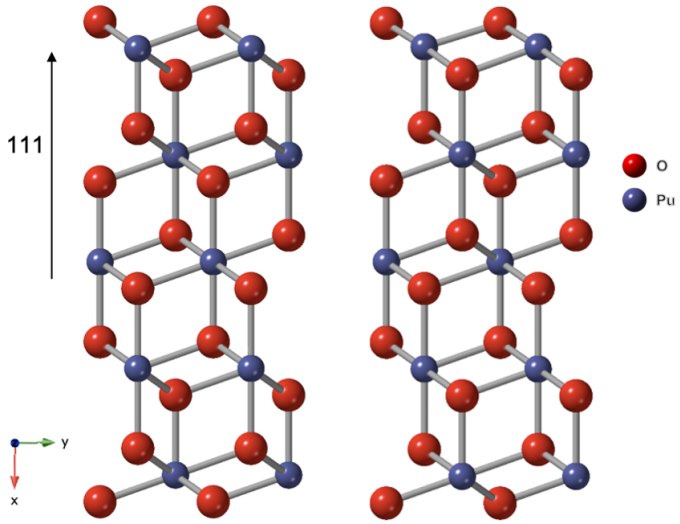


Figure 4.4: The (111) surface, LHS before relaxation, RHS after relaxation.

4.2.4 *Morphology*

The calculated relaxed surface energies and attachment energies were used to predict the equilibrium growth morphology by generating a Wulff construction [98]. As can be seen by Figure 4.5, the Wulff construction for PuO_2 was found to be octahedral. This is because the (111) surface was predicted have the lowest surface energy, thus dominating the morphology and resulting in an octahedral shaped crystallite. An octahedral Wulff construction was also found by Jomard *et al.* [51] for PuO_2, and in multiple studies of UO_2 [96], [134].

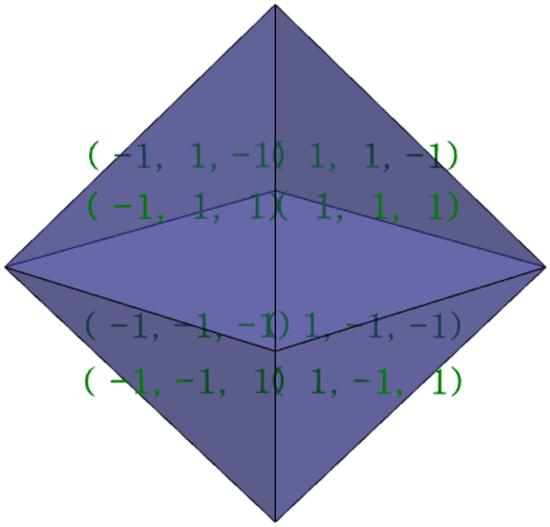


Figure 4.5: Wulff construction for PuO_2.

4.3 Defective Surfaces

4.3.1 *Isolated Surface Defects*

Isolated defects were modelled on the surface of PuO_2. The interstitials were placed in octahedral interstitial sites (the same interstitial sites as in bulk PuO_2). The defect energies were then compared with the respective bulk defect energies. To normalise the defect energies ($E_{D,Surf}$), an energy correction term (E_{Corr}) was added to the defect energies ($E^{F,Corr}_{D,Surf}$). Segregation energies (E^{Seg}_{D}) were calculated to determine if there was an energetic preference for a defect to form at the surface or in the bulk. An endothermic segregation energy indicates an energetic preference for the defect to form in the bulk rather than at the surface. Table 4.2 displays the results of the isolated defect simulations, including the bulk values ($E^{F}_{D,Bulk}$) calculated in Chapter 3 for comparison. The correction terms and calculated segregation energies are also displayed.

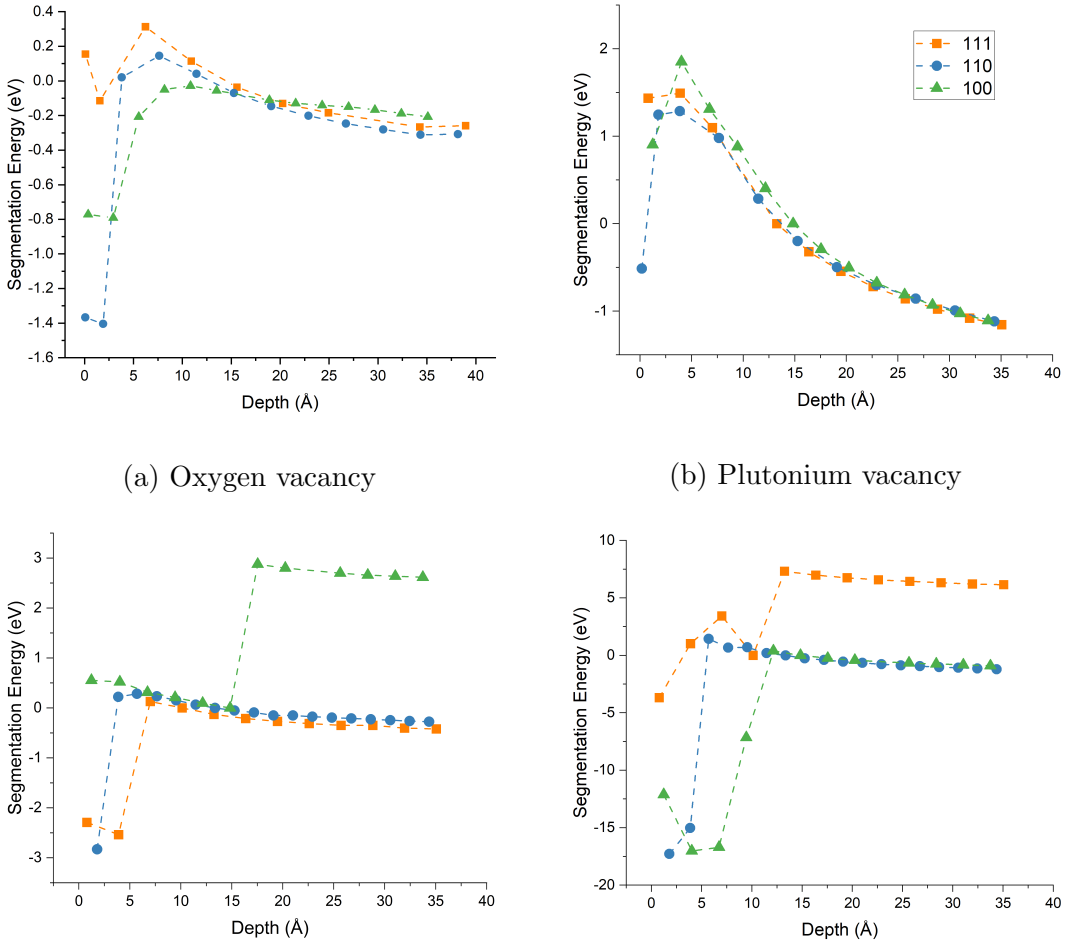
Table 4.2: Isolated defect energies on PuO_2 surfaces

(hkl)	Defect	Defect Energy (eV)					
		$E^{F,Reg1}_{D,Surf}$	$E^{F,Reg2}_{D,Surf}$	$E^{F}_{D,Bulk}$	E_{Corr}	$E^{F,Corr}_{D,Surf}$	E^{Seg}_{D}
(100)	$V^{\bullet\bullet}_{O}$	38.28	39.05	17.09	21.96	16.32	-0.77
	$V^{''''}_{Pu}$	39.28	38.38	80.03	-41.65	80.93	0.90
	O''_{i}	-33.99	-32.93	-11.75	-21.17	-12.82	-1.07
	$Pu^{\bullet\bullet\bullet\bullet}_{i}$	-17.22	-7.61	-59.97	52.37	-69.59	-9.62
(110)	$V^{\bullet\bullet}_{O}$	17.94	19.30	17.09	2.21	15.72	-1.37
	$V^{''''}_{Pu}$	77.32	77.83	80.03	-2.20	79.52	-0.51
	O''_{i}	-13.09	-10.27	-11.75	1.49	-14.58	-2.83
	$Pu^{\bullet\bullet\bullet\bullet}_{i}$	-43.94	-47.13	-59.97	12.84	-56.78	3.19
(111)	$V^{\bullet\bullet}_{O}$	26.52	26.36	17.09	9.27	17.25	0.15
	$V^{''''}_{Pu}$	65.16	63.73	80.03	-16.30	81.47	1.44
	O''_{i}	-19.13	-17.20	-11.75	-5.45	-13.69	-1.93
	$Pu^{\bullet\bullet\bullet\bullet}_{i}$	-42.36	-40.26	-59.97	19.72	-62.08	-2.11

In agreement with the literature [137], [147], [151], a lower oxygen vacancy formation energy was found on the (110) surface (15.72 eV) than the (111) surface (17.25 eV). Wellington *et al.* [140] suggests that this order of energetic stabilities may be due to the lower coordination number of plutonium on the (110) surface, in addition to the higher surface energy of the (110) surface.

It is evident from Table 4.2 that there are no clear trends between the segregation energies of defects on the different surfaces. The only consistency is that there is an energetic preference for plutonium interstitials to form on the surface rather than in the bulk. For the (111) surface, the majority of defects have a thermodynamic drive to form in the bulk, and this is likely due to the energetic stability of the pure (111) surface.

To investigate the effect of the depth of a defect on the segregation energy, extensive simulations were performed for each point defect at each layer of the crystal for each surface. The results are displayed in Figure 4.6.



(a) Oxygen vacancy

(b) Plutonium vacancy

(c) Oxygen interstitial

(d) Plutonium interstitial

Figure 4.6: Defect segregation energies at varying depths for different defects on each low index surface: (a) oxygen vacancy (b) plutonium vacancy (c) oxygen interstitial (d) plutonium interstitial.

For oxygen vacancies on each surface, there is an exothermic segregation energy

for formation at $\sim$ 3 Å, i.e. just below the top surface layer. This segregation energy is the least pronounced for the (111) surface. However, in UO_2, Bo *et. al* [151] calculated oxygen vacancy formation energies of 5.95 and 6.08 eV for the first and second layers respectively on the (111) surface and 5.38 and 5.59 eV on the (110) surface. Thus, it is predicted that the second layer may be less thermodynamically favourable for oxygen vacancy formation.

4.3.2 *Intrinsic Defects*

As in the bulk, point defects are unlikely to form on the surface due to the requirement of the lattice to be charge neutral. Therefore, intrinsic defects were modelled. Multiple configurations of intrinsic defects were simulated for each surface, so a labelling system was required. Figures 4.7, 4.8 and 4.9 display the initial layers of the (100), (110) and (111) surfaces, respectively, with atoms numerically labelled and interstitial sites alphabetically labelled. The defects simulated are given names corresponding to these diagrams. For example, a plutonium Frenkel pair where the vacancy is the plutonium ion 'PU1' and the interstitial is located at site 'A' is referred to as a 'PU1_A' configuration.

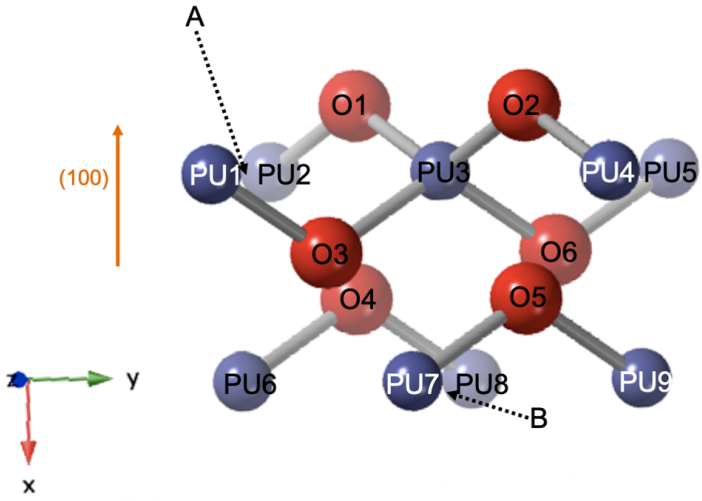


Figure 4.7: The (100) surface with ions labelled numerically and interstitial sites labelled alphabetically.

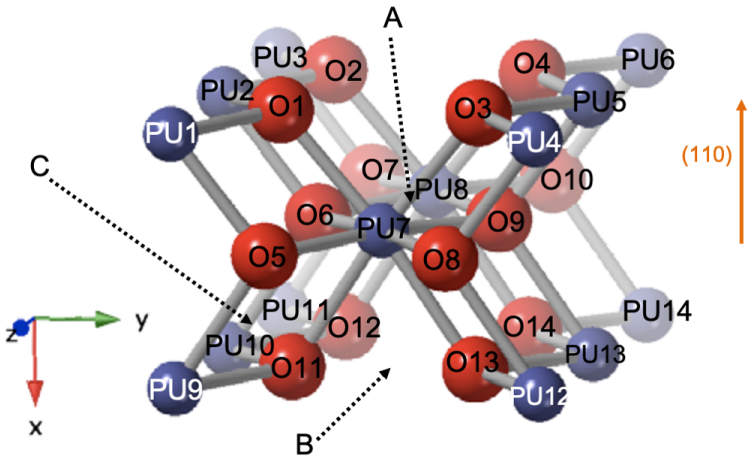


Figure 4.8: The (110) surface with ions labelled numerically and interstitial sites labelled alphabetically.

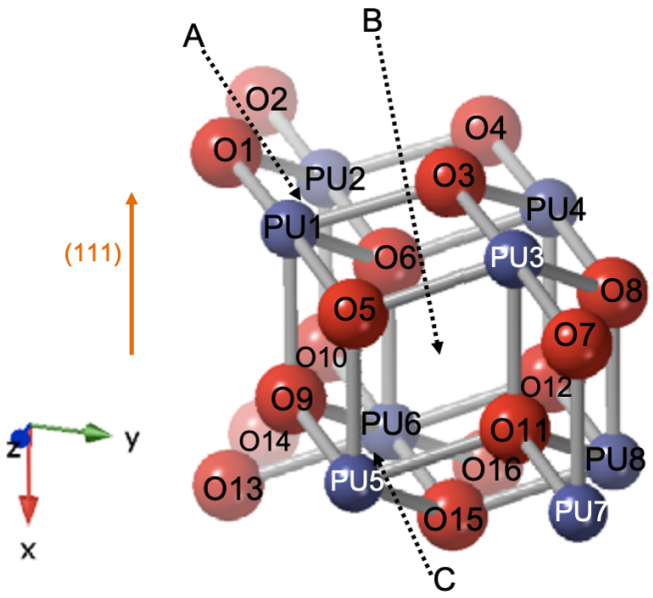


Figure 4.9: The (111) surface with ions labelled numerically and interstitial sites labelled alphabetically.

Table 4.3 displays the results from the intrinsic defect simulations on the (100), (110) and (111) surfaces. For many of the Frenkel pair simulations, a defect energy of 0 eV/Defect was calculated (e.g. the (110) O3_B OFP). This may be because the vacancy and interstitial recombined and annihilated, so in the relaxed state no defect was present. In the defect simulations in bulk PuO_2 OFP recombination was also observed, and was avoided by ensuring the oxygen ions were separated by a lattice plutonium ion as discussed in Section 3.5.0.3. On the (111) surface, the 'O8_A' OFP

configuration was determined to have a defect energy of 2.54 eV/Defect, meaning the independent defects were sufficiently separated to prevent recombination. The oxygen vacancy ′O8′ was located on the third layer of ions.

Table 4.3: Intrinsic Defects on the (100), (110) and (111) Surfaces. Energies in eV/Defect

(hkl)	Oxygen Frenkel Pair			Plutonium Frenkel Pair			Schottky Trio		
	Config.	E_D^F	E_D^{Seg}	Config.	E_D^F	E_D^{Seg}	Config.	E_D^F	E_D^{Seg}
(100)	O2_B	0.00		PU5_A	13.54	5.67	O2_O1_PU5	0.52	-1.41
	O2_A	0.05		PU5_B	4.19	-3.67	O2_O1_PU3	-0.20	-2.13
	O5_A	-0.01		PU3_A	0.05		O3_O1_PU3	0.78	-1.15
	O10_A	1.71	-0.36				O3_O4_PU4	-0.02	-1.94
	O6_B	0.00							
	O7_A	0.08							
(110)	O3_B	0.00		PU6_A	0.00		O3_O2_PU6	0.73	-1.20
	O2_B	0.00		PU5_C	0.00		O3_O4_PU6	0.74	-1.19
	O3_A	DNC*		PU5_A	1.61	-6.26	O3_O1_PU7	0.69	-1.24
	O3_C	0.00		PU7_C	0.00		O3_O11_PU7	1.06	-0.87
	O10_A	0.00							
(111)	O3_B	0.00		PU4_B	0.00		O3_O2_PU2	1.59	-0.34
	O8_A	2.54	0.47	PU4_C	7.68	-0.19	O3_O1_PU2	1.99	0.06
	O3_C	2.14	0.07	PU4_A	2.24	-5.63	O3_O2_PU3	1.59	-0.34
	O2_A	2.59	0.52				O6_O2_PU2	2.08	0.15
	O1_C	1.87	-0.20						

* Did Not Converge (DNC)

For the (100) surface, the Schottky trio had the lowest defect formation energy and the PuFP the highest. This follows the order of the thermodynamic stability of defects in the bulk. For the (110) surface, the Schottky trio had a lower defect formation energy than the PuFP. However all OFP configurations considered either recombined or did not converge so a complete order of intrinsic defect stability could not be determined. It would be of interest for future work to grow the surface in the y and z directions, so that Frenkel pairs could be situated across a larger surface area to prevent recombination.

For each surface the Schottky trio configurations had low defect formation energies. Work by Sun *et al.* [137] found PuO_2 surfaces to be stabilised when multiple oxygen vacancies were on the surface. It may be of interest to see if further surface stabilisation would be gained by multiple Schottky trio defects being present

on surfaces, and if these will be possible helium trapping sites. Furthermore, the segregation energies of Schottky trios are much more exothermic on the (100) and (110) surfaces than the (111) surface. This suggests that the Schottky trios may stabilise the less energetically stable surfaces, so there is thermodynamic drive for the defects to form at the surface rather than in the bulk.

For the (111) surface, as in the bulk, the OFP and Schottky trio are the most energetically stable defects. It is notable that the PuFP has a highly exothermic segregation energy (-5.63 eV/Defect) and therefore may form at the surface. It is predicted that all three of these defects are likely to occur on the (111) PuO_2 surface. If any of these defect sites are favourable for helium accommodation, then helium may migrate to the surface to become trapped within such defect sites.

4.4 Conclusions

The (111) surface was found to be the most energetically stable surface for pure PuO_2. Thus, octahedral shaped PuO_2 crystallites are predicted. The (100) surface was predicted to be the least energetically stable, in agreement with the literature.

In bulk PuO_2, OFPs and Schottky trios were found to have the lowest defect formation energies and therefore be the most thermodynamically favourable defects. The same thermodynamic energy preference of defects was found for surface PuO_2. However, for the (111) surface the PuFP defect formation energy was much lower than in the bulk, resulting in a strongly exothermic segregation energy. This indicates that there is a thermodynamic drive for PuFPs to form at the surface rather than in the bulk of (111) terminated PuO_2.

Chapter 5

Static Helium Incorporation

In this chapter static simulation methods are used to model helium incorporation in PuO_2. First the Dremov [44] potential is fitted to a standard form and evaluated against other available interatomic potentials for helium in PuO_2. Then helium clustering is investigated. Parts of this work are as published in:

E. Murray , N. Palmer , W. Neilson , R. Jackson , M. Read , H. Steele and R. Orr. *Atomistic Simulation of Helium Incorporation in PuO_2. Proceedings of the WM Symposia*, 2022, **22512** [152].

5.1 Literature Review

There are limited studies of helium behaviour in PuO_2, however investigating its behaviour is vital to understanding the future of stored PuO_2 due to the generation of radiogenic helium within the sealed canisters. A key starting point in understanding helium behaviour in PuO_2 is establishing the most favourable site for He to occupy. A recent DFT study by Neilson *et al.* [132] investigated the accommodation of helium in PuO_2, finding the most stable helium location to be interstitial sites. They found that whilst plutonium vacancies pose a favourable site for helium, when solution energies are calculated (which also account for the stability of the trap site), He accommodation in Pu vacancies is less energetically favourable than interstitial sites. Freyss *et al.* [130], [153] also found the interstitial site to be the most energetically stable site for helium to occupy in PuO_2.

Tian *et al.* [131] used GGA methods to study the behaviour of helium in PuO_2 over a range of stoichiometries. They found positive incorporation energies for all considered trap sites, meaning energy has to be provided to incorporate He. The

most favourable site for helium to occupy was found to be oxygen vacancies, interstitial sites and Pu vacancies for hypo-, perfect and hyper-stoichiometry, respectively. This is in contrast with the findings of Neilson *et al.* [132], which found interstitial He to be favourable across a range of stoichiometries. The calculations performed by Tian *et al.* [131] relied on a point defect model constructed for UO_2. However, UO_2 exhibits higher oxidation states which allow for large hyper-stoichiometry generated by clusters of oxygen interstitials. As Neilson *et al.* [132] generated a point defect model specifically for PuO_2 their results are likely to be more reliable.

Gryaznov *et al.* [154] used DFT to study He in UO_2, PuO_2, and MOX fuel. Their work studied interstitial helium incorporation, and found that helium accommodation in PuO_2 has a higher energy than in UO_2. Kuganathan *et al.* [155] used DFT with dispersion corrections to study helium trapping and clustering in ThO_2. In agreement with the aforementioned studies on PuO_2, they found the Octahedral Interstitial Site (OIS) to be the most favourable interstitial site for helium accommodation. When defects were considered in the ThO_2 lattice, Kuganathan *et al.* [155] found the actinide vacancy to be the most favourable. The actinide vacancy was also found to be the most stable site for He incorporation in UO_2 by Yun *et al.* [156]. However, as noted by Neilson *et al.* [132], both Kuganathan *et al.* [155] and Yun *et al.* [156] did not calculate the solution energies which would account for the probability of the actinide vacancy trap sites being available to He. Via calculation of solution energies, Crocombette [157] found the He solution site to be the interstitial position in UO_2.

Palmer [93] used atomistic static simulations to investigate helium behaviour in PuO_2. In contrast to the *ab initio* work of Neilson *et al.* [132], their work found the most favourable defect for He to occupy to be an oxygen vacancy. However, Palmer [93] performed their simulations using the U—He potential of Grimes *et al.* [158], due to a Pu—He being unavailable in the literature. Whilst UO_2 and PuO_2 are both fluorite lattices and are frequently compared, the use of a U—He potential may have resulted in the disagreement of Palmer's [93] work with newer *ab initio* results.

Helium incorporation in metallic Pu has been studied by Dremov *et al.* [44] and Ao *et al.* [159]. Via DFT Dremov *et al.* [44] calculated unit-cell energies of α-Pu and δ-Pu lattices containing point defects and a contaminant He atom. The resulting cell energies were employed to develop a new Pu—He interatomic potential. Subsequent molecular dynamics simulations implemented this potential to investigate the dynamics of individual He atoms in the δ-Pu lattice. The dynamics

of an isolated He bubble in a δ-Pu lattice and the evolution of bubble shape over time were also simulated. In agreement with work by Dremov *et al.* [44], Ao *et al.* [159] found the formation of helium bubbles to be favourable. Ao *et al.* [159] predicts the bubble growth mechanism to be dislocation loop punching, which is a common phenomenon in metals.

5.2 Dremov Potential

Dremov *et al.* [44] developed interatomic potentials from experimental data and DFT calculations for modelling helium incorporation in Pu metal which describe the Pu—He and He—He interactions. For modelling helium incorporation in PuO_2, a He—O potential is also required and shall be discussed in Section 5.3. The exp-6 potential employed by Dremov *et al.* [44] to model helium in metallic plutonium takes the form of,

$$\Phi(r) = \epsilon \left\{ \left(\frac{6}{\alpha - 6} \right) \exp\left[\alpha \left(1 - \frac{r}{r^*} \right) \right] - \left(\frac{\alpha}{\alpha - 6} \right) \left(\frac{r^*}{r} \right)^6 \right\}. \tag{5.1}$$

From Equation 5.1 it can be seen that the exp-6 potential comprises three parameters: the characteristic diameter, r^*, the potential well depth, ϵ, and the gradient of the exponential function, α. The parameters for the Pu—He interatomic potential were optimised by fitting to the results of *ab initio* DFT calculations. The parameters for the He—He interatomic potential were as found by Ree *et al.* [160]. The exp-6 potential is not included in the library of two-body interatomic potentials currently available within the GULP code, employed in our simulation studies of PuO_2. Rather than producing a 'Table' file of interpolated values, a more efficient solution was to fit an existing analytical function to these data, such as the Lennard-Jones (LJ), Morse or Buckingham forms shown in Equations 5.2– 5.4.

$$\Phi_{\text{Lennard-Jones}} = 4\epsilon \left[\left(\frac{\sigma}{r} \right)^{12} - \left(\frac{\sigma}{r} \right)^{6} \right], \tag{5.2}$$

$$\Phi_{\text{Morse}} = D_e \left[\left(1 - \exp\left(-a \left(r - r_0 \right) \right) \right)^2 - 1 \right], \tag{5.3}$$

$$\Phi_{\text{Buckingham}} = A \exp\left(\frac{-r}{\rho} \right) - \frac{C}{r^6}. \tag{5.4}$$

On examining the form of the exp-6 potential, the potential energy tends to -ϵ when the inter-ionic separation, r, equals the characteristic diameter. As $\epsilon << r^*$,

the potential range is taken as approximately r^*. The parameters employed in the Dremov potential are presented in Table 5.1.

Table 5.1: Dremov *et al.* [44] parameters for the exp-6 potential

Parameter	δ-Pu—He	α-Pu—He	He—He
α	11.8	12.8	13.6
ϵ (eV)	0.007	0.007	0.00091
r^* (nm)	0.4	0.4	0.297
r^* (Å)	4.0	4.0	2.97

r^* was converted from nm to Å for consistency with units employed in GULP. Using parameters for the δ-Pu—He interaction, the exp-6 function is plotted in Figure 5.1.

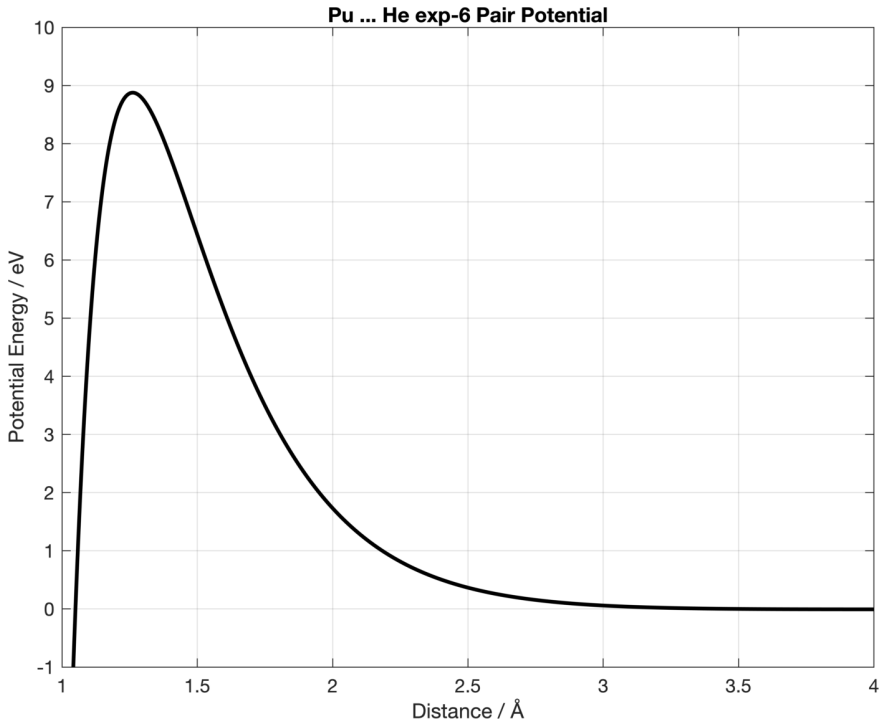


Figure 5.1: The exp-6 potential: δ-Pu—He interaction.

Figure 5.1 illustrates the function tending towards zero at the characteristic diameter, in this case 4.0 Å. The first derivative of this function defines the maximum at 1.26 Å. The unphysical attraction region below this will not be used in the fitting routine and to use the potential for molecular dynamics, solutions such as the Born-Mayer form or ZBL splining will be required for robust simulations.

Lennard-Jones potentials are typically employed in the simulation of gases, Morse potentials for systems exhibiting a degree of covalency and Buckingham potentials

for strongly ionic systems. These analytical functions were fitted to the above region of the exp-6 potential. Upon comparison of the suggested potentials, from a theoretical perspective the Buckingham potential is easier to justify since the repulsion between overlapping electron densities, due to the Pauli principle, takes an exponential form at reasonable distances. However, the Lennard-Jones potential with typical 12-6 exponents, is more robust since repulsion increases faster with decreasing distance than the attractive dispersion term.

For covalently bonded atoms, it is often preferable to Coulomb subtract the interaction and to describe it with either a harmonic or Morse potential. In doing so, the result is a potential where the parameters have physical significance. For instance, in the case of the Morse potential the parameters relate to the dissociation energy of the diatomic species, the equilibrium bond length and a third term, which coupled with the dissociation energy, relates to the vibrational frequency for the stretching mode.

5.2.1 *Fitting Procedure*

MATLAB was employed for the curve fitting procedure and the code (detailed in Figure 5.2) includes several options for greater control over the resulting parameters. For example, without bounds there are several parameters which would satisfy the fit to a Buckingham potential, but desirable ranges are A = 100.0 - 2000.0, ρ = 0.0 - 0.8 and C = 0.0 - 300.0. These are specified with the 'Lower' and 'Upper' bounds in addition to a 'StartPoint' for each.

```
% Fitting the Buckingham Form to these data within the range from 1.27 to 4.0 angs
% Buckingham = A * exp(- r / RHO) - (C/r^6)

 myfitoptions = fitoptions('Method','NonlinearLeastSquares',...
       'Robust', 'On', ...
       'Display','iter',...
       'Lower',[100.0 0.0 0.0],...
       'Upper',[2000.0 0.8 300.0], ...
       'StartPoint',[500.0 0.01 0.0])

myfittype = fittype('a * exp(-x/rho) - (c/x^6)',...
    'dependent',{'y'},'independent',{'x'},...
    'coefficients',{'a','rho','c'},...
    'options', myfitoptions)

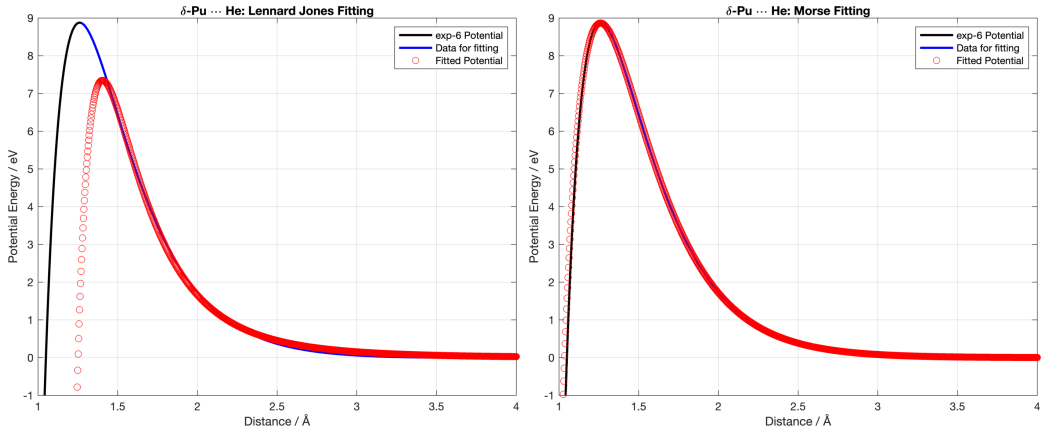
[myfit, gof] = fit(x',y',myfittype)
```

Figure 5.2: Screenshot displaying MATLAB code used for the fitting procedure.

5.2.2 *δ-Pu—He*

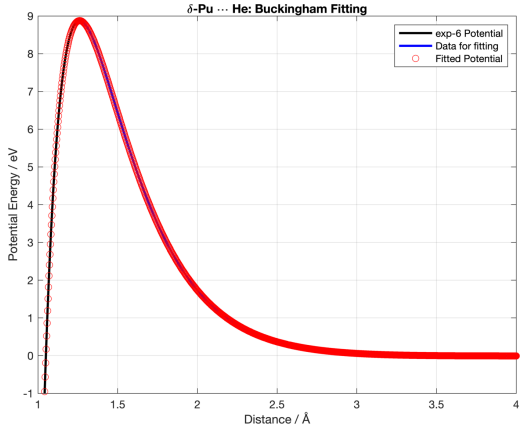
Figure 5.3 plots the δ-Pu—He exp-6 potential over the range 1.0 - 4.0 Å (black line), indicating with a blue line the part of the potential used in the fitting procedure (1.27 - 4.00 Å) and respective potential fits shown with red circles. Of the alternate functional forms, Lennard-Jones provides the poorest fit (r = 0.9987). The LJ potential becomes unphysically attractive at a slightly greater separation distance than the original potential, and crucially has negative parameters which do not relate to a physical meaning. Both the Morse and Buckingham potentials give excellent agreement and could be employed (although it should be noted that the Morse De term is negative). If the close range unphysical attraction is to be avoided, the Born-Mayer form also gives excellent agreement and remains repulsive at close range.

Parameters from the MATLAB fitting procedure are listed in Table 5.2 along with the r-square goodness of fit.

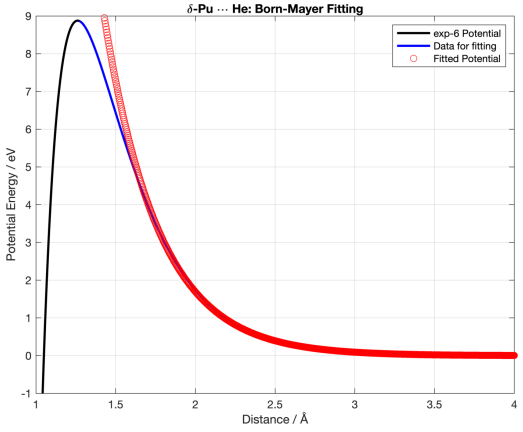


(a)

(b)



(c)



(d)

Figure 5.3: Function fitting to the δ-Pu—He using (a) Lennard-Jones, (b) Morse, (c) Buckingham and (d) Born-Mayer.

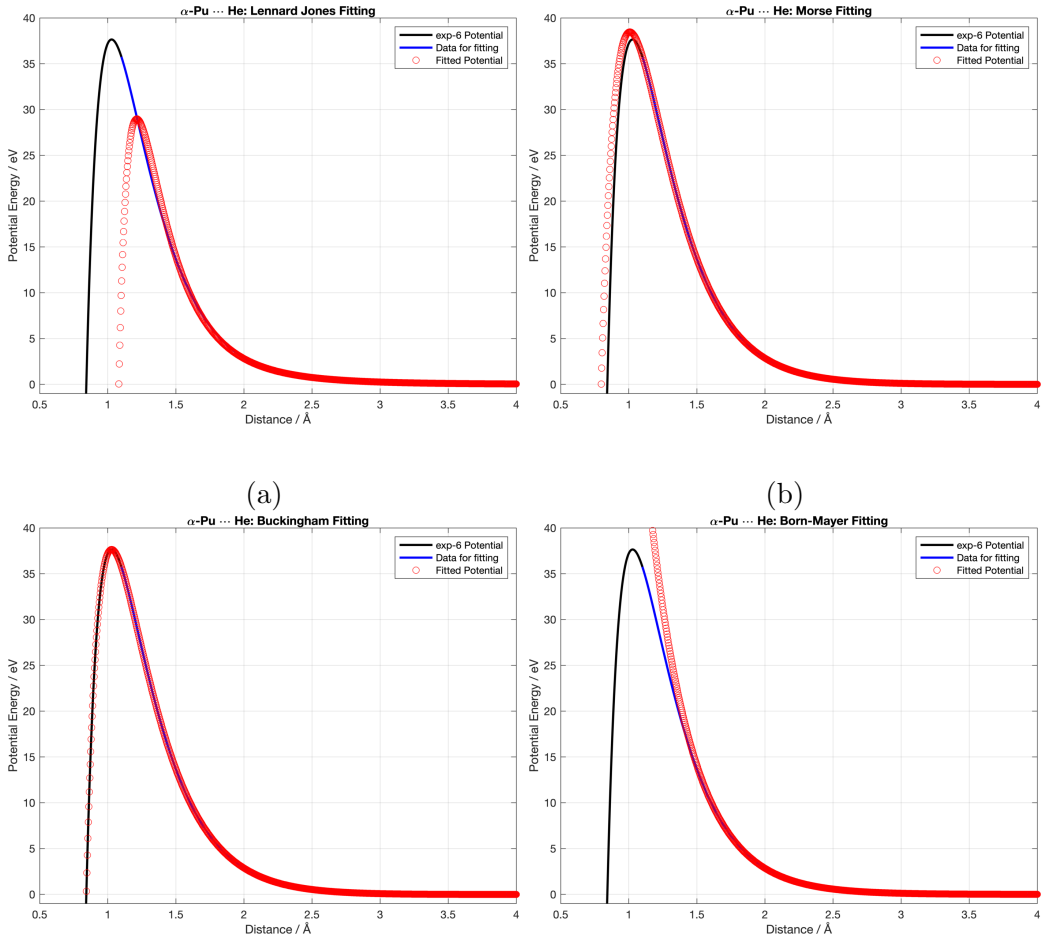
Table 5.2: Fitting Results for δ-Pu—He

Form	Parameters			r-square
Lennard-Jones				
$\Phi = 4\epsilon\left[\left(\frac{\sigma}{r}\right)^{12} - \left(\frac{\sigma}{r}\right)^{6}\right]$	ϵ / eV	σ / Å		
	-7.347795	1.251321		0.9987
$\Phi = \left(\frac{A}{r^{12}}\right) - \left(\frac{B}{r^{6}}\right)$	A / eV Å^{12}	B / eV Å^{6}		
	-433.154307	-112.831360		0.9987
Morse				
$\Phi = D_e\left[\left(1 - \exp\left(-a\left(r - r_0\right)\right)\right)^2 - 1\right]$	D_e / eV	a / Å^{-1}	r_0 / Å	
	-8.866495	3.084057	1.260295	1.0000
Buckingham				
$\Phi = A\exp\left(\frac{-r}{\rho}\right) - \frac{C}{r^6}$	A / eV	ρ / Å	C / eV Å^{6}	
	964.930832	0.338983	58.332690	1.0000
Born-Mayer				
$\Phi = A\exp\left(\frac{-r}{\rho}\right)$	A / eV	ρ / Å		
	578.645861	0.342776		0.9998

5.2.3 *α-Pu—He*

Figure 5.4 plots the α-Pu—He exp-6 potential over the range 0.5 - 4.0 Å (black line), indicating with a blue line that part of the potential used in the fitting procedure (1.10 - 4.00 Å) and respective potential fits shown with red circles. In a similar manner to the δ-Pu—He fitting results, Lennard-Jones provides the poorest fit (r = 0.9994) of the alternate functional forms. It becomes unphysically attractive at a slightly greater separation distance than the original potential, and crucially has negative parameters which do not relate to a physical meaning. Both the Morse and Buckingham potentials give excellent agreement and could be employed (although it should again be noted that the Morse *De* term is negative). If the close range unphysical attraction is to be avoided, the Born-Mayer form also gives excellent agreement and remains repulsive at close range.

Parameters from the MATLAB fitting procedure are listed in Table 5.3 along with the r-square goodness of fit.



(a) (b)

(c) (d)

Figure 5.4: Function fitting to the α-Pu—He using (a) Lennard-Jones, (b) Morse, (c) Buckingham and (d) Born-Mayer.

Table 5.3: Fitting Results α-Pu—He

Form	Parameters			r-square
Lennard-Jones				
$\Phi = 4\epsilon\left[\left(\frac{\sigma}{r}\right)^{12} - \left(\frac{\sigma}{r}\right)^{6}\right]$	ϵ / eV -28.980565	σ / Å 1.080939		0.9994
$\Phi = \left(\frac{A}{r^{12}}\right) - \left(\frac{B}{r^{6}}\right)$	A / eV Å^{12} -294.971576	B / eV Å^{6} -184.915581		0.9994
Morse				
$\Phi = D_e\left[\left(1 - \exp\left(-a\left(r - r_0\right)\right)\right)^2 - 1\right]$	D_e / eV -38.469686	a / Å^{-1} 3.296974	r_0 / Å 1.007686	1.0000
Buckingham				
$\Phi = A\exp\left(\frac{-r}{\rho}\right) - \frac{C}{r^6}$	A / eV 2237.225424	ρ / Å 0.312500	C / eV Å^{6} 53.970824	1.0000
Born-Mayer				
$\Phi = A\exp\left(\frac{-r}{\rho}\right)$	A / eV 1698.000943	ρ / Å 0.313015		0.9999

5.2.4 *He—He*

Figure 5.5 plots the He—He exp-6 potential over the range 0.5 - 3.0 Å (black line), indicating with a blue line that part of the potential used in the fitting procedure (0.652 - 2.970 Å) and respective potential fits shown with red circles. Note that for helium self interactions, the characteristic diameter (r^*) is 2.97 Å. In a similar manner to both α-Pu and δ-Pu, Lennard-Jones provides the poorest fit (r = 0.9999) of the alternate functional form. This is considered surprising for a gas atom interaction. Again, the LJ potential becomes unphysically attractive at a slightly greater separation distance than the original potential, and has negative parameters which do not relate to a physical meaning. Both the Morse and Buckingham potentials give excellent agreement (although it should be noted that the Morse De term is negative) and could be employed. If the close range unphysical attraction is to be avoided, the Born-Mayer form also gives excellent agreement and remains repulsive at close range. Parameters from the MATLAB fitting procedure are listed in Table 5.4 along with the r-square goodness of fit.

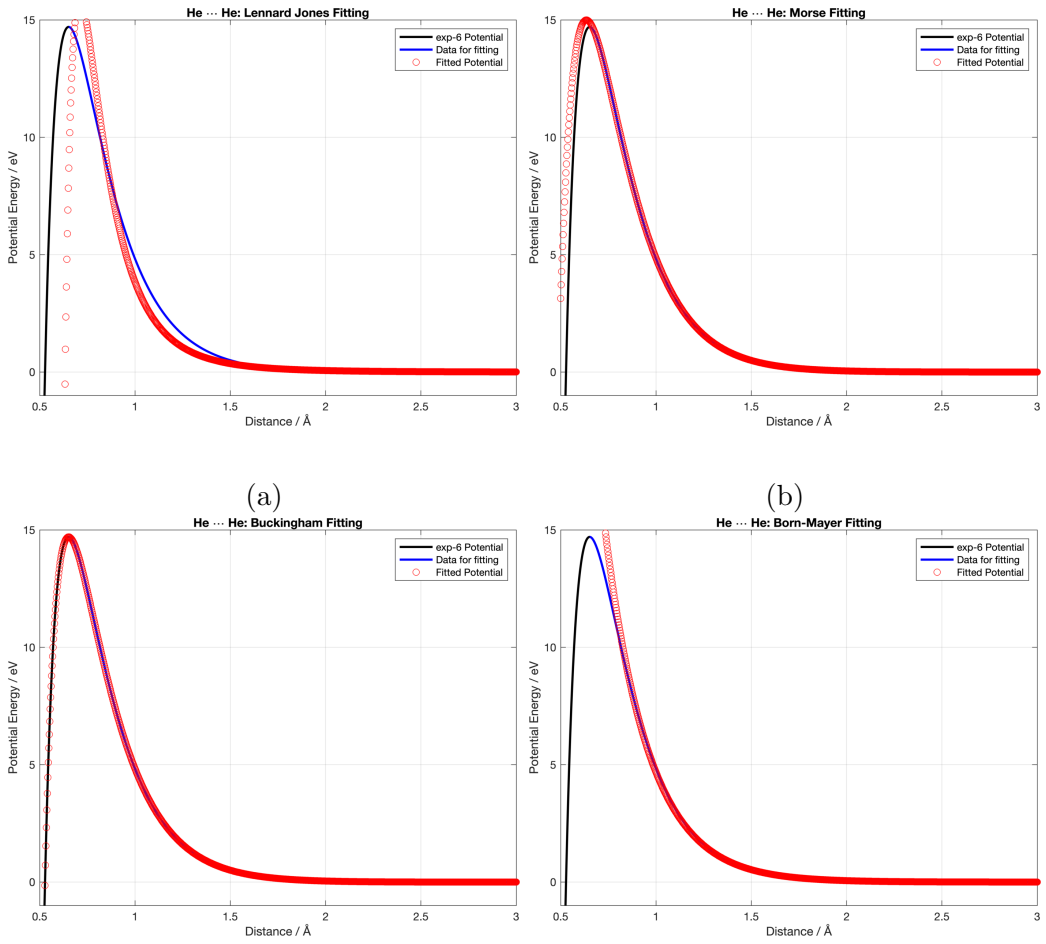


Figure 5.5: Function fitting to the He—He using (a) Lennard-Jones, (b) Morse, (c) Buckingham and (d) Born-Mayer.

Table 5.4: Fitting Results He—He

Form	Parameters			r-square
Lennard-Jones				
$\Phi = 4\epsilon\left[\left(\frac{\sigma}{r}\right)^{12} - \left(\frac{\sigma}{r}\right)^{6}\right]$	ϵ / eV -15.868463	σ / Å 0.633348		0.9999
$\Phi = \left(\frac{A}{r^{12}}\right) - \left(\frac{B}{r^{6}}\right)$	A / eV Å^{12} -0.264424	B / eV Å^{6} -4.096831		0.9999
Morse				
$\Phi = D_e\left[\left(1 - \exp\left(-a\left(r - r_0\right)\right)\right)^2 - 1\right]$	D_e / eV -14.998137	a / Å^{-1} 4.730518	r_0 / Å 0.634502	1.0000
Buckingham				
$\Phi = A\exp\left(\frac{-r}{\rho}\right) - \frac{C}{r^6}$	A / eV 579.140590	ρ / Å 0.218382	C / eV Å^{6} 1.117649	1.0000
Born-Mayer				
$\Phi = A\exp\left(\frac{-r}{\rho}\right)$	A / eV 368.043090	ρ / Å 0.229029		0.9999

5.2.5 *Summary*

For He interactions with δ-Pu, α-Pu and other He atoms, the analytical form which consistently provides the best fit to the Dremov exp-6 potentials is that of the Buckingham. Both Lennard-Jones and Morse potentials could only reproduce the original form with negative parameters which bring into question the validity and do not relate to physical properties. Upon inspection it was found that the when q1 or q2 = 0, the exp-6 and Buckingham potentials are equivalent. As such, for use in GULP, the fitted parameters for the Buckingham potential are used to implement the Dremov potential.

5.3 Helium Potential Evaluation

Prior to this work, Helium in PuO_2 has not been modelled via potential methods using a Pu—He potential. Therefore, there are limited available potential models available for comparison. Combinations of potentials by three authors have been considered.

5.3.1 *Grimes Potential*

The Lennard-Jones potentials of Grimes *et al.* [158] were derived for UO_2 via *ab initio* calculations. This set of potentials has previously been used by Palmer [93] to model helium in PuO_2 due to the limited availability of a Pu—He model. The parameters of the potential are presented in Table 5.5.

Table 5.5: Parameters of the Grimes potential [158]

(a) Short range parameters, r_{max} is 15 Å. All are of Lennard-Jones form

Interaction	A_{ij} (eV Å^{-12})	B_{ij} (eV Å^{-6})
He—He	69.3559	0.493712
He—O	2247.836	11.762
Pu—He	500.425	7.366

(b) Shell model parameters, cut-off distance is 0.60 Å

Ion	q_{shell} (e C)	k (eV Å^{-2})
Pu^{4+}	6.54	206.77
O^{2-}	-4.40	296.2
He	-1.00	72.70

5.3.2 *Aziz Potential*

Aziz *et al.* [161] developed an accurate intermolecular potential for helium. The potential is of Lennard-Jones type for the He—He interaction. It possess almost the correct Hartree-Fock repulsion and the correct long range behaviour. It was

developed by fitting the potential form to accurate intermediate temperature second virial coefficients and thermal conductivity data. The parameters of the potential are presented in Table 5.6.

Table 5.6: Parameters of the Aziz He—He potential [161]

Interaction	ϵ/k (K)	σ (Å)
He—He	10.22	2.556

5.3.3 *Dremov Potential*

Dremov potentials for He—He and Pu—He interactions as determined in Section 5.2 are detailed in Table 5.7.

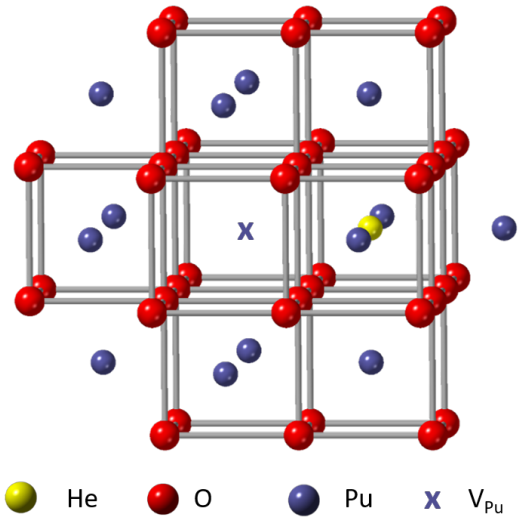
Table 5.7: Parameters of the Dremov potential fitted to a Buckingham potential

Interaction	A (eV)	ρ (Å)	C (eV Å^6)	Cut-off (Å)
δ-Pu—He	964.930832	0.338983	58.332690	4.00
He—He	579.140590	0.218382	1.117649	2.97

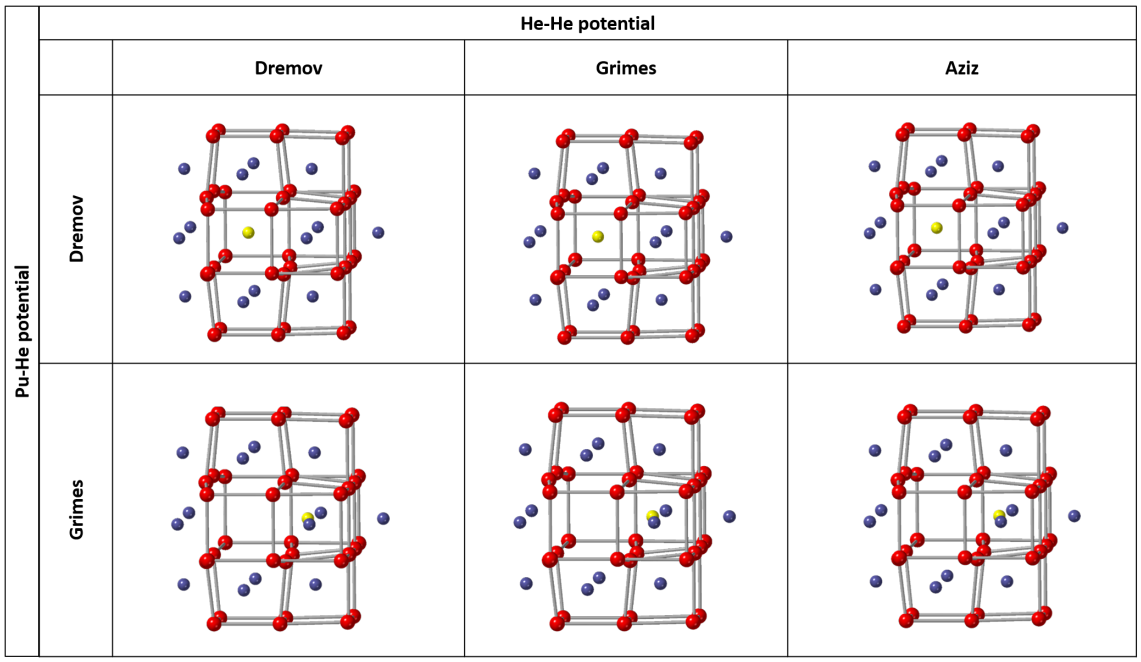
5.3.4 *Evaluation*

From the literature one He—O potential, three Pu—He potentials and two He—He potentials have been identified. This work will therefore use the He—O potential of Grimes *et al.* [158]. The aim next was to establish which Pu—He and He—He potentials to use in combination with the He—O potential. From the literature a the key result was identified. The result was that a plutonium vacancy will be a trapping site for He in PuO_2 [132]. Therefore, if a combination of the potentials can produce this result then this potential will be considered for use.

Simulations were employed in which a helium atom was input in an interstitial site adjacent to a plutonium vacancy, as can be seen in Figure 5.6a.



(a) Input



(b) Outputs

Figure 5.6: Visualisations from the study of helium potentials to examine if the helium atom migrated to a plutonium vacancy upon atomic relaxation. Displaying (a) input configuration, and (b) output configurations of all potential combinations.

As displayed in Figure 5.6b, when the Grimes Pu—He potential was used in combination with all available He—He potentials, the helium remained in its input interstitial site. This is in contrast to when the Dremov Pu—He potential was used, in which case the He migrated to occupy the plutonium vacancy site. The behaviour exhibited by helium when modelled using the Dremov Pu—He potential is what is expected from established literature findings. Therefore, the Grimes Pu—He potential is not suitable for use in this work. Next, it was decided that the Dremov He—He potential would be used in combination with the Dremov Pu—He potential as it was developed to reproduce the most recent experimental data [44].

In summary, the potentials used throughout this chapter to model helium in PuO_2 are the Lennard-Jones He—O potential of Grimes *et al.* [158] and the Buckingham potentials of Pu—He and He—He fitted in this work from those of Dremov *et al.* [44].

5.4 Helium Incorporation in Pure PuO_2

5.4.1 *Single Helium*

The starting point for investigating the incorporation of helium in PuO_2 was determining the most favourable site for a He atom to occupy in defect-free PuO_2. From the lattice structure, the suggested interstitial sites were the Octahedral Interstitial Site (OIS), an edge-centred position (between two O atoms) and a face-centred position. These are the sites which have been considered for He incorporation in ThO_2 and UO_2 [155] [156]. A single He atom was inserted in each of these sites and the lattice was relaxed according to the Mott-Littleton procedure.

The incorporation energies for the three sites were calculated to be: 1.06 eV at the OIS, 5.6 eV at the edge-centred position and 7.07 eV at the face-centred position. As the incorporation energy of He at an OIS is significantly lower than the other considered sites, it is the most energetically favourable site for He to occupy in defect-free PuO_2. He occupying an OIS can be seen in Figure 5.7 and it can be seen that there is no distortion to the unit cell. In contrast, when helium was added to the edge-centred and face-centred positions, there was distortion to the unit cell. This distortion will have contributed to the higher incorporation energies.

The energy of incorporation of helium at every available site in the PuO_2 lattice was evaluated to both ensure a more energetically favourable site had not been overlooked by previous studies. Additionally, such evaluation could aid in in the determination of helium migration pathways. A helium atom was inserted in a

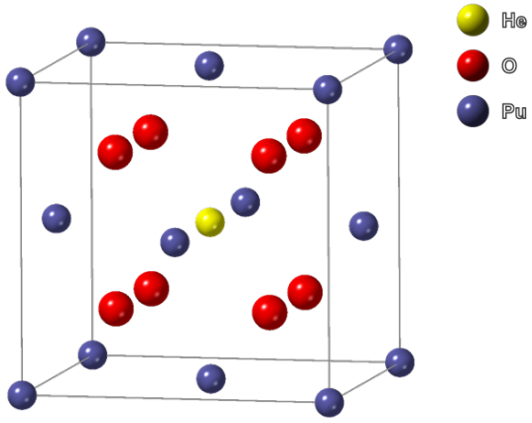


Figure 5.7: PuO_2 unit cell with Helium interstitial in the OIS, the most energetically stable site in defect-free PuO_2.

lattice site and the 'fix' command applied in GULP, which forces the He atom to remain in its input coordinates whilst the lattice is relaxed around it. This was repeated in 0.1 Å intervals across the entire PuO_2 unit cell by separating the z-axis into planes.

Figure 5.8 displays the 'energy profile map' of helium in PuO_2. The colour map indicates the incorporation energy at each square coordinate (in eV where blue is low and red is high). It can be seen that (0.5,0.5,0.5) is the deepest blue and therefore has the lowest energy, as such it is the most energetically favourable site for a helium interstitial to occupy. This coordinate corresponds to the Octahedral Interstitial Site (OIS) defined earlier. Towards the limits of the graph ((0.3,0.3,0.3) and (0.7,0.7,07)) the colour is red corresponding to high energies at these sites (around 9.0 eV). The high energy is because these coordinates are approaching a lattice oxygen site in the unit cell so there will be repulsion and limited space for the helium atom in such areas.

As no site was found to have a lower incorporation energy than the OIS, it is concluded that it is the most energetically favourable site for He to occupy and is the likely position helium will occupy in pure PuO_2. The magnitude of the He incorporation energy of 1.06 eV is similar to that found in the literature for He occupying the OIS in PuO_2, of 1.02 eV and 1.48 eV by Gryaznov *et al.* [154] and Tian *et al.* [131] respectively. Additionally, work by Yun *et al.* [156] in UO_2 and Kuganathan *et al.* [155] in ThO_2 also found the OIS to be the most stable site for He incorporation. Experimentally, Garrido *et al.* [162] used nuclear reaction analysis and Rutherford backscattering spectrometry to find that the OIS is the site

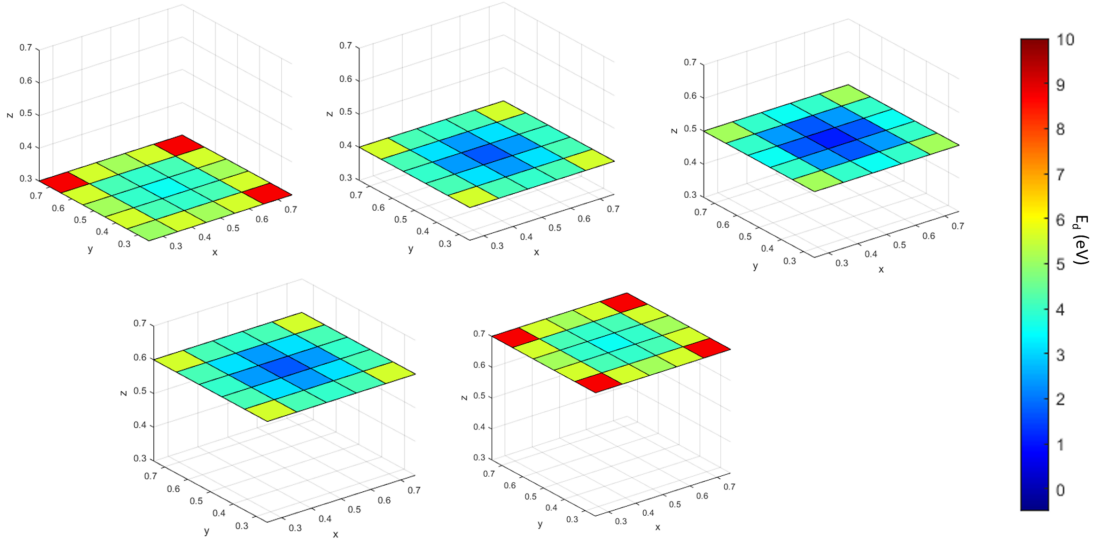


Figure 5.8: Energy profile map of the incorporation energy of helium at lattice sites in PuO_2. The colour bar corresponds to the magnitude of the defect energy with red being high and blue being low. The lattice was divided into five planes in the z-axis.

occupied by He in single crystals of UO_2. These findings give confidence in the fitted He—He and Pu—He potentials.

5.4.2 *Two Helium Atoms*

Three configurations of two He atoms in defect-free PuO_2 were considered:

(i) In separate OISs aligned in the (100) direction

(ii) In separate OISs aligned in the (110) direction

(iii) In separate neighbouring edge-centred positions

For both configurations (i) and (ii), upon atomic relaxation, the He atoms remained in their initial OISs with incorporation energies of 2.13 and 2.11 eV respectively. It is suggested that the slightly lower incorporation energy of the (110) configuration could be due to the He atoms not being screened from each other by a lattice plutonium ion.

When two He atoms were placed in configuration (iii), they migrated upon atomic relaxation. Figure 5.9 shows how upon relaxation the two He atoms migrate in the

direction of the closest OIS to form a dumbbell configuration with an interatomic He-He distance of 1.39 Å. The incorporation energy for the He to form a dumbbell was 5.25 eV, significantly higher than that of He in two neighbouring OISs. Therefore, whilst two He atoms are energetically more stable in separate OISs than in the dumbbell configuration, if two He atoms are close together (for example, knocked nearby during a decay event) then they are likely to form the dumbbell configuration. This result was also found in ThO_2 [155] and UO_2 [156].

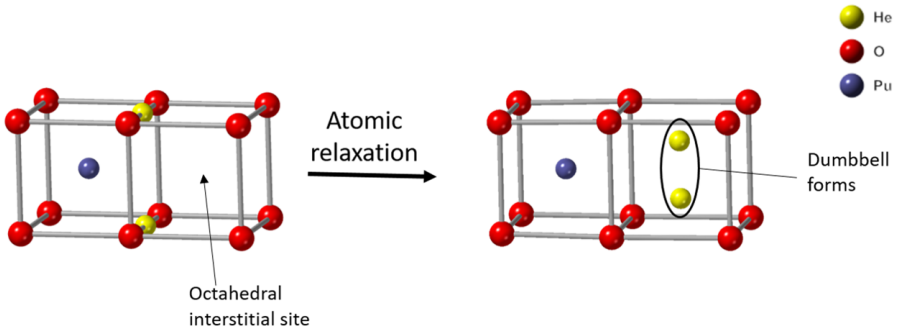


Figure 5.9: Two He atoms initially in edge-centred positions form a dumbbell configuration around the OIS upon atomic relaxation.

Yun *et al.* [156] proposed two mechanisms for helium dumbbell formation in UO_2:

(a) Helium atoms from separate OIS migrate to the same OIS via edge-centred positions

(b) One helium migrates from an OIS to join a helium atom in an OIS

Figure 5.10a and b displays mechanisms a and b respectively. Helium atoms were inserted and fixed at the coordinates of the three positions displayed in Figure 5.10 for each mechanism. Energy minimisation for each configuration was performed and the defect energies at each position were calculated, from this the energy pathway could be plotted.

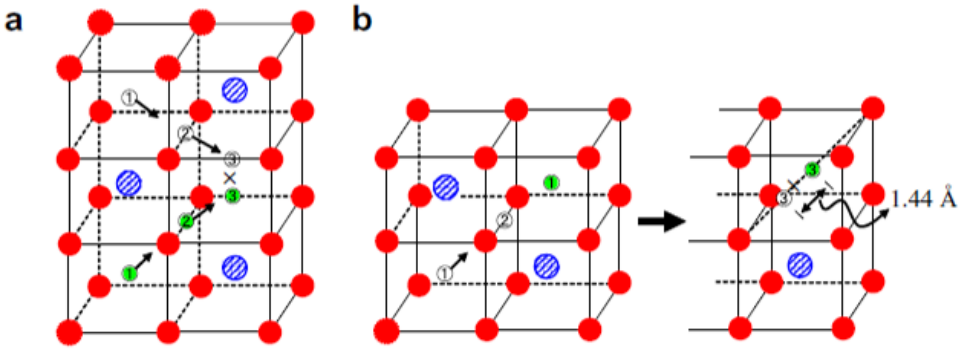


Figure 5.10: Mechanisms for helium dumbbell formation. In (a) helium atoms migrate from separate OISs, in (b) one helium joins another in an OIS. Figure from [156], oxygen atoms are red, plutonium atoms are blue.

The energy pathways for the two dumbbell formation mechanisms are displayed in Figure 5.11. It can be clearly seen that the energy barrier for mechanism a (Figure 5.11a) is significantly higher than for mechanism b (Figure 5.11b). This result was also found by Yun *et al.* [156] in UO_2. From this it is suggested that dumbbell formation primarily occurs via mechanism b.

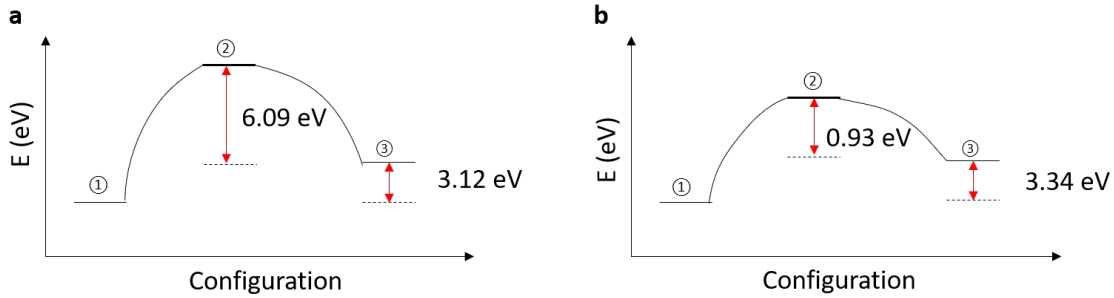


Figure 5.11: Energy barrier between two configurations when two He atoms move from different OISs and form a dumbbell. (a) Two He atoms move simultaneously to the nearest empty OIS, and (b) one He moves to the other He trapped at an OIS.

5.4.3 *Helium Build-Up*

For the accommodation of increasing numbers of interstitial helium atom in the PuO_2 lattice, multiple configurations for each number of helium atoms were simulated. For each number of helium atoms, the lowest energy was obtained when the helium atoms occupied separate OISs. The difference in energy for how the He occupied OISs were distributed through the lattice was negligible. Figure 5.12

displays the linear increase in energy that results from the successive addition of helium atoms into separate OISs.

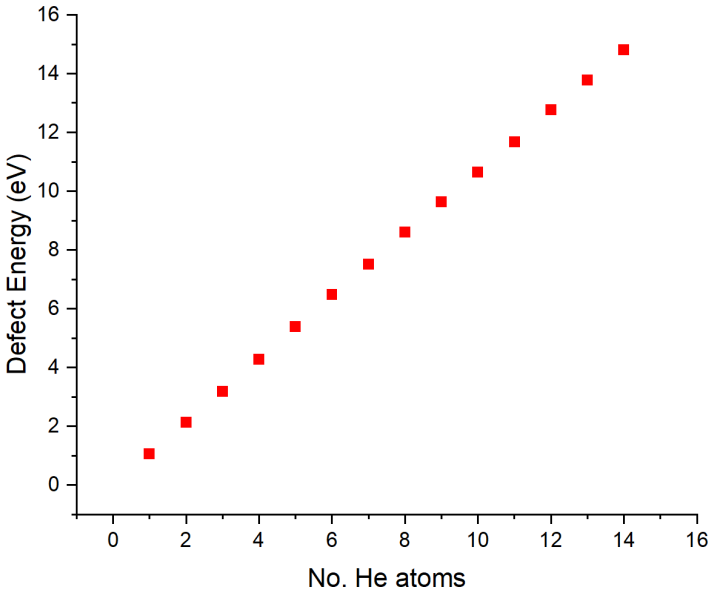


Figure 5.12: Defect energy of He interstitials in separate OIS as a function of the number of He atoms. There is a linear increase in defect energy as the number of He atoms in the lattice increases.

5.5 Helium in Defective PuO_2

5.5.1 *Single Helium*

Due to decay events, intrinsic defects will be present in PuO_2. Such defects will be in addition to the inherent disorder exhibited within lattices above 0 K driven by thermodynamics. It is of interest if any of these defect sites may act as 'traps' for the radiogenic He atoms generated. Trap sites could act as possible seed locations for helium bubble nucleation. The defects considered were: a plutonium vacancy (V_{Pu}), an oxygen vacancy (V_O), a divacancy (V_{PuO}) and a Schottky trio vacancy (V_{PuO_2}). From here on, for simplicity, the Kröger Vink notation has been dropped as the vacancies are always assumed to have full charges. As such, $V_{Pu}^{''''} = V_{Pu}$, $V_O^{\bullet\bullet} = V_O$, $\left[V_{Pu}^{''''} : V_O^{\bullet\bullet}\right]^{''} = V_{PuO}$), and $\left[V_{Pu}^{''''} : 2V_O^{\bullet\bullet}\right]^{x} = V_{PuO_2}$.

In each instance a helium atom was added to the centre of the defect site and

the lattice allowed to relax. The incorporation energies, E_{inc}, were calculated via,

$$E_{inc} = E_{V_X}^{He} - E_{V_X}. \tag{5.5}$$

Where X is the vacancy type (X = Pu, O, PuO or PuO_2), $E_{V_X}^{He}$ is the energy of helium occupying the vacancy and E_{V_X} is the energy of the empty vacancy site. The calculated incorporation energies are listed in Table 5.8.

Table 5.8: Incorporation energies of He at different vacancies in AO_2. Where A is an actinide

Defect	Incorporation Energy (eV)			
	PuO_2		ThO_2	UO_2
	This work	Tian [131]	Kuganathan [155]	Petit [163]
V_O	1.28	0.90	0.68	2.2
V_A	-0.23	0.24	0.32	-7.4
V_{AO}	-0.23	0.23	0.31	-6.6
V_{AO_2}	-0.22	0.17	0.25	-6.0

From Table 5.8 it can be seen that helium occupation is least favourable in an oxygen vacancy. This result was also found by Petit *et al.* [163], Tian *et al.* [131] and Kuganathan *et al.* [155] for He in UO_2, PuO_2 and ThO_2 respectively. Much work has been done on the defect chemistry of PuO_2, and it is widely acknowledged that the V_{Pu} (and correspondingly the PuFP) has a much higher defect energy than a V_O, OFP and Schottky trio [164] [49]. This order of defect stability was also found in this work in Chapter 3.

The trapping energies, E_T, were calculated relative to the incorporation energy obtained for helium occupying an OIS, E_{OIS}^{He}, as follows,

$$E_T = E_{inc} - E_{OIS}^{He}. \tag{5.6}$$

A negative E_T value indicates an energy decrease of the system when He moves from an OIS to the defect site. A positive value means that energy is required to incorporate He at the defect site. As $E_{OIS}^{He} = 1.06$ eV, the calculated trapping energies were negative for all defect sites listed in Table 5.8 excluding the oxygen vacancy which had a trapping energy of 0.22 eV. Therefore there is an energetic drive for He to join Pu vacancies, divacancies and Schottky trios. In contrast, due to the positive trapping energy for He at an oxygen vacancy, there is an energetic barrier for the He to join this site.

To further the understanding of He behaviour in the presence of vacancies, an energy profile plot was constructed for He when a V_{Pu} and V_O were independently present. Figures 5.13 and 5.14 display the energy profiles for Helium incorporation across lattice sites surrounding an V_O and a V_{Pu} respectively. The colour bar is used to display the defect energy of helium at each site with deeper blue being lower energy so more favourable sites and red being higher energy, less favourable. It must be noted that the colour bars in plots 5.13 and 5.14 are of a different scale. Figure 5.13 is 0.0 - 10.0 eV and Figure 5.14 is -0.5 - 2 eV, this is due to the defect energies being significantly lower for He in the presence of a V_{Pu} compared to an V_O and thus ensures the colours are distinguishable.

In Figure 5.13 it can be seen that the deepest blue areas correspond to the OIS rather than the V_O site. In contrast in Figure 5.14 the area with the deepest blue corresponds directly to the Pu vacancy site. Surrounding the Pu vacancy there is an area of low defect energy (below 0.5 eV). Such a region suggests that a Pu vacancy site could be a potential seed location for helium clustering, as it is likely it can accommodate multiple He atoms in the large region of low defect energy. In the oxygen vacancy system, the region of low defect energy is approximately 2 eV, so it is less favourable than surrounding a Pu vacancy. However the region extends out to the OIS and as such He clusters may develop from helium atoms sequestered in neighbouring OIS and oxygen vacancies as a cluster develops.

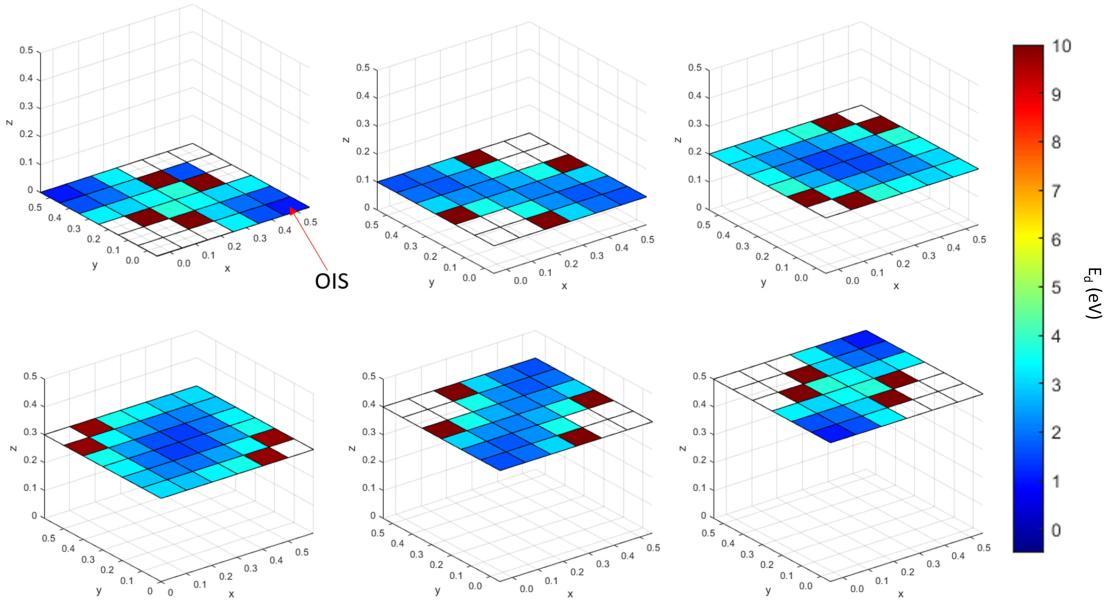


Figure 5.13: Energy profile map of a helium atom at various locations surrounding an oxygen vacancy at (0.25,0.25,0.25).

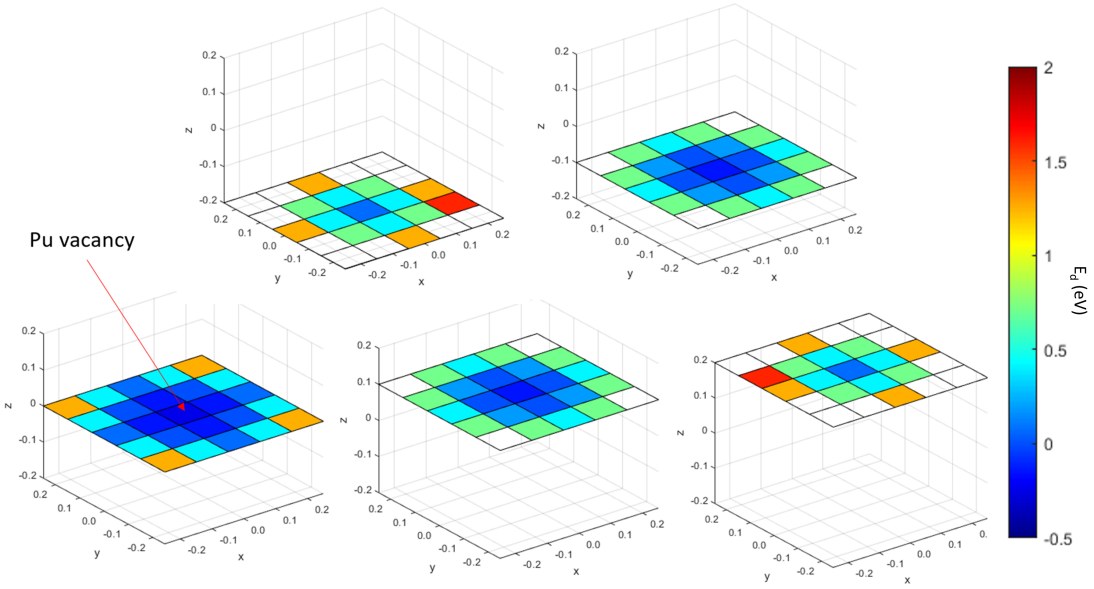


Figure 5.14: Energy profile map of a helium atom at various locations surrounding an plutonium vacancy at (0.5,0.5,0.5).

Helium incorporation at a Pu vacancy may be more favourable than at an O vacancy simply due to the larger available vacant volume in a V_{Pu}. DFT simulations have recently been performed to calculate the charge density of He at OIS, V_O and V_{Pu}. The findings were of charge densities of 2.05, 2.06 and 2.02 for He incorporation at an OIS, V_O and V_{Pu} respectively [152]. It is evident that the lowest charge density is when He occupies a V_{Pu}. As discussed by Yun *et al.* [156], helium prefers to occupy the site with the lowest electron density due to its filled-shell electronic configuration.

However, plutonium vacancies (and PuFPs) have a high defect energy, so although they are the most favourable site for He, they may not be the majority site available to He [164] [49]. In Chapter 4 it was found that plutonium Frenkel pairs are more stable at the (111) surfaces of PuO_2 than in the bulk. As such, it is suggested that helium could migrate to, and be accommodated at, surface plutonium vacancies.

5.5.2 *Helium Build-Up*

5.5.2.1 Isolated Vacancies

It has been established that plutonium vacancies are favourable for He accommodation and so helium is likely to migrate to such sites. Next, it was required to

determine how much He a V_{Pu} can accommodate, and if a V_O becomes favourable for He accommodation when there is multiple helium atoms. Tables A.1.1 and A.2.1 (Appendix A) display the input and relaxed configurations of all the trialled helium configurations surrounding a V_{Pu} and V_O respectively.

For two helium atoms surrounding an oxygen vacancy, three of the helium configurations considered were: separate OIS (2_OIS), one in V_O one in an OIS (O_OIS) and both He in dumbbell at the V_O (DB_O). These configurations before and after relaxation can be viewed in Table A.2.1. Figure 5.15 displays the defect energies of these configurations. The lowest defect energy was obtained when the helium atoms were located in separate OISs, where they remained upon relaxation. The second most stable configuration was O_OIS, with only a slightly higher defect energy. This is in contrast to the findings of Kuganathan [155] in ThO_2, in which they found the most stable configurations to have one He occupying an oxygen vacancy. The helium dumbbell configuration was trialled in the V_O site, and the defect energy was shown to be significantly higher. This could suggest that the build up of He is unfavourable in an oxygen vacancy and that an oxygen vacancy may not be a seed location for helium bubbles.

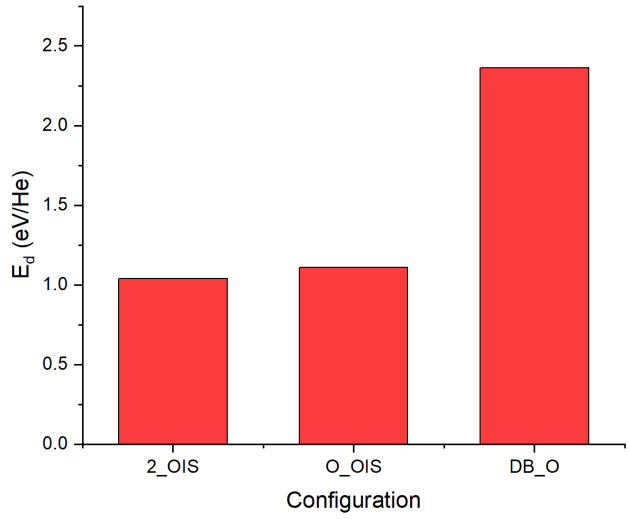


Figure 5.15: Defect energies of three configurations of two helium atoms and an oxygen vacancy.

Multiple configurations of up to six He atoms surrounding an V_O were considered, in all cases it was found that there was no clustering of helium surrounding the V_O. The lowest energy configurations were obtained when helium atoms occupied

surrounding isolated OISs, or when one He occupied the V_O with the rest in surrounding isolated OISs. The difference in energy between these two configurations was often negligible. In other considered configurations with the helium atoms clustered around the V_O, upon relaxation the atoms would disperse to separate OISs, or remain with a significantly high defect energy. For 7-12 He, only He in separate OIS configurations were considered.

Next, helium configurations surrounding a plutonium vacancy were considered. Unlike for the oxygen vacancy configurations, helium in a dumbbell configuration at a plutonium vacancy was favourable and often configurations including this alongside He in OIS had a low defect energy. This suggests that helium clustering is favourable at a V_{Pu}. When helium atoms were placed in separate OISs, upon relaxation the helium atoms would migrate to form clusters surrounding the V_{Pu}, this was found for 1-6 He atoms. Figure 5.16 displays the input and relaxed configurations of six He atoms surrounding V_{Pu} and a V_O. When the He atoms surround a V_{Pu} (Figure 5.16a) it is evident that the He atoms migrate to cluster around the V_{Pu} in an octahedral formation. This is due to V_{Pu} being an energetically favourable site for He atoms. In contrast, Figure 5.16b shows that when six helium atoms surround an oxygen vacancy upon relaxation, the helium atoms remain in the initial OISs. There is no energetic drive for the helium atoms to migrate towards the V_O site.

5.5.2.2 Divacancy

The same process of building up helium configurations and finding the most stable configurations was repeated for a divacancy (a V_{Pu} and V_O). In all configurations it was found that helium would migrate towards the V_{Pu}, rather than the V_O (Table A.3.1). For six He initially occupying an OIS, upon relaxation they migrated to form the octahedral configuration as displayed in Figure 5.16, but with an oxygen vacancy neighbouring. When this configuration was formed in the divacancy the defect energy per He was slightly lower than when simply at a V_{Pu} (0.27 and 0.30 eV/He respectively). This may be due to the larger void space available due to the oxygen vacancy.

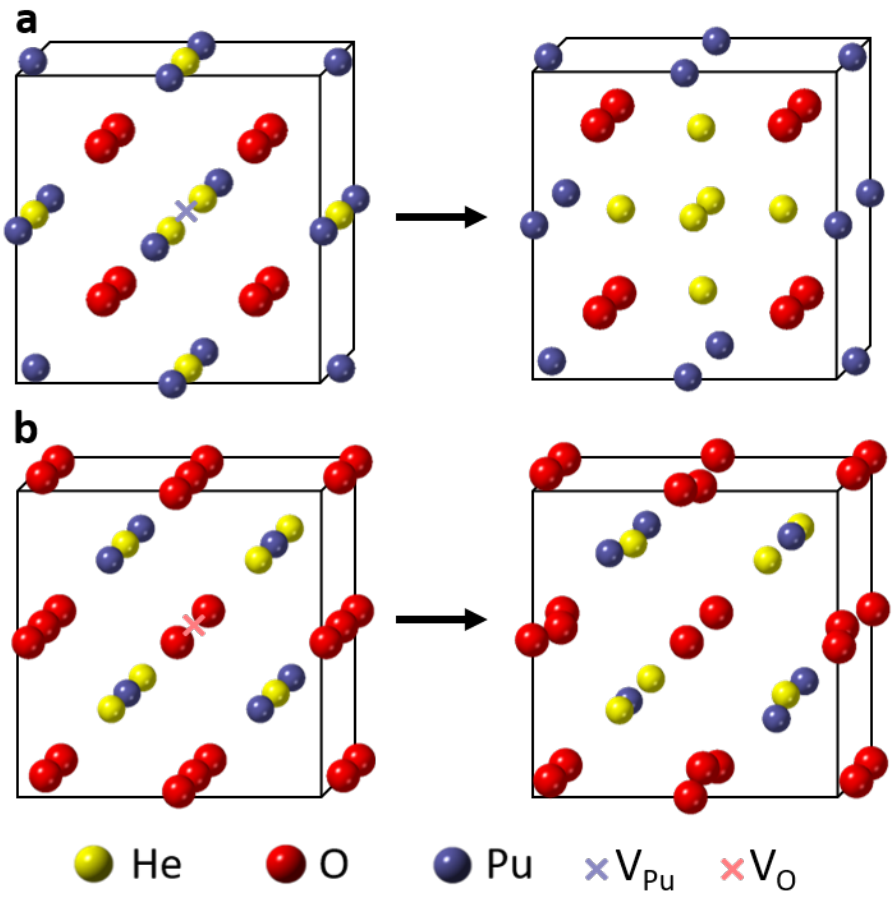


Figure 5.16: Six helium atoms in OISs surrounding a V_{Pu} (a) and a V_O (b), before and after relaxation.

5.5.2.3 Schottky Trio

A Schottky trio defect was generated in the lattice and helium atoms were built up in many configurations surrounding and within the defect. For the simulations of one helium atom in a Schottky trio, it was found that the exhibited behaviour was similar to when occupying a divacancy. That is, when a helium atom was input in a neighbouring OIS, upon relaxation the helium migrated to the plutonium vacancy with a defect energy of -0.22 eV/He (Figure 5.18b). When the helium was located in a distant OIS, it no longer migrated to the plutonium vacancy and the defect energy was 1.05 eV/He. Finally, when the helium was input in either oxygen vacancy, it remained in the input site but with a higher defect energy of 1.77 eV/He. As such it is more favourable for He to remain in an isolated OIS than migrate to an oxygen vacancy within a Schottky trio.

Six configurations of two helium atoms and a Schottky trio were considered. Figure 5.17 displays the defect energy per helium atom obtained for each configuration. The input and relaxed output structures of these configurations can be viewed in Table A.4.1. The highest energy configurations were ′O1_O2′ and ′2_OIS_Dist′ corresponding to the two helium atoms being in separate oxygen vacancies, and separate ′distant′ (one nearest neighbour position away) OISs, respectively. When the helium atoms in the oxygen vacancies were allowed to relax, they migrated to the distant OIS. As such, O1_O2 and 2_OIS_Dist have the same defect energy, 1.05 eV/He. The second highest energy configurations were Pu_O1 and Pu_O2, which were comprised of one He in the V_{Pu} site and the other He in each V_O site. As was expected, both available oxygen vacancies output the same defect energy. Upon inspection of the relaxed configurations it was found that in both cases the helium located at a V_O site migrated to an OIS. Therefore it is suggested that the 0.41 eV/He defect energy obtained was due to it being an average of He in an isolated OIS, and He at a V_{Pu}.

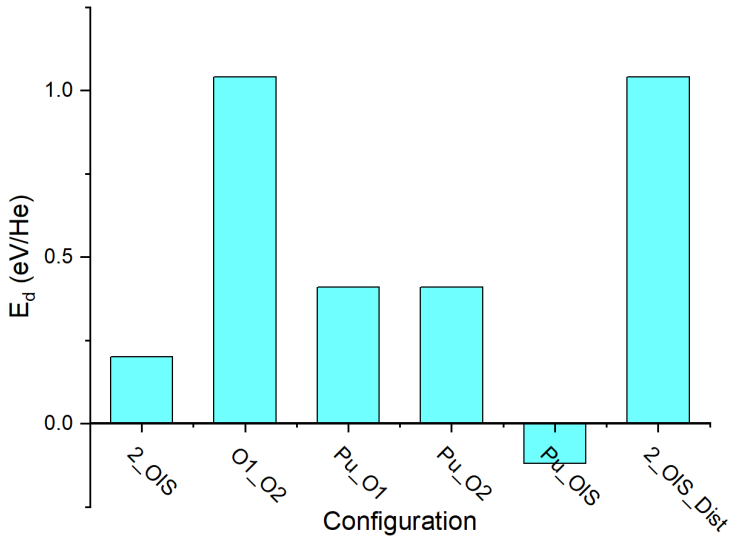


Figure 5.17: Defect energies of six configurations of two helium atoms and a Schottky trio defect.

The two lowest energy configurations of two helium atoms in a Schottky trio were ′2_OIS′ and ′Pu_OIS′ corresponding to two He atoms in neighbouring OISs and one He at a V_{Pu} and the other in an adjacent OIS. Upon relaxation, the two helium atoms in OISs migrate to the centre of the void space with an interatomic

separation of $\sim$ 1.9 Å, with a defect energy of 0.20 eV/He (as displayed in Figure 5.18c). For the 'Pu_OIS' configuration, the He in the OIS migrates towards the V_{Pu} upon relaxation, with the other He migrating slightly from the V_{Pu} site to also have a helium interatomic distance of $\sim$ 1.9 Å and a defect energy of -0.12 eV/He. It is suggested that the difference in defect energy is due to the relaxed configuration of the '2_OIS' input being centred about the Schottky void space, and the relaxed configuration of the 'Pu_OIS' being centred about the V_{Pu}.

From these simulations it was found that helium would migrate from a neighbouring OIS to join a He in a V_{Pu}, but would not migrate from an V_O to join the He. When the helium migrated from an oxygen vacancy, the OIS it occupied was in a position shielded from the V_{Pu}. Therefore, it is suggested that if it migrated to a neighbouring OIS instead, it could have made the next hop to the Pu vacancy site and that this V_O-OIS-V_{Pu} could be a possible clustering migration pathway. However, for five He surrounding the Schottky trio in the 'Pu_O1_O2_2_OIS' configuration, it was found that the He in oxygen vacancies migrate to form a cluster. As such, there could be a cumulative effect for the clustering of multiple helium atoms. It is suggested that when at least five helium atoms are clustered it becomes favourable for He in an V_O to migrate to the cluster rather than to a shielded OIS, and thus once a cluster becomes a certain size, cluster growth could become more favourable.

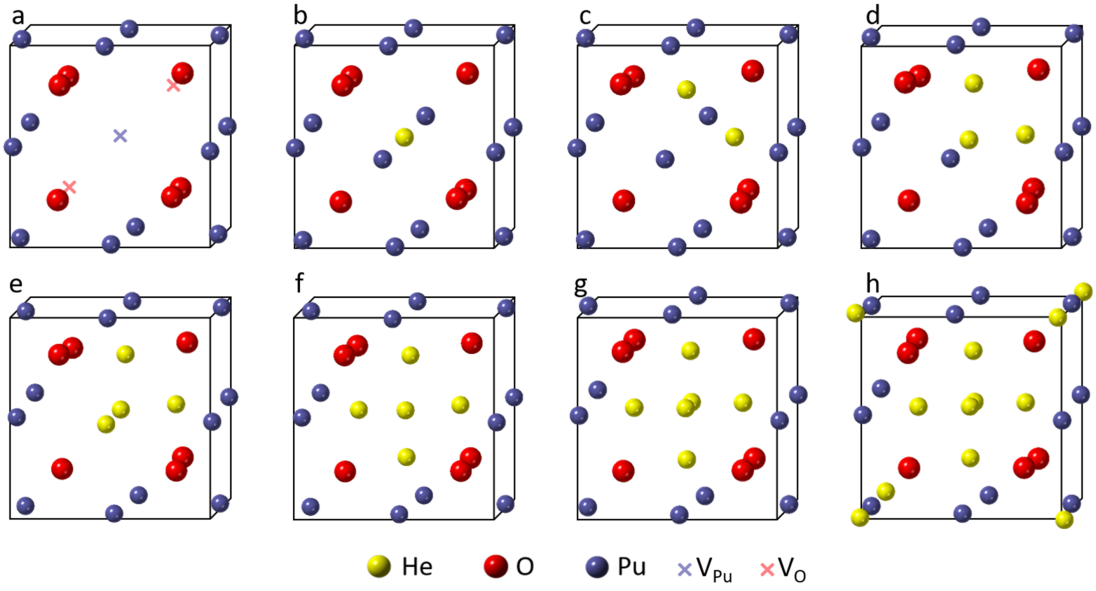


Figure 5.18: Relaxed He configurations surrounding a Schottky trio.

The build up process of multiple configurations was repeated for up to 6 He atoms in the Schottky defect. Figure 5.18 displays the relaxed structures of He atoms when initially inserted in OISs neighbouring a Schottky trio. It can be seen from Figure 5.18 that the He atoms cluster around the V_{Pu} rather than the V_O and form stable configurations. Figures 5.18d, e, f, and g show the He atoms in trigonal planar, tetrahedral, square planar and octahedral formations respectively. As seen in Figure 5.18h, when over six He atoms are present (in this case 12), the additional He atoms do not join the cluster but remain in neighbouring OISs. The relaxed configurations are comparable to those found by Kuganathan *et al.* [155] when investigating helium build up in ThO_2.

5.5.2.4 Frenkel Pairs

Multiple configurations were considered for 1-6 helium atoms surrounding a plutonium Frenkel pair. The input and output configurations and their associated defect energies can be viewed in Table A.5.1. Helium atoms in the vicinity of the PuFP behaved in a corresponding manner to when in the vicinity of an isolated Pu vacancy, or a Schottky trio. That is, the minimum energy configurations were when the He migrated from OIS to cluster around the plutonium vacancy forming the same configurations as were displayed in Figure 5.18.

For the build up of helium atoms surrounding an oxygen Frenkel pair, the helium atoms were found to behave in the same manner as discussed for surrounding an oxygen vacancy. As such, it was found that the clustering of helium is not favourable at an OFP.

An interesting result was found for two helium atoms in a dumbbell configuration in an OIS adjacent to the OFP (DB_OIS). As can be seen in Figure 5.19, upon relaxation of the lattice there is a rearrangement not just of the helium atoms, but also of a lattice oxygen atom. The lattice oxygen atom migrates to the neighbouring oxygen vacancy, leaving a new vacancy in its place, which one of the helium atoms migrates to. This is a surprising result as it is the only example found thus far of a relaxation causing a lattice structural rearrangement. As found in Section 5.4.2, a dumbbell configuration of helium atoms is stable and suggested to form within PuO_2. Thus, it is suggested that if an OFP is generated in the vicinity of He in a dumbbell configuration, this rearrangement may occur and in this circumstance a helium will occupy an oxygen vacancy. It must be noted that this configuration has a higher energy (1.17 eV/He) than for two He in separate OIS (1.05 eV/He).

When investigating helium clustering in UO_2, Yun *et al.* [156] found that when

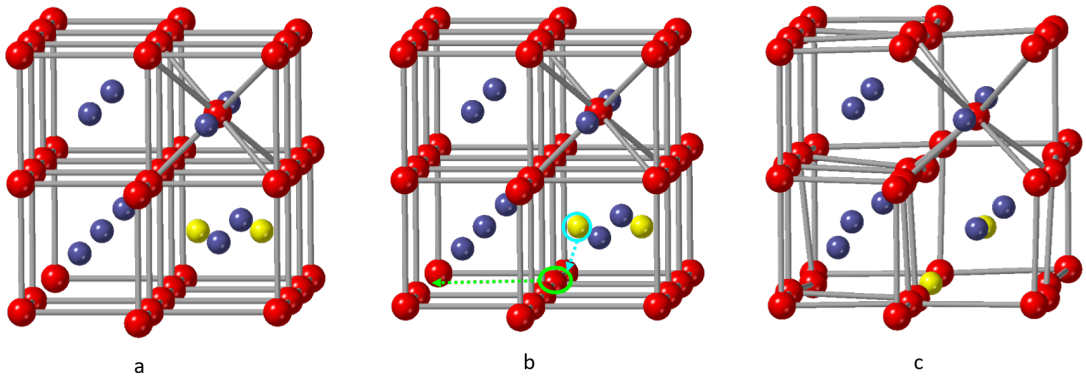


Figure 5.19: Graphic displaying two He atoms in a dumbbell configuration at an OIS by an oxygen Frenkel pair and the relaxation pathway: (a) displays the initial configuration, (b) displays the migration pathways, and (c) displays the relaxed configurations.

six He atoms surround an OIS in otherwise perfect PuO_2, upon relaxation lattice oxygen and uranium atoms are displaced. This displacement results in Frenkel pair formation and thus generates void space for He to cluster in. Unlike the findings of Yun *et al.* [156], aside from in the DB_OIS configuration, no such lattice ion rearrangement has been found in this work.

As was discussed in Section 3.5.0.3, whilst OFPs are a stable defect and predicted to be likely to form in PuO_2, the oxygen interstitial and vacancy must be separated by a lattice Pu to prevent recombination and so make the defect stable. It was therefore of interest to see if the inclusion of helium could prevent the recombination of other OFP configurations. The ′OFP3′ configuration was trialled, as is displayed in Figure 5.20a, upon relaxation this defect annihilates itself. It can be seen from Figure 5.20b that when a helium is input in the V_O site, although the oxygen interstitial migrates towards the V_O upon relaxation, the He atom remains in the vicinity and prevents the recombination of the OFP. This is a notable result, as it implies that the generation of He in PuO_2 results in the feasibility of more oxygen Frenkel pairs remaining after formation. This in turn means there may be more oxygen interstitials able to become mobile within the lattice. Furthermore, the inclusion of helium in the oxygen vacancy may lead to helium diffusion or further helium atoms clustering around the site.

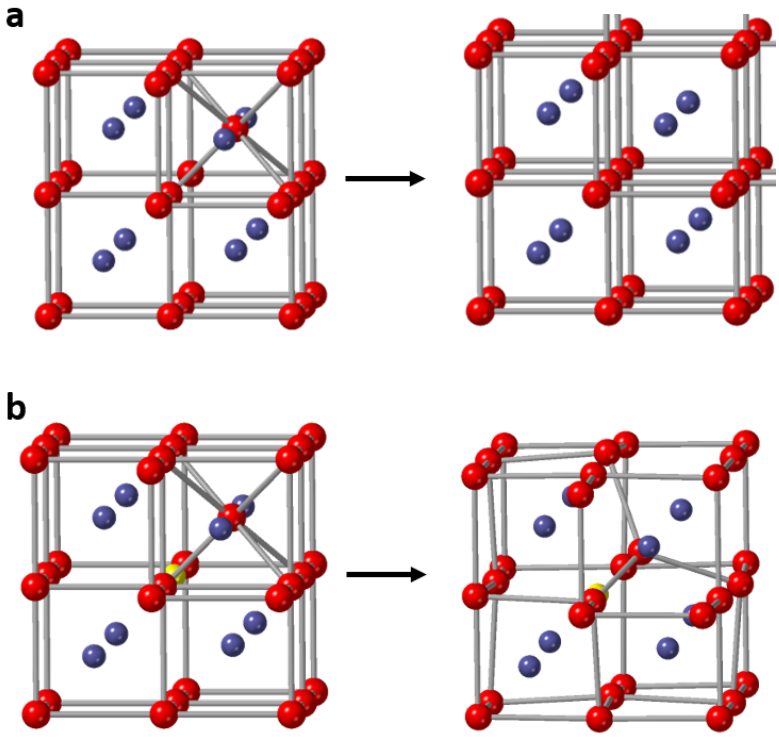


Figure 5.20: Graphic displaying OFP3 configuration. Figure (a) displays OFP before and after relaxation, the Frenkel pair recombines. Figure (b) has a He atom accommodating the oxygen vacancy site which prevents the recombination of the OFP.

The build up of helium atoms surrounding OFP3 displayed the same behaviour as for the initial OFP; no clustering was observed to be energetically favourable. The configurations of helium and OFP3 can be viewed in Table A.7.1. However, configurations considered in which no helium occupied the oxygen vacancy site resulted in the oxygen Frenkel pair recombining upon relaxation.

5.5.2.5 Incorporation Energies

For each defect site considered excluding OFP3, Figure 5.21 shows the calculated normalised incorporation energy when the He atoms were input in separate neighbouring OISs. The most notable finding from Figure 5.21 is the distinction between incorporation energies of purely oxygen related defects and plutonium related defects. The oxygen defects (V_O and OFP) display a roughly linear energy of 1.06 eV, regardless of how many helium atoms are in the simulation. However, for the plutonium related defects the incorporation energy for one He is negative, meaning the lattice is energetically more stable when He occupies the defect site than when

it is vacant. Between two and six helium atoms the incorporation is roughly 0.2 eV for all defects (V_{Pu}, PuFP, Schottky and Divacancy), then begins to increase for the remainder of the graph. It is therefore evident that He aggregation is favourable when a V_{Pu} is present.

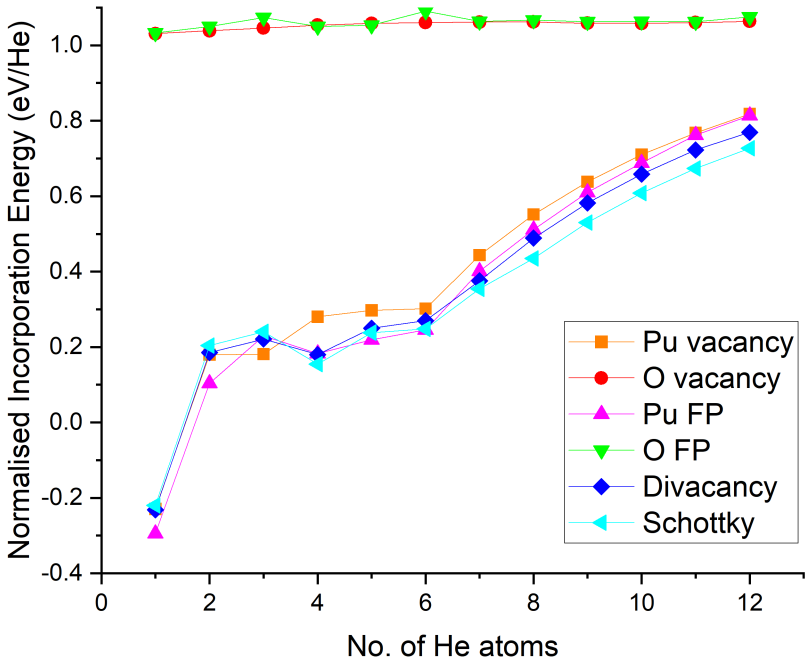


Figure 5.21: Normalised incorporation energy of He at various defect sites for up to 12 He atoms.

It was of interest to find at which point it is no longer favourable for a He atom to join a cluster of He atoms surrounding a defect. To find this, the successive incorporation energy was calculated. When the energy exceeds the 1.06 eV (illustrated by the dashed line in Figure 5.22) it requires more energy for the He atom to join the cluster than to remain isolated in an OIS. For a V_{Pu} and a PuFP this point was determined to be seven He atoms, for the divacancy eight He and for the Schottky trio nine He. This suggests that for each V_{Pu} there is an energetic preference for up to six He to aggregate at it, and another He can occupy the site for each V_O that is present. If N_{He} is the number of He atoms, and n and m are the number of V_{Pu} and V_O respectively, then it is no longer energetically favourable for additional He atoms to join a cluster when $N_{He} > 6m + n$.

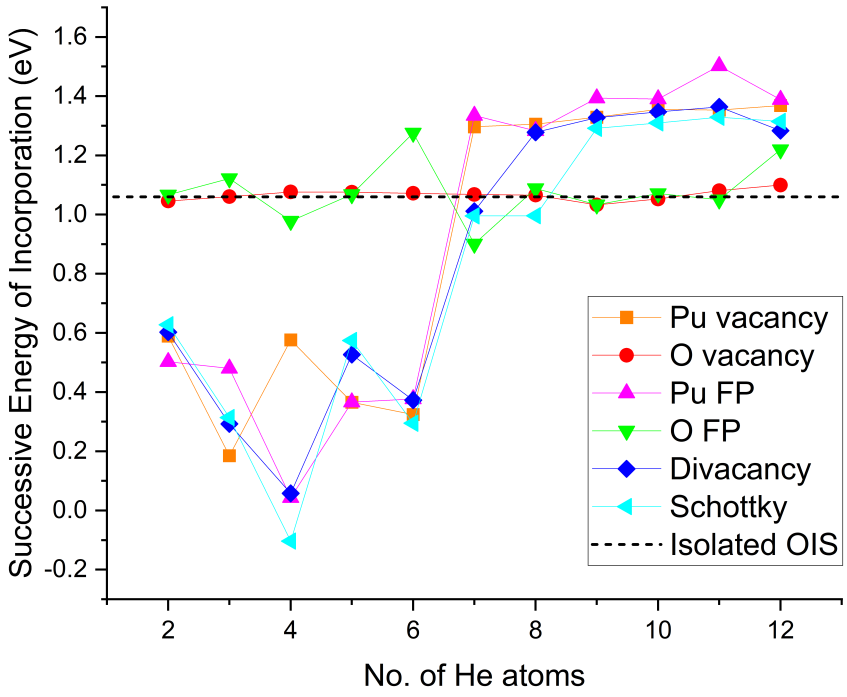


Figure 5.22: Successive energy of incorporation of Helium at defect sites. Black dashed line at 1.06 eV is the incorporation energy of He at an isolated OIS for comparison.

5.6 Conclusions

Atomistic simulations have been employed to study the incorporation of helium in PuO_2. The Buckingham potential was found to provide an excellent fit with the Dremov potential and is suitable for use in modelling He—He and Pu—He interactions.

Helium was fixed at an array of interstitial positions across the PuO_2 fluorite lattice and it was found that inclusion at the OIS has the lowest incorporation energy. Therefore helium is most likely to occupy an OIS in defect-free PuO_2. Helium incorporation at Pu vacancies was found to have a negative trapping energy, so there is an energetic drive for helium to migrate to Pu vacancy sites, and be sequestered there. However, there is a high defect energy associated with the formation of plutonium vacancies, so the trap sites may not be particularly prevalent within PuO_2. This is in agreement with the literature [132].

In Chapter 4 it was found that there is an energetic drive for PuFPs to migrate to PuO_2 surfaces. As plutonium vacancies are favourable sites for helium incorporation, this could imply an energetic drive for helium to migrate to PuO_2 surfaces

to become trapped at plutonium vacancy sites, each of which are predicted to be able accommodate up to six helium atoms.

He atoms will form clusters surrounding defects with a V_{Pu}, such as a Schottky trio. No clustering was observed when only an V_O or OFP was present. The maximum energetically favourable size of the cluster is $6m + n$ where m and n are number of V_{Pu} and V_O respectively. As Schottky trio defects are both energetically stable defects within the lattice, and energetically favourable for helium to occupy, it is predicted that Schottky trio defects are a likely seed location of the nucleation of helium clusters.

Chapter 6

Molecular Dynamics of Plutonium Dioxide

After evaluating suitable interatomic potentials for use in molecular dynamics, this chapter explores oxygen and plutonium diffusion in PuO_2 over a range of temperatures and time periods.

6.1 Literature Review

Molecular dynamics simulations enable temperature effects to be considered in the study of PuO_2 over time scales of the order of nanoseconds. Just in the last twenty years the capabilities have increased rapidly due to the increasing computational abilities and more widely available HPC facilities. In 2000, Yamada *et al.* [165] performed a study of a 3x3x3 PuO_2 supercell containing 324 atoms for 6 ps in which the variations of specific heat and thermal conductivity with temperature were calculated and were found to be in good agreement with experimental data. More recently in 2018, studies of 70x70x70 PuO_2 supercells containing millions of atoms have been performed by Balboa *et al.* [166] for 100 ps to study collision cascades. Such rapid expansion of computational abilities truly captures the exponential and continuing growth of the field of computational chemistry.

There have been multiple interatomic potentials used and developed specifically for molecular dynamics studies of PuO_2. The Arima *et al.* [111] potentials have been implemented by many authors, for example in the study of thermal conductivities of PuO_2 by Mingjie *et al.* [167]. More recently Cooper *et al.* [122] published a many-body potential with updated parameters to more accurately reproduce the melting point of PuO_2. The Cooper potential has also been implemented widely

by many authors, for example by Rahman *et al.* [168] in their study of primary radiation damage in PuO_2 and by Wang *et al.* [121] in their investigation of the kinetics of point defects in PuO_2.

Many of the molecular dynamics studies of PuO_2 have focused on the oxygen self-diffusion within the lattice. Via NEB calculations Wang *et al.* [121] found that oxygen point defects have a much higher mobility than plutonium defects. In agreement with this, all available studies find oxygen diffusion to be significantly higher than plutonium diffusion within PuO_2 [121], [122], [169]. Fast anion diffusion in comparison to cation diffusion is found in many other fluorite structured compounds such as YSZ, CaF_2, SrF_2, and CeO_2 [129], [170]. Via molecular dynamic simulations of YSZ, Lau *et al.* [171], Aidhy *et al.* [109], and Kilo *et al.* [172] found the anions to be highly mobile, whilst the cations were slow moving. From inspection of local lattice structures in NEB studies of anion and cation migration in YSZ, Dong *et al.* [129] suggests the reason for the higher anion mobility in comparison to the cation mobility in fluorite systems may be due to the fluorite structure being much more open for anion migration than for cation migration.

As noted by Kato *et al.* [173], experimental high temperature PuO_2 data are limited so there are shortcomings in discussing high temperature diffusion. However, some experimental studies of diffusion in PuO_2 are available. Gas-phase isotope exchange was used by Deaton *et al.* [174] and Bayoglu *et al.* [175] to calculate oxygen diffusion activation energies in stoichiometric PuO_2 of 177 and 187 kJ mol^{-1} respectively. These values are in good agreement with those calculated theoretically via molecular dynamics studies by Cooper *et al.* [122].

Studies of diffusion in PuO_2 are often performed on MOX fuel. Computational studies of $(U_{0.8},Pu_{0.2})O_2$ at 2500 K by Yamada *et al.* [165] found that the oxygen ions were mobile and the cations showed no diffusive behaviour. Cooper *et al.* [122] studied a range of MOX fuel compositions and found that oxygen diffusivity increases as the plutonium composition increases in $(U_x,Pu_{1-x})O_2$. Rahman *et al.* [168] employed the Cooper potential to investigate collision cascades in PuO_2, finding that the number of residual defects in PuO_2 is higher than in MOX and UO_2. It is suggested that the presence of additional defects due to higher Pu content may lead to the higher diffusivity of oxygen in MOX than in UO_2. From this it is therefore suggested oxygen diffusivity may be even higher in PuO_2 [176] [177].

6.2 Potential Evaluation

It was required to establish which potential model was the most suitable for use in molecular dynamics simulations. Although the Read potential was found to be the most suitable for use in static simulations (Section 3.2.3), it is well known that core-shell models perform poorly in molecular dynamics [113]. The potentials considered were the Read [49], Cooper [122], and Arima [111] potentials; all of which were described in Chapter 3. The Cooper and Arima potentials were specifically developed for use in molecular dynamics simulations.

6.2.1 *Lattice Parameter*

The lattice parameter (L_{param}) was calculated over a range of temperatures to evaluate which potential could best replicate the experimental temperature expansion data of Yamashita *et al.* [178].

First, it was required to determine what size supercell to use, as a larger system is more accurate, but require increased processing time. As such, there is a trade off between computational accuracy and processing demands. A 2x2x2 system was set up from experimental atomic data [124]. This system was then replicated in OVITO in three-dimensions to generate larger lattices up to 10x10x10. Each system was run for 1 ns at 1000 K and the average lattice parameter calculated. As can be seen in Table 6.1, the standard deviation decreased as the system size increased. However, the increase in computational demands for the 10x10x10 supercell was considered inordinate for the slight decrease in standard deviation. Due to this, it was determined that the 6x6x6 supercell was suitable for the work detailed in this chapter.

Table 6.1: Lattice parameter as a function of the PuO_2 supercell size for 1 ns simulations at 1000 K

Supercell Size	No. Atoms	L_{param} ($\AA$)	σ
2x2x2	96	5.438755	0.017347
4x4x4	768	5.436541	0.009991
6x6x6	2592	5.431079	0.003779
8x8x8	6144	5.43198	0.002638
10x10x10	12000	5.435528	0.001923

For each potential in turn, molecular dynamics was run on the 6x6x6 supercell for 1 ns in 100 K intervals between 300-2000 K. At each temperature the average lattice

parameter was calculated and the results were then compared with experimental data from Yamashita *et al.* [178] as displayed by Figure 6.1.

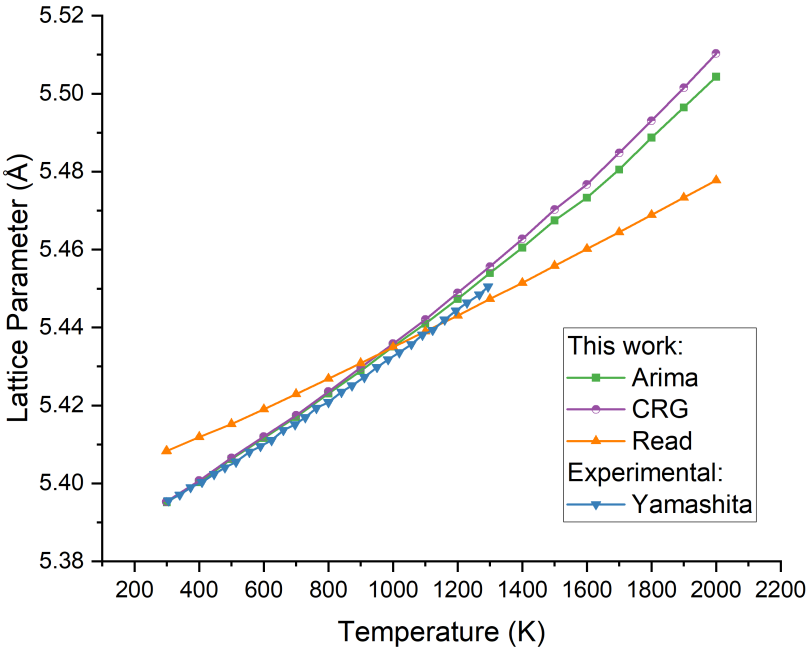


Figure 6.1: Lattice parameter as a function of temperature for three different interatomic potentials in comparison to experimental data of PuO_2.

From Figure 6.1 it can be seen that the Read potential provides the poorest agreement with experimental data and as such it will not be used for our molecular dynamics simulations. This poor performance is likely due to it being a core-shell model which is not suited to molecular dynamic modelling. Both the Cooper and Arima potential perform well, with them both generating lattice parameters closely aligned to the experimental data.

Balboa *et al.* [166] performed further detailed analysis of both the Arima and Cooper potential, including assessment of their performance in calculating structural, thermodynamic and mechanical properties. In their detailed evaluation they find the Cooper potential to have the overall best performance as the Arima potential fails to produce the expected phase transition above 2100 K. As such, throughout all LAMMPS molecular dynamics studies presented in this work the Cooper potential will be used to model PuO_2.

6.2.2 *Defect Calculations*

To evaluate the performance of the Cooper potential, intrinsic defect calculations were performed. The calculated defect energies were evaluated against the values calculated in Section 3.6. First, energy minimisation was performed on a pure PuO_2 lattice. Next, defects were generated and then a conjugate gradient energy minimisation process was performed. The difference in energy between the pure lattice and the lattice containing the defect was equal to the defect energy, E_d.

The three Schottky configurations considered in Chapter 3 were again considered here with configurations Sch.1, Sch.2 and Sch.3 having defect energies of 1.59, 1.66 and 1.95 eV respectively. Therefore, the configuration with the lowest defect energy and thus most likely to form is Schottky configuration Sch.1, which is in agreement with the calculations detailed in Chapter 3.

Table 6.2: Intrinsic defect energies in PuO_2 calculated in LAMMPS

Defect	E_d (eV/Defect)
OFP	2.47
PuFP	4.75
Schottky	1.59

Table 6.2 displays the results of the defect calculations. It should be noted that it was challenging to calculate a value for OFP, due to the majority of the configurations recombining. The oxygen interstitial and oxygen vacancy had to be separated by multiple lattice ions to prevent recombination. It was found that the order of stability of intrinsic defects within PuO_2 is Schottky < OFP < PuFP. This is in agreement with the results included in Chapter 3, and thus in agreement with the available literature. The reproduction of this finding again gives confidence in the use of the Cooper potential for further simulations.

6.3 Diffusion in PuO_2

The diffusion of oxygen and plutonium in PuO_2 was investigated over a range of temperatures. First, a pure PuO_2 lattice was considered. Molecular dynamics calculations were run on a 6x6x6 PuO_2 supercell for 1.5 ns with an initial 0.5 ns equilibriation period every 100 K between 1000-3000 K. The MSD of the atoms was calculated every 0.1 ps and plotted against time. A linear line of best fit was plotted after the equilibration period had elapsed as displayed in Figure 6.2.

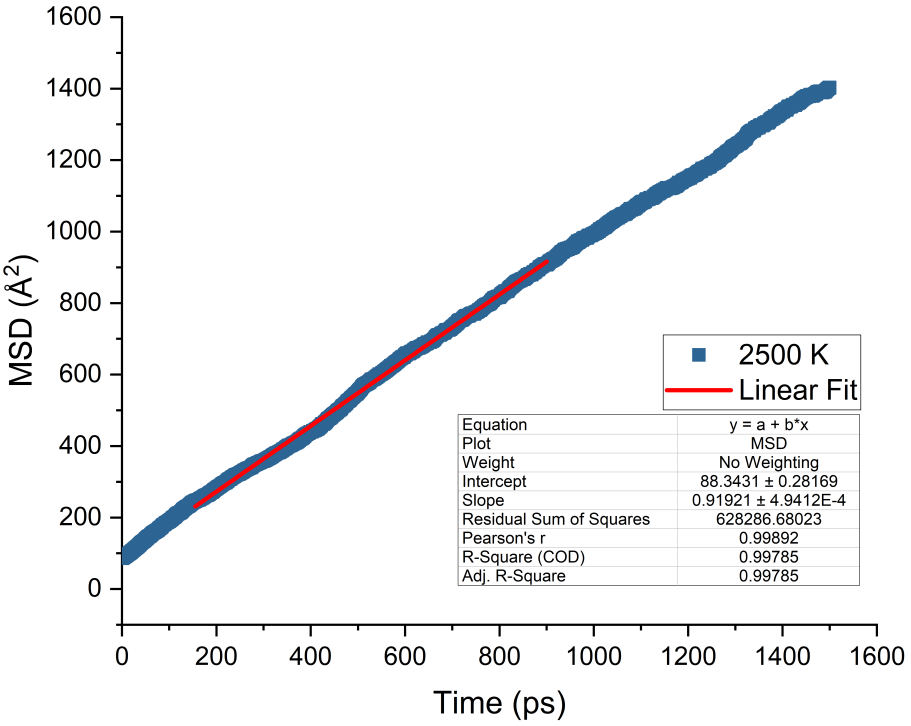


Figure 6.2: MSD versus time for oxygen at 2500 K in PuO_2. The red line indicates the linear line of best fit, with the fit details displayed.

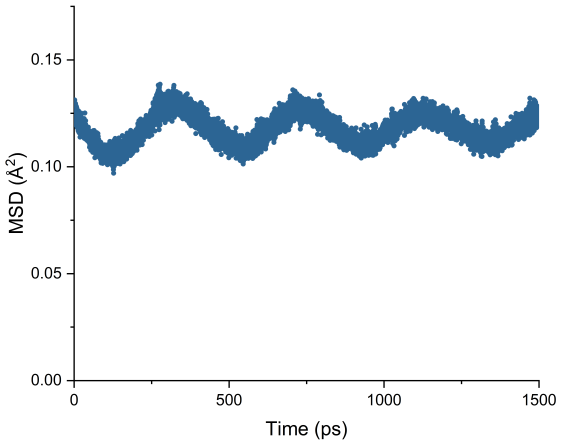
The gradient of the line was calculated and from this the diffusivity, D, was calculated via [179],

$$D = \frac{< R^2 >}{6t}. \tag{6.1}$$

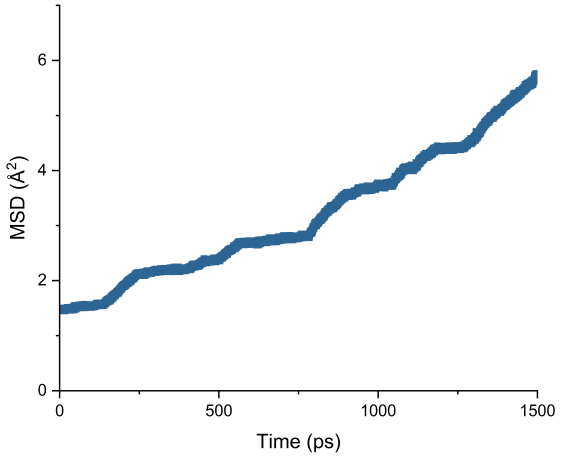
From Figure 6.2, the calculated gradient was 0.9192 ± 4.9412 x10^{-4}. Using Equation 6.1 this value was then divided by six to result in a calculated diffusivity value of 0.1532 x 10^{-4} ± 0.8235 x 10^{-4} Å^2 ps^{-1}. The diffusivity values would then be multiplied by a factor of 1x10^4 to result in units of cm^2 s^{-1} and plotted logarithmically against $\frac{1}{T}$.

Figures 6.3 and 6.4 display the MSD of oxygen and plutonium respectively, at a 1200 K, b 2000 K, and c 2700 K.

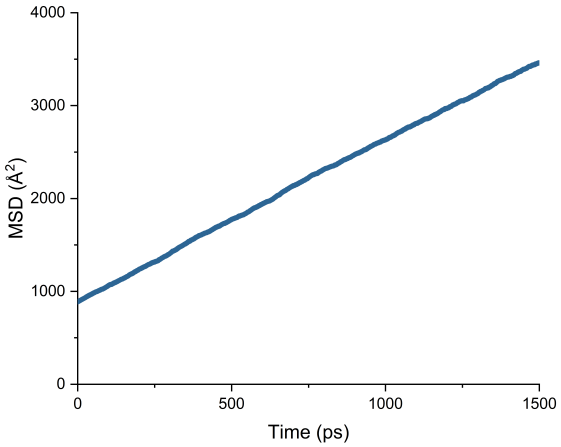
From both Figures 6.3a and 6.4a it is evident that at 1200 K, neither oxygen or plutonium exhibit diffusive behaviour, instead the atoms are simply vibrating about their lattice sites with the MSD not exceeding 0.2. The fluctuations in displacement of both oxygen and plutonium corresponds with the natural volume variation of the simulation cell as displayed in Figure 6.5.



(a) 1200 K.

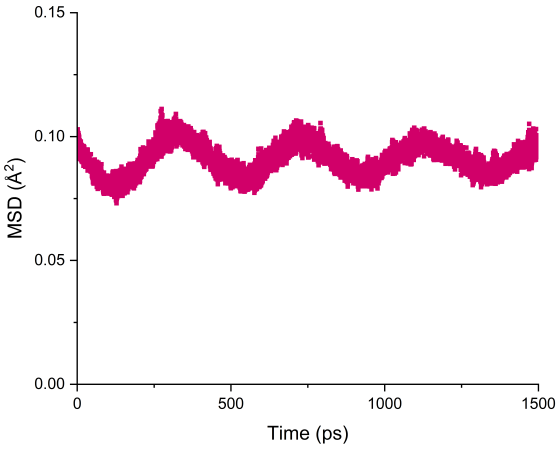


(b) 2000 K.

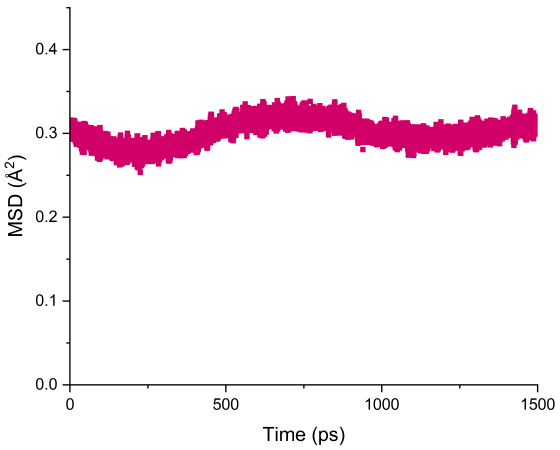


(c) 2700 K.

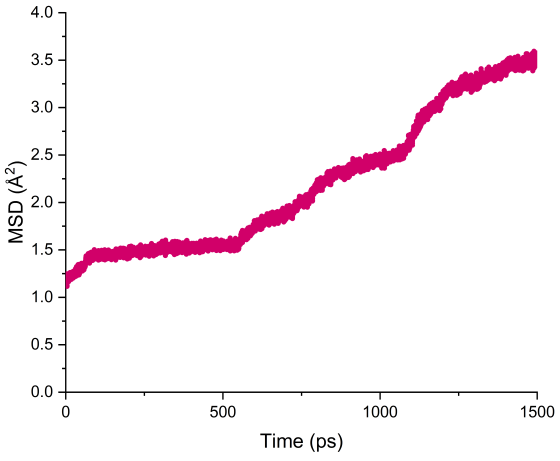
Figure 6.3: Oxygen MSD in PuO_2 at three temperatures.



(a) 1200 K.



(b) 2000 K.



(c) 2700 K.

Figure 6.4: Plutonium MSD in PuO_2 at three temperatures.

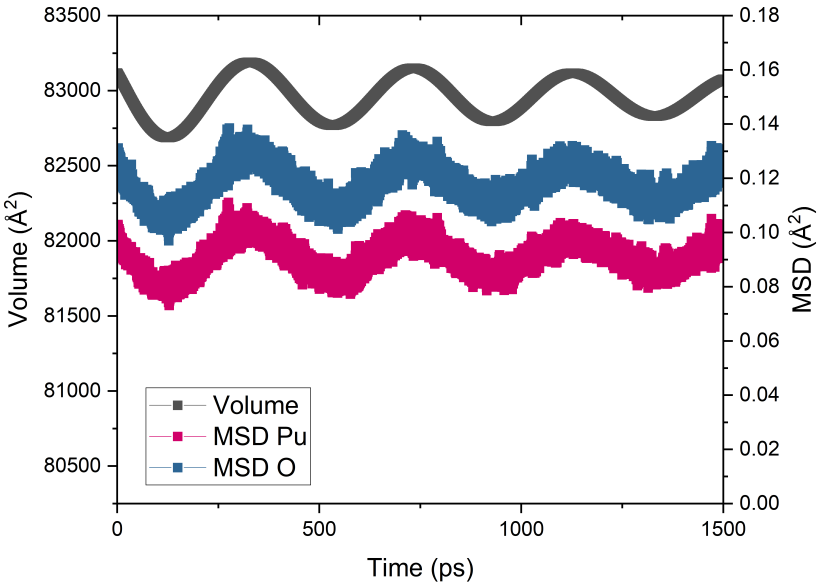


Figure 6.5: The volume variation of the simulation cell, and the Pu and O mean squared displacements as a function of time at 1200 K.

At 2000 K, oxygen begins to exhibit diffusive behaviour as can be seen from the increasing MSD in Figure 6.3b. However, as can be seen from Figure 6.4b, plutonium atoms exhibit no diffusive behaviour at 2000 K; they remain vibrating at their lattice sites. The MSD plots at 2000 K are comparable to those of Pu and O in $(U_{0.8},Pu_{0.2})O_2$ simulated by Yamada *et al.* [165] at 2500 K, and of O in PuO_2 by Yu *et al.* [112]. Finally, it can be seen from Figures 6.3c and 6.4c that at 2700 K both oxygen and plutonium have enough energy to exhibit diffusive behaviour. The MSD of plutonium at 2700 K after 1.5 ns is several orders of magnitude lower than that of oxygen, indicating that plutonium is still much less mobile than oxygen at 2700 K.

The calculated diffusivities of oxygen and plutonium at each temperature are plotted in Figure 6.6. The diffusivities were plotted logarithmically against $\frac{1}{T}$ to enable the calculation of the diffusion activation energy, E_a, from the gradient via the Arrhenius equation,

$$\ln D = -\left(\frac{E_a}{k_B T}\right) + \ln D_0, \tag{6.2}$$

where D_0 is the pre-exponential factor. As such, regions in Figure 6.6 of constant gradient, and thus activation energy, indicate temperature regimes with a common diffusion mechanism.

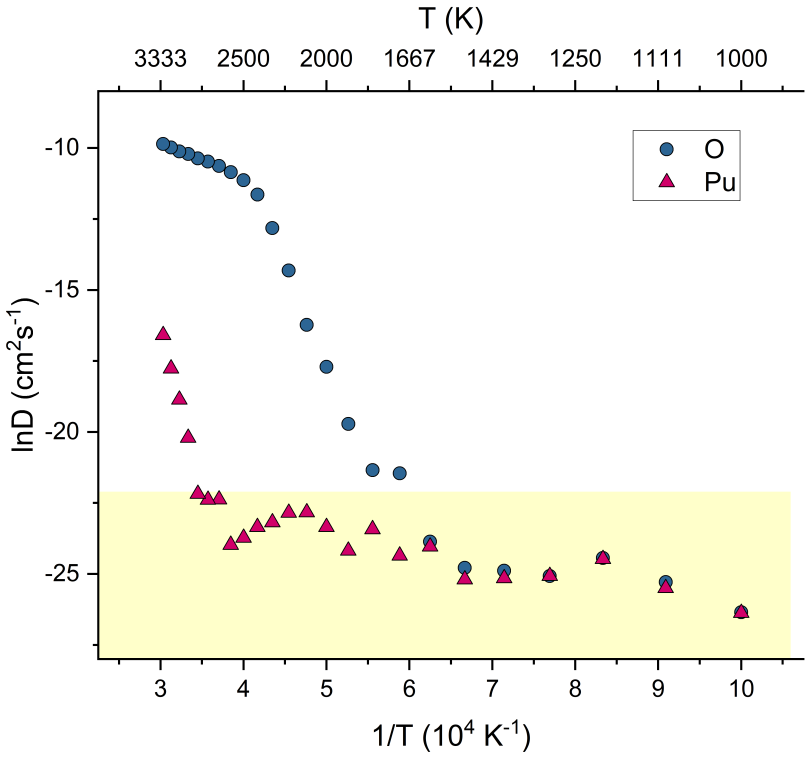


Figure 6.6: Oxygen and plutonium diffusivity as a function of temperature in PuO_2. The yellow region indicates no diffusive behaviour.

Three regions of interest can be identified in Figure 6.6:

- **R1 (1000 - 1500 K):** no diffusive behaviour, both O and Pu are simply vibrating about their lattice sites
- **R2 (1500 - 2400 K):** O exhibits diffusive behaviour, Pu remains at lattice sites
- **R3 (> 2400 K):** O exhibits diffusive behaviour, Pu becomes mobile

Two regions of constant gradient can be identified in Figure 6.6 for oxygen corresponding to R2 and R3. These two regions were expected due to the phase transition of oxygen at approximately 0.8 T_m as discussed by Günay *et al.* [180] and Cooper *et al.* [113]. By fitting a line of best fit to region R2 and R3, the diffusion activation energies were calculated to be 6.18 eV in R2 and 1.07 eV in R3 which are comparable to the values calculated by Cooper *et al.* [122]. Deaton *et al.* [174] and Bayoglu *et al.* [175] used gas-phase isotope exchange to calculate oxygen diffusion activation

energies in stoichiometric PuO_2 of 1.83 and 1.94 eV respectively. Although these values are lower than the values calculated in this work, PuO_2 will not exist in a pure form due to radioactive decay events which result in defect generation. The presence of defects may reduce the oxygen activation energy as will be discussed in the following section.

It is evident that plutonium diffusivity is much lower than oxygen diffusivity, which is as expected from analysis of the MSD plots at three temperatures. At temperatures approaching the melting point of PuO_2 (R3), Pu exhibits some diffusive behaviour. Below 2700 K, the Pu ions are simply vibrating about their lattice sites. Due to the high temperatures required for Pu diffusion, no experimental data of Pu diffusion in PuO_2 is available in the literature. Riemer *et al.* [181] investigated Pu diffusion in hypostoichiometric MOX fuel, finding that similarly to U in UO_2 [182], increasing hypostoichiometry increases cation diffusivity. A detailed summary of the available literature of U diffusion in UO_2 is provided by Boyarchenkov *et al.* [183].

Unlike plutonium diffusion, there has been much investigation of oxygen diffusivity in PuO_2 both theoretically [121], [122], [169] and experimentally [174], [175], [184]. Figure 6.7 plots the available oxygen diffusivity data from the literature. It can be seen that the diffusivities calculated in this work are in good agreement with available data. The diffusivities are almost identical to those calculated by Cooper *et al.* [122], due to the same potentials being used.

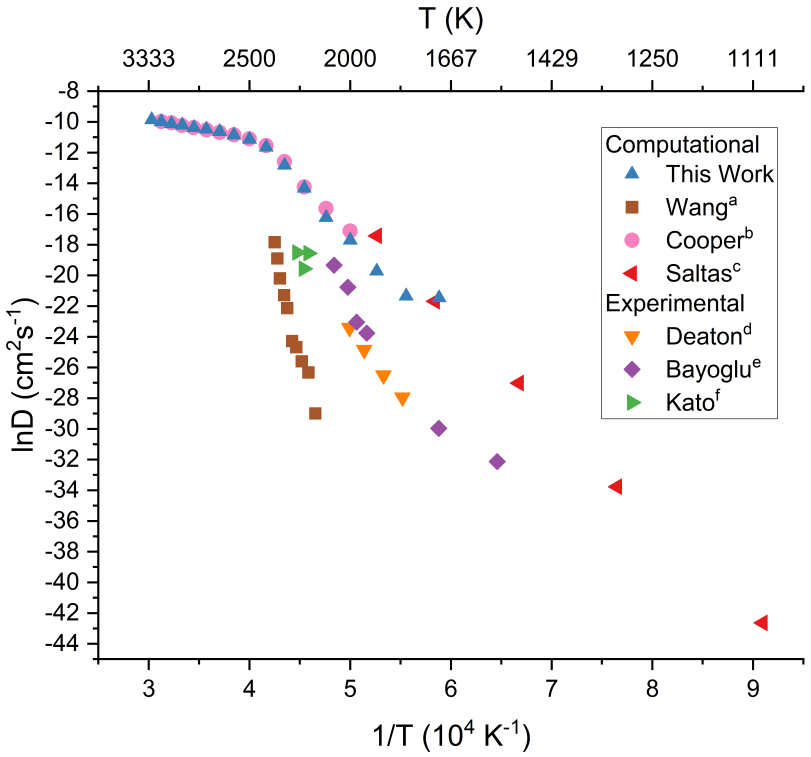


Figure 6.7: Oxygen diffusivity as a function of temperature in PuO_2 by this work and available data [a][121], [b][122], [c][169], [d][174], [e][175], [f][184].

It was of interest to analyse the number of vacancies present in the lattice throughout the simulation. Figure 6.8 plots the number of vacancies in the lattice every 50 ps for three high temperature simulations (2500, 2700 and 2900 K). It can be seen from Figure 6.8 that the length of the simulation has no correspondence with the number of defects. There is fluctuation in the number of vacancies during the simulation due to the ongoing thermal generation and annihilation of Frenkel pairs. It is likely that the MSD and therefore calculated diffusivity are impacted by the number of vacancies in the system. This is due to the fact that when vacancies are in the system, there will be displaced atoms which may be mobile, or other atoms may use a vacancies to assist in inter-site hops. Thus, the fluctuation in the number of defects in the lattice, may correspond to fluctuations in MSD during the simulation.

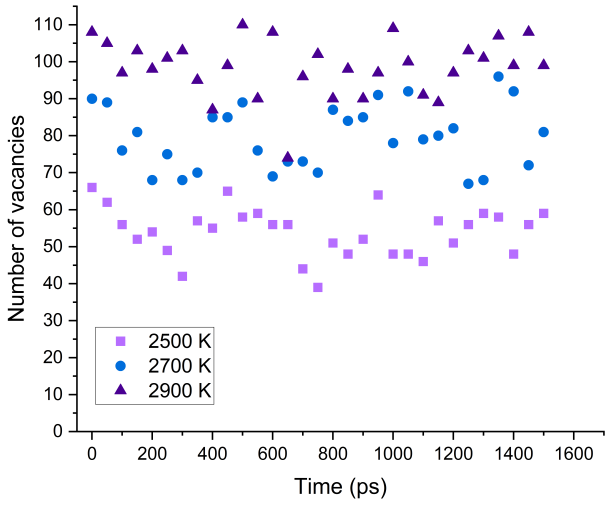


Figure 6.8: Number of vacancies within the system as a function of simulation time for three temperatures: 2700 K, 2800 K, and 2900 K.

6.4 Diffusion in Defective PuO_2

PuO_2 will not exist as a perfect lattice structure. Rather, intrinsic defects generated during collision cascades following decay events will be present [115]. Schottky trio defects were generated to simulate a defective lattice, as Schottky trios were calculated to have the lowest defect energy in PuO_2 (Table 6.2). Three concentrations of Schottky trios were considered corresponding to expected defect levels within stored PuO_2 [53]. Table 6.3 displays the three Schottky concentrations considered along with the number of Pu and O vacancies each comprised.

For each Schottky concentration, three lattices were generated. Each lattice was composed of different Schottky trio distributions via random elimination of oxygen and plutonium atoms in quantities corresponding to Table 6.3. The lattices were minimised and during the minimisation it was found that the vacancies tend to

Table 6.3: The three Shottky concentrations considered and the number of constituent Pu and O vacancies

Schottky Concentration	Number of V_{Pu}	V_O
0.50%	4	8
2.0%	17	34
4.0%	34	68

cluster to form small void areas, analysis of which is plotted in Figure 6.9.

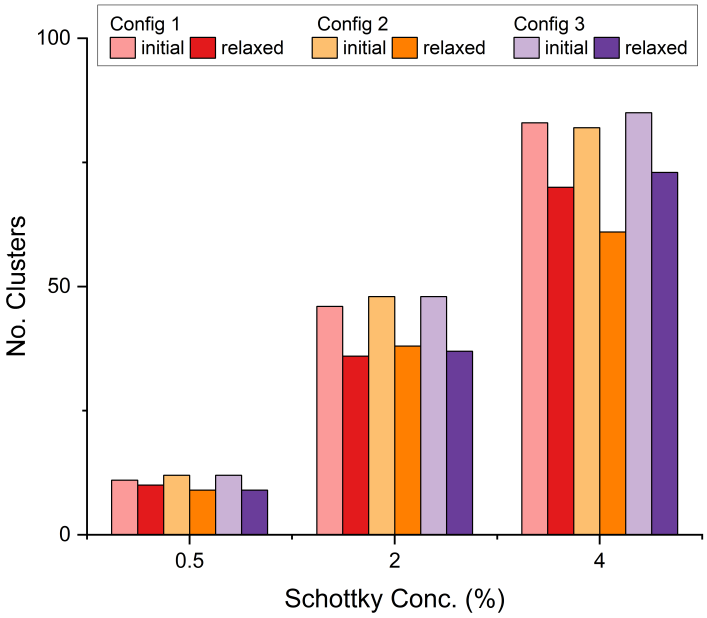


Figure 6.9: Number of clusters before and after energy minimisation (performed at 0 K) for three configurations of lattices containing 0.5, 2 and 4% Schottky trios.

Figure 6.9 displays the results from cluster analysis of the vacancies in each lattice before and after energy minimisation. A lower number of clusters means that some of the vacancies have clustered together. In all cases it was found that after relaxation the number of clusters decreased. Additionally, similar clustering behaviour was found for each configuration. This clustering behaviour could suggest that voids may be present in PuO_2, which could be available as cluster nucleation sites for radiogenic helium.

Molecular dynamics calculations were then run for each lattice over a range of temperatures between 1700-3500 K in 100 K intervals. The diffusivities at each temperature were calculated for each Schottky configuration and the results averaged. Figures 6.10 and 6.11 display the diffusivities for oxygen and plutonium respectively.

From Figure 6.10 it can be seen that the inclusion of defects within PuO_2 increases the diffusivity of oxygen below 2300 K (below the oxygen phase transition). When Schottky defects are present in the lattice oxygen exhibits diffusion at temperatures that in the initially defect free lattice no diffusion was exhibited (yellow highlight in Figure 6.10). This result is in accordance with findings by Wang *et al.* [121], who found that increases in defect concentrations significantly increase

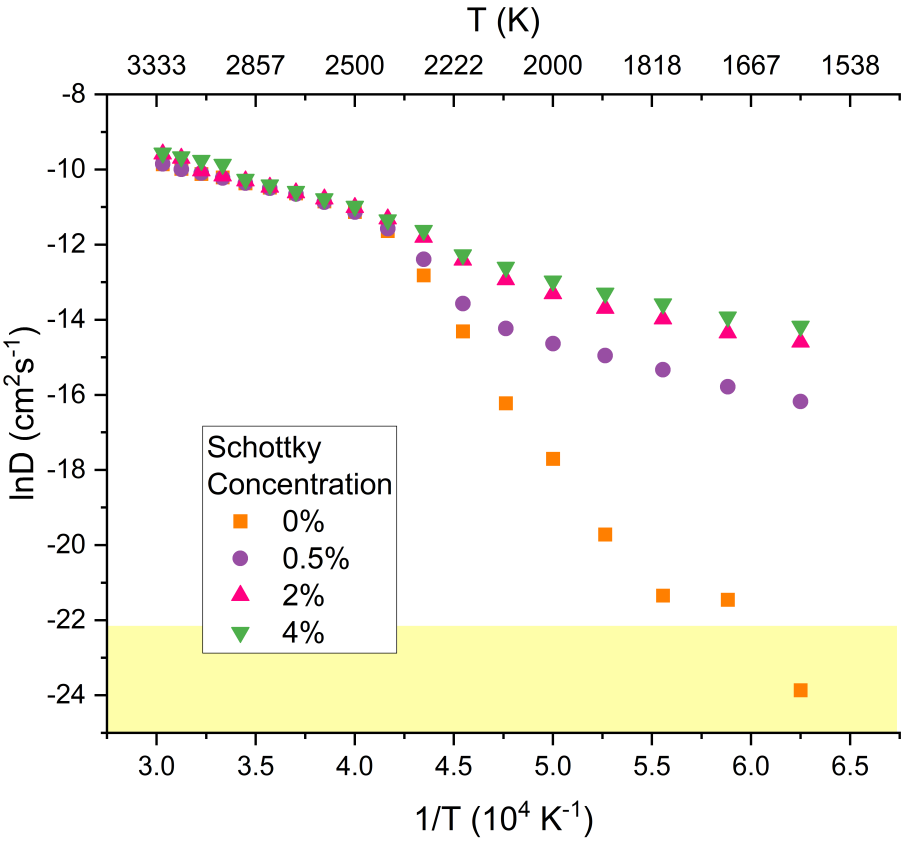


Figure 6.10: Oxygen diffusivity as a function of temperature in PuO_2 with increasing concentrations of Schottky defects. The yellow highlight indicates lnD values that correspond to no diffusion.

oxygen diffusivity. Above 2300 K in all considered lattices oxygen displays near identical diffusivity. From this, it is predicted that in the high temperature region the dominating factor is the phase change, rather than the inclusion of vacancies.

It can be seen from Figure 6.11 that plutonium diffusivity increases when vacancies are present. There is limited increase in diffusivity with higher vacancy concentrations. Above 3000 K, Pu begins to exhibit increased diffusive behaviour as found by Wang *et al.* [121] for PuO_2 and Günay *et al.* [180] for UO_2. Such high temperatures are when the lattice is melting and so the lattice becomes amorphous leading to Pu becoming fully mobile.

The diffusion activation energies were calculated via the Arrhenius equation for oxygen in each Schottky concentration. As the Arrhenius equation applies to temperature intervals in which there is a constant gradient, the calculations were per-

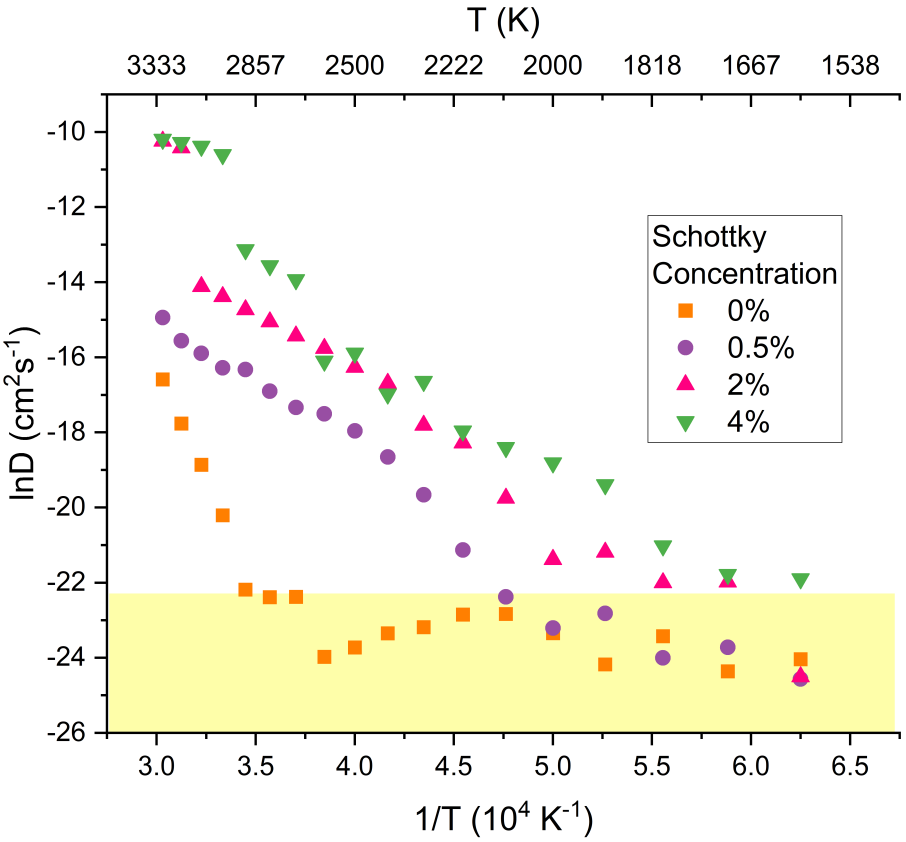


Figure 6.11: Plutonium diffusivity as a function of temperature in PuO_2 with increasing concentrations of Schottky defects. The yellow highlight indicates lnD values that correspond to no diffusion.

formed in the R2 and R3 temperature intervals for oxygen diffusion, the outputs for which are included in Table 6.4a and 6.4b respectively. The diffusion pre-exponential factors were also calculated as displayed in Table 6.4 and are comparable to those calculated by Potashnikov *et al.* [185] for oxygen diffusion in UO_2.

As can be seen from Table 6.4a, when defects are in the system, the oxygen diffusion activation energy is reduced by approximately four fifths. The lower diffusion activation energy enables oxygen to have higher mobility at lower temperatures. The calculated diffusion activation energies in the R2 region when Schottky defects are present are now comparable to those calculated experimentally by Deaton *et al.* [174] and Bayoglu *et al.* [175]. This is likely due to PuO_2 samples containing defects, generated by radioactive decay events and their resultant collision cascades.

In the superionic temperature range (R3), the activation energies and diffusion

Table 6.4: Parameters calculated from Arrhenius behaviour exhibited by oxygen in PuO_2 in the mid and high temperature regimes (R2 and R3)

(a) R2 1700 - 2300 K

Schottky %	E_a (eV)	$D_0(cm^2s^{-1})$	r-square
0.0	6.15 ± 0.24	6.54E+07	0.99563
0.5	1.34 ± 0.13	1.22E-03	0.97110
2.0	1.21 ± 0.11	2.00E-02	0.97566
4.0	1.06 ± 0.06	1.15E-03	0.99047

(b) R3 2300 - 3500 K

Schottky %	E_a (eV)	$D_0(cm^2s^{-1})$	r-square
0.0	1.23 ± 0.10	4.23E-03	0.96502
0.5	1.22 ± 0.07	3.97E-03	0.97844
2.0	1.24 ± 0.06	5.05E-03	0.98662
4.0	1.26 ± 0.08	5.54E-03	0.98797

pre-factors, as listed detailed in Table 6.4b, showed little variance with Schottky concentration. It is suggested that this is because oxygen is mobile regardless of defects at such high temperatures, due to it having gone through the phase transition to a superionic phase as discussed by Wang *et al.* [121].

Much work has been done investigating oxygen diffusion in MOX fuel. Wang *et al.* [121] found that the diffusion coefficients of oxygen in stoichiometric PuO_2 are significantly lower than those in non-stoichiometric PuO_2 across the whole temperature range studied. They therefore conclude that the diffusivity of oxygen atoms in PuO_2 greatly depends on the presence of defects with higher defect concentrations enhancing oxygen diffusion, as has been found in this work.

Figure 6.12 shows the trajectory of oxygen and plutonium at 1700 K with 2% Schottky concentration, for clarity only six randomly selected oxygen ions trajectories are displayed. The results show that the plutonium ions remain at their sites, simply vibrating at the lattice sites, whereas the oxygen ions have begun to make hops around the lattice.

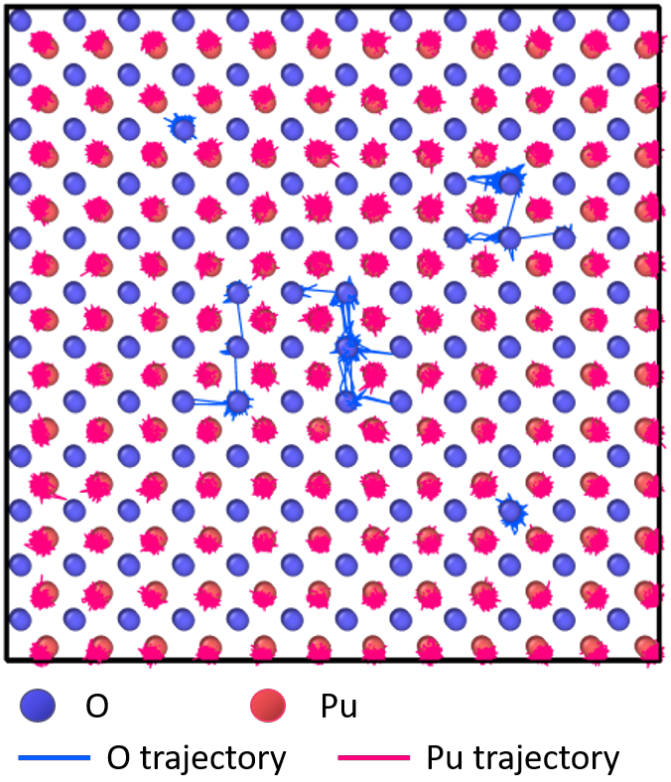


Figure 6.12: Trajectories of oxygen and plutonium ions in PuO_2 with a 2% Schottky concentration at 1700 K (only six O trajectories are displayed).

6.5 Conclusions

Three interatomic potentials were evaluated for use in modelling PuO_2 over a wide range of temperatures. The Cooper potential [122] was determined to most accurately reproduce experimental data.

It was found that oxygen has a much higher mobility than plutonium in PuO_2. This may be due to the formation energies of oxygen defects being lower than those of plutonium defects as was determined in Chapter 3, leading to lower energy barriers for migration. Additionally, as suggested by Dong *et al.* [129] when studying YSZ, the higher anion mobility in comparison to the cation mobility may be due to the fluorite structure itself, being more open for anion migration. The diffusivities calculated for PuO_2 are in good agreement with the literature values giving confidence in the use of the Cooper potential for continued studies of PuO_2. Furthermore, the finding of higher anion mobility than cation mobility is in good agreement with other fluorite systems such as YSZ [109], [129], [171].

The inclusion of Schottky defects significantly increases oxygen diffusivity in the

lower temperature regime (R1) whilst having little effect on plutonium diffusivity. Due to this, it is predicted that oxygen will be mobile within PuO_2 under storage conditions as intrinsic defects will be present, while plutonium will be mainly immobile.

Chapter 7

Helium Diffusion

This chapter presents studies of helium diffusion in PuO_2 over a range of temperatures, time periods, helium concentrations and defect concentrations. Some sections of this chapter have been published in:

E. Murray, Y. Zhou, P. Slater, R. Smith, P. Goddard, and H. Steele. "Atomistic Simulation of Helium Diffusion and Clustering in Plutonium Dioxide" *Physical Chemistry Chemical Physics*, vol. 24, pp. 20 709–20 720, 35 2022 [186].

7.1 Literature Review

Limited studies of helium diffusion in PuO_2 are available. Instead, comparison can be drawn from studies of helium in related nuclear fuel materials such as metallic Pu, UO_2 and MOX fuel. Luzzi *et al.* [187] provides a detailed review of helium diffusion behaviour in nuclear materials from data available from the literature.

Roudil *et al.* [188] reported that helium diffusion is negligible within the time and temperature range of long-term dry storage and geological disposal. In contrast, from the study of a 37 year old sample of $^{238}PuO_2$, Talip *et al.* [189] observed the opening of grain boundaries due to alpha radiation damage and release of a substantial fraction of the accumulated radiogenic helium.

At relatively low temperatures ($T < \sim 1300$ K) Talip *et al.* [189] found the dominant helium release mechanism in UO_2 to be atomic diffusion, in which only a small fraction of helium atoms are released via the diffusion of single helium atoms to grain boundaries. For temperatures between approximately 1300 and 1500 K, Talip *et al.* [189] found that the trapping of helium in bubbles and the diffusion of helium to grain boundaries occur at the same rate. Between approximately 1500

and 1600 K they found all helium atoms to be trapped by existing bubbles leading to increasing bubble growth. For the final temperature region studied by Talip *et al.* [189] (T > 1600 K), helium release was suggested to be due to the diffusion of helium bubbles to grain boundaries.

Helium migration in sintered UO_2 disks was studied by Guilbert *et al.* [190]. The disks contained a helium concentration of 0.2 at% introduced by ion implantation. Similarly to Talip *et al.* [189], they found helium to be mobile at temperatures as low as 873 K. However, in contrast to Talip *et al.* [189], Guilbert *et al.* [190] found the helium atoms would become trapped at implantation induced defects, rather than be released at grain boundaries.

As discussed by Garcia *et al.* [191] and El-Genk *et al.* [192], the discrepancy in published helium diffusivity data can likely be accredited to the differences in material microstructures, annealing conditions, techniques to introduce helium and the helium concentration in samples. However, despite the many differences in samples considered, three main trends have been identified within the literature.

The first conclusion which can be drawn from the literature is that increasing defect content in actinide dioxides leads to higher helium diffusivity at lower temperatures. It has frequently been found that experimental methods of helium addition to an actinide dioxide which lead to the generation of higher damage levels in the crystal lattice (e.g. doping), result in higher helium diffusivity values [188], [190], [191], [193], [194]. This is in comparison to methods such as helium infusion, which induce fewer defects in the crystal lattice and in turn lead to the finding of higher helium diffusion activation energies [195]–[198].

Secondly, helium diffusion has been found to be more favourable with increasing plutonium concentration. For example, helium diffusion has been found to have a lower diffusion activation energy in MOX samples than in UO_2 samples [199] [200]. Via release measurements carried out in a Knudsen-cell with an online mass spectrometer, Ronchi *et al.* [200] calculated the activation enthalpies of helium in a range of materials. The activation enthalpies calculated for PuO_2 and $(Pu_{0.1},U_{0.9})O_2$ were 1.73 and 2.02 eV respectively, with the activation enthalpy in UO_2 being significantly higher with a value of 2.99 eV. Similarly, Nakajima *et al.* [198] reported that they determined helium activation energies to be approximately 2 eV higher in UO_2 than in PuO_2.

Upon evaluation of the findings of Ronchi *et al.* [200] and the results of their nuclear reaction analysis experiments of radioactive samples, Pipon *et al.* [199] suggests that alpha self-irradiation enhances helium atomic diffusion due to the re-

sulting higher concentrations of defects. Thus, due to the higher radioactivity of plutonium, more radiogenic defects are generated in samples containing higher Pu concentrations, leading to higher helium diffusivities. This conclusion was thoroughly evaluated by Luzzi *et al.* [187] in their literature review and proven valid.

Finally, as concluded by Nakajima *et al.* [198], because increasing Pu content leads to increasing defect levels in the lattice, the trend of decreasing activation energies with increasing Pu content suggests the existence of a vacancy assisted helium diffusion mechanism in actinide dioxides. Specifically, oxygen vacancy assisted diffusion has been found to be a key mechanism for helium diffusion in UO_2 via DFT [156] [201] and MD simulations [202] [203].

Govers *et al.* [203] studied helium diffusion in UO_2 over a range of stochiometries. Their work found that in hypo-stoichiometric UO_2, the helium diffusion activation energy calculated was as low as 0.5 eV. Via NEB calculations they found this energy barrier corresponded to an oxygen vacancy assisted diffusion mechanism. Govers *et al.* [203] also found that in systems with no extrinsic oxygen vacancies (i.e. stoichiometric and hyperstoichiometric systems), oxygen vacancies would be generated at elevated temperatures and these used in helium diffusion pathways. Additionally, at high temperatures Govers *et al.* [203] found that direct jumps between octahedral sites was possible and occurred in addition to the oxygen vacancy assisted pathways.

Following on from the work of Govers *et al.* [203], Liu *et al.* [201] proposed a new diffusion mechanism of helium in UO_2; the asymmetric hop. In this mechanism the helium migrates OIS-OIS via an oxygen vacancy site, in which the oxygen is pushed away by the helium for the migration. Thus, helium diffusion is no longer rate limited by the oxygen vacancy migration steps in the asymmetric hop mechanism. Yakub [202] found similar possible pathways, however rather than an asymmetric hop, their work found the direct OIS-OIS migration to go via an occupied oxygen or uranium site. In agreement with Liu *et al.* [201], Yakub *et al.* [202] found the migration of helium atoms via vacancies to dominate at higher temperatures.

7.2 Helium Potential

To model helium in PuO_2 via molecular dynamical methods, the Cooper potential [113] was employed for the PuO_2 interactions (as discussed in Section 3.2.1.5). As detailed in Chapter 5 the Dremov potential [44] for He—He and Pu—He was fitted to a Buckingham potential for use in modelling helium in PuO_2 in static simulations. This set of helium potentials developed were trialled for molecular dynamics simula-

tions. However, it was found that helium atoms would migrate 'through' plutonium atoms, which is unphysical. It is suggested that this was because, as was found in Chapter 6, potentials developed for static simulations are frequently not robust enough for molecular dynamical simulations. As was discussed during the fitting procedure (Section 5.2), the unphysical attraction region was not used in the fitting routine. This region is required for robust simulations such as molecular dynamics. Therefore, a potential suitable for molecular dynamics simulations was required.

As suggested in Chapter 5 a ZBL splinning function is suitable as it is robust. The screened Coulomb ZBL potential [74] [204] was therefore used for the Pu—He interaction with inner and outer cutoff parameters of 4.5 and 5.5 for the ZBL region. The screened Coulomb ZBL potential is a standard that is generally used in most computer simulations with empirical potential calculations, as it has been fitted to a large data bank of experimental measurements. The ZBL function is as follows,

$$E_{ij}^{ZBL} = \frac{1}{4\pi\epsilon_0}\frac{Z_i Z_j e^2}{r_{ij}}\phi(r_{ij}/a) + S(r_{ij}), \tag{7.1}$$

where,

$$a = \frac{0.46850}{Z_i^{0.23} + Z_j^{0.23}}, \tag{7.2}$$

$$\begin{aligned}\phi(x) = 0.18175e^{-3.19980x} + 0.50986e^{-0.94229x} \\ +0.28022e^{-0.40290x} + 0.02817e^{-0.20162x},\end{aligned} \tag{7.3}$$

ϵ_0 is the electrical permittivity of the vacuum, e is the charge of an electron, and Z_i and Z_j are the charges of the two atoms [205]. $S(r)$ is a switching function which ramps the energy and force smoothly to zero between the inner and outer cutoff,

$$S(r) = \begin{cases} C & \text{if } r < r_1 \\ \frac{A}{3}(r-r_1)^3 + \frac{B}{4}(r-r_1)^4 + C & \text{if } r_1 < r < r_c, \end{cases} \tag{7.4}$$

where r_1 is the inner cutoff, r_c is the outer cutoff and coefficients A, B and C are computed by LAMMPS to perform the shifting and smoothing via [205],

$$A = (-3E'(r_c) + (r_c - r_1)E''(r_c))/(r_c - r_1)^2, \tag{7.5}$$

$$B = (2E'(r_c) - (r_c - r_1)E''(r_c))/(r_c - r_1)^3, \tag{7.6}$$

$$C = -E(r_c) + \frac{1}{2}(r_c - r_1)E'(r_c) - \frac{1}{12}(r_c - r_1)^2 E''(r_c). \tag{7.7}$$

For the He—He interaction, the Aziz potential [206] was used. This potential

was considered due to its use by Gai *et al.* [207] in their LAMMPS simulations of the interactions with irradiation of helium bubbles in bcc Fe. The Aziz potential has the Hartree-Fock-dispersion form [208] and is reported to have a good agreement with the *ab initio* results.

$$V(x) = \in \left(A \exp(-\alpha x + \beta r_{ij}^2 - F(x) \sum_{j=0}^{2} c_{2j+6}/x^{2j+6} \right), \tag{7.8}$$

where $\in$ is the Lennard-Jones energy parameter, $x = r_{ij}/r_m$, and

$$F(x) = \begin{cases} \exp\left[-(\frac{D}{x} - 1)^2 \right] & \text{if } x < D \\ 1 & \text{if } x \geq D. \end{cases} \tag{7.9}$$

Table 7.1 displays the parameters used for the potential as developed by Aziz *et al.* [206].

Table 7.1: Parameters of the Aziz potential to describe the He—He interaction [161]

Parameter	Value
A	1.86924404E+5
α	10.571754
c_6	1.35186623
c_8	0.41495143
c_{10}	0.17151143
β (Å^{-2})	-2.358
D (Å)	1.438
e (eV)	9.441093E-4
r_m (Å)	0.2968

The He—O LJ potential of Parfitt *et al.* [209] was employed in this work with parameters of $\epsilon = 1.5386 \times 10^{-2}$ eV and $\sigma = 0.24000$ nm. This potential was developed for use in molecular dynamics simulations and its parameters were derived from Hartree-Fock calculations of Grimes *et al.* [158].

7.2.1 *Helium Incorporation*

Via energy minimisation calculations in an 8x8x8 PuO_2 supercell, helium incorporation at an OIS was found to have an incorporation energy of 1.7 eV. Helium incorporation energies in larger supercell sizes were calculated to ensure convergence. Table 7.2 displays the results, from which it can be seen that a value of 1.7 eV was

also found for increasingly large supercell sizes. As discussed in Section 5.4.1, the OIS has been found to be the most stable site for He in defect-free UO_2 [156] [162] and ThO_2 [155]. Helium inclusion at other interstitial sites such as the edge-centred position (between two oxygen sites) were trialled, but no other site was found to have a lower incorporation energy. From here on, when interstitial He is referred to, it occupies an OIS.

Table 7.2: Incorporation energy of helium occupying an OIS for increasingly large supercells

Supercell Size	4x4x4	6x6x6	8x8x8	10x10x10	12x12x12	20x20x20	30x30x30
E_{inc} (eV)	1.69	1.69	1.69	1.70	1.69	1.70	1.72

Next, helium incorporation at defect sites were investigated. The incorporation energies alongside values from the literature are plotted in Figure 7.1. It was found that helium is most stable in V_{Pu} sites with an incorporation energy of 0.19 eV which is in good agreement with the 0.16 eV value calculated by Neilson *et al.* [164] via DFT. Favourable helium incorporation in actinide vacancies has also been found in UO_2 [163] and ThO_2 [155]. However, PuFPs are unstable in PuO_2 [132]. So whilst V_{Pu} sites are the most energetically favourable for He to occupy, they may not represent the majority site available to He.

The order of helium incorporation stability found was in agreement with the findings in Chapter 5. Of the defect sites considered, helium incorporation is most favourable in a plutonium vacancy and least in an oxygen vacancy. As these results are in agreement with the available literature, they give confidence in the use of the ZBL [74], Aziz [206] and Parfitt [46] set of potentials detailed above to simulate helium in PuO_2 via molecular dynamics.

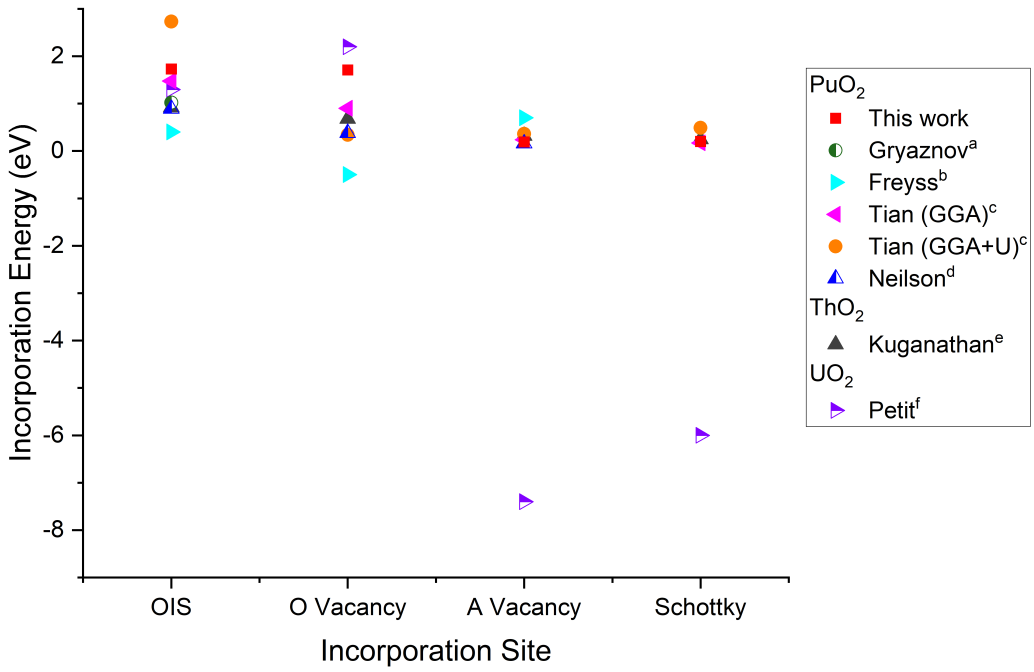


Figure 7.1: Helium incorporation energies at sites in AO_2 where A is an actinide. Results of this work and other authors for PuO_2 ([a][154], [b][130], [c][131], [d][132]), ThO_2 ([e][155]) and UO_2 ([f][163]).

7.3 Migration Pathways

The possible migration pathways of helium between two OISs were modelled and evaluated via NEB calculations. A direct hop from OIS to OIS in a defect-free lattice had a migration barrier of 2.4 eV. Upon inspection of the minimum energy pathways it was found that helium migrates via an edge-centred position. The edge-centred position is where the energy saddle point is.

Next, vacancies were generated between the OISs and the relative energy barriers are displayed by Figure 7.2. It can be seen that when the migration is via an oxygen vacancy (V_O), the energy barrier is significantly reduced to ~ 0.6 eV. Therefore, it is predicted that helium interstitial hopping will be greatly increased by the presence of oxygen vacancies.

For the plutonium vacancy (V_{Pu}) assisted pathway, the midpoint has the lowest energy. Thus, there is an energetic drive for helium to migrate to the V_{Pu}. The migration energy barrier occurs for the helium to then leave to an OIS. This is in alignment with the negative trapping energy found for helium at a V_{Pu} calculated

in Section 5.5.1. From these results it is suggested that if plutonium vacancies are present, helium diffusion could be reduced as the helium atoms could become trapped at V_{Pu} sites.

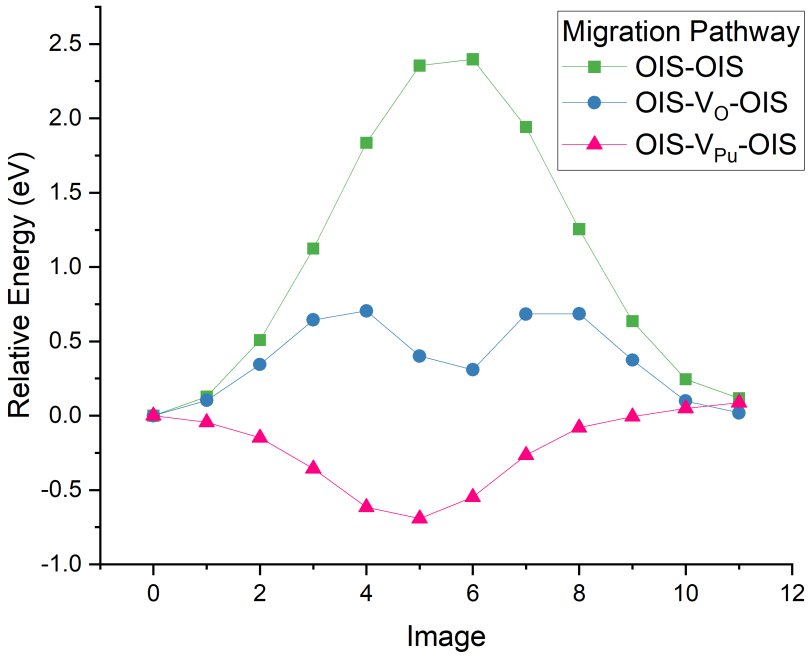


Figure 7.2: Relative energy barriers for different helium migration pathways between two interstitial sites in PuO_2 from NEB calculations. A direct OIS-OIS hop (green squares) has the highest energy barrier, migrating via an V_O (blue circles) has a much lower energy barrier and via a V_{Pu} (pink triangles) there is a negative energy at the plutonium vacancy site.

Oxygen vacancy assisted helium migration has been found to be the energetically favourable mechanism in UO_2 with energy barriers comparable to this work [156], [201]–[203], [210]. In UO_2, Grimes *et al.* [158] found the energy barrier for helium diffusion between interstitial sites to be high (3.8 eV). However, in agreement with the energy barriers displayed in Figure 7.2, when vacancies were in the vicinity of the pathway the diffusion barrier was reduced. Due to the presence of defects in reactor generated fuel, Grimes *et al.* [158] predicts helium to be mobile in UO_2. Under helium infusion conditions in UO_2, in which vacancy concentrations are low, the atomic diffusion of helium has been found to be much slower than in radiation damaged materials [197] [198], suggesting helium migration is vacancy assisted.

In PuO_2, Stan *et al.* [211] calculated an oxygen migration activation energy of 0.45 eV. Via molecular dynamics simulations, Wang *et al.* [121] calculated the

migration barriers in PuO_2 for an V_O and V_{Pu} to be 0.31 and 2.57 eV respectively, and so predicts that oxygen vacancies will have a higher mobility than plutonium vacancies. Similarly to the findings of Liu *et al.* [201] in UO_2, in PuO_2 oxygen and helium migration barriers are of a similar order.

7.4 Helium Diffusion

A fluorite PuO_2 lattice with a helium concentration of 0.5 at% was constructed by randomly inserting He atoms into OISs in an 8x8x8 lattice. A concentration of 0.5 at% was chosen due to it being comparable to that of helium within PuO_2 after many years within storage [188] [212]. The system was then evolved for 4 ns at 100 K intervals between 1000-3000 K after a 1 ns equilibration period. Figure 7.3 plots the diffusivity of He, O and Pu calculated at each temperature. Three regions of interest (R1, R2 and R3) are highlighted.

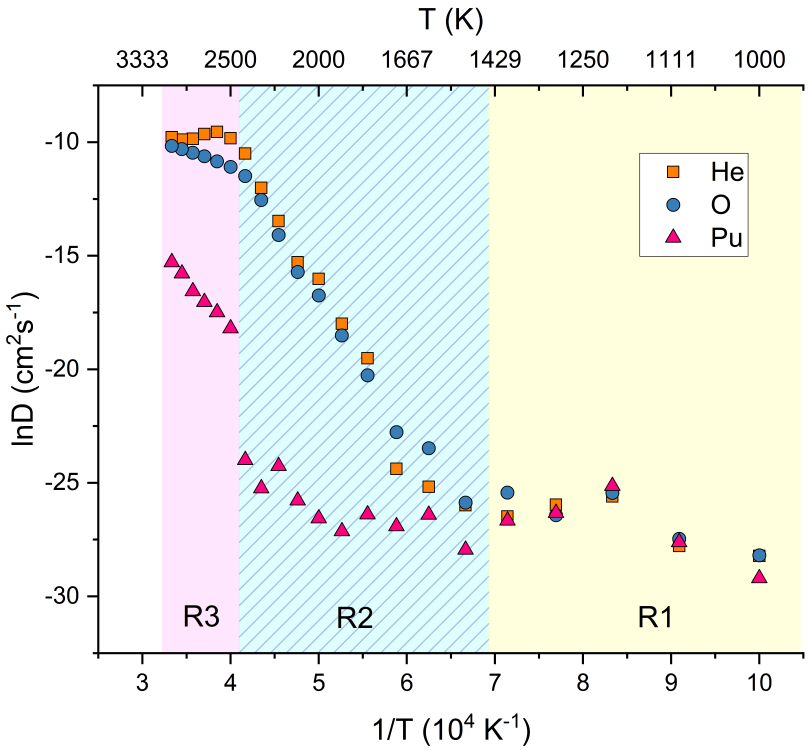


Figure 7.3: Diffusivity as a function of temperature for He, O and Pu in PuO_2. 0.5% He concentration, simulation evolved for 4 ns at every 100 K between 1000-3000 K. Three regions are highlighted, R1, R2 and R3, and are discussed in the text.

The lowest temperature region R1 (1000-1500 K) displays no diffusion. Here

atoms only vibrate around their lattice sites over the simulation time scale. The fluctuations in displacement corresponds with the natural volume variation of the simulation cell as was displayed in Figure 6.5.

In R2 the diffusivity of He and O increases with increasing temperature, with their diffusion closely aligned. The helium diffusion activation energy calculated from the Arrhenius behaviour exhibited in R2 was 5.53 eV, which is comparable to that of oxygen in this region (5.95 eV). These activation energies reinforce the NEB calculation findings of helium inter-site hopping via oxygen vacancies being energetically favourable. From this, it is predicted that the main helium diffusion mechanism is oxygen vacancy assisted. Furthermore, Belle *et al.* [195] found helium gas diffusion rates to correspond with those of cation self-diffusion in UO_2, and from this concluded that fission gases diffuse via cation sites. In the same manner, the findings of comparable He and O activation energies in this work give merit to the proposed mechanism of oxygen vacancy assisted helium diffusion.

Above 2500 K (R3), the oxygen diffusion levels off. This may be due to the temperature being roughly 0.8 T_m, at which it has been suggested that the oxygen sublattice goes through a Bredig phase transition and becomes amorphous [122]. In R3 it can also be observed from the increase in plutonium diffusivity that plutonium becomes mobile. Additionally in R3, there is a plateau in helium diffusivity. It is suggested that the helium diffusivity plateau could be due to V_{Pu} sites becoming available and trapping helium. However, these temperatures are very close to the melting point of PuO_2, so results must be treated with caution.

The MSD of Pu, O and He at temperatures corresponding to each region (1200, 2000 and 2800 K) are plotted in Figure 7.4. This enables the comparison of atomic behaviour in the three regions.

From Figure 7.4, it can be seen that at 1200 K, helium exhibits limited diffusive behaviour and at 2000 K helium is beginning to migrate. At 2800 K helium exhibits diffusive behaviour, but after roughly 2 ns the MSD plateaus. On comparison with the MSDs plotted for O and Pu at these temperatures it is suggested that helium and oxygen exhibit similar diffusive behaviour. It is further suggested that the plateau in helium MSD could correspond to the availability of plutonium vacancies to trap helium (due to the mobility of Pu at 2800 K). Helium atoms could cluster at the available V_{Pu} sites, thus limiting helium diffusion.

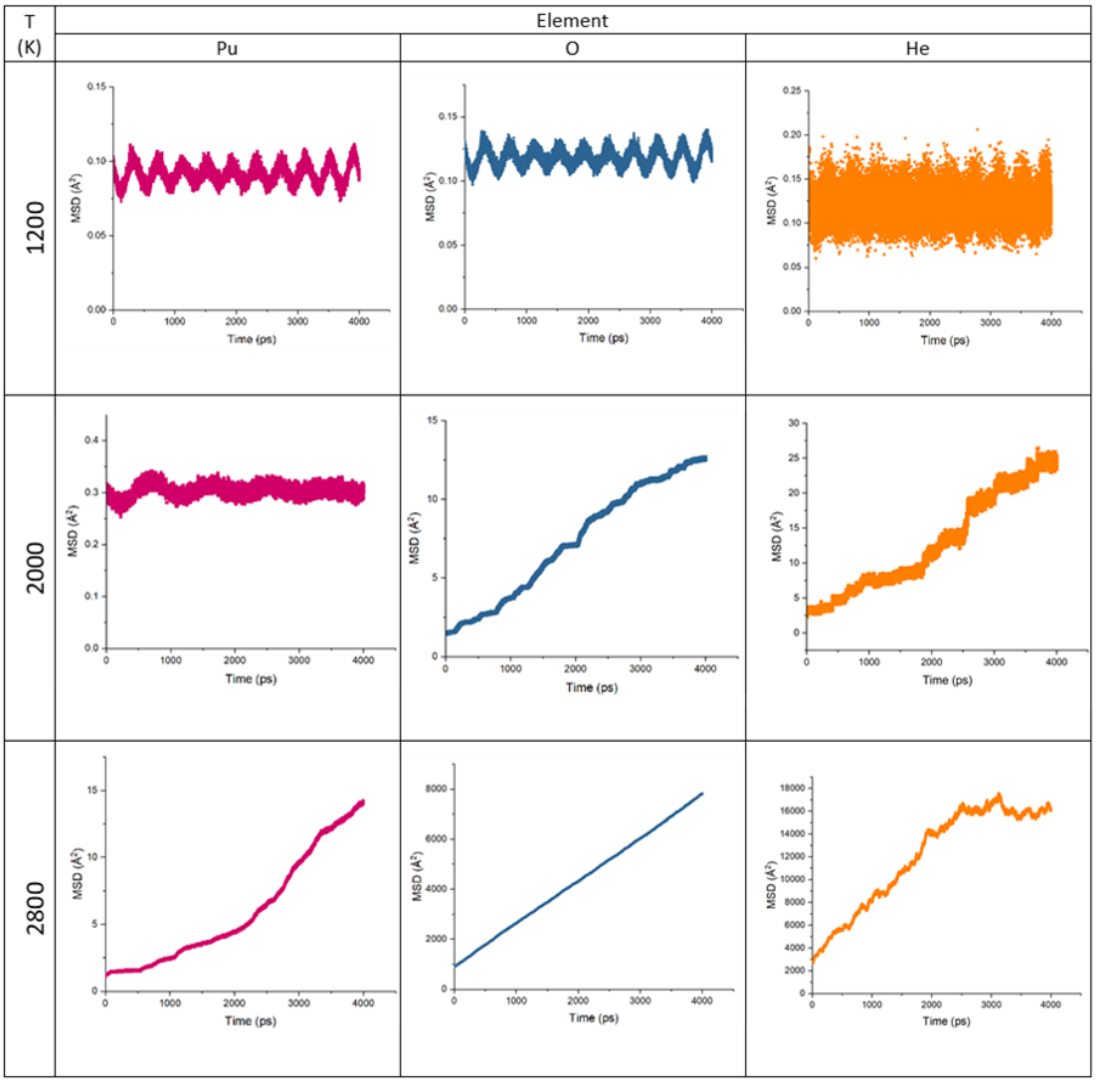


Figure 7.4: MSD of Pu, O and He in an 8x8x8 supercell at 1200, 2000 and 2800 K.

Figure 7.5 displays the final configurations of helium atoms when the lattice was evolved at 2000 K and 2800 K for 4 ns after a 1 ns equilibration period. It can be seen that at 2000 K the helium atoms are in interstitial sites, with one oxygen vacancy present. In contrast, at 2800 K there are many plutonium and oxygen vacancies, with a helium cluster beginning to nucleate. Thus, it is suggested that the helium atoms sequestered in the cluster at 2800 K have resulted in the plateau region seen for the helium MSD in Figure 7.4. This increases confidence in the suggestion that the plateau region (R3) of helium diffusivity in Figure 7.3 may be due to helium becoming trapped in plutonium vacancy sites and the resulting cluster nucleation.

To ensure the validity of the results and that the helium behaviour was not simply due to the lattice being insufficiently large, these simulations were repeated

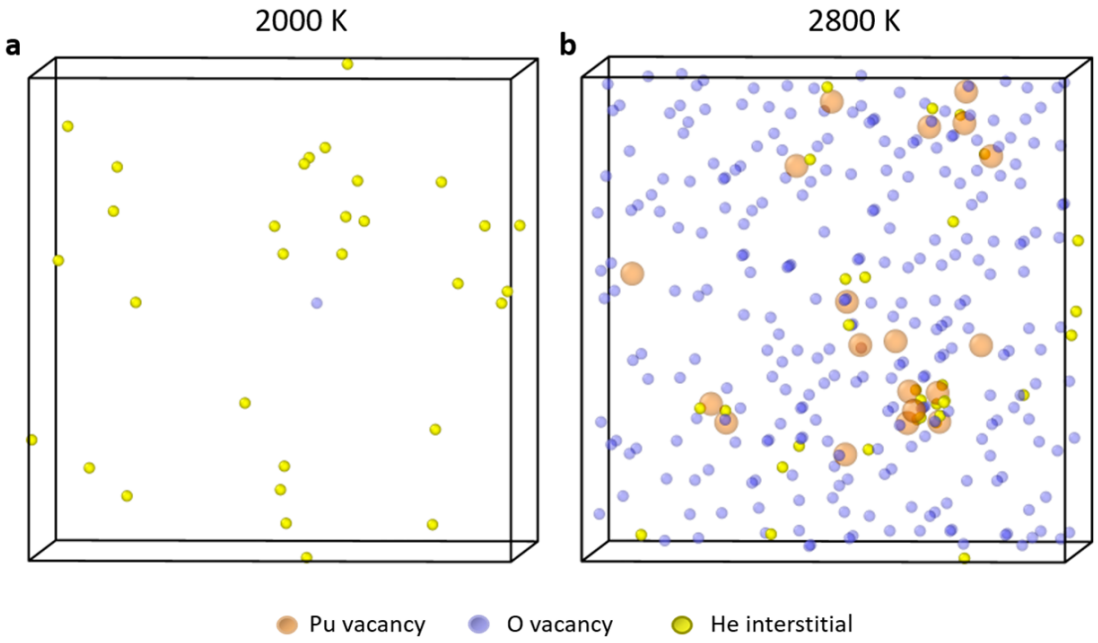


Figure 7.5: Visualisation of helium atoms, plutonium vacancies and oxygen vacancies after 4 ns. The lattice was initially defect-free with 0.5% He input in OIS, molecular dynamics was run with temperatures of (a) 2000 K and (b) 2800 K.

for 10x10x10 and 12x12x12 supercells, the results of which are included in Appendix B. Upon comparison with the results of the different supercell sizes, it was found that the fundamental features of the He diffusion in PuO_2 are not affected by the number of atoms present in the simulations. However, increasing the number of particles in the system increases the computational workload substantially, so these simulations required significantly more processing time than the 8x8x8 supercells. As such, all simulations presented in this chapter were performed using an 8x8x8 supercell with a box length of 43.1857 Å.

7.4.1 *Literature Comparison*

Figure 7.6 displays an aggregation of available data for helium diffusivity in PuO_2 and UO_2 from the literature, determined both experimentally and computationally.

From Figure 7.6 it can be seen that the diffusivity values calculated in this work are within the range of values found in the literature. However, the R2 region of Arrhenius behaviour has a steeper gradient than those from the literature. A steeper gradient results in a higher diffusion activation energy. It is suggested that the higher diffusion activation energy calculated in this work is due to the lattice being initially pure, whereas the experimental values (Ronchi [200] and Pipon [199])

have shallower gradients, which may be due to defects being present in the lattice and aiding in helium diffusion. Inherent defects are present in all solids above 0 K due to thermodynamics. As temperatures increase, so do the number of inherent defects. The number of defects present in a lattice is also increased by radiation damage.

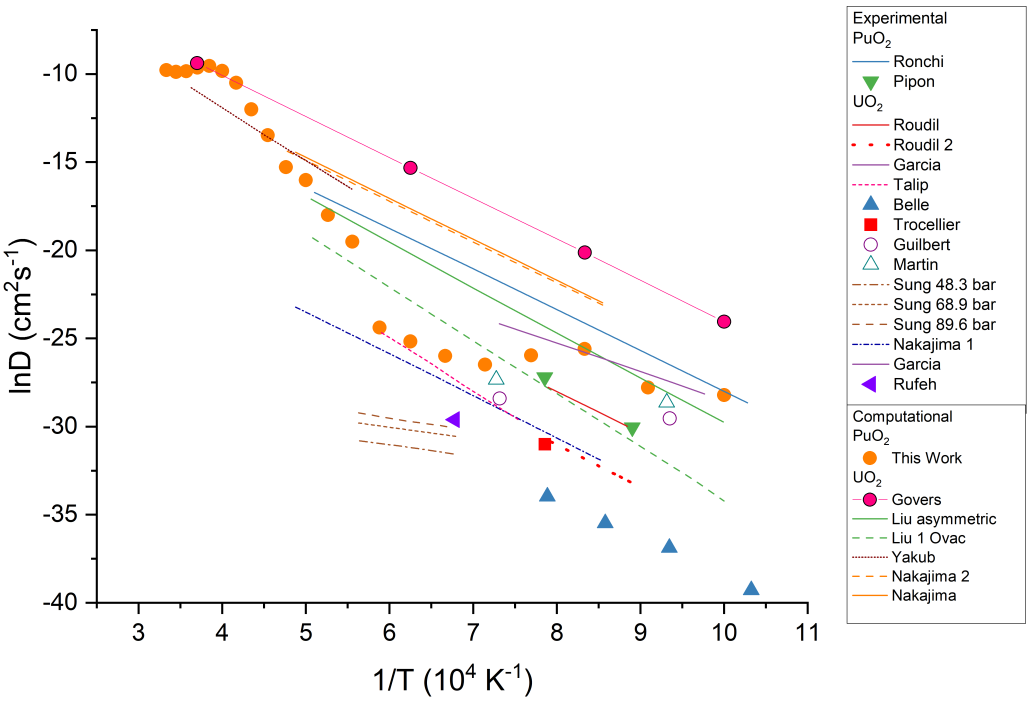


Figure 7.6: Diffusivity as a function of temperature for all available literature data of helium diffusion experimentally in PuO_2 (Ronchi [200], Pipon [199]) and UO_2 (Roudil [188], Garcia [191], Talip [189], Belle [195], Trocellier [194], Guilbert [190], Martin [193], Sung [196], Nakajima [198], Rufeh [197]. And computational data of UO_2 (Govers [203], Liu [201], Yakub [202] and Nakajima [198]).

The impact of defects being present in the lattice can be interpreted from the experimental data plotted in Figure 7.6. As discussed by Luzzi *et al.* [187] in their evaluation of helium diffusivity in oxide nuclear fuels, the level of damage in a lattice can be categorised by the experimental technique used. Figure 7.7 displays the three helium introduction techniques:

- Infusion, in which a sample is placed in a pressurised helium atmosphere for a certain infusion time [195]–[198]
- Doping, in which there is an internal source of helium in the sample via the

introduction of an α-emitting element [189], [199], [200]

- Ionic implantation, in which a beam of $^{3}He^{+}$ hits and penetrates the sample [188], [190], [191], [193], [194]

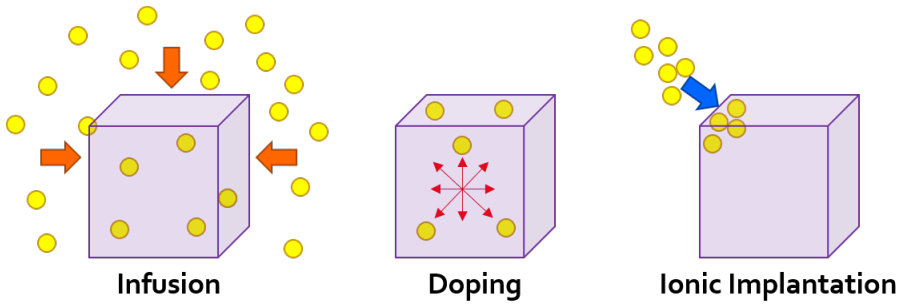


Figure 7.7: Three mechanisms of helium generation in nuclear fuel samples for experimental analysis. Adapted from [187].

Of the experimental methods of helium introduction, infusion is anticipated to generate samples with fewer defects. Four of the experimental data plotted in Figure 7.6 were from infusion methodology: Belle *et al.* [195], Sung *et al.* [196], Rufeh *et al.* [197], and Nakajima *et al.* [198]. It can clearly be seen that 'Belle', 'Nakajima 1', 'Sung' (at all three pressures) and 'Rufeh' data points have the lowest diffusivity values. As such, it is suggested that samples containing fewer defects result in lower helium diffusivity. As discussed by Luzzi *et al.* [187], samples generated via ion infusion can be compared to fresh nuclear fuel.

7.4.2 *Helium Concentration*

Systems with increasing helium concentrations were then generated with randomly distributed helium atoms occupying separate OISs. The percentage volume expansion as a function of the helium concentration at 298 K was calculated, and is displayed in Figure 7.8. The volume expansions as a function of helium concentration in UO_2 [156] and metallic Pu [45] are also included in Figure 7.8 for comparison. It can be seen that for PuO_2, UO_2 and Pu, a linear volume expansion with increasing helium concentration is predicted. The higher expansion coefficient for Pu metal may be due to it not being a fluorite structure.

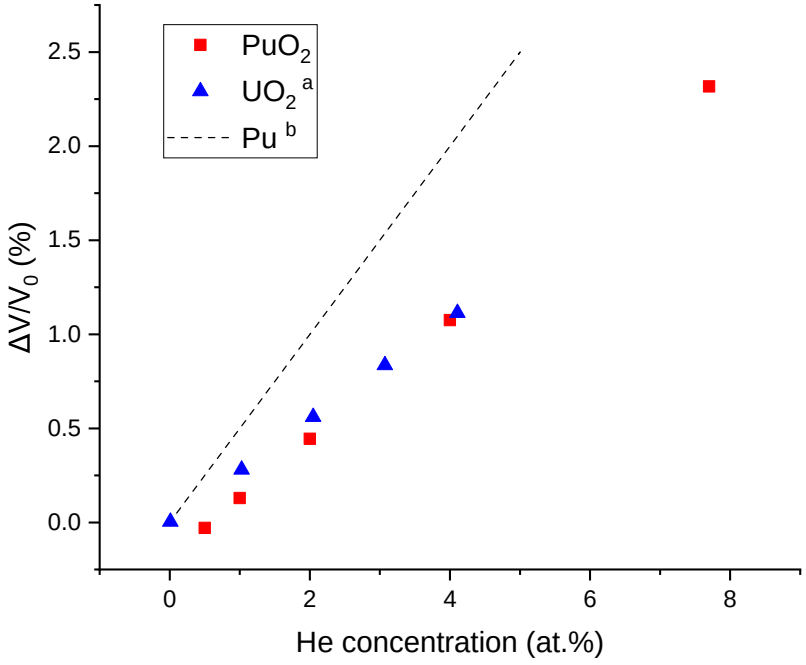


Figure 7.8: Percentage volume expansion as a function of the helium concentration in PuO_2, UO_2 and Pu. [a][156] [b][45]. Experiments show a typical volume expansion of 1% after large irradiation doses (Helen Steele, private communication) indicating a maximum He concentration of 5%.

Molecular dynamics was run on lattices containing 0.5, 2, 4, and 10% helium for 1 ns over a 1000-3000 K temperature range. The diffusivity of helium in each of these simulations is displayed in Figure 7.9. Below 1750 K no long scale diffusion was exhibited by helium regardless of helium concentration. For all of the helium concentrations, the bounds of R1 remain consistent. However R2 becomes much smaller for increasing helium concentrations. Unlike the findings of Roudil *et al.* [188] in UO_2, an increase of diffusion coefficients with increased helium concentration was found. It can be seen that the plateau in helium diffusivity is reached at lower temperatures for higher helium concentrations. For example, R3 behaviour begins at 2500 K for the lattice containing 2% He and at 2000 K for the lattice containing 10% He. This could be due to the higher helium concentrations forcing helium clusters to form which then limit helium diffusivity.

To further understand the finding of R3 behaviour at lower temperatures for lattices containing higher helium concentrations, the configurations of the lattices after 1 ns were inspected in OVITO. Figure 7.10 displays the configurations of the

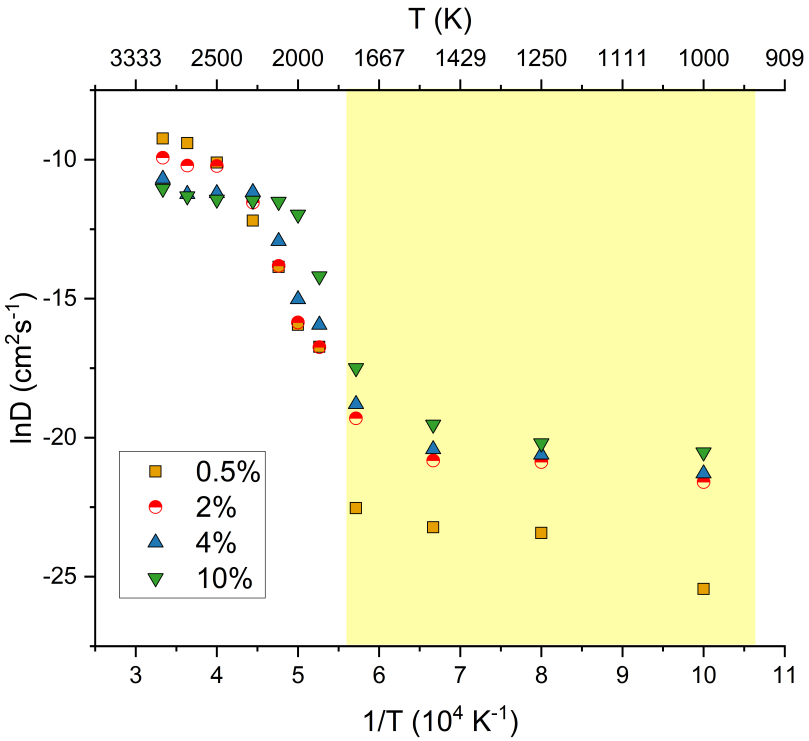


Figure 7.9: The variation of helium diffusivity in PuO_2 as a function of temperature for four different helium concentrations (0.5, 2, 4 and 10 %). In the highlighted region no diffusive behaviour is exhibited. At 1750 K, the diffusivity starts to increase with increasing temperature. The high temperature diffusivity plateau region begins at lower temps for higher He concentrations.

lattices with 2, 4 and 10% helium after MD was run for 1 ns at 2000 and 2500 K. The helium atoms and oxygen and plutonium vacancies are displayed with the lattice atoms hidden for clarity. It can be seen that for the 2 and 4% helium concentration lattices, there is no helium clustering at 2000 K, but clustering can be seen at 2500 K. However, for the 10% helium lattice, clusters can be seen to have formed at 2000 K and then continued to grow at 2500 K. It is therefore suggested that higher helium concentrations led to clustering at lower temperatures and so, as displayed by Figure 7.4.2, may lead to lower helium mobility, due to trapped helium being less mobile.

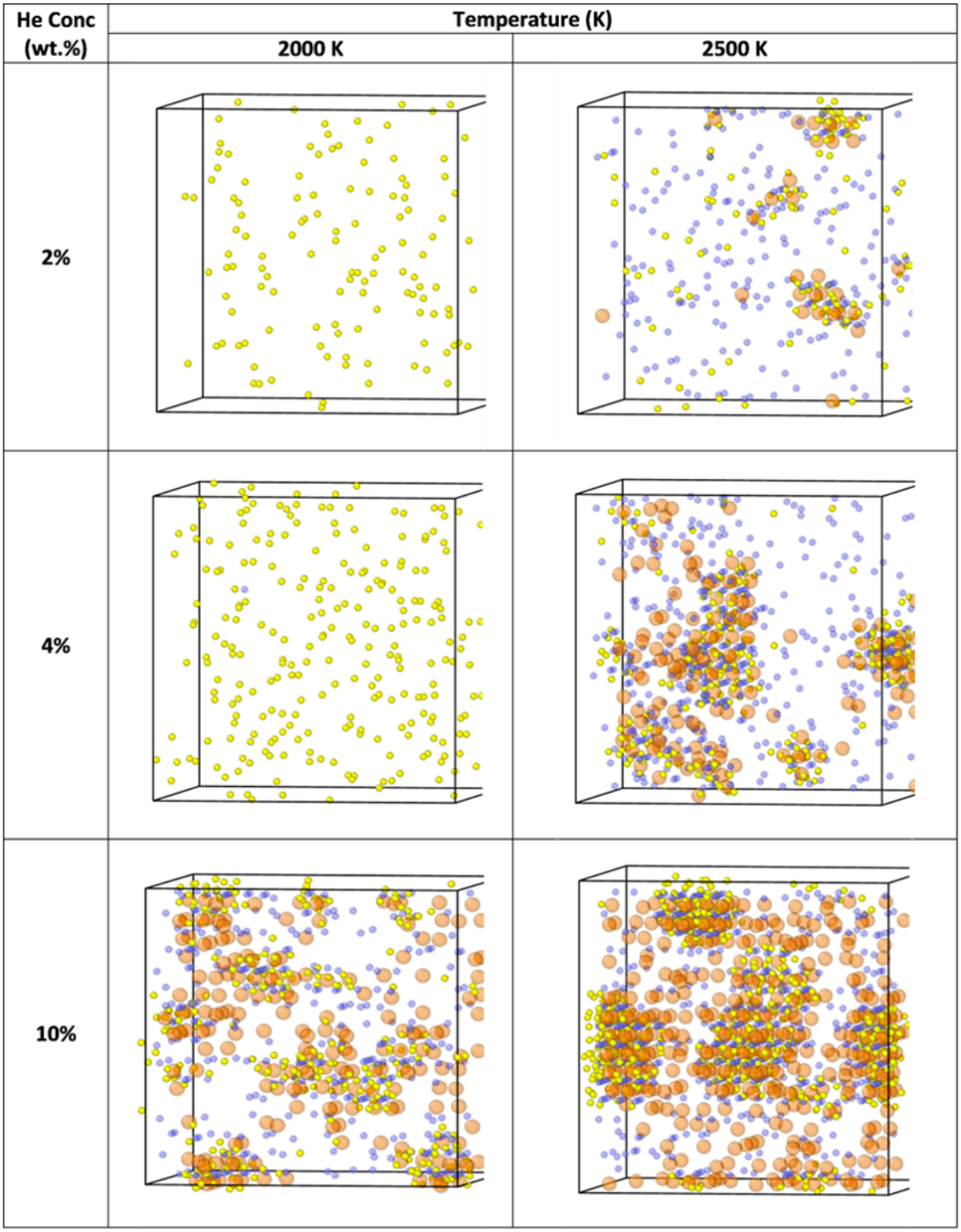


Figure 7.10: Visualisation of helium atoms (yellow) and oxygen and plutonium vacancies (blue and pink respectively) after 1 ns in PuO_2 at 2000 K (LHS) and 2500 K (RHS) at three different helium concentrations. For clarity, oxygen and plutonium ions are not displayed. It can be seen that at higher helium concentrations (10%), helium clustering occurs at lower temperatures.

Cluster analysis was performed on each lattice at each temperature after 1 ns. A large helium cluster was defined as one containing ≥9 helium atoms. Figure 7.11 displays a bar chart of the percentage of helium atoms occupying large clusters after 1 ns. It can be seen that for the lattice containing 0.5% helium, no large helium clusters formed at any temperature during 1 ns. For the lattice containing 2% helium, at 2500, 2750 and 3000 K (the three highest temperatures considered) roughly half of the helium atoms occupy large clusters. Therefore, it is found that large helium clusters are formed at lower temperatures in lattices containing higher helium concentrations. After 1 ns, the average percentage helium occupying a cluster is approximately 50, 65 and 80% for helium concentrations of 2, 4 and 10% respectively. Thus, it is suggested that higher helium concentrations lead to helium clustering occurring more rapidly.

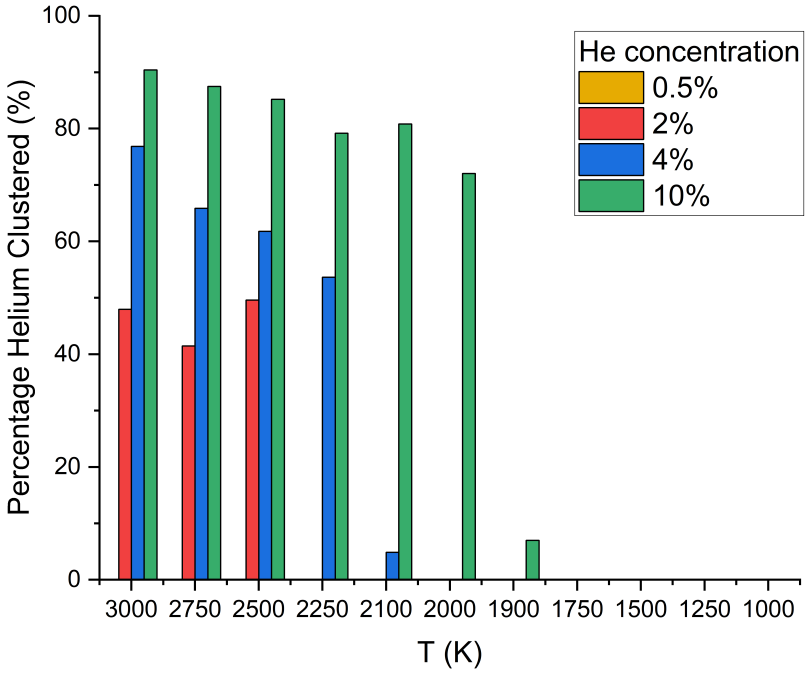
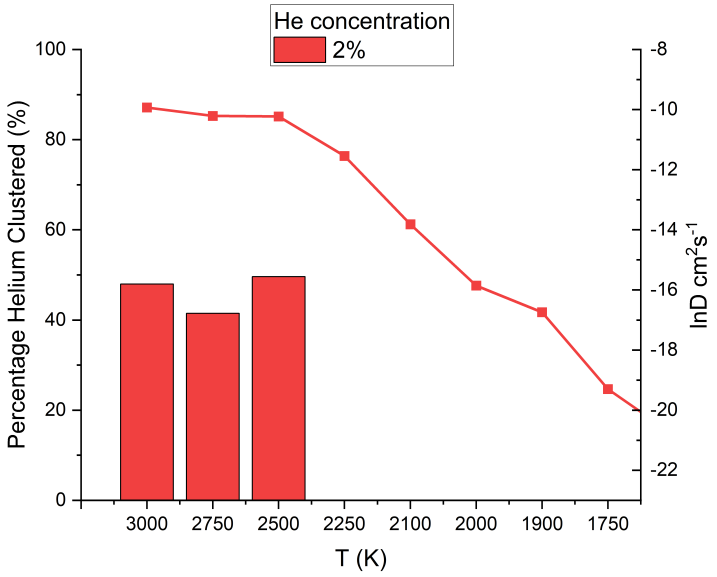


Figure 7.11: Bar chart displaying the percentage of helium atoms which occupy large clusters in lattices containing 0.5, 2, 4 and 10% helium over a range of temperatures.

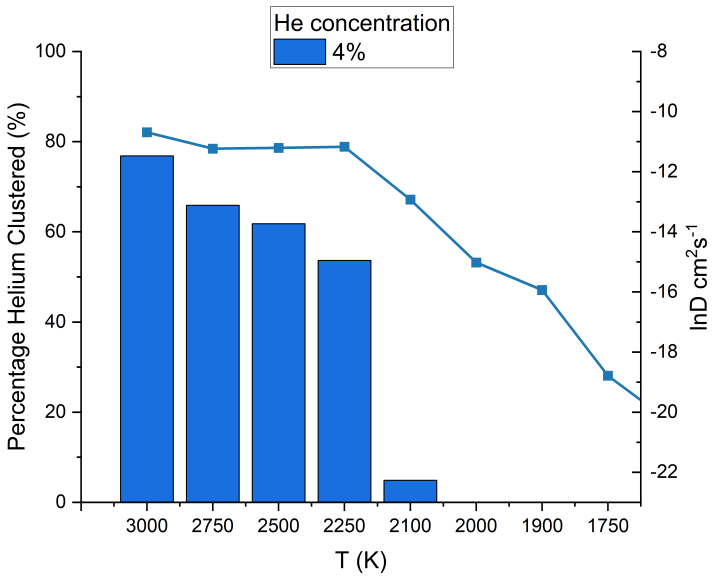
Upon comparison of Figure 7.11 with Figure 7.9, it can be seen that there is a correspondence between helium clustering and the diffusivity plateaus. Figure 7.12 displays the helium clustering and diffusivity for each helium concentration separately for further comparison. From Figure 7.12 it can clearly be seen that the plateau in helium diffusivity and the formation of large helium clusters occur at

concurrent temperatures. Furthermore, the higher the percentage helium clustering, the lower the average of the diffusivity plateau. For example, it can be seen for the 10% helium lattice, which has the highest percentage of helium occupying clusters, the average lnD value is $\sim$ 11 cm^2s^{-1}. From this it can be suggested that higher concentrations of helium clustering lead to lower average helium diffusivities. This is likely due to clustered helium being trapped and so having lower diffusivity. Therefore the higher the percentage of helium trapped in a cluster, the lower the average helium diffusivity.

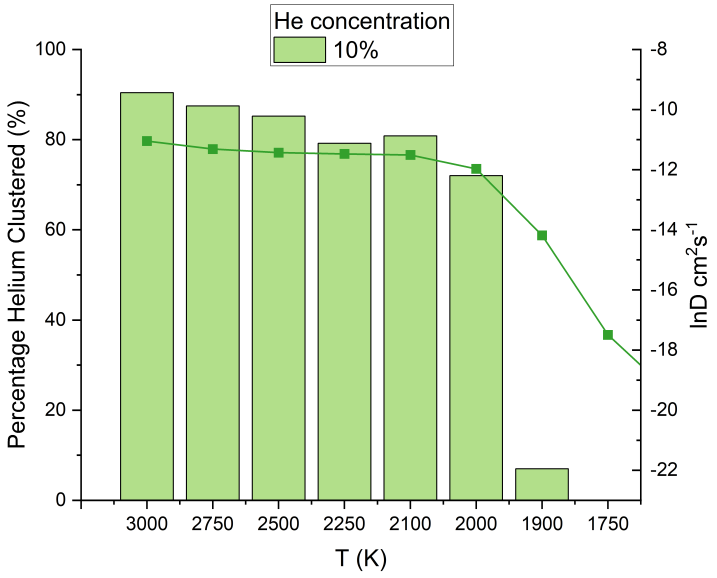
A detailed analysis of helium clustering behaviour will be performed in the following chapter.



(a) 2%



(b) 4%



(c) 10%

Figure 7.12: Bar and line chart showing the percentage helium clustered (left-axis bar chart) and the helium diffusivity (right-axis line chart) for lattices with different helium concentrations over a range of temperatures.

7.4.3 *Migration Pathways Analysis*

The output files of all diffusion simulations were inspected in OVITO with oxygen and plutonium vacancies visualised and helium trajectories plotted. In all cases helium atoms did not leave their initial sites until temperatures of 1500 K, and upon inspection it was observed that helium inter-site hops occurred in the vicinity of an oxygen vacancy. Figure 7.13a displays the trajectories of the He atoms in PuO_2 with 2% He at 2100 K. From the trajectories it can be observed that some helium atoms are mobile and have made interstitial hops. Figure 7.13b displays a specific time period of the 2100 K simulation and it can be seen that the helium migration is aided by an oxygen vacancy.

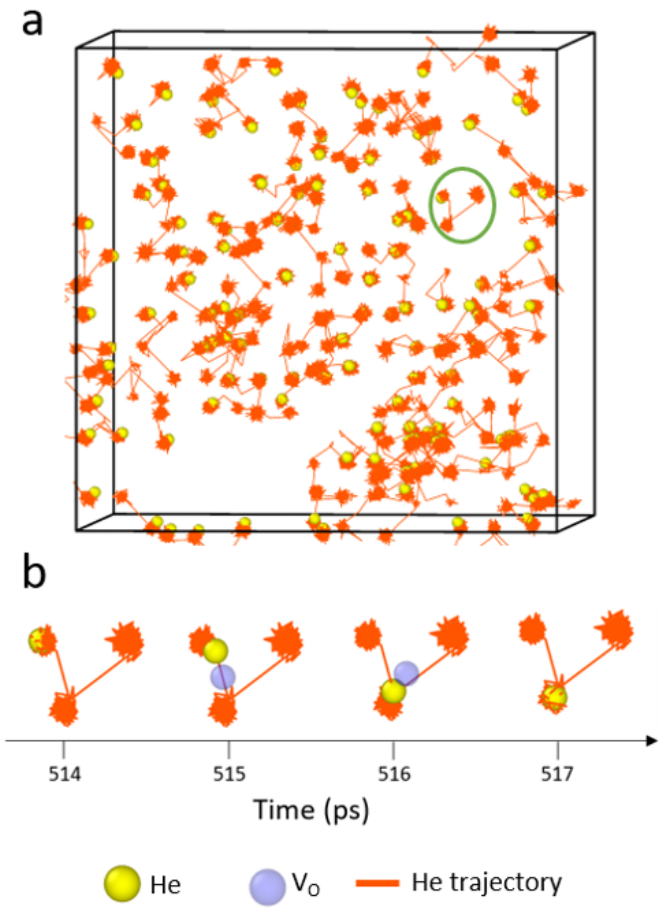


Figure 7.13: Trajectory of He atoms in initially defect-free PuO_2 at 2100 K (a) displays the trajectory of all He atoms during 1 ns, it is evident there is inter-site hopping (b) displays a snapshot of a He inter-site hop from the area circled in green in (a). The time period in (b) is 514-517 ps and illustrates that part of a He atoms trajectory. It can be seen that at 515 ps an oxygen vacancy is generated in the vicinity of the He and the He uses this to migrate to a neighbouring OIS.

Figure 7.14 displays the configuration of helium atoms after 1 ns at 1200 and 2400 K, with the lattice vacancies visualised. It can be seen that at 1200 K there are no vacancies present. Correspondingly, at this temperature helium is not mobile. At 2400 K there are many oxygen vacancies as oxygen is mobile at this temperature. It is suggested that due to the presence of these oxygen vacancies in R2, helium is mobile via the OIS-V_O-OIS pathway.

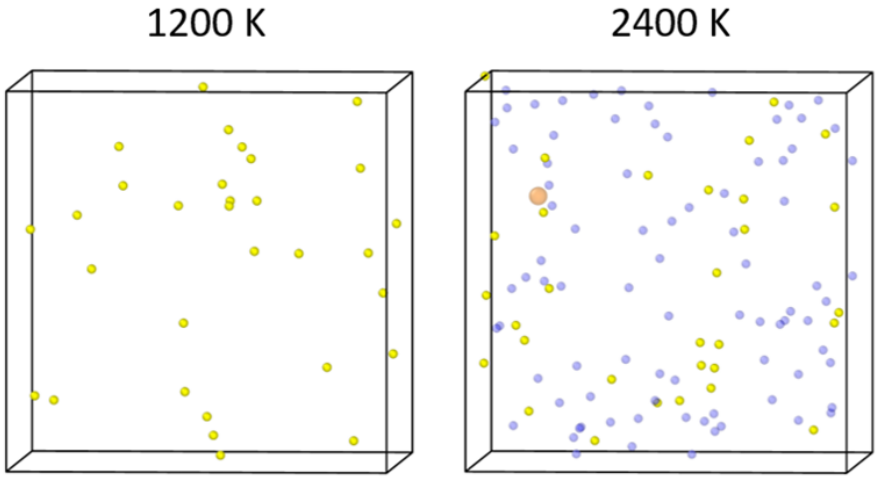


Figure 7.14: Configurations of helium atoms (yellow) alongside oxygen vacancies (blue) and plutonium vacancies (pink) after 1 ns at 1200 K (LHS) and 2400 K (RHS).

The helium diffusion energy barrier in defect-free PuO_2 was calculated to be 5.3 eV from the Arrhenius behaviour exhibited in R2 in Figure 7.1. The value of 5.3 eV was surprising, since the barrier determined from NEB for the direct OIS-OIS hop was previously calculated as 2.4 eV. Further analysis of He diffusion at 2000 K showed that over 1 ns, twelve He hop events occurred; nine of which were via the O vacancy mechanism (OIS-V_O-OIS) and three via the direct OIS-OIS hop. The barrier to displace an O atom into an interstitial site was calculated to be 6.0 eV and for the He atom to diffuse via the O vacancy mechanism another 0.6 eV is required. Thus the 5.3 eV barrier can be seen as an average from the different He diffusion mechanisms. The calculated helium diffusion barrier therefore implies that the attempt frequency for the direct OIS-OIS hop is several orders of magnitude smaller than that of a hop via an oxygen vacancy. This analysis was repeated at 1800 and 1900 K with similar attempt frequencies found.

From the NEB calculations in displayed Figure 7.2, a 0.4 eV difference in energies between the OIS and the V_O site was determined. However, the energy barriers of

the constituting hops in the OIS-V_O-OIS pathway are calculated to be 0.7 eV for OIS-V_O and 0.3 eV for V_O-OIS. From the Arrhenius equation, (if a prefactor of 1.0E13 is assumed) at 1500 K an OIS-V_O jump would be expected every 22 ps and an OIS-V_O jump every 1 ps on average. OIS-OIS would occur every 10 ms. Thus, movement both ways via the O vacancy mechanism is possible over the time scale of the simulations.

The molecular dynamics simulations performed in this work show that oxygen vacancy assisted inter-site hopping is the dominant helium diffusion mechanism in PuO_2. Limited experimental data of helium diffusion in PuO_2 is available, but some studies of oxygen diffusion in PuO_2 exist [174] [175]. The relatively low defect energy of OFPs [49] [121] combined with the low diffusion barriers for O defects determined by Stan *et al.* [211] indicates that oxygen vacancies will be prevalent in the system, so will be available to assist helium migration.

Oxygen vacancy assisted inter-site hopping has also been found to be the main diffusion mechanism of He in UO_2 [201]–[203]. Deaton *et al.* [174] and Bayoglu *et al.* [175] used gas-phase isotope exchange to calculate oxygen diffusion activation energies in stoichiometric PuO_2 of 1.834 and 1.938 eV respectively. In UO_2, Ichinomiya *et al.* [213] found the migration of the single oxygen interstitial to be much slower than that of the vacancy. The low defect energy of OFPs [49] [121] indicate that O type defects will be dominating the system, especially at low temperatures, so will be available to assist helium migration.

7.5 Defect Inclusion

7.5.1 *Schottky Trios*

Structures with different concentrations of Schottky trios were generated in the lattice by randomly removing atoms corresponding to missing PuO_2 concentrations of 0.5, 2 and 4% and the system was then relaxed. The helium concentration in these systems was fixed at 2% and each system evolved for 700 ps with an initial 300 ps equilibration period over a range of temperatures (1000-3000 K in 250 K intervals).

Figure 7.15 displays the MSD at each temperature for the helium atoms in the lattice with 2% Schottky trios. As expected, it can be seen that when the temperature of the simulation is higher, the MSD of helium increases, as the atoms will have higher kinetic energies. From each of these MSD curves, and those of lattices with the other Schottky concentrations, the helium diffusivity was calculated

via Equation 6.1.

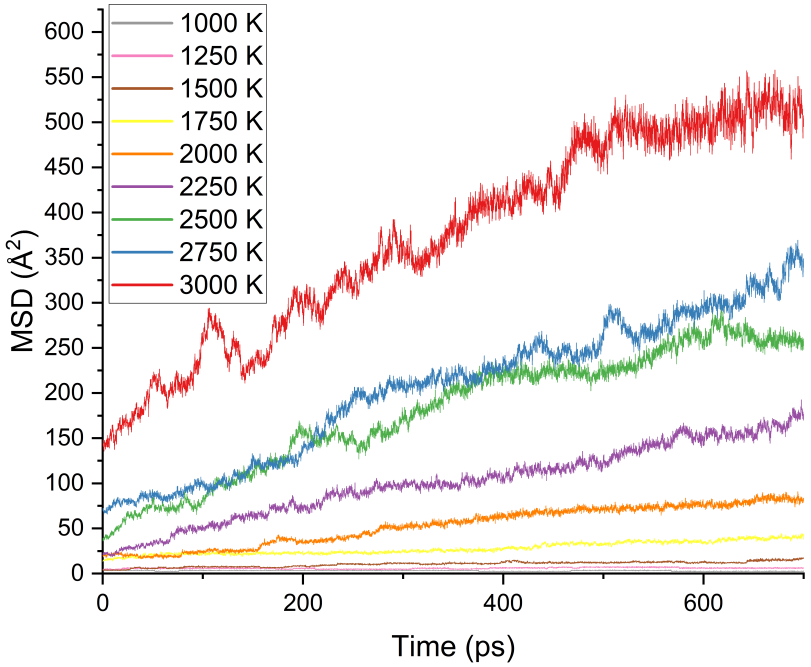


Figure 7.15: Helium MSD as a function of time over a range of temperatures for a PuO_2 lattice with 2% Schottky trios and a 2% helium concentration.

Figure 7.16 displays the calculated diffusivities. It is evident that as the number of vacancies in the lattice increases, the diffusivity is greatly increased at lower temperatures. When no defects are initially in the lattice, helium exhibits no diffusive behaviour below 1750 K. Helium diffusivity below 1750 K when vacancies are initially present is likely due to the reduction in the helium migration energy barrier given by oxygen vacancy assisted migration.

The diffusivity of helium in PuO_2 when defects are present (displayed in Figure 7.16) is much more comparable to the diffusivity values from the literature plotted in Figure 7.6. This correspondence is likely due to the presence of defects in the samples, from radioactive decay or from the helium injection method as discussed previously.

The helium diffusion activation energies, E_a, were calculated via the Arrhenius equation (Equation 6.2) for each Schottky concentration. Table 7.3 displays the values. It can be seen that the activation energy is greatly reduced for systems containing Schottky defects. However, it was found that the increase in Schottky concentration from 0.5 to 4% has little influence on the helium activation energies.

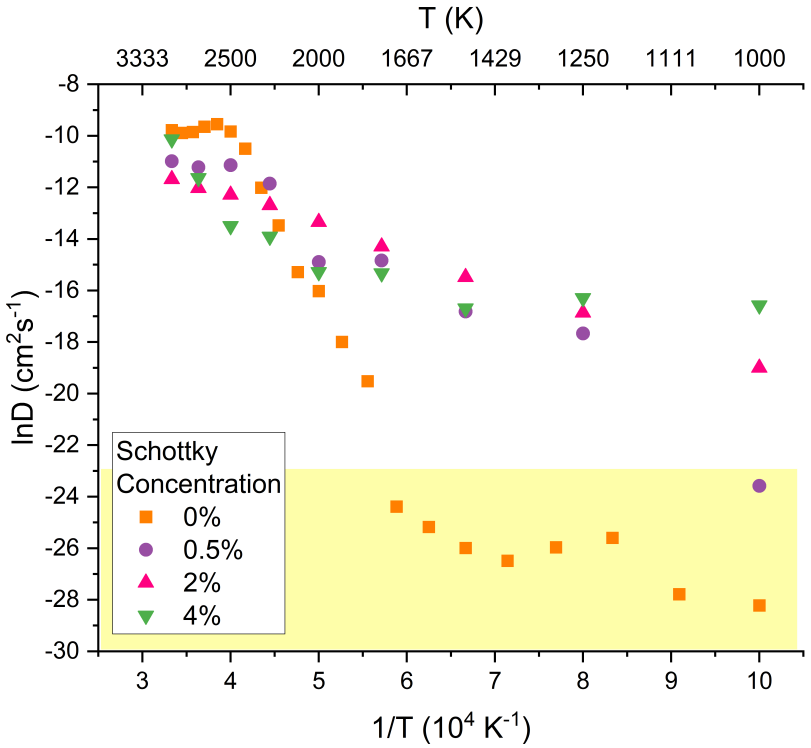


Figure 7.16: Helium diffusivity as a function of temperature for four different Schottky defect concentrations in PuO_2. The helium concentration was 2% with all helium atoms initially randomly inserted into OIS. In the lower temperature range when oxygen vacancies would not be being thermally generated, the higher Schottky concentrations have higher He diffusivity. The highlighted region indicates no diffusive behaviour.

Table 7.3: Parameters calculated from Arrhenius behaviour exhibited by helium in PuO_2 with various Schottky concentrations

Schottky Conc.	E_a (eV)	D_0 (cm^2s^{-1})	r-square
0%	5.53 ± 0.29	7.32E+06	0.98972
0.5%	0.90 ± 0.24	7.72E-05	0.90527
2%	1.01 ± 0.05	5.13E-04	0.99667
4%	0.97 ± 0.26	1.04E-04	0.90169

Ronchi *et al.* [200] and Talip *et al.* [189] calculated helium migration activation energies in ^{238}Pu-doped UO_2 of 2.00 eV and 2.59 eV respectively. Their values are higher than those calculated in this work (Table 7.3) and it is suggested that this may be due to the samples being ^{238}Pu-doped UO_2 rather than PuO_2. Due to the

increased radioactivity of Pu, more intrinsic defects are predicted to be generated in pure PuO_2. Such defects may reduce the helium migration activation energy and as such lead to lower helium E_a values in PuO_2 [187].

As discussed in Section 7.4.1, experimental studies of UO_2 have found that helium diffusion is greater when defects are present in the system. Martin *et al.* [193] studied helium implanted uranium dioxide using nuclear reaction analysis prior to and following heavy ion irradiations. They found the heavy ion irradiation enhanced the mobility of He, and suggested this was due to the increase in defects in the system. Similarly, Nakajima *et al.* [198] used single-crystal samples and found helium solubility to be much lower than those given by poly-crystalline samples. It was presumed this was due to the single-crystal samples having fewer defects and so subsequently lower helium diffusivity.

The diffusivity of helium can be compared to that of oxygen in lattices with the same Schottky concentrations. The oxygen diffusivity in such lattices was investigated in the previous chapter (Section 6.4), the results have been included again here for reference (Figure 7.17). It was found that increases in Schottky concentrations resulted in increased oxygen diffusivity at lower temperatures. Furthermore, the activation energies listed in Table 7.3 when Schottky defects are present in the system are similar to those which were calculated for oxygen (Table 6.4a). From this, it is evident that oxygen and helium diffusivity are similarly affected by the presence of defects, suggesting that the increased helium diffusivity is due to the increased oxygen mobility.

The diffusion of helium in PuO_2 can be compared to existing studies of oxygen diffusion behaviour in UO_2. There is a correspondence to the three regimes defined by Günay [214]. Firstly, Günay [214] defines an extrinsic region (1200-1750 K) where diffusion is assisted by irradiation induced defects. Next there is the intrinsic region (1800-2600 K), in which diffusion is due to the thermal energy results; here the lattice energy is high enough for dynamic Frenkel defects to frequently form and recombine. The intrinsic region corresponds to the R2 region defined earlier in this work, suggesting that at temperatures where oxygen Frenkel pairs are being generated, these assist in helium migration. In this region in Figure 7.16 it can be seen that when defects are already present in the lattice, standard Arrhenius behaviour is exhibited, as vacancies are already present to assist mobility. Finally, Günay [214] defines the superionic region (2600-3200 K) in which the Bredig transition and melting takes place. Above this temperature the oxygen sublattice totally melts and behaves like a liquid with the uranium sublattice remaining solid. It can be

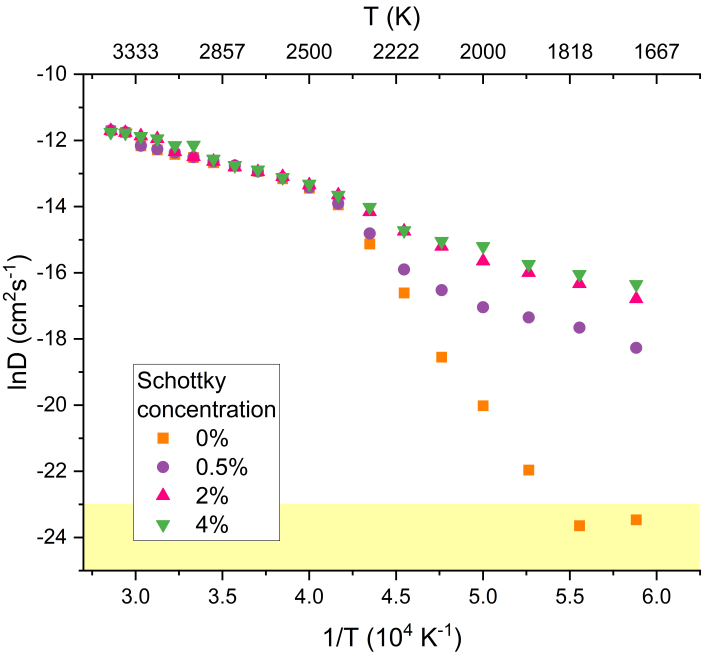


Figure 7.17: Oxygen diffusion coefficients as a function of temperature in PuO_2 at four different Schottky defect concentrations. The yellow highlight indicates data points when no diffusive behaviour was exhibited.

seen that in this R3 region for all Schottky concentrations in Figure 7.17 the oxygen diffusivity is the same.

7.5.2 *Frenkel Pairs*

7.5.2.1 Oxygen Frenkel Pairs

Lattices containing different concentrations of oxygen Frenkel pairs (0.5, 2 and 4%) were generated and the helium diffusivities in such lattices are plotted in Figure 7.18. It can be seen that the inclusion of OFPs has limited impact on the diffusivity of helium in PuO_2. No diffusive behaviour is exhibited for temperatures below 1500 K for lattices containing OFP concentrations of 0.5% and 2%. This was surprising, as it was anticipated that helium would be more mobile due to the increased availability of oxygen vacancies for diffusion.

However, upon inspection of the trajectory files it was found that the oxygen Frenkel pairs would quickly recombine. This is likely due to the high mobility of oxygen Frenkel pairs. Thus, oxygen Frenkel pairs are highly likely to recombine and at low temperatures are unlikely to reform. As such, unlike in the lattices containing

Schottky defects, there is little increase in helium diffusivity at low temperatures in Figure 7.18. For lattices containing oxygen Frenkel pair concentrations of 4%, the diffusivity of helium at low temperatures was increased. This was likely due to the increased probability of more oxygen Frenkel pairs remaining at any one time.

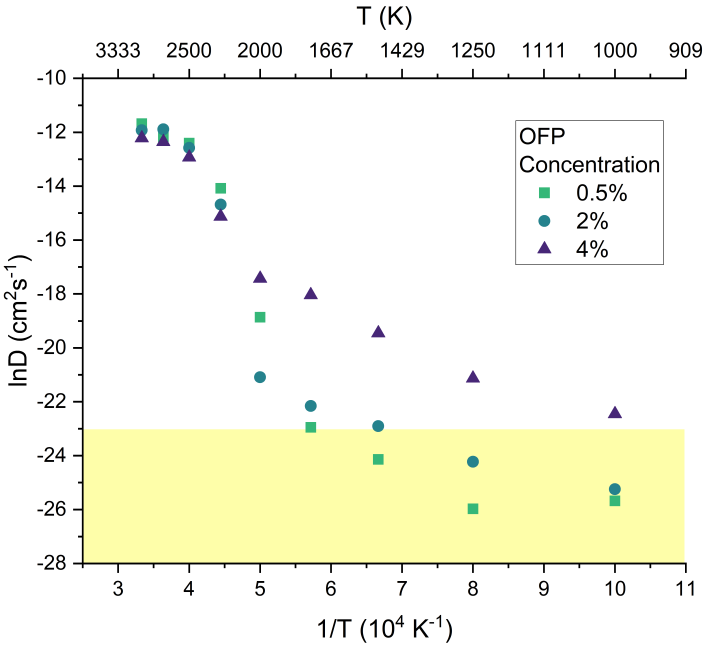


Figure 7.18: Diffusivity of helium in PuO_2 with the lattice containing different concentrations of randomly distributed oxygen Frenkel pairs. The yellow highlighted region indicates no diffusive behaviour.

7.5.2.2 Plutonium Frenkel Pairs

Lattices containing different concentrations of plutonium Frenkel pairs (0.5, 2 and 4%) were also generated and the simulations repeated. Figure 7.19 displays the calculated helium diffusivities. It can be seen that increasing PuFP concentrations resulted in limited impact on helium diffusivity. Again, it was found that the Frenkel pairs were quickly recombining, this recombination was likely due to the high defect energy of PuFPs as was calculated earlier in this work.

The diffusivities of helium in all lattices containing PuFPs were on average slightly higher than those calculated for the initially pure lattice (Figure 7.3). Upon inspection of the configurations during the simulations it was found that oxygen defects were generated in the vicinity of PuFPs and these enabled increased oxygen assisted helium diffusion at lower temperatures.

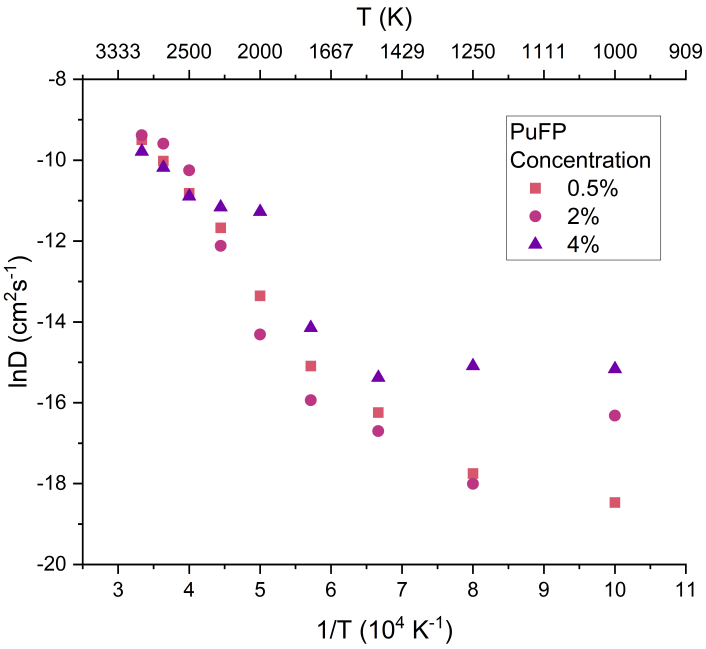


Figure 7.19: Diffusivity of helium in PuO_2 with the lattice containing different concentrations of randomly distributed plutonium Frenkel pairs.

7.5.3 *Helium Input Position*

7.5.3.1 Schottky Trios

In the aforementioned simulations, helium atoms were input in interstitial sites. It was of interest to see if helium diffusion would be affected if the helium atoms were input in V_O or V_{Pu} sites. Helium was added to these sites in the 2% Schottky lattice. The helium concentration was 2%. Figure 7.20 displays the diffusivity of helium over a range of temperatures for the three input sites. It can be seen that at higher temperatures (T > 2500 K) the input site has little effect on helium diffusivity. At lower temperatures helium diffusivity is reduced when input in a plutonium vacancy. This finding is in accordance with the migration energy barriers discussed previously as plutonium vacancies are predicted to act as helium trap sites. From inspection of the trajectories in the low temperature region (T < 1500 K) it was found that almost all helium atoms when input in a V_{Pu}, remained in the V_{Pu}.

The Arrhenius parameters were calculated from Figure 7.20 with the fitted regions displayed on the graph. As can be seen from Table 7.4, the activation energies for helium input at an OIS or V_O are approximately equal. Additionally these activation energies are very similar to that calculated for oxygen diffusion in 2%

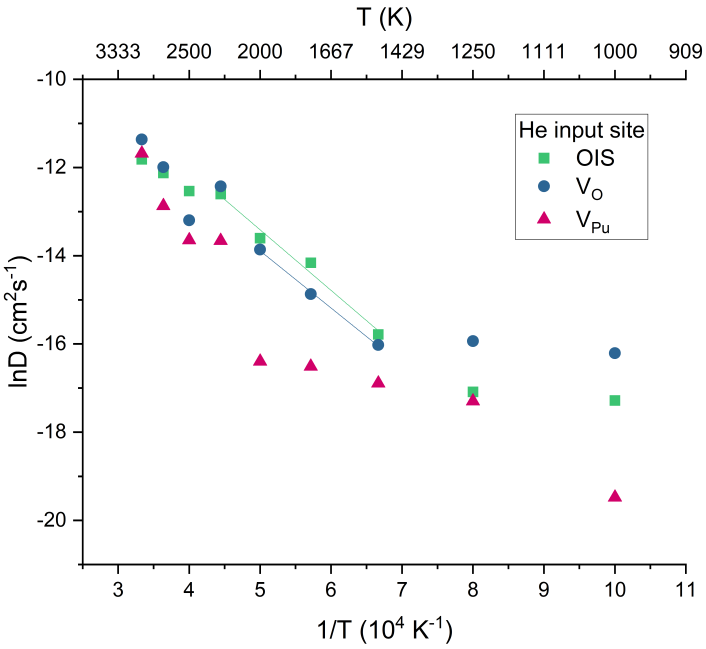


Figure 7.20: Helium diffusivity in a PuO_2 lattice with a 2% concentration of Schottky trio defects. The helium atoms were input in OIS, V_O and V_{Pu} in separate simulations for comparison. The lines of best fit for the Arrhenius behaviour calculations are also plotted.

Schottky in the previous chapter. These comparable activation energies reinforce the finding that helium diffusion is governed by the availability of oxygen vacancies and therefore the diffusivity of oxygen. No Arrhenius behaviour was exhibited for helium input in V_{Pu} sites.

Figure 7.21 displays the trajectories of the He atoms when input in V_{Pu} and V_O sites at 2250 K. It can be observed that when the helium atoms were input in a V_{Pu} (Figure 7.21b) there is significantly less inter-site hopping than when the helium atoms begin in an V_O (Figure 7.21a). From inspection in OVITO it was found that none of the helium atoms input in an V_O (Figure 7.21b) remained in their input

Table 7.4: Parameters calculated from Arrhenius behaviour exhibited by helium in PuO_2 with a 2% Schottky concentration with different helium input sites

He input site	E_a (eV)	D_0 (cm^{2}s^{-1})	r-square
OIS	1.01 ± 0.05	5.13E-04	0.99667
V_O	1.12 ± 0.06	6.05E-04	0.99817

sites. In contrast, 56% of He input in a V_{Pu} remained in the same V_{Pu} site. Upon analysis of the final states of Figure 7.21, it was found that in both cases roughly 70% of He occupy V_{Pu} sites, with the remaining 30% occupying OIS. Zero helium atoms occupy V_O sites, suggesting that oxygen vacancies are not helium trap sites. Rather, it has been determined that oxygen vacancies facilitate helium migration. The finding of plutonium vacancies acting as helium traps is in agreement with the energy barrier calculated from Figure 7.2 for helium to leave a V_{Pu}. Similarly, a reduction in helium diffusivity was also found by Govers *et al.* [203] in UO_2, when He atoms are input at V_U sites.

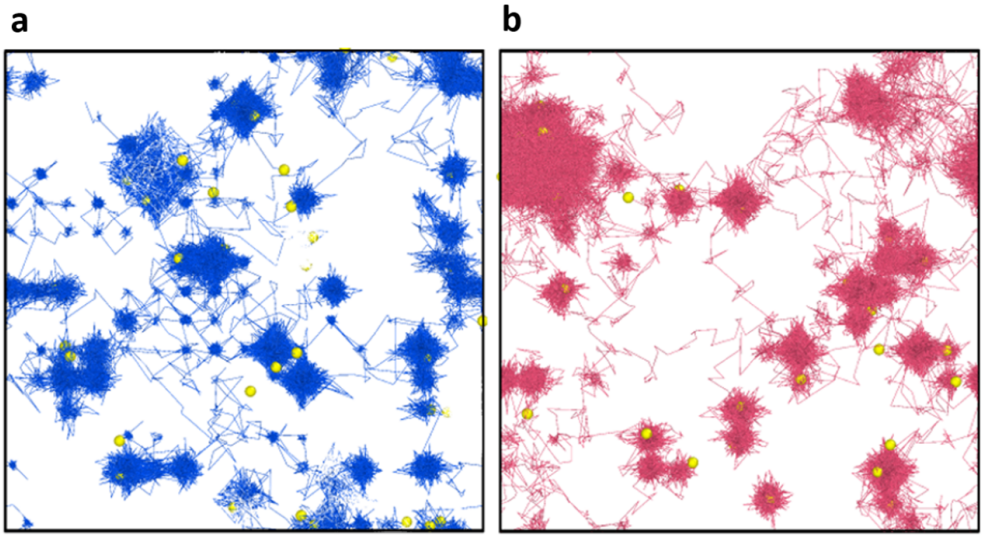


Figure 7.21: Trajectory of helium atoms in PuO_2 with a 2% Schottky defect concentration at 2250 K over 1 ns. (a) Displays the trajectory when the helium started in V_O sites (blue lines) and (b) when the helium atoms started in V_{Pu} sites (pink lines). There is much less inter-site hopping when helium atoms are input at plutonium vacancies.

It must be noted that these simulations were only run for 1 ns. It is predicted that if the simulations were run for 5 ns, a plateau in helium diffusivity may be observed at high temperatures. It is suggested that such behaviour would be due to helium atoms migrating to form clusters surrounding the plutonium vacancies in the Schottky defects and becoming trapped. The behaviour would be similar to that displayed in Figure 7.3.

7.5.3.2 Plutonium Frenkel Pairs

Figure 7.22 displays the diffusivity of helium in a PuO_2 lattice containing 0.5% PuFPs when starting in an OIS or V_{Pu}. It can be seen that regardless of the helium input site, the calculated values of helium diffusivity were similar. This finding was unexpected, as plutonium vacancies are proposed to act as helium traps and so were anticipated to reduce helium mobility. Furthermore, when helium atoms occupied V_{Pu} sites in the lattice containing Schottky trios (Figure 7.20), at low temperatures the helium diffusivity was significantly lower.

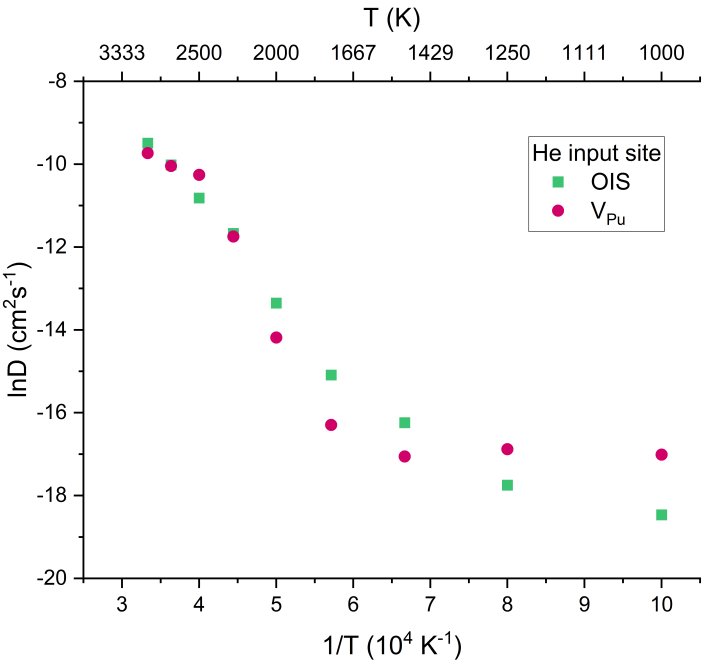


Figure 7.22: Helium diffusivity in a PuO_2 lattice with a 0.5% concentration of plutonium Frenkel pairs. The helium atoms were input in OIS and PuFPs in separate simulations for comparison.

Upon inspection of the simulations, it was found that the majority of plutonium Frenkel pairs would recombine; the Pu interstitials displaced He atoms from V_{Pu} sites. Figure 7.23 displays the configurations of the simulation at t=0 and after 1 ns illustrating the PuFP recombination. It can be concluded that the energetic benefit of helium being in the Pu vacancy was outweighed by the drive for plutonium Frenkel pairs to recombine, as the defect energy of a PuFP is high [49], [121], [130], [131].

Due to the annihilation of the plutonium Frenkel pairs forcing helium atoms into

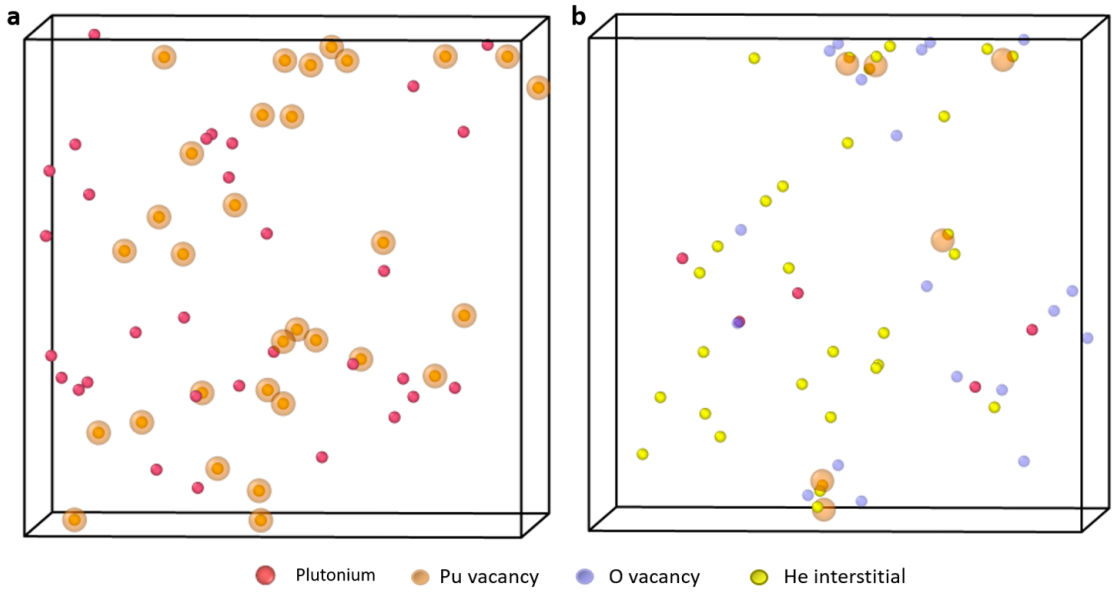


Figure 7.23: Visualisation from MD simulation of a PuO_2 lattice with 0.5% He and 0.5% PuFPs, with the He input in the V_{Pu} sites at 2250 K. (a) Displays the input configuration, the PuFPs can be seen with helium atoms occupying the vacancy sites. (b) Displays the configuration after 1 ns, the majority of the PuFPs have recombined with helium atoms now in interstitial sites.

OISs, the similarity of diffusivities displayed in Figure 7.22 can easily be explained; in both cases the majority of helium atoms occupy OISs throughout the simulation. As can be seen in Figure 7.23 at high temperatures oxygen vacancies are available. It was found that helium is mobile via these oxygen vacancies.

In addition, at lower temperatures oxygen defects were rapidly generated surrounding the PuFPs. Figure 7.24 displays the configuration of lattice after MD has been run at 1250 K for 2 ps (the second dump file, time step 2000, before PuFP recombination). Oxygen vacancies surrounding the PuFPs can be seen in Figure 7.24. This generation of oxygen defects at lower temperatures when PuFPs are present is likely due to the distortion the lattice will experience from accommodating the PuFP as discussed in Section 3.6.1. Also, the additional oxygen defects may be present in the vicinity of plutonium vacancies to stabilise the negative charge. As such, the helium diffusivity in these simulations can be understood by the presence of oxygen vacancies available for helium migration.

Upon comparison of Figures 7.3 and 7.22, which display helium diffusivity in pure PuO_2 and PuO_2 with a 0.5% PuFPs concentration respectively, it can be seen that the helium diffusivity values in both lattices are almost identical above approximately 1500 K. In the lower temperature region, the higher diffusivity values

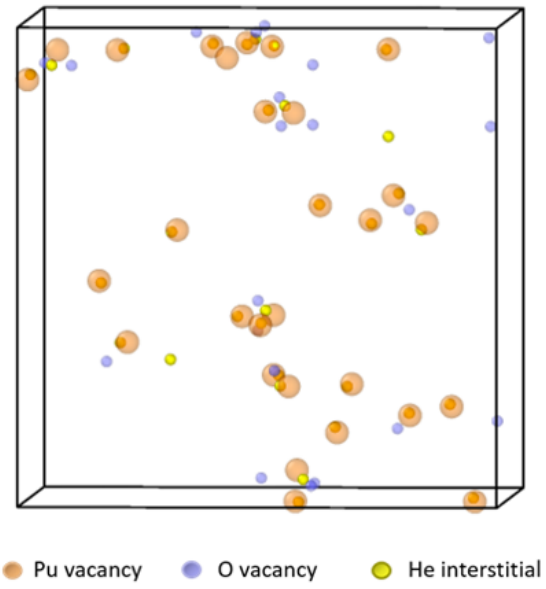


Figure 7.24: Visualisation from molecular dynamics simulation of a PuO_2 lattice with 0.5% He and 0.5% PuFPs, with the He input in the V_{Pu} sites at 1250 K at 2 ps. Pu and O atoms have been removed for clarity.

for helium displayed in figure 7.22 may be due to the presence of oxygen vacancies at lower temperatures to stabilise the PuFPs. Once helium has been ejected into an OIS from a V_{Pu} due to PuFP recombination, helium can migrate via the OIS-V_O-OIS pathway due to the presence of additional oxygen vacancies. Therefore, as was found for the initially pure lattice, it can be concluded that the governing factor of helium diffusivity is the generation of oxygen type defects.

Finally, it is noted that these simulations indicate that the occupation of a plutonium vacancy by a single helium atom is not sufficient to prevent PuFP recombination.

7.5.3.3 Plutonium Vacancies

To enable the diffusion behaviour of helium input in V_{Pu} to be investigated, a lattice was generated containing 0.5% Pu vacancies with no respective interstitials. As such, the lattice was no longer charge neutral. Two initial configurations were considered: helium occupying OISs and helium occupying plutonium vacancies. These simulations were run for 700 ps after a 300 ps equilibration period.

Figure 7.25 displays the diffusivities of helium when starting in the OIS and V_{Pu} sites. In the low temperature region ($T < 1500$ K) it can be seen that helium atoms

input in plutonium vacancies exhibit no diffusive behaviour, they remained in their input V_{Pu} sites. For helium atoms input in OIS, the majority (87%) remained in their input sites with a few diffusing to a V_{Pu} via oxygen vacancy assisted diffusion. The oxygen vacancies were observed to be generated in the vicinity of some plutonium vacancies, likely to stabilise them.

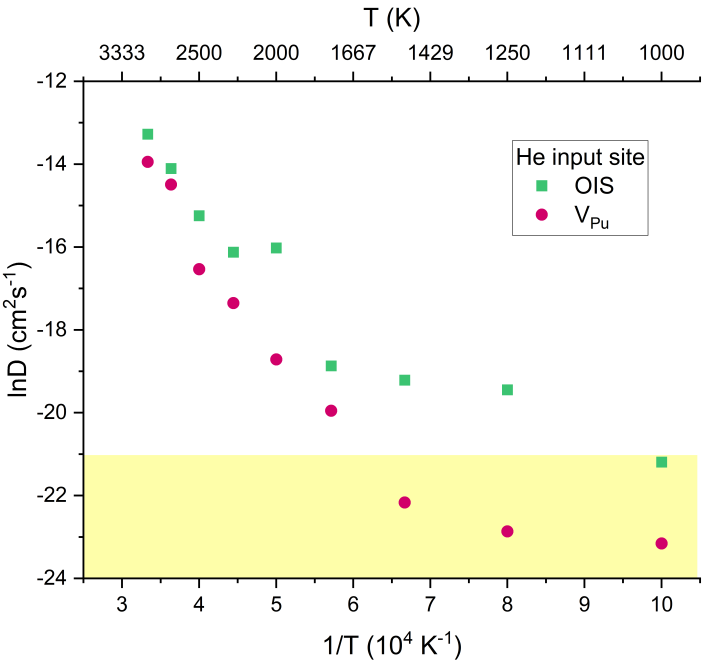


Figure 7.25: Helium diffusivity in a PuO_2 lattice with a 0.5% concentration of plutonium vacancies. The helium atoms were input in OIS and V_{Pu} in separate simulations for comparison. The yellow highlighted region indicates no diffusive behaviour.

In the higher temperature region of Figure 7.25 (T > 1500 K) the calculated diffusivity values of helium when input in OISs and V_{Pu}s were surprisingly similar. To understand the behaviour of helium in these simulations the trajectories of helium atoms were analysed further.

Figure 7.26 illustrates the trajectories of the He atoms during two time intervals for both starting configurations at 2250 K. It can be seen that whilst the diffusivity value calculated for He from both simulations was similar, trajectories of the helium atoms show significant differences. During the first interval (0-300 ps) the He occupying plutonium vacancies oscillate around their vacancy site and some oxygen vacancies are generated surrounding some of the V_{Pu} sites. Conversely, the OIS start system displays lots of interstitial site hopping and high levels of diffusion,

with many helium atoms migrating to the plutonium vacancies. The second time period shows similar behaviour for both simulations, with almost all helium atoms occupying V_{Pu} sites. This suggests that helium will always diffuse to plutonium vacancies if they are available. Additionally, it was found for the simulation in which helium was input in plutonium vacancies, two helium atoms exhibited diffusion via oxygen vacancies generated in the vicinity of plutonium vacancies.

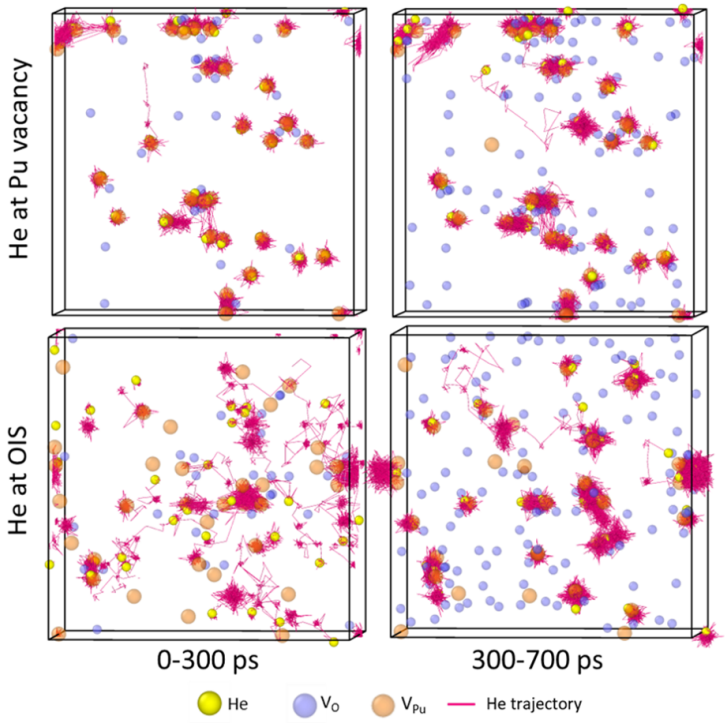


Figure 7.26: Trajectory of helium atoms in PuO_2 with 0.5% plutonium vacancies at 2250 K. The simulation is split into two time periods. The top row illustrates the trajectory when He is input at V_{Pu} sites and the bottom row when He is input at OISs. 0-300 ps shows He in OIS with high mobility. 300-700 ps shows He occupying V_{Pu} sites.

In contrast, Govers *et al.* [203] found that in UO_2, when the lattice contains uranium vacancies, He diffusion is greatly decreased when a He is input at a V_U versus at an OIS. However, their simulations were run for 25 ps, so it is suggested that the duration was not long enough for the He to migrate from the OIS to the V_U sites, as found in this work.

Comparing the diffusivity values of Figure 7.25 to those of the lattice with PuFPs (Figure 7.22) it can be seen that the diffusivities are on average slightly lower for the lattice containing only V_{Pu} defects. It is suggested that this is due to the increase in lattice distortion for PuFP accommodation versus that of a V_{Pu}. As was

discussed in Chapter 3, PuFP lattice distortion occurs around both the vacancy and the interstitial plutonium site. This increase in lattice distortion could enable the formation of more oxygen Frenkel pairs and therefore more oxygen vacancies would be available for helium diffusion in the lattice containing PuFPs.

7.5.3.4 Oxygen Frenkel Pairs

A lattice with 0.5% oxygen Frenkel pairs was constructed and helium input in the oxygen vacancies and OISs in separate simulations. Figure 7.27 displays the diffusivities calculated from the molecular dynamics simulations. It can be seen that there is little difference in helium diffusivity when starting in an oxygen vacancy or an OIS. This was expected as the energy barrier for an V_O-OIS hop was calculated in Section 7.3 to be 0.3 eV. Upon inspection of the trajectories it was indeed found that helium would migrate from an V_O to an OIS within the first 100 ps of the simulation, likely due to the low energy barrier for migration. Therefore the input position of a helium atom in a lattice with OFPs has limited influence on helium diffusivity as helium will either start in, or migrate to an OIS.

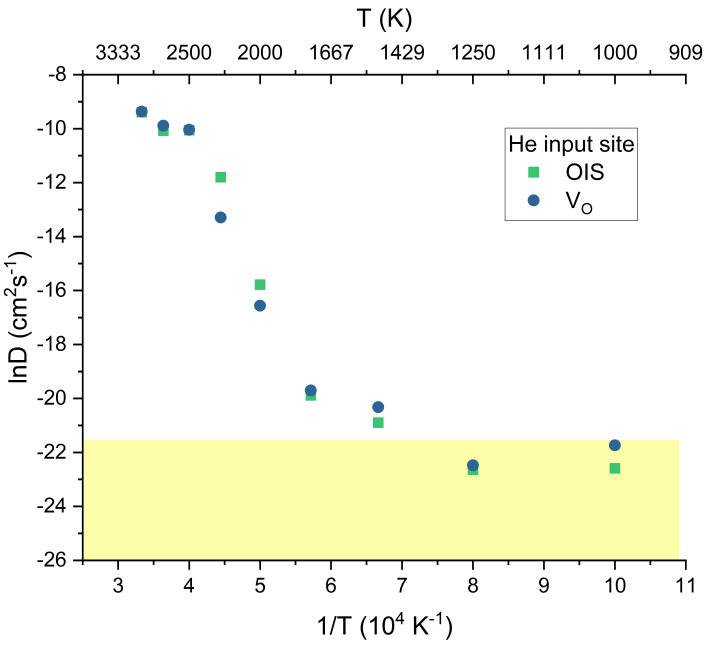


Figure 7.27: Helium diffusivity in a PuO_2 lattice with a 0.5% concentration of oxygen Frenkel pairs. The helium atoms were input in OIS and V_O in separate simulations for comparison. The yellow highlighted region indications no diffusive behaviour.

Figure 7.28 displays the configurations of the oxygen Frenkel pairs and helium

atoms at t=0 and t=1 ps. It can be seen that some helium atoms immediately make the V_O-OIS hop. However, unlike the lattice containing PuFPs discussed in Section 7.5.3.2, helium migration to OISs was not due to Frenkel pair recombination. Instead, it was due to the hop being energetically feasible.

From 7.28 it can be seen that the oxygen Frenkel pairs remain in the lattice, despite the helium atoms no longer occupying some of the oxygen vacancies. It was observed that many of the oxygen Frenkel pairs did recombine and in the higher temperature simulations more were then generated. This was expected; the continual formation and annihilation of oxygen Frenkel pairs has been predicted for PuO_2 due to the low formation energy of such defects [49]. The generation of dynamic oxygen Frenkel pairs is more frequent at higher temperatures. At lower temperatures those which recombine are unlikely to be regenerated elsewhere [187], resulting in no long scale diffusion below 1400 K as dispalyed in Figure 7.28. Due to OFPs being mainly governed by temperature regardless of the input, the diffusivities plotted in Figure 7.27 are similar to those found in initially defect-free PuO_2 (Figure 7.3).

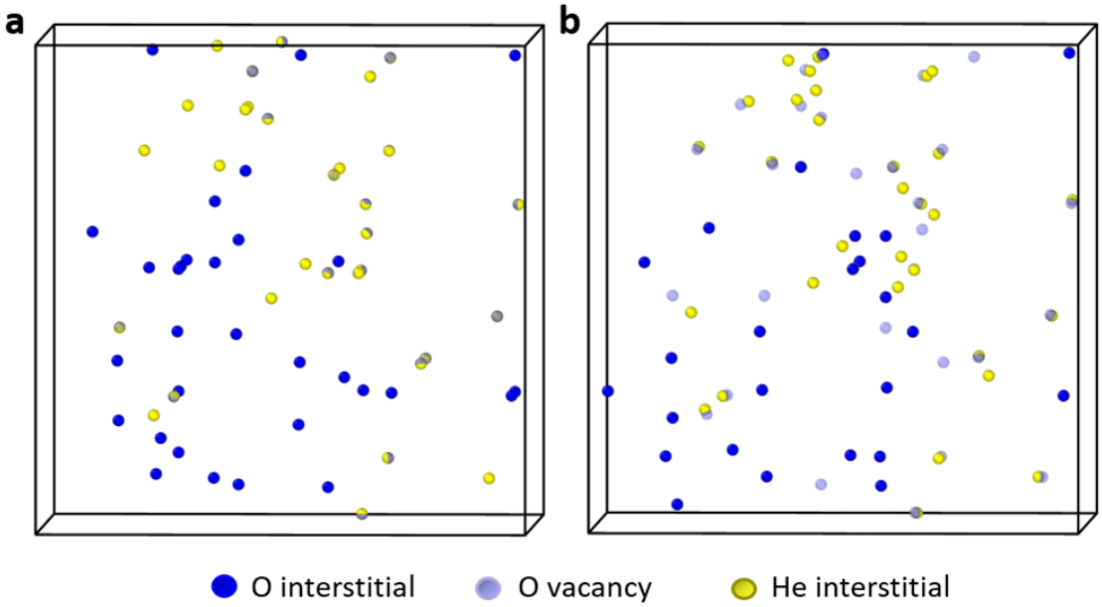


Figure 7.28: Visualisation from MD simulation of a PuO_2 lattice with 0.5% He and 0.5% oxygen vacancies, with the He input in the V_O sites. (a) Displays the input configuration, the OFP can be seen with helium atoms occupying the vacancy sites. (b) Displays the configuration after 1 ps, some helium atoms now occupy OIS, but the OFPs have not recombined.

Although both oxygen and plutonium Frenkel pair recombination has been observed, with helium then occupying OISs, a significant difference in mechanism was

identified. For the lattice containing PuFPs, helium is ejected from the vacancy due to the Frenkel pair recombination. In the lattice containing OFPs, helium migrates from the Frenkel pair due to the low energy barrier for the V_O-OIS pathway, then the OFP often recombines.

7.5.3.5 Oxygen Vacancies

A lattice containing 0.5% oxygen vacancies and 0.5% helium atoms was constructed. Molecular dynamics simulations were run over a range of temperatures with all helium atoms input in either OISs or oxygen vacancies. The simulations had an initial 300 ps equilibration period, then were evolved for a further 700 ps. Figure 7.29 displays the diffusivities calculated from these simulations.

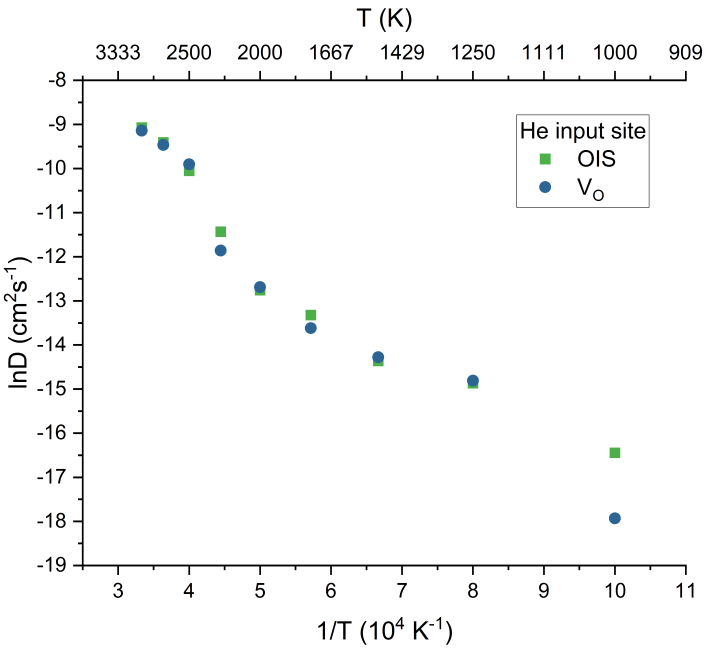


Figure 7.29: Helium diffusivity in a PuO_2 lattice with a 0.5% concentration of oxygen vacancies. The helium atoms were input in OIS and V_O in separate simulations for comparison.

It can be seen from Figure 7.29 that the helium input in a lattice containing oxygen vacancies has little impact on the diffusivity values calculated. It was found that the diffusivity values were higher than those calculated for the lattice containing OFPs, which is likely due to the oxygen vacancies remaining in the lattice throughout the simulation. Therefore, oxygen vacancies are always present in the lattice to

facilitate helium diffusion via the OIS-V_O-OIS mechanism. Continual annihilation and generation of OFPs was observed in the lattice containing OFPs. Due to this, oxygen vacancies were not always available, especially in the low temperature region in which oxygen is less mobile.

The MSDs of helium input in OISs and oxygen vacancies at 2250 K are plotted in Figure 7.30. It can be seen that unlike the lattice containing plutonium vacancies, there is little difference in the MSD of helium atoms input in interstitial or vacancy sites. As discussed in Section 7.5.3.4, this is likely due to the low energy barrier for an V_O-OIS hop, resulting in helium quickly leaving the initial V_O sites and then in both scenarios diffusing via the OIS-V_O-OIS pathway.

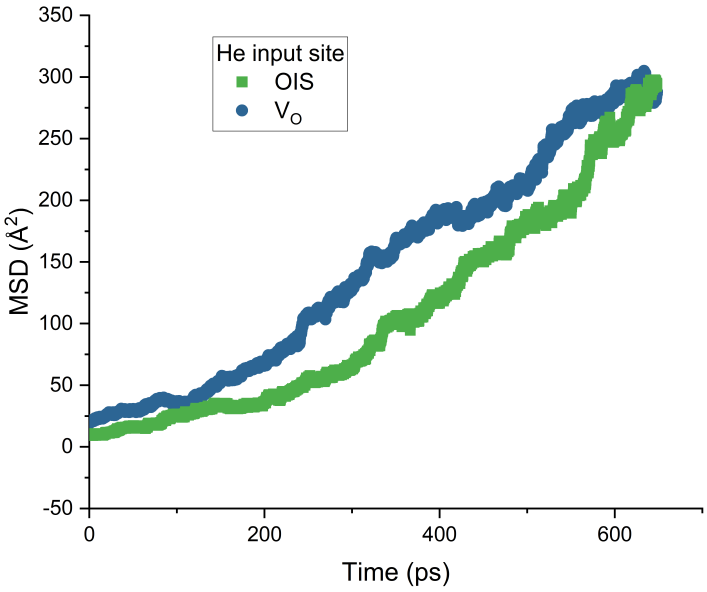


Figure 7.30: Helium MSD in a PuO_2 lattice with a 0.5% concentration of oxygen vacancies at 2250 K. The helium atoms were input in OIS and V_O in separate simulations for comparison.

7.6 Conclusions

The ZBL [74], Aziz [206] and Parfitt [46] potentials were used in combination to investigate helium diffusion in PuO_2. Results calculated via these potentials have been evaluated against a range of literature values and as such proved to be suitable.

NEB calculations were performed to calculate helium migration energy barriers in PuO_2. The main helium diffusion mechanism proposed is oxygen vacancy assisted inter-site hops with helium and oxygen having comparable diffusion rates. Plutonium vacancies have been found to act as traps for helium, significantly reducing helium diffusion. The helium migration energy barriers calculated in this work are of a similar order to those found for helium diffusion in UO_2 [203].

It has been determined that in defect-free PuO_2, helium exhibits limited diffusive behaviour until the temperature exceeds 1500 K. Helium diffusion under 1500 K will occur but by rare events which take place over longer timescales than those considered in this work. However, it was found that when vacancies are present within the lattice, the helium diffusion energy barrier is significantly reduced and helium atoms exhibit diffusive behaviour at lower temperatures (via OIS-V_O-OIS pathways). Therefore whilst the storage of PuO_2 will be at temperatures well below 1500 K, due to the presence of defects within the lattice we suggest that helium will be mobile in PuO_2 under conditions relevant to storage.

It is suggested that a main factor governing He diffusion in nuclear materials is the level of damage present in the lattice, with oxygen vacancies dramatically increasing He diffusion rates. As PuO_2 has higher radioactivity which leads to higher rates of self-irradiation damage, it is predicted that there may be higher rates of He diffusion in PuO_2 than in UO_2.

A correlation between helium clustering and a reduction in diffusivity has also been found.

Chapter 8

Helium Clustering

This chapter investigates helium clustering behaviour in PuO_2 via three computational techniques: energy minimisation, nudged elastic band calculations and molecular dynamics simulations. Some of this work has been published in:

E. Murray, Y. Zhou, P. Slater, R. Smith, P. Goddard, and H. Steele. "Atomistic Simulation of Helium Diffusion and Clustering in Plutonium Dioxide" *Physical Chemistry Chemical Physics*, vol. 24, pp. 20 709–20 720, 35 2022 [186].

8.1 Literature Review

From analysis of helium clustering in a range of materials, Wolfer [45] suggests that helium atoms and lattice vacancies are likely to cluster together in Pu, and these clusters could act as precursors to helium bubbles. Helium clusters were observed in an annealed Pu-Ga alloy by Zocco [215] via Transmission Electron Microscopy (TEM). Zocco [215] found helium to move and agglomerate, forming fine bubbles in grain interiors and larger bubbles in grain boundaries. This corroborates with molecular dynamics simulations of Pu performed by Ao *et al.* [56], in which they found grain boundaries to be energetically favourable for interstitial helium atoms. From analysis of irradiated MOX fuel pins, Katsuyama *et al.* [216] predicts that helium clustered at grain boundaries may be released from the lattice. Roudil *et al.* [188] used mass spectrometry to measure helium outgassing from a natural uranium oxide sample. It was found that about 33% of the helium was trapped in the matrix and vacancy defects. From high-resolution TEM analysis, helium was observed to have coalesced in small bubbles with an average maximum size of 20 nm.

Discussion of what factors may determine helium clustering in PuO_2 can be

drawn from studies of UO_2. Garcia *et al.* [191] implanted UO_2 samples with approximately 0.1 at% He. From their experiments, Garcia *et al.* [191] suggests that the concentration of helium does not control bubble nucleation. Rather, the level of damage in the lattice controls bubble formation. They found the bubble nucleation mechanism is akin to heterogeneous nucleation and results from the formation of vacancy clusters in the core of damage cascades, which act as sinks for insoluble elements. Garcia *et al.* [191] predicts that bubble nucleation will hinder helium movement at temperatures below 1273 K.

From measuring helium release from aged UO_2 samples, Talip *et al.* [189] also predicts helium to be mobile at temperatures above 1300 K, and that the helium will migrate to form and join bubbles. However, in contrast to the predictions of Garcia *et al.* [191], Talip *et al.* [189] found that between 1500 to 1600 K, all helium atoms are trapped by existing bubbles. As such, the helium release rate decreases and bubble growth becomes significant. Above 1600 K, they suggest that the release of helium may be via the diffusion of bubbles to grain boundaries.

A key part of this study is investigating the He:Vacancy ratios of stable clusters within PuO_2. At present, no studies discussing this are available for PuO_2, however some for UO_2 and Pu are available, in addition to other metals.

Van Brutzel *et al.* [217] used molecular dynamics to investigate helium bubbles in UO_2. They studied four bubble sizes (diameters: 1, 2, 5 and 10 nm) over a range of temperatures and from this determined a saturation concentration of helium atoms that can be incorporated into the bubble. The concentration limit was equal to a He:Vacancy ratio of 1.6:1.

Liu *et al.* [218] investigated fission gas bubbles in UO_2. Their study focused mainly on xenon and found that xenon clusters on average had xenon to uranium vacancy ratios of approximately 1:1. Liu *et al.* [218] determined a key factor in bubble nucleation rates to be the low mobility of uranium ions, which led to fewer nucleation sites for xenon. They also suggest that helium will have a much higher mobility than xenon.

Via molecular dynamics simulations, Ao *et al.* [219] studied He:Vacancy ratios of helium in metallic Pu. Their work found the maximum energetically favourable cluster to have a He:Vacancy ratio of 6:1. This is significantly higher than that of He in Ga stabilised δ-Pu by Robinson *et al.* [220], in which a maximum stable ratio of 2:1 was determined. Similar ratios to that calculated by Robinson *et al.* [220] were obtained in UO_2 by Van Brutzel *et al.* [217] and Liu *et al.* [218] for He and Xe respectively.

Defining a cluster by its He:Vacancy ratio enables direct comparison of clusters of different sizes. For example, in iron, Gai *et al.* [207] found the optimal He:Vacancy ratio to increase from 1:1 for roughly five vacancies, up to approximately 4:1 for clusters containing 36 vacancies. As such, it is of importance to study clusters of significantly different sizes to ensure predictions remain correct. Helium is likely to be significantly more mobile in iron than PuO_2 due to the diffusion barrier being only 0.06 eV, compared to the 2.4 eV value calculated for interstitial helium in this work. Similarly to Gai *et al.* [207], Shi *et al.* [221] found the He:Vacancy ratio to be around 1.5:1 in most stable clusters in iron.

8.2 Energy Minimisation

8.2.1 *Procedure*

In Chapter 5 it was determined that plutonium vacancies are the most favourable sites for helium to occupy in PuO_2. From this, it was found that helium clusters can grow surrounding plutonium vacancies, plutonium Frenkel pairs, divacancies and Schottky trios. As discussed by Neilson *et al.* [132], plutonium vacancies are energetically unstable in PuO_2 so have a low helium solution energy. Therefore, a Schottky trio was selected as the seed site for He clustering as it is both an energetically stable defect in PuO_2, containing a stable V_{Pu}, and has a low helium incorporation energy.

To investigate and compare clusters, clusters were defined by their He:Vacancy ratio. Three seed comprised of 1, 2 and 4 Schottky trios were chosen which contained 3, 6 and 12 vacancies respectively. A He:Vacancy cluster containing 1 Pu and 2 O vacancies can be written as both He_nV_3 and He_nSch_1. Where V indicates vacancy, Sch indicates Schottky trio and n is the number of He atoms. From the 2:3 He:Vacancy clusters displayed Figure 8.1a, it can be seen that this enabled comparison of larger clusters due to their common He:Vacancy ratios.

As displayed by Figure 8.1b, for each He_nV_m cluster, there are many configurations for the n He atoms. An iterative procedure was followed to find the lowest energy and therefore most stable configuration. The procedure was as detailed in the schematic in Figure 8.2. The procedure consisted of two minimisation steps: first helium atoms were added to the vacancy area then the lattice minimised via a damped dynamics method. Next the helium atoms were randomly displaced in the x, y, z directions and the lattice was minimised again via the conjugate gradient method. At this point the relaxed structure was inspected; if helium atoms had dis-

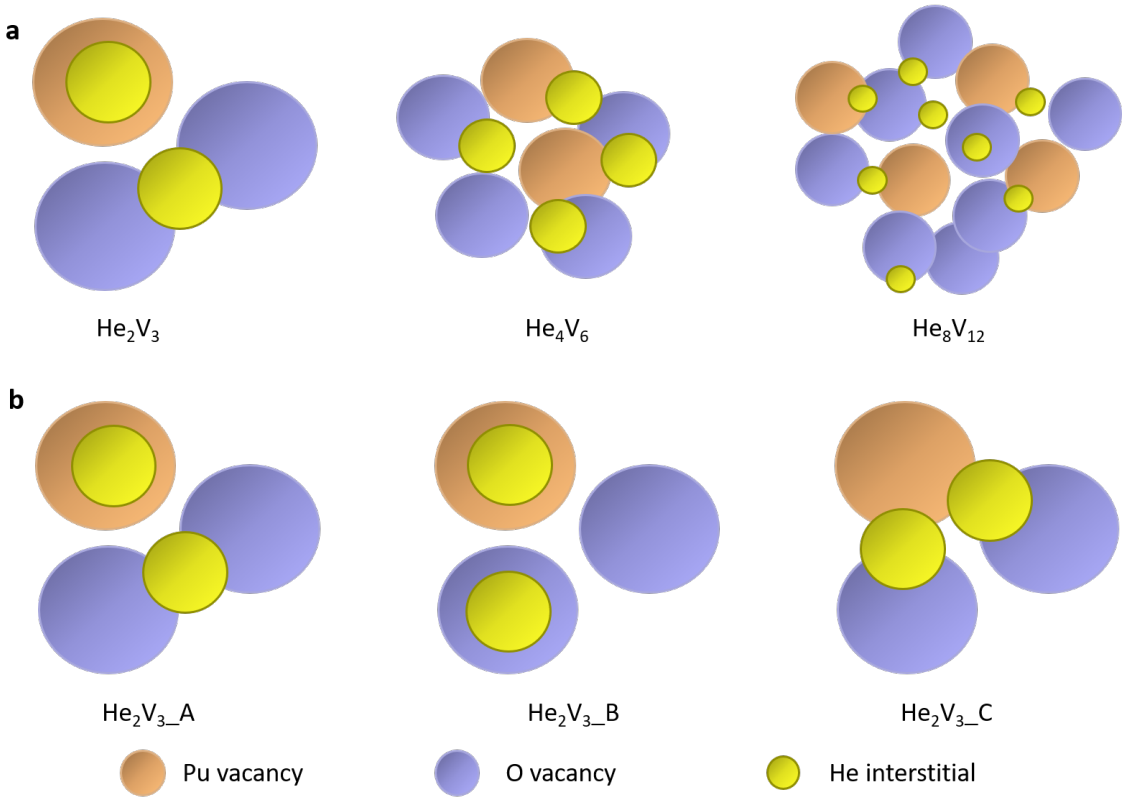


Figure 8.1: Examples of naming conventions of He:Vacancy clusters. (a) Displays examples of He:Vacancy clusters which all have a 2:3 ratio, but are based on 1, 2 and 4 Schottky trio defects. (b) Displays three possible configurations of the He_2V_3 cluster.

banded, the configuration was disregarded. If instead the helium atoms remained clustered in the vacant area, the minimum energy was recorded.

By following this procedure at least 10 configurations for each He:Vacancy ratio were trialled. Due to the high energy barriers of He migration, random walks were often unable to find new stable cluster configurations. Instead many different input configurations were manually tested, similarly to Chapter 5.

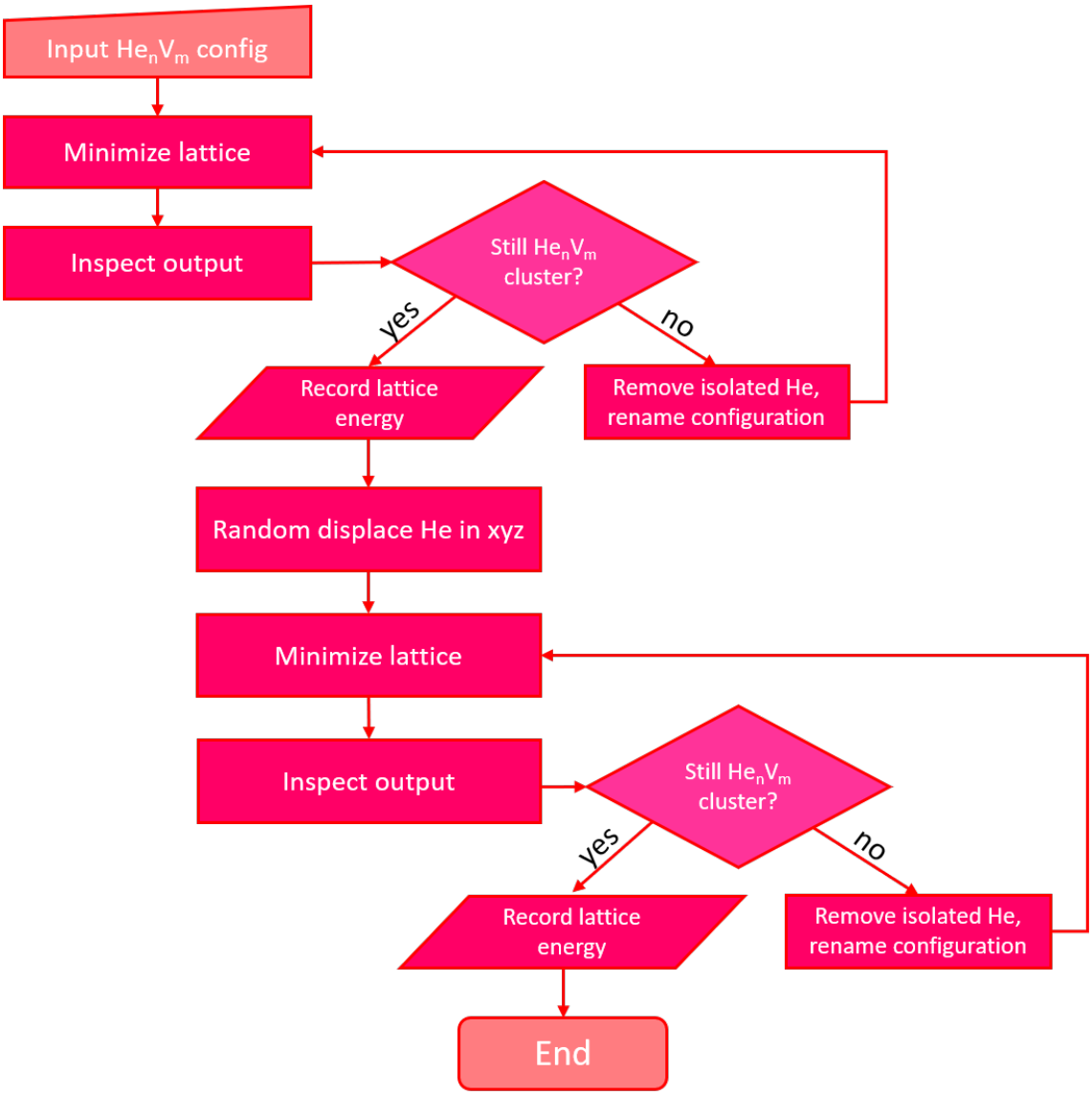


Figure 8.2: Flow chart detailing methodology followed for helium cluster energy minimisation calculations.

8.2.2 *Example:* He_3V_3

The procedure detailed in Figure 8.2 was performed for many configurations of up to 14 helium atoms surrounding one Schottky trio (three vacancies).

Figure 8.3 displays a schematic of an example energy minimisation procedure for a He_3V_3 configuration. The sub figures show as follows:

(a) The He_3V_3 configuration is input and the energy minimisation procedure run

(b) The configuration of the minimised He_3V_3 configuration. The lattice energy of this configuration will be recorded. The helium atoms will then be randomly

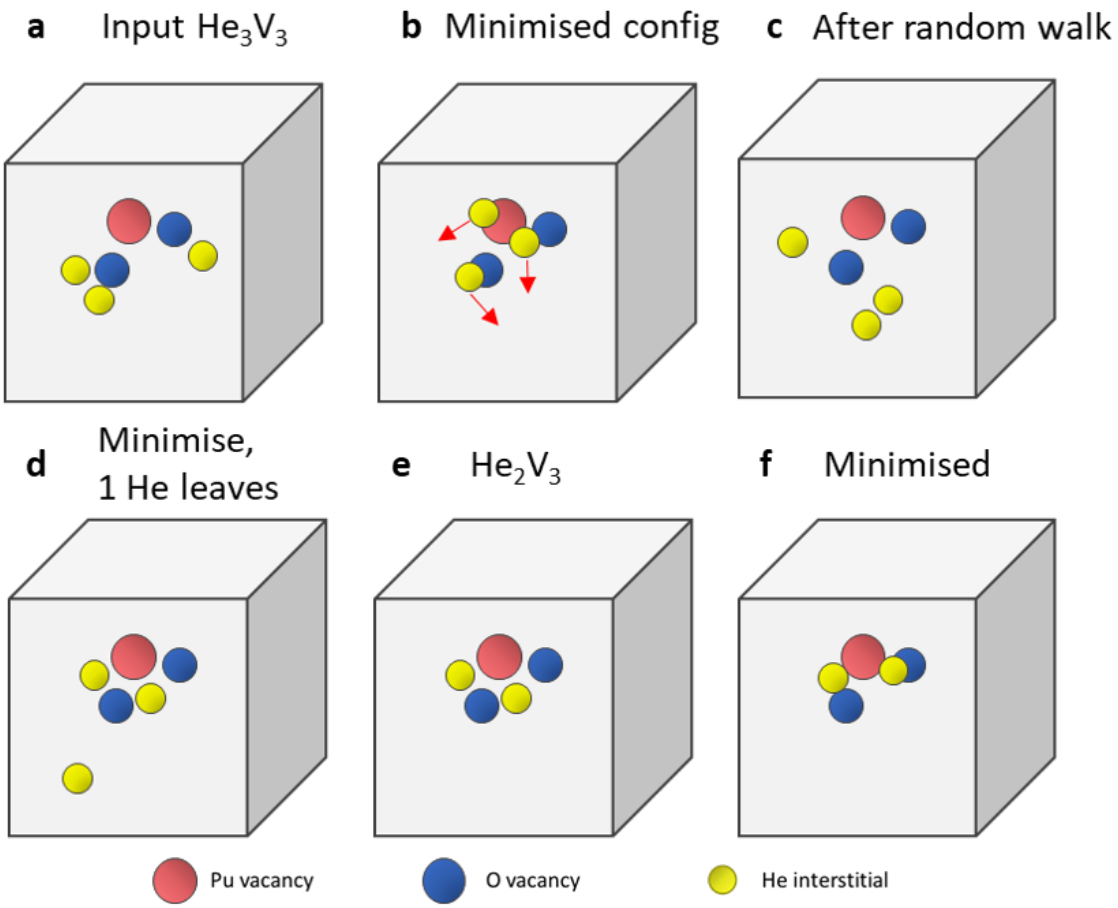


Figure 8.3: Example schematic of the energy minimisation procedure outlined in Figure 8.2. Each subfigure is discussed in the text.

displaced in x, y, z directions as shown by the arrows

(c) The helium atoms after they have been randomly displaced

(d) The configuration after the second energy minimisation, it can be seen that one helium atom is no longer part of the cluster

(e) The outside helium atom has been removed and so the cluster renamed to be a He_2V_3 configuration

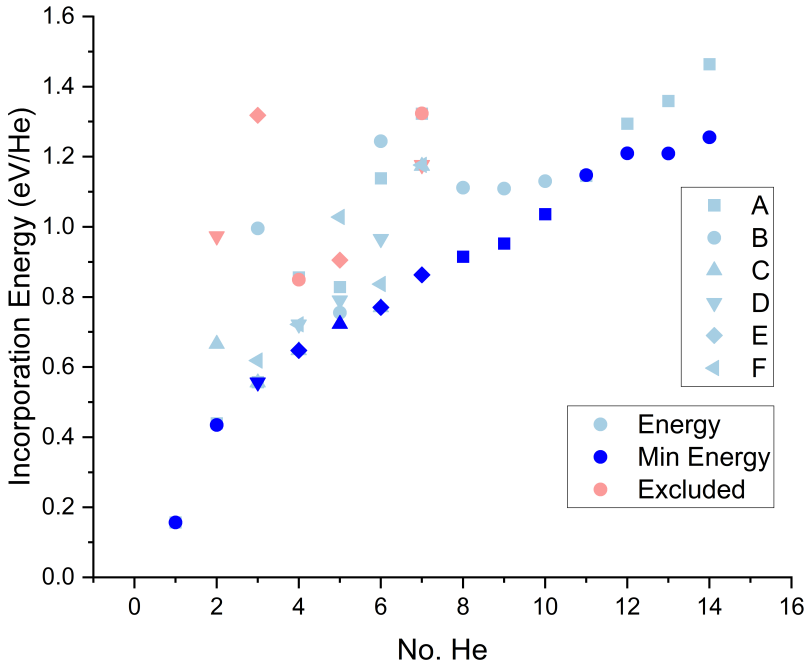
(f) The minimised configuration of the He_2V_3 cluster, the lattice energy will be recorded

It was found that in the majority of iterations, after the random walk, one or more helium atoms would become isolated from the cluster during the energy minimisation (e.g. as can be seen in Figure 8.3d). It is suggested that this was due

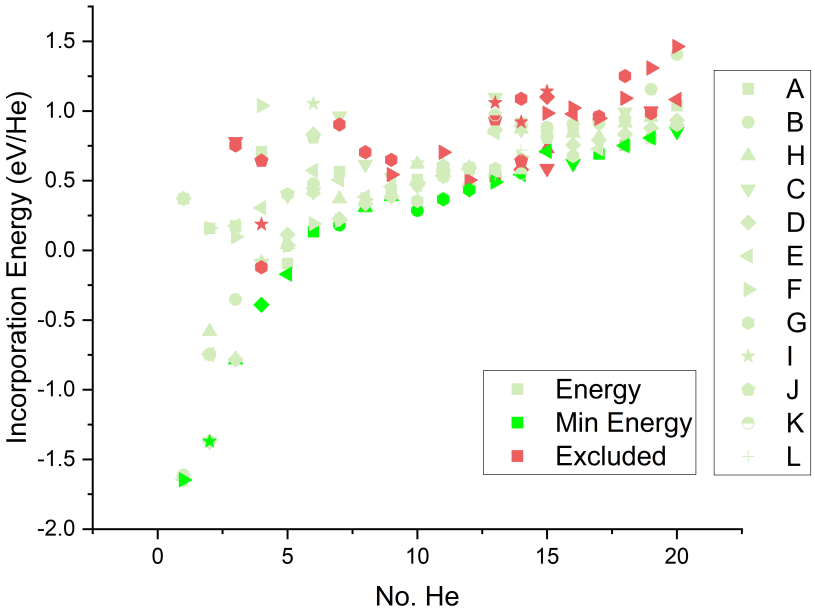
to the high energy barriers for helium migration and relatively low energy of helium incorporation in an interstitial site. As such, many input configurations had to be manually generated and the procedure detailed in Figure 8.2 performed many times.

8.2.3 *Results*

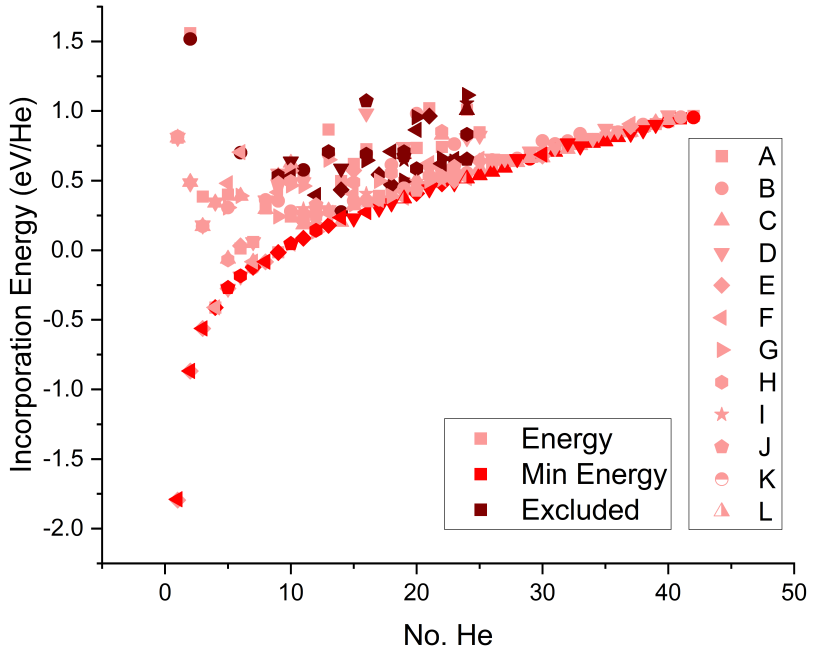
Figure 8.4 displays the calculated incorporation energies from the minimum energy configurations found via the methodology detailed above. It can be seen that for each cluster there is a range of configurations with a range of defect energies. The energies which were excluded due to helium migrating from the cluster, but only to a second or third nearest neighbour OIS, are also included but highlighted as ′excluded′.



(a) He_nV_3



(b) He_nV_6



(c) He_nV_{12}

Figure 8.4: Plots of the incorporation energies of multiple configurations of helium in clusters containing 1, 2 and 4 Schottky trios.

Figure 8.5 plots the minimum energy configurations obtained from four separate input configurations for the He_3V_6 cluster. It can be seen than configuration C resulted in the lowest incorporation energy. Of the other three configurations plotted in Figure 8.5, A was the only other viable option, but was eliminated due to it having a higher incorporation energy than C. Configurations B and D were non viable due to a helium atom leaving the cluster to an OIS (B) or with an V_O (D). From configuration B the helium atom which left the cluster was removed, and the cluster rerun for the He_2V_6 cluster calculation.

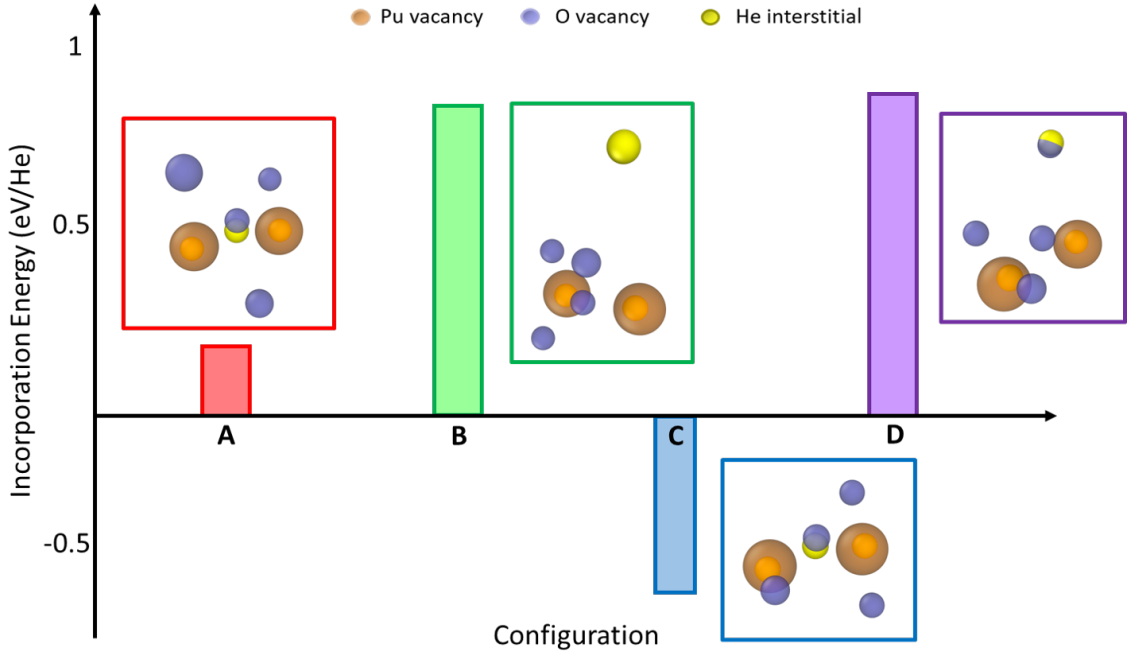


Figure 8.5: Incorporation energies and the minimum energy configurations for four different He_3V_6 input configurations (A, B, C and D). The output configurations are displayed colour coordinated with the bar chart energy for each configuration.

8.2.4 *Trapping Energies*

The normalised trapping energy was then calculated for the minimum energy configuration of each He:Vacancy ratio. The trapping energies E_T were calculated relative to the incorporation energy value obtained for He in an OIS as follows:

$$E_T = \frac{E_{\mathrm{Sch}_m}^{\mathrm{He}_n} - nE_{OIS}^{He} - mE_{Sch}}{n} \tag{8.1}$$

Where $E_{\mathrm{Sch}_m}^{\mathrm{He}_n}$ is the energy of n He atoms clustered at m Schottky trios, E_{OIS}^{He} is the incorporation energy of one He at an OIS equal to 1.7 eV. E_{Sch} is the defect

energy of an isolated Schottky trio. A negative E_T value indicates an energy decrease of the system when He migrates from an OIS to the cluster. A positive value means that energy is required to incorporate He at the cluster.

As seen by Figure 8.6, for all three seed sizes considered, a similar trend was found. The trapping energy increases rapidly up to a He:Vacancy ratio of approximately 0.5:1. Clusters with ratios larger than this size have a steady addition energy rate. The trapping energies are negative so there is an energetic drive for the helium atom to join the cluster rather than to remain isolated in the lattice. However at ratios greater than $\sim$ 3.5:1, no stable configurations could be found, with the helium atoms always leaving the cluster upon energy minimisation.

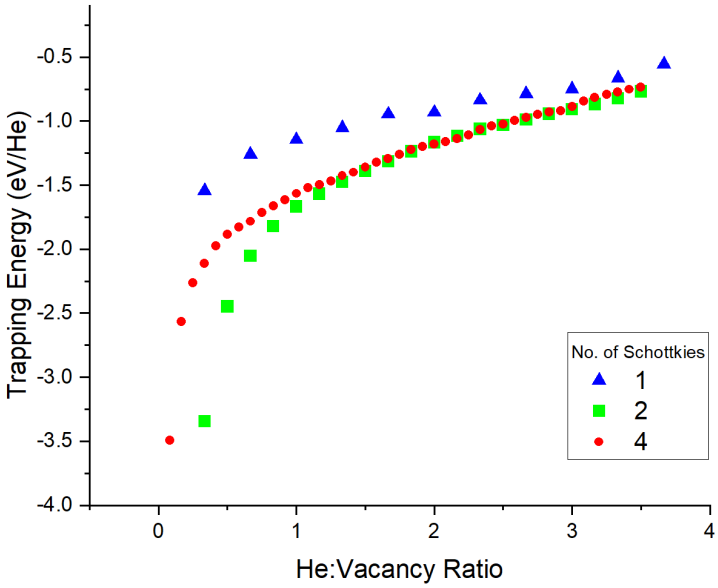


Figure 8.6: Trapping energies of He atoms at Schottky void sites as a function of a cluster's He:Vacancy ratio. A more negative trapping energy means a more energetically favourable site for helium to occupy. Three seed locations for the clusters were considered, made of 1, 2 and 4 Schottky defect clusters.

The successive incorporation energy for each He addition to a cluster was calculated. The energy of incorporation of a single He in an OIS was found to be 1.7 eV, so when the addition of He to a cluster is greater than this value, it would be more energetically favourable for the helium to remain at an isolated site rather than join the cluster. As shown by Figure 8.7, it was found that for all three Schottky sizes, the point at which the successive He addition energy exceeds that of 1.7 eV (orange line on plot) was when the ratio is roughly 3.2:1 helium atoms per vacancy.

In comparison, for metallic Pu, Ao *et al.* [219] found the maximum n/m ratio in a He_nV_m cluster to be 6:1 and the most energetically stable ratio to be 1:1 [222].

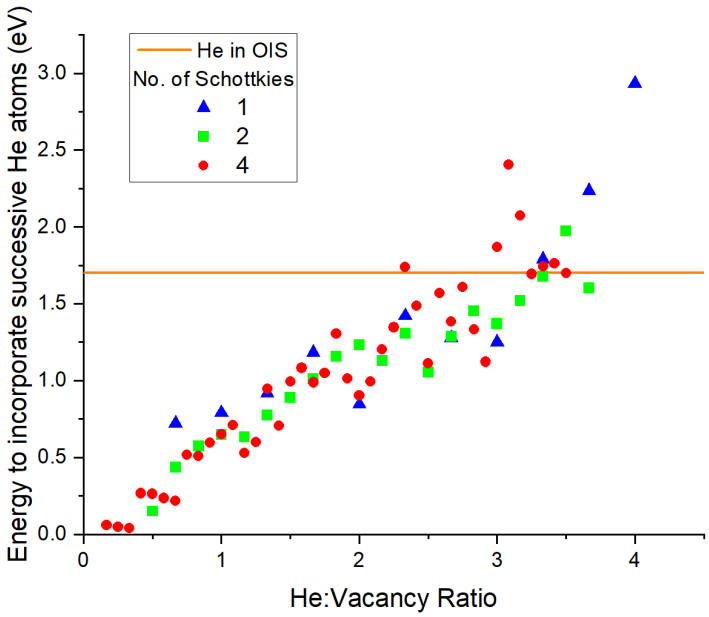


Figure 8.7: Energy to incorporate successive He atoms at Schottky void sites as a function of the cluster's He:Vacancy ratio. The orange straight line at 1.7 eV is the energy to incorporate He at an isolated OIS. When the incorporation energy is greater than this line it is less favourable for an additional He to join the cluster than to exist in isolation occupying an OIS.

8.3 Energy barriers

In order to gain an understanding of He accumulation into bubbles, a study was carried out to investigate the energetics of the barriers for He to diffuse into an existing bubble from an interstitial site. The migration energy barriers were calculated for He interstitials joining and leaving the minimised cluster configurations found in Section 8.2.3.

8.3.1 *Nearest Neighbour Position*

It was required to determine how far an interstitial site must be from a cluster so as to be considered 'distant', i.e. not to be affected by the cluster's strain field. For this, the six successively further nearest neighbour sites were identified. Figure 8.8 displays a schematic of nearest neighbour sites indicating how more distant sites were

assigned higher numbers. Table 8.1 displays the coordinates of each OIS considered. Helium was located in each OIS and the energy barrier for helium to migrate to the cluster from each site was then calculated.

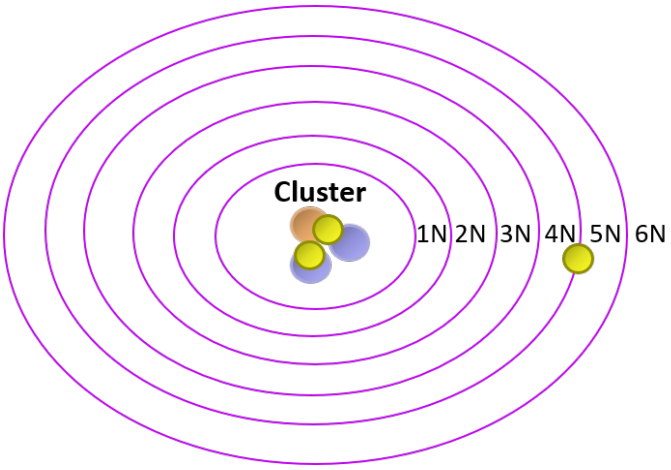


Figure 8.8: Schematic displaying the nearest neighbour positions surrounding a He_2V_6 cluster with a helium atom occupying the 5th nearest neighbour position (5N).

Table 8.1: Coordinates of the nearest neighbour octahedral interstitial sites moving further outwards

N	x (Å)	y (Å)	z (Å)
1	8.09	11.30	5.44
2	8.09	8.10	2.70
3	8.09	11.30	0.00
4	8.09	8.10	-2.68
5	8.09	11.30	-5.39
6	8.09	8.10	-8.10

Figure 8.9 displays the energy barriers for one helium atom to join a He_nV_3 helium cluster (where n = 2, 4, 6) from 1-6 nearest neighbour positions. It can be seen that for each cluster considered, the energy barrier for helium to join a cluster from the 1N position is significantly lower than for sites further away. This is likely due to the fact that at the 1N position, the helium atom is not screened by other lattice atoms from the cluster. The 6N input site will be used for all future calculations as this is a sufficient distance (approx. 18.7 Å) such that the barrier calculations for the larger clusters considered will not be skewed.

For all the minimum energy configurations found in Section 8.2.3, helium was added from the 6N position and then removed back to the 6N position and the

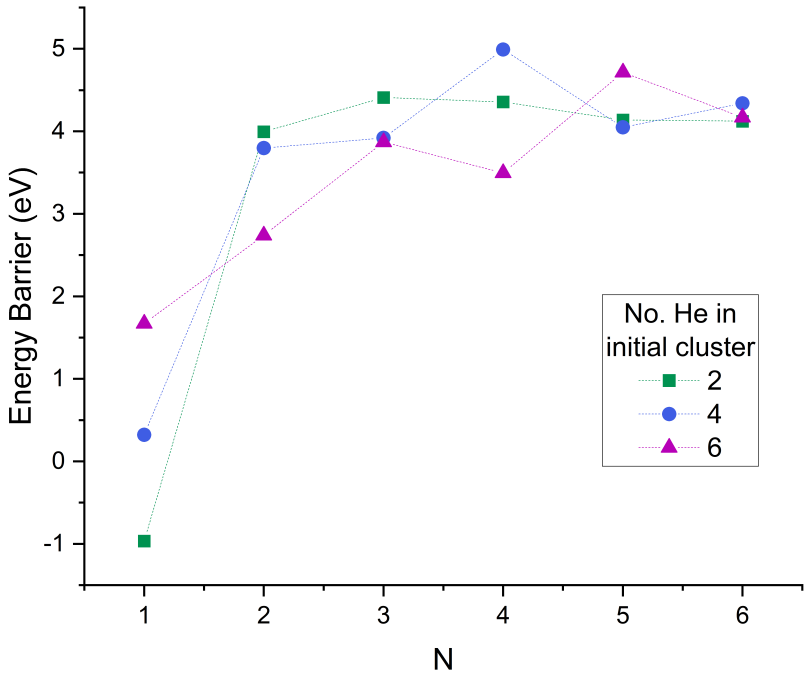
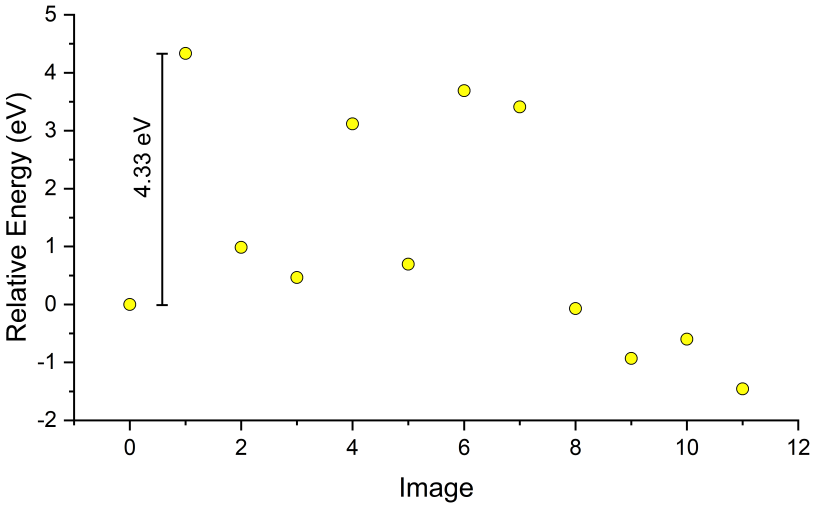


Figure 8.9: Graph displaying the energy barrier for one helium atom to join a He_nV_3 cluster (where n = 2, 4, 6) from 1-6 nearest neighbour positions (N).

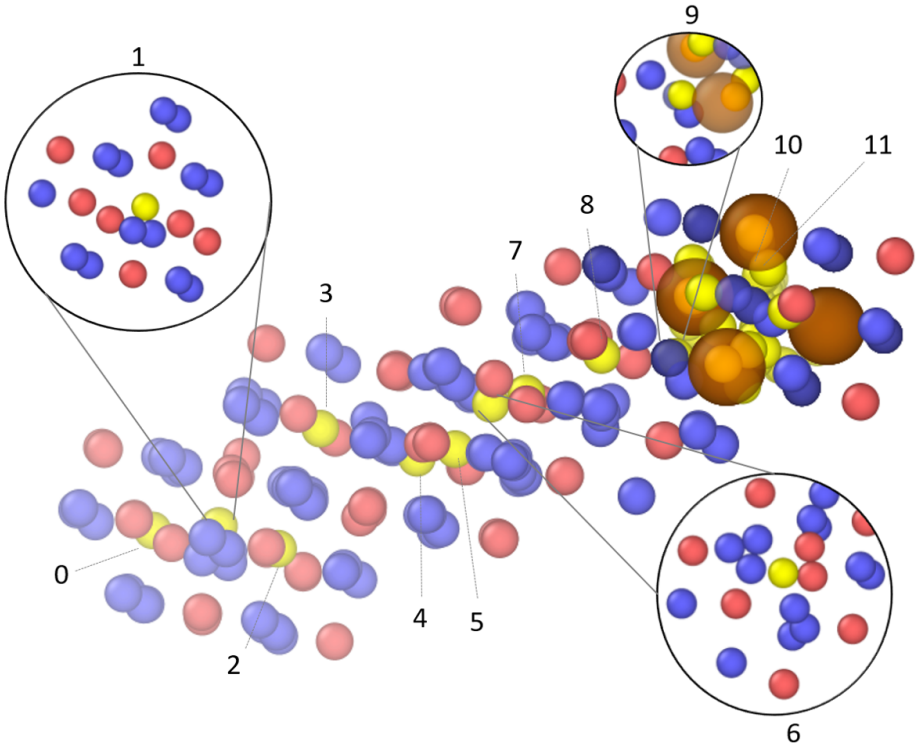
energy barriers calculated via NEB. 12 images were used for each calculation and the energy barriers calculated via the subtraction of the energy of the initial image from the highest energy image.

8.3.2 *Example: 1 He joins a He_6V_{12} cluster*

Figure 8.10 displays the results of the calculation of one helium atom joining a He_6V_{12} cluster. Figure 8.10a displays the relative energies of each image (relative to the image 0 energy). It can be seen that image 1 is the maximum energy configuration and as such the energy barrier is calculated from the energy difference of image 1 and 0, equalling 4.33 eV.



(a) Relative energy at each image



(b) Schematic of each image

Figure 8.10: Energy barrier calculation for a helium atom joining a He_6V_{12} cluster. (a) Displays the relative energies at each image from the calculation. (b) Displays the migration pathway for a helium atom. The helium configurations from images 1, 6 and 9 are highlighted and discussed in the text. Each helium atom is labelled according to its corresponding image.

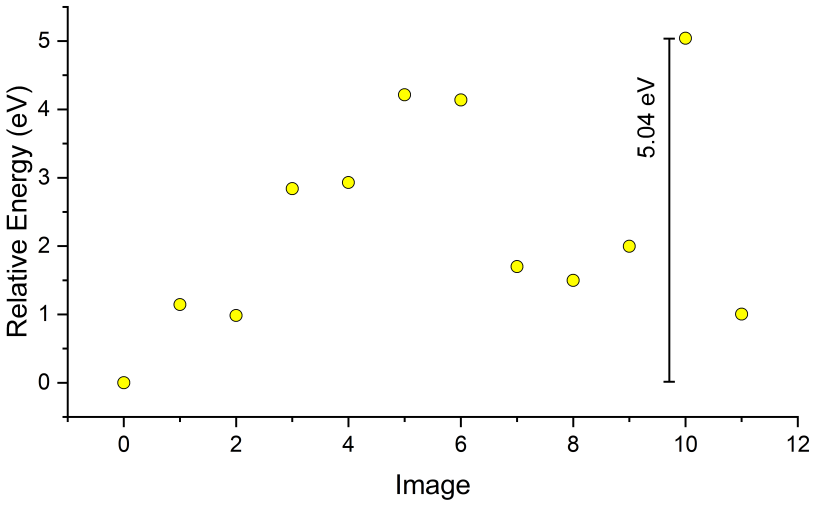
Image 1 is highlighted in the figure and it can be seen that helium is close to occupying an edge-centred site; it is just beyond two oxygen atoms. This is a high energy configuration as was found in Chapter 5. In images 2, 3, 5 and 8, helium occupys an OIS and these images have correspondingly low relative energies. It is found that helium migrates via OIS hops going through edge-centred sites in which oxygen is sightly displaced forming a temporary OFP. This mechanism is as suggested by Liu *et al.* [201] and Yakub *et al.* [202] for helium migration in UO_2. As such, the high energy images (1, 4, 6 and 7) all correspond to the transition state in the OIS-OIS hop. In image 9, helium has joined the cluster and occupies an oxygen vacancy. In image 10 helium has migrated further into the cluster, and finally in image 11 the cluster forms the minimum energy configuration.

8.3.3 *Example: 1 He leaves a $He_{17}V_{12}$ cluster*

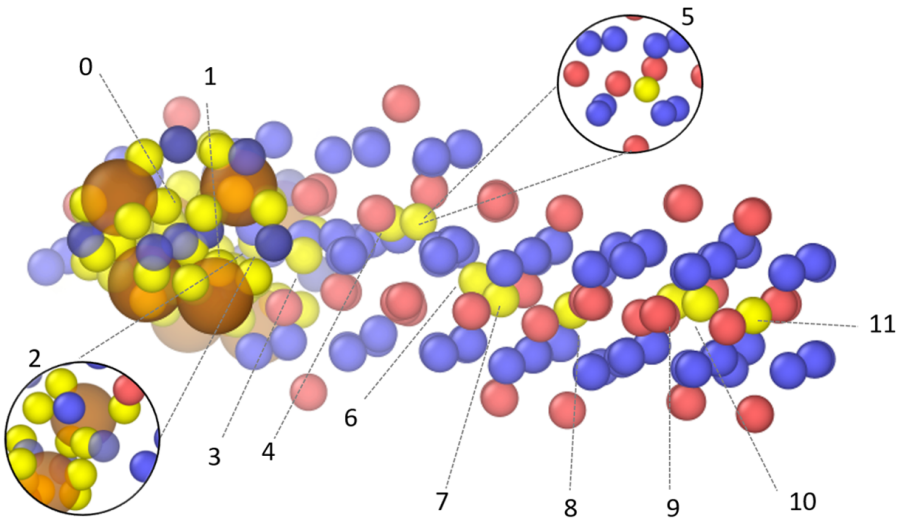
Figure 8.11 displays the results of the calculation of one helium atom leaving a $He_{17}V_{12}$ cluster. Figure 8.11a displays the relative energies of each image (relative to the energy of image 0). It can be seen that image 10 is the maximum energy configuration and as such the energy barrier is calculated from the energy difference of image 10 and 0, equalling 5.04 eV.

Image 2 is highlighted in Figure 8.11b, it can be seen that the helium atom is occupying an oxygen vacancy site. As such, the migration pathway for helium both the joining and leaving a cluster has been found to be via an oxygen vacancy assisted hop (Figure 8.10b). Image 5 is also highlighted, in which the helium atom is not occupying an OIS, corresponding to the relatively high energy of this image (approx. 4.5 eV).

It can be seen that the migration pathway for helium to leave a cluster is much the same as for joining. It is via OIS hops with the high energy barriers corresponding to helium in edge-centred positions.



(a) Relative energy at each image



(b) Schematic of each image

Figure 8.11: Energy barrier calculation for a helium atom leaving a $He_{17}V_{12}$ cluster. (a) Displays the relative energies at each image from the calculation. (b) Displays the migration pathway for a helium atom. The helium configurations from images 2 and 5 are highlighted and discussed in the text. Each helium atom is labelled according to its corresponding image.

8.3.4 *Results*

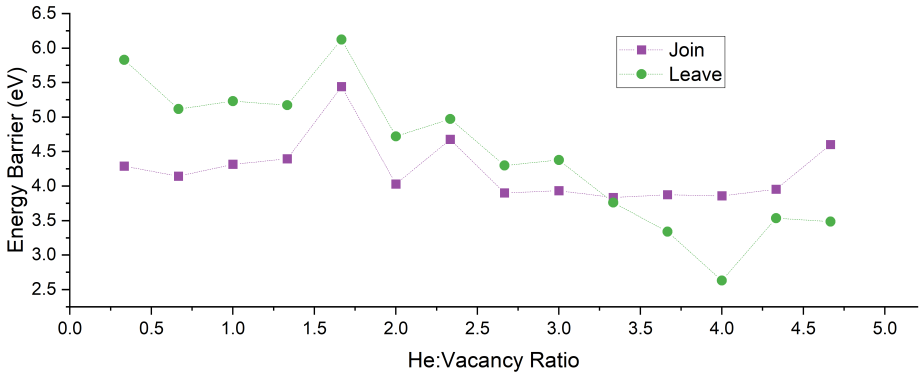
Figure 8.12 plots the energy barriers calculated for helium atoms joining and leaving a He_nV_m cluster. It can be seen that it initially requires more energy for helium to

leave a cluster than for it to join one. For a He_nV_3 cluster (Figure 8.12a), it can be seen that at a He:Vacancy ratio of approximately 3.5:1, the energy favourability reverses; it requires less energy for helium to leave the cluster than to join it. A similar trend was found for helium joining and leaving for He_nV_6 and He_nV_{12} clusters (Figures 8.12b and 8.12c respectively).

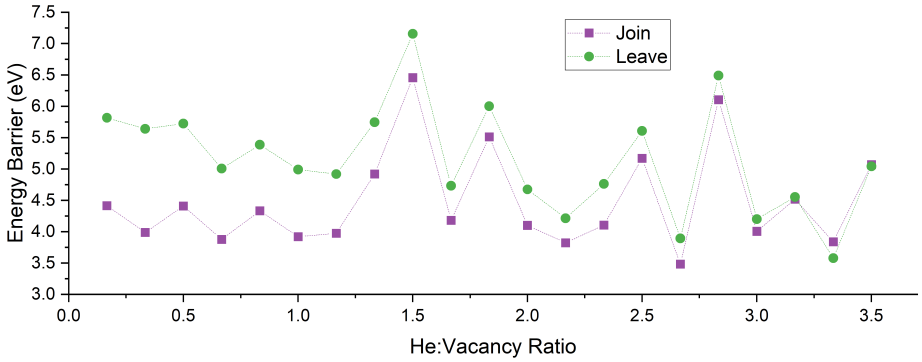
From the energy barriers plotted in Figure 8.12, the difference in energy barrier was calculated by,

$$\Delta E_b = E_{\text{join}} - E_{\text{leave}}. \tag{8.2}$$

A negative value for ΔE_b means more energy is required for a He interstitial to join a cluster, than to leave it; it is energetically unfavourable for additional helium atoms to join the cluster. Thus, the point at which ΔE_b becomes negative, is the point at which the maximum energetically favourable He:Vacancy ratio has been found.



(a) He_nV_3



(b) He_nV_6



(c) He_nV_{12}

Figure 8.12: Energy barriers for a helium joining (purple squares) or leaving (green circles) a cluster with various He:Vacancy ratios.

As displayed by Figure 8.13, the same trend was found for all three Schottky seed sizes; as the He:Vacancy ratio increases, ΔE_b decreases. At low He:Vacancy ratios the energy to join is lower than the energy to leave a cluster, so it is energetically favourable for helium atoms to join the cluster from interstitial sties. However, when the He:Vacancy ratio exceeds $\sim$ 3:1, the opposite is true. ΔE_b becomes negative, indicating that it now requires more energy for a He atom to join the cluster than to leave it, so this is the size at which the clusters are no longer energetically favourable.

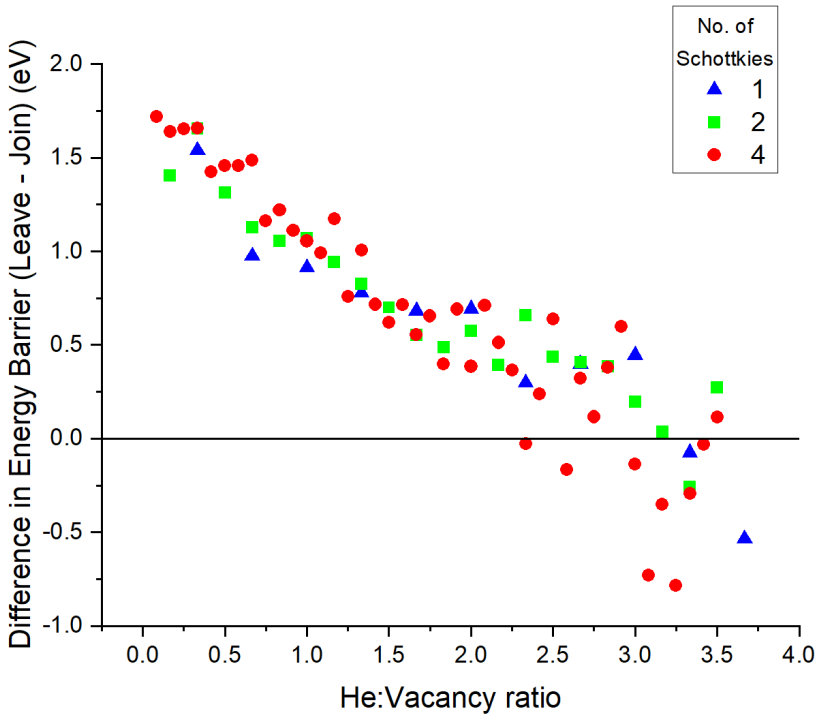


Figure 8.13: Difference in energy barriers for a He interstitial to join and leave a cluster as a function of a cluster's He:Vacancy ratio. When the energy difference becomes negative, it requires more energy for helium to join the cluster than to leave it, so the maximum energetically favourable He:Vacancy ratio is at this point. Three Schottky seed location sizes were considered (1, 2 and 4 Schottkies) and the average maximum stable He:Vacancy ratio was $\sim$ 3:1.

8.4 Molecular Dynamics, Schottky Void

Molecular dynamics simulations were run over a range of temperatures with various helium concentrations to investigate if helium clusters would form. When clusters did form cluster analysis was performed to determine the He:vacancy ratio of each and find if the clusters were of the ratios predicted by Sections 8.2 and 8.3. The helium concentrations generated were: 0.5, 1, 2, 4, 7.7 and 14.3 at%. Table 8.2 displays the number of helium atoms input for each concentration. Helium interstitials were randomly distributed in OISs throughout the lattice. These concentrations were chosen as they correspond to fractions of OIS filled.

Table 8.2: Helium concentrations considered and the number of helium atoms they correspond to

He Conc. (at.%)	0.5	1	2	4	7.7	14.3
No. He	32	64	128	256	512	1024

A lattice was generated which contained three Schottky trios in the centre of the lattice as displayed in Figure 8.14. This lattice was energy minimised to ensure that the configuration was relaxed. Helium atoms were added to OISs and the simulation run at three temperatures (750, 1500 and 2250 K) for 1 ns. Some of the simulations were then run for an additional 4 ns.

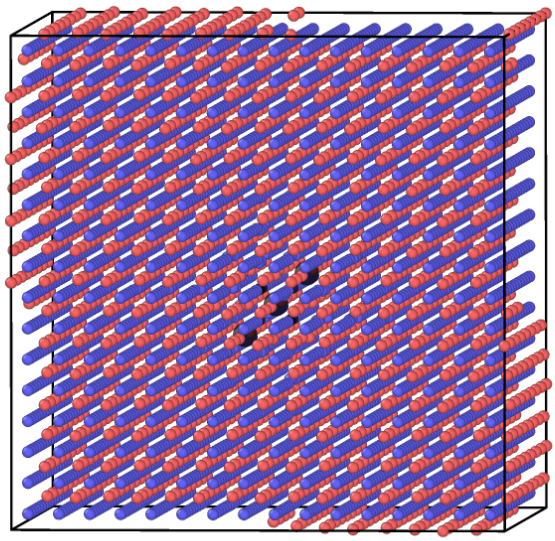


Figure 8.14: PuO_2 lattice with three Schottky trios clustered in the centre. The vacancies are displayed in black, Pu atoms in pink and O atoms in blue.

Throughout this section the helium atoms and oxygen and plutonium vacancies are coloured corresponding to the legend displayed in Figure 8.15.

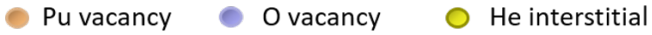
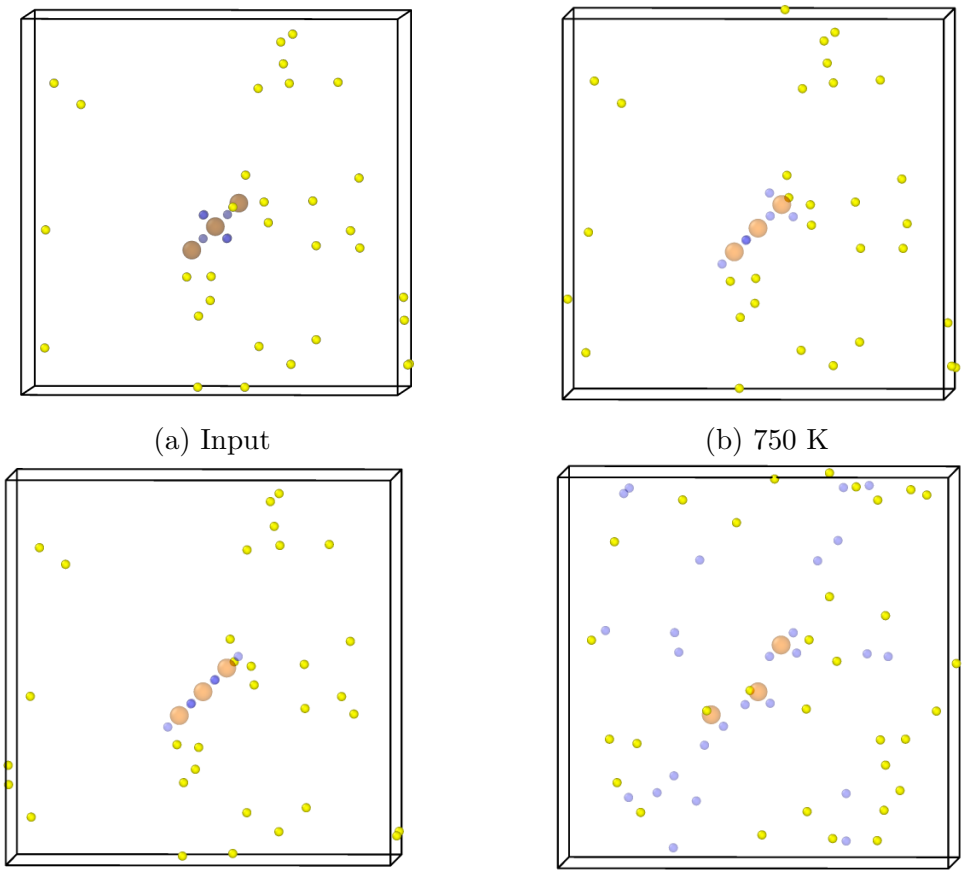


Figure 8.15: Legend of the colours of Pu vacancies (pink), O vacancies (blue), and He interstitials (yellow).

8.4.1 *0.5% Helium*

Figure 8.16 displays the initial and final configurations of a lattice containing a 0.5% helium concentration and a central Schottky trio cluster. It can be seen that after 1 ns at all three temperatures no cluster forms. At 2250 K (Figure 8.16d), two helium atoms have migrated and are trapped at plutonium vacancy sites.



(a) Input

(b) 750 K

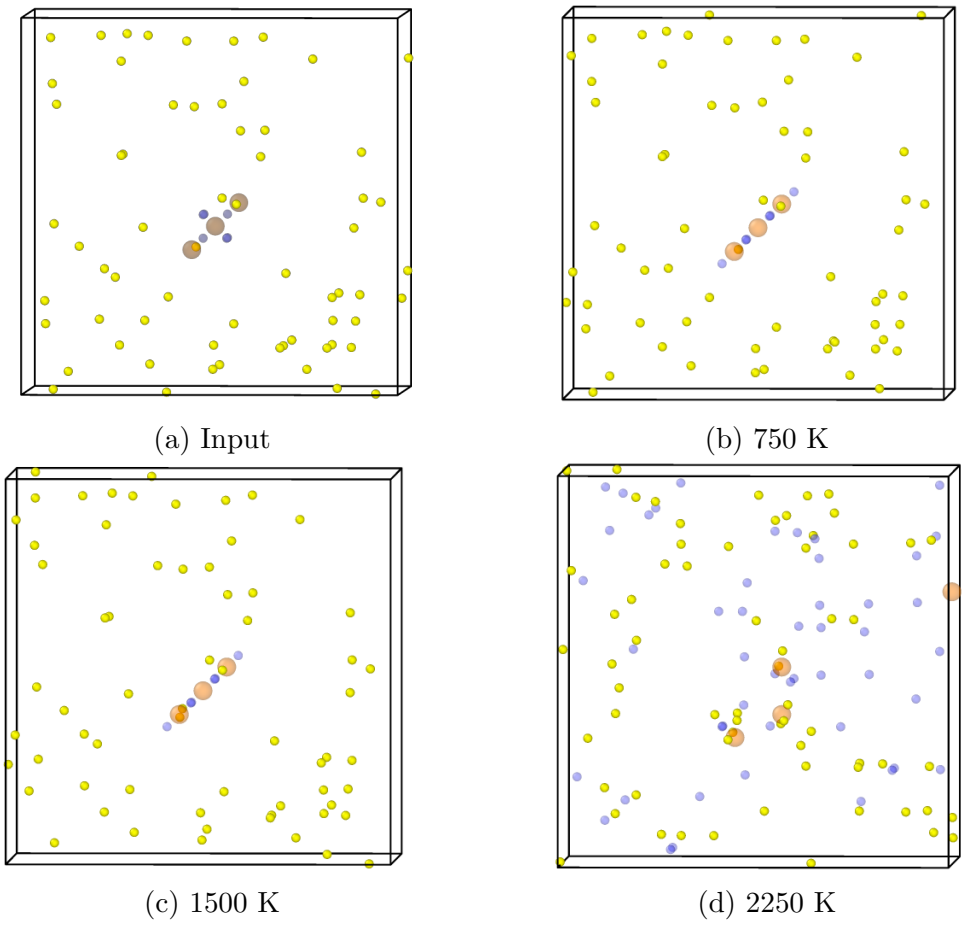
(c) 1500 K

(d) 2250 K

Figure 8.16: Lattice containing 0.5% helium and a cluster of three Schottky trios in the centre. (a) Displays the input configuration. (b), (c) and (d) are the configurations after molecular dynamics was run at 750, 1500 and 2250 K respectively.

8.4.2 *1% Helium*

Figure 8.16 displays the initial and final configurations of a lattice containing a 1% helium concentration and a central Schottky trio cluster. It can be seen that after 1 ns at all three temperatures no helium bubble forms. At 2250 K (Figure 8.16d), the Shottky trios have disbanded and some clustering has begun to occur around one of the plutonium vacancy sites. Molecular dynamics was run on this lattice for an additional 4 ns at 2250 K.



(a) Input (b) 750 K

(c) 1500 K (d) 2250 K

Figure 8.17: Lattice containing 1% helium and a cluster of three Schottky trios in the centre. (a) Displays the input configuration. (b), (c) and (d) are the configurations after molecular dynamics was run at 750, 1500 and 2250 K respectively.

8.4.2.1 2250 K, 5 ns

As can be seen from Figure 8.18, after the 1% He system was evolved for a further 4 ns at 2250 K, a helium cluster formed. Upon inspection of the cluster it was found that it was a $He_{24}V_{22}$ cluster which is within the predicted stable ratio size found

in Sections 8.2 and 8.3.

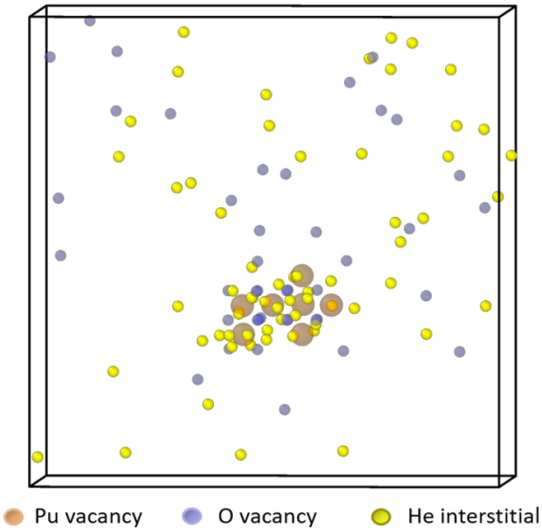
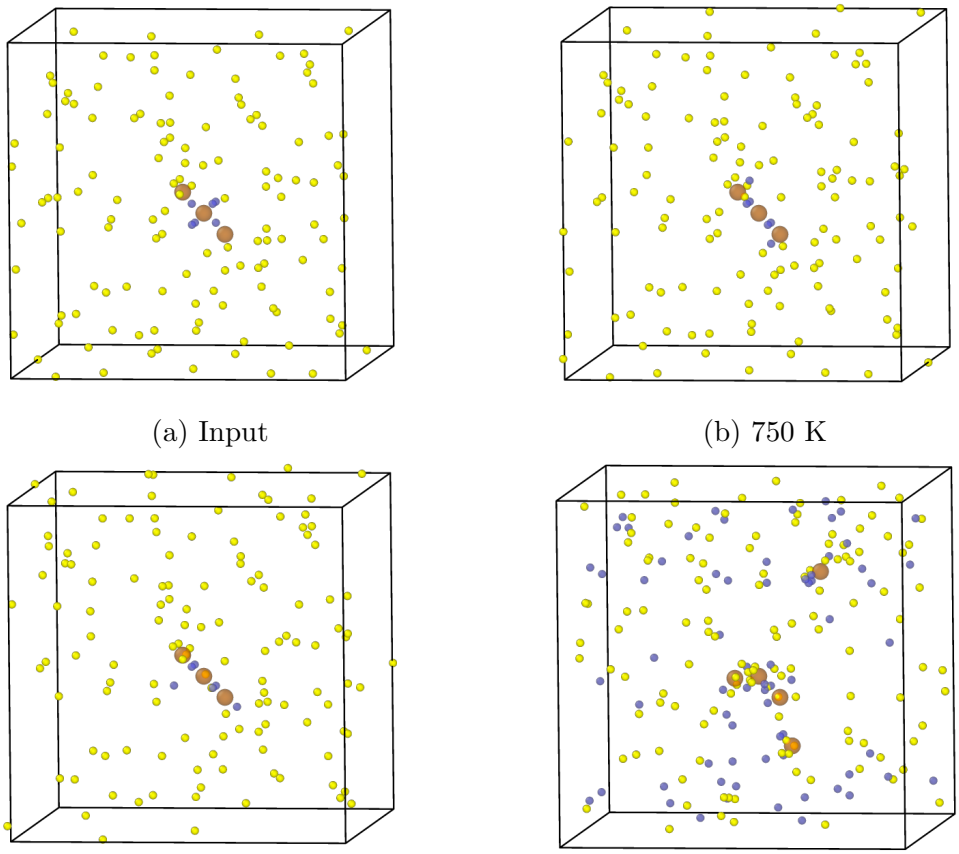


Figure 8.18: Configuration of helium atoms and oxygen and plutonium vacancies after a 5 ns simulation at 2250 K with initial input of 1% helium atoms in OISs.

8.4.3 *2% Helium*

Figure 8.19 displays results from simulations of a lattice containing 2% helium with a cluster of three Schottky trios in the centre of the lattice. Molecular dynamics calculations were run at three temperatures: 750, 1500 and 2250 K, with the configurations after 1 ns displayed in Figures 8.19(b), (c) and (d) respectively. It can be seen that little has changed in the lattice after 1 ns at 750 and 1500 K. At 2250 K however, many oxygen vacancies are present in the lattice and 13 helium atoms have clustered around the Schottky trio. This is as expected from the findings of Chapter 7; helium atoms migrate through the lattice via oxygen vacancies which are mobile at temperatures exceeding 1500 K.



(a) Input (b) 750 K

(c) 1500 K (d) 2250 K

Figure 8.19: Lattice containing 2% helium and a cluster of three Schottky trios in the centre. (a) Displays the input configuration. (b), (c) and (d) are the configurations after molecular dynamics was run at 750, 1500 and 2250 K respectively.

8.4.3.1 1500 K, Trajectories

It was of interest to see if helium would migrate towards the central void to cluster when no defects were distributed through the lattice. As displayed in Figure 8.19b, at 750 K one helium atom occupied the Schottky defects. Upon inspection of the trajectories it was found that this helium migrated from a neighbouring OIS.

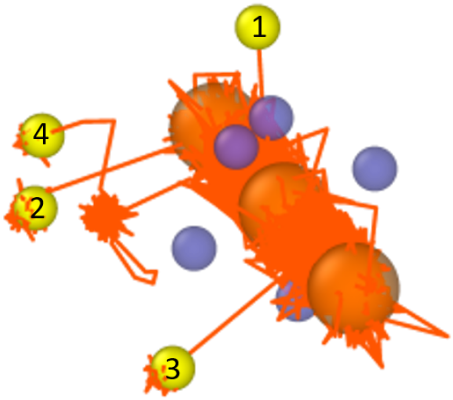
At 1500 K, four helium atoms occupy the Schottky defects after 1 ns. Further analysis of the migration pathways of the helium atoms into the void space in this simulation was performed and is displayed in Figure 8.20. From this it was observed that the helium atoms which migrate to the Schottky cluster during the 1 ns simulation were all initially in 1, 2 or 3N nearest neighbour positions. Interestingly, each helium atom migrated via a slightly different migration pathway.

The first helium atom to migrate into the cluster ('He 1' Figure 8.20b) is initially located 1 nearest neighbour site from the vacancy cluster. Due to its proximity it immediately (1 ps) migrates into the cluster and remains within the cluster for the rest of the simulation. As can be seen from the trajectory in Figure 8.20b, the helium atom is not static within the cluster. Rather, it migrates about the cluster occupying the plutonium vacancy sites.

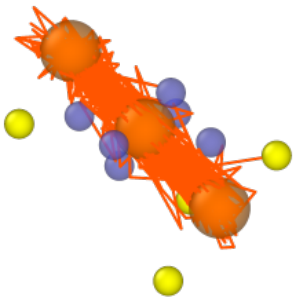
After 470 ps, the second helium atom migrates to the cluster. Figure 8.20c displays the migration pathway. The pathway was a direct hop to an oxygen vacancy site within the cluster. Lattice plutonium and oxygen atoms surrounding the helium atom have also been displayed to depict the pathway. It can be seen that the helium atom migrates through two oxygen atoms (via an edge-centred position). As was discussed in Section 7.3, Figure 7.2, the energy barrier for helium from an OIS to the edge-centred position is high (2.4 eV).

The third helium atom migrates via a direct hop through an oxygen vacancy into a plutonium vacancy site within the lattice. The final helium atom migrates via an OIS-V_O-OIS hop, and then via a direct hop through an oxygen vacancy into a plutonium vacancy site within the lattice.

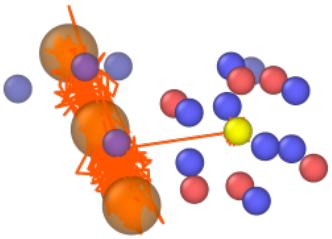
From the migration pathways found for helium to migrate to a three Schottky cluster within 1 ns at 1500 K, it is suggested that when helium atoms occupy first and second nearest neighbour sites from the cluster, migration via pathways with higher energy barriers become viable. This may due to the energetic favourability of helium occupying a cluster with a low He:Vacancy ratio. Helium atoms from interstitial sites further from the cluster (e.g. 3N as displayed in Figure 8.20e), may migrate via the OIS-V_O-OIS mechanism until close enough to make a direct hop into the cluster.



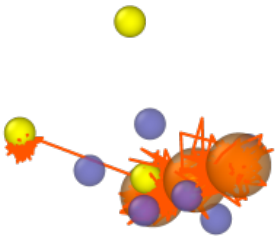
(a) Trajectories of clustered He



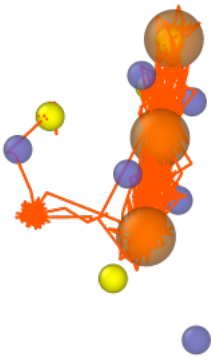
(b) He 1 (1 ps)



(c) He 2 (470 ps)



(d) He 3 (482 ps)

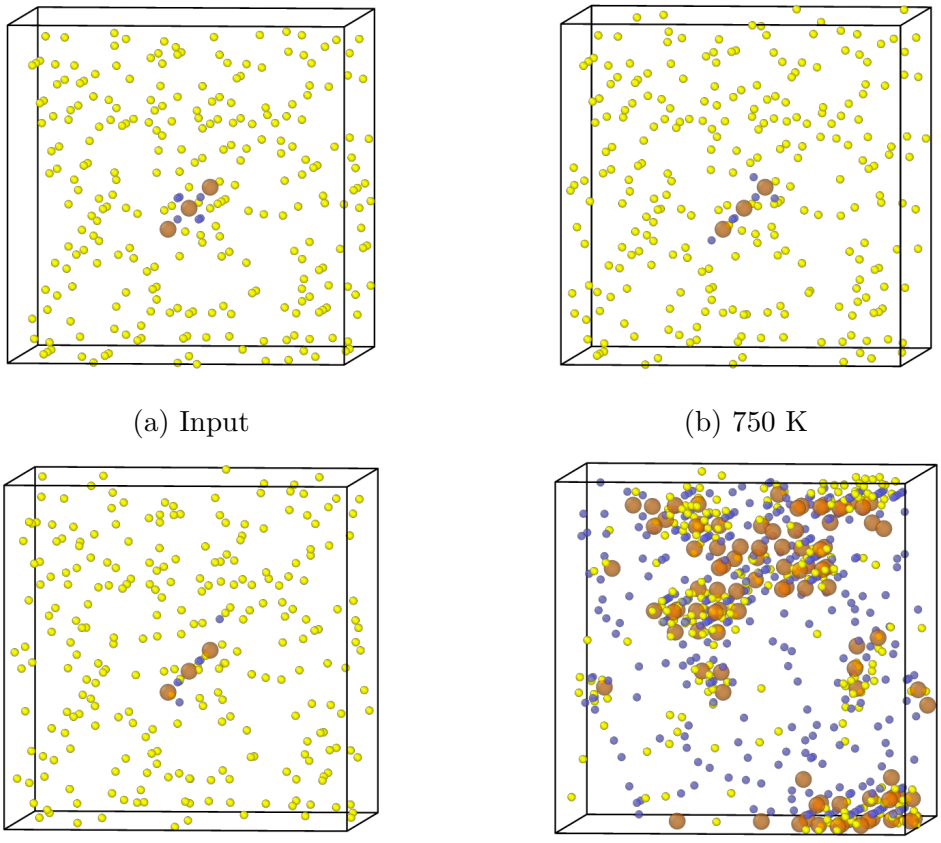


(e) He 4 (648 ps)

Figure 8.20: Helium migration to a cluster of three Schottky trios during a 1 ns simulation at 1500 K. (a) Displays the trajectories (orange) of all four helium atoms which migrate into the vacancies, they are labelled in order of migration time. (b), (c), (d) and (e) display detail of how the migration occurred and are discussed in the text.

8.4.4 *4% Helium*

Figure 8.21 displays results from simulations of a lattice containing 4% helium with a cluster of three Schottky trios in the centre of the lattice. Molecular dynamics calculations were run at three temperatures: 750, 1500 and 2250 K, with the configurations after 1 ns displayed in Figures 8.21(b), (c) and (d) respectively. It can be seen that at 750 and 1500 K little has changed in the lattice after 1 ns. At 2250 K however, multiple helium clusters have begun to form. To understand this further, this lattice was evolved for an additional 4 ns.



(a) Input (b) 750 K

(c) 1500 K (d) 2250 K

Figure 8.21: Lattice containing 4% helium and a cluster of three Schottky trios in the centre. (a) Displays the input configuration. (b), (c) and (d) are the configurations after molecular dynamics was run at 750, 1500 and 2250 K respectively.

8.4.4.1 2250 K, 5 ns

Figure 8.22 displays the 4% He lattice at various time steps. The formation of a helium cluster can be seen at 650 ps around the initial input defect. Additional

clusters can be seen to have nucleated elsewhere in later time frames. Upon inspection it was found that temporary PuFPs were often formed in the vicinity of oxygen vacancies, allowing a helium atom to occupy a V_{Pu}. Instead of the He atom being ejected by recombining Pu (as is the case with a single He atom), when the number of helium atoms close to a V_{Pu} was three or more, the PuFP no longer recombined and a Schottky defect was formed. An example of this is the He_6V_4 cluster identified at 650 ps in Figure 8.22. Thus, a high local He concentration can itself generate defects after which the cluster becomes immobile.

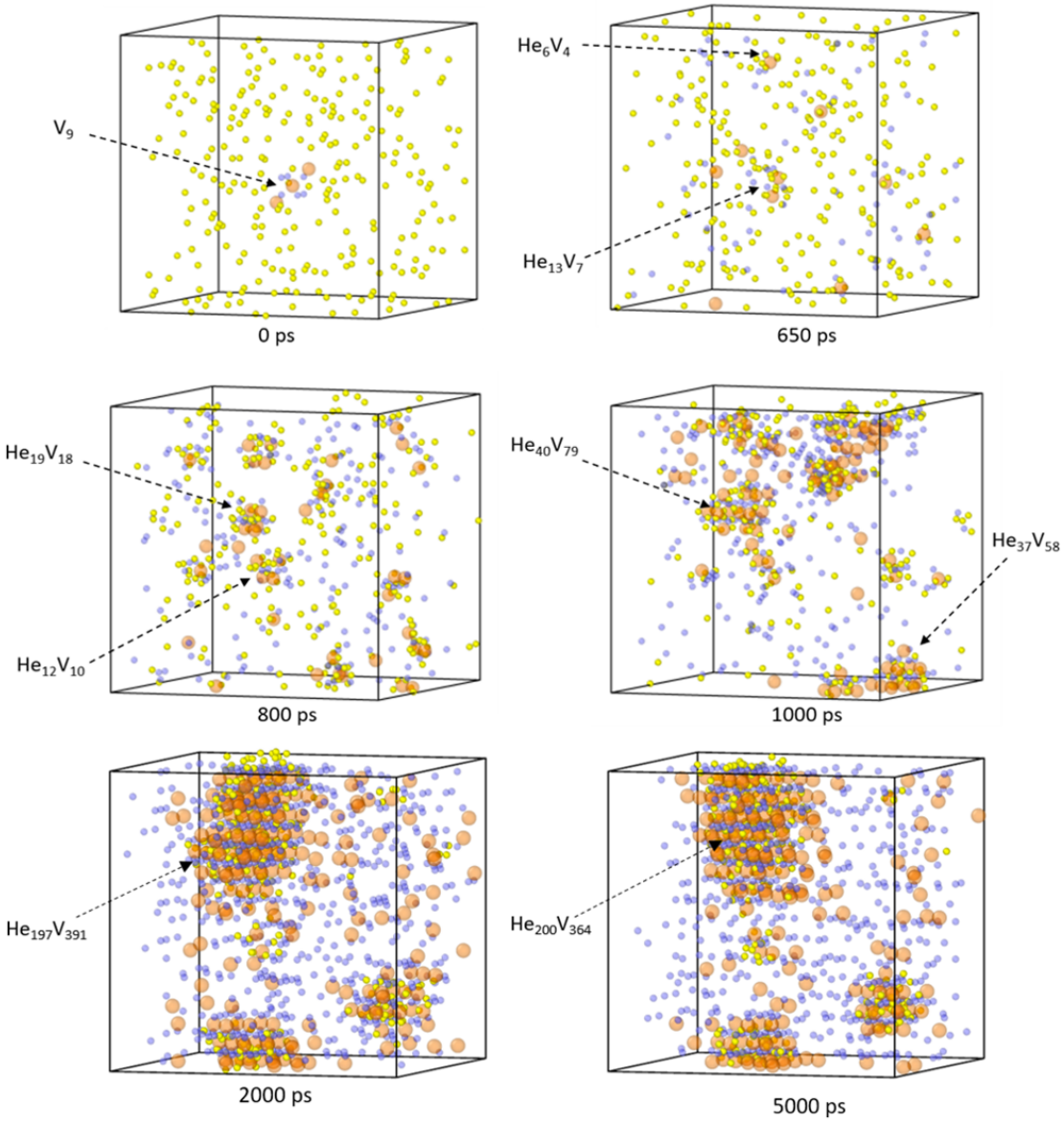
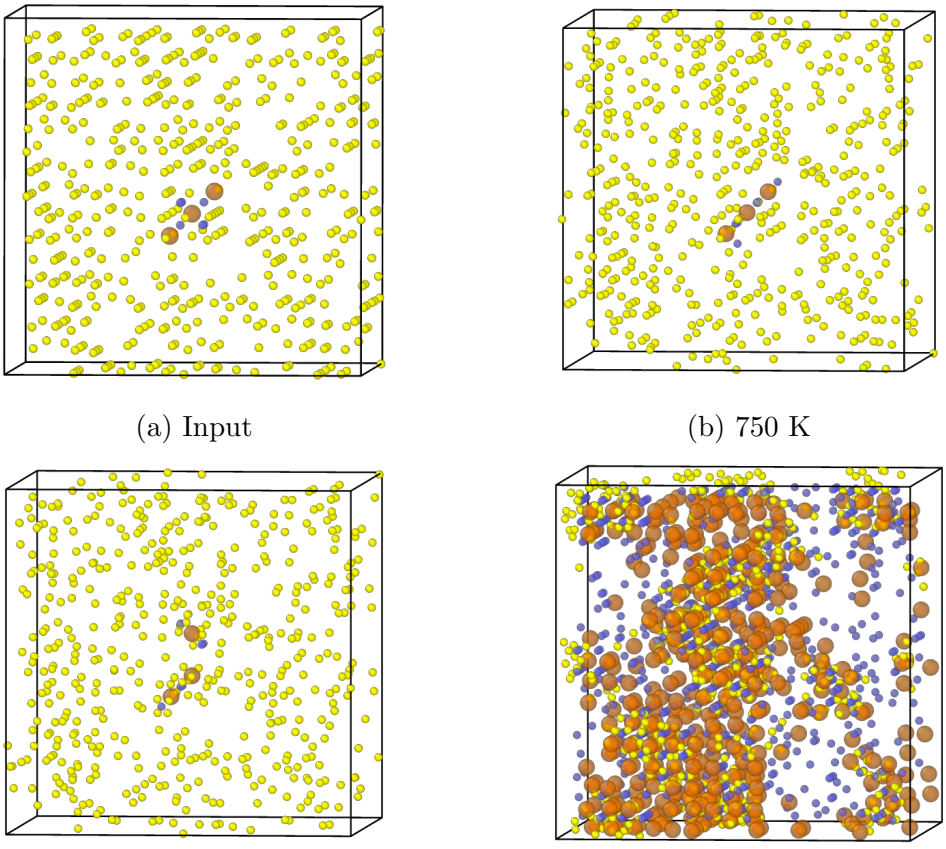


Figure 8.22: PuO_2 supercell with 4% He concentration. Initially three Schottky trios were input in the centre of the lattice with the He atoms randomly occupying OISs. Cluster formation is shown at different times and He:Vacancy ratios labelled.

8.4.5 *7.7% Helium*

A lattice was generated with a 7.7% helium concentration, this is equivalent to a quarter of the available OISs being occupied with helium atoms. This is a significantly high helium concentration and unlikely to occur in PuO_2 storage scenarios. However, it was of interest to find if the predicted maximum He:Vacancy ratios would be followed in a lattice so saturated with helium. Figure 8.23 displays the input configuration, and the configurations after 1 ns at 750, 1500 and 2250 K. It can be seen that helium clustering occurs at all temperatures, with significant clustering at 2250 K.



(a) Input

(b) 750 K

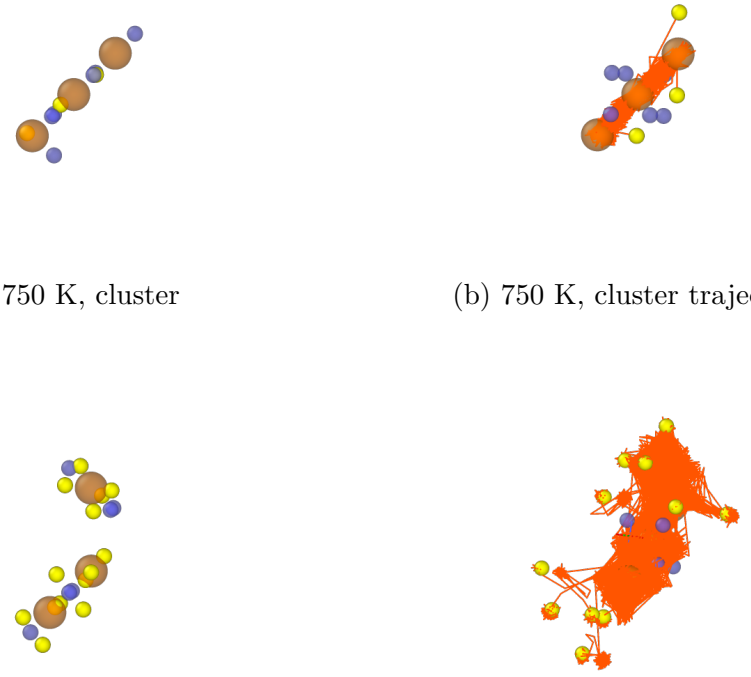
(c) 1500 K

(d) 2250 K

Figure 8.23: Lattice containing 7.7% helium and a cluster of three Schottky trios in the centre. (a) Displays the input configuration. (b), (c) and (d) are the configurations after molecular dynamics was run at 750, 1500 and 2250 K respectively.

8.4.5.1 750 and 1500 K, Trajectories

Figures 8.24a and 8.24c display the helium atoms occupying the Schottky vacancies after 1 ns at 750 and 1500 K respectively. As anticipated, more helium atoms occupy the cluster at 1500 K. This is likely because at higher temperatures, helium atoms have more energy and so can overcome migration energy barriers. Additionally, higher temperatures result in oxygen being more mobile and so oxygen vacancies are more readily available for helium migration.



(a) 750 K, cluster

(b) 750 K, cluster trajectory

(c) 1500 K, cluster

(d) 1500 K, cluster trajectory

Figure 8.24: Lattice containing 7.7% helium and a cluster of three Schottky trios in the centre, (a) and (c) display the helium atoms clustered at 750 and 1500 K respectively, (b) and (d) display the initial position of the helium atoms which join the cluster and their trajectories (orange) for 750 and 1500 K respectively.

Figures 8.24b and 8.24d display the helium atoms which migrate to the Schottky vacancies in their input sites, in addition to the trajectories of the migration pathways. The migration pathways are very similar to those plotted for the lattice containing 2% helium in Figure 8.20. In Figure 8.24b it can be seen that the

helium atoms migrate directly from nearest neighbour positions into the vacancies, this pathway is identical to that followed by ′He 1′ in Figure 8.20b and occurs immediately in the simulation. In Figure 8.24d it can be seen that some of the helium atoms migrate via interstitial hops as was found in the ′He 4′ pathway in Figure 8.20e. It should be noted that the only vacancies present in the lattice containing the clusters displayed in Figure 8.23 are displayed in the figure.

From comparison of helium migration pathways in the 2 and 7.7% helium lattices, it is suggested that when defects are not distributed through the lattice, the determining factor in helium atoms migrating to a cluster is the vicinity of helium atoms to the cluster. If the helium atoms are within 3N of the cluster, it is likely that they will migrate. As such, more helium atoms have not migrated to the vacancies in the 7.7% He lattice because the helium concentration is higher. Rather, they have migrated because more of the helium atoms were located in close proximity to the vacancy cluster. Due to the increased number of helium atoms this was statistically more likely than in the lower helium concentration simulations.

It can be concluded that at temperatures below 1500 K, in a 1 ns time frame helium atoms will not migrate across the lattice to join a vacancy cluster even when the helium concentration is very high. It is predicted that defects must be distributed throughout the lattice to enable the migration. At higher temperatures (e.g. 2250 K), intrinsic defects are thermally generated and as such are available to helium for migration. Due to this, helium clusters are seen to form at elevated temperatures. These findings are in agreement with the predictions of Garcia *et al.* [191] for helium behaviour in UO_2.

8.4.5.2 2250 K, Cluster Analysis

Figure 8.25 displays the configuration of helium atoms after running molecular dynamics for 1 ns at 2250 K. Only the helium atoms are displayed with the lattice atoms and defects hidden for clarity. It can be seen that the helium atoms have migrated to form clusters, which are colour coded according to size. The largest 12 clusters are labelled.

The breakdown of how many helium atoms and vacancies are in each cluster is detailed in Table 8.3. It can be seen that every cluster has a He:Vacancy ratio below 1:1. This means, in every cluster there are more vacancies than helium atoms. The clusters are much less saturated by helium atoms than the maximum values predicted from the findings of Sections 8.2 and 8.3.

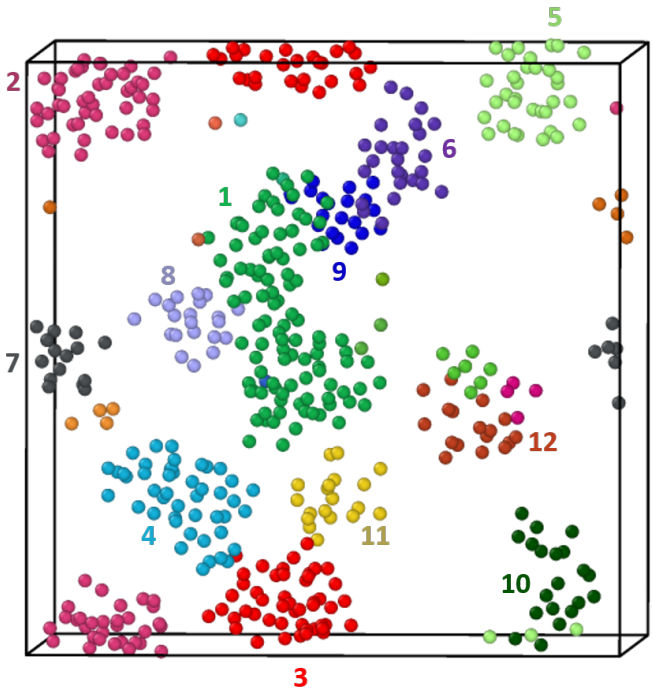


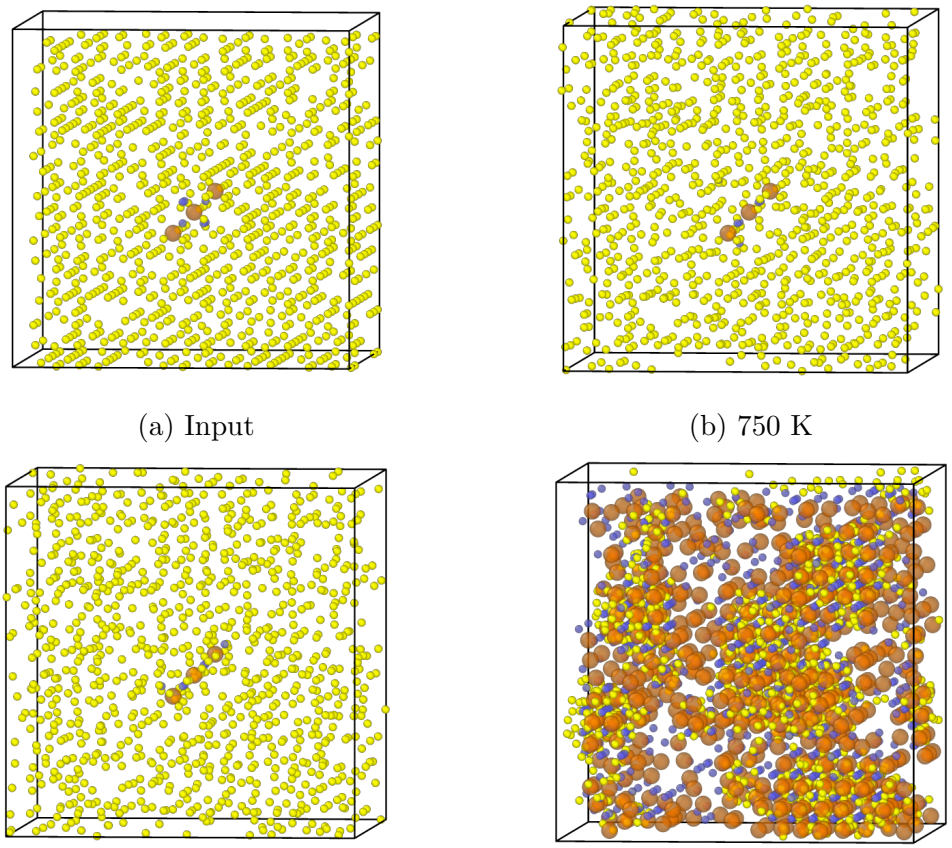
Figure 8.25: Lattice containing 7.7% helium after molecular dynamics has been run for 1 ns at 2250 K. Only helium atoms are displayed. Cluster analysis has been performed and the helium atoms coloured according to which cluster they occupy. 12 clusters are labelled.

Table 8.3: Detailing the number of helium atoms and vacancies in each cluster displayed in Figure 8.25 and the He:Vacancy ratio calculated for each

Cluster Identifier		Number of		Ratio (:1)
Number	Colour	Helium	Vacancies	
1	Green	103	139	0.74
2	Pink	78	110	0.71
3	Red	76	123	0.62
4	Baby Blue	46	66	0.70
5	Pale Green	36	44	0.82
6	Purple	26	34	0.76
7	Grey	21	30	0.70
8	Lilac	21	33	0.64
9	Blue	21	27	0.78
10	Dark Green	20	21	0.95
11	Yellow	19	33	0.58
12	Brown	17	25	0.68

8.4.6 *14.3% Helium*

The final helium concentration considered was 14.3%, in which half of the available OISs were occupied by helium atoms. Figure 8.26 displays the input configuration, and the configurations after 1 ns at 750, 1500 and 2250 K. As in the lattice containing a 7.7% helium concentration, it can again be seen that helium clustering occurs at all temperatures, with significant clustering at 2250 K. As was found for the 7.7% He lattice, at 750 K, three helium atoms migrate to the vacancies. These helium atoms migrated from nearest neighbour OISs.



(a) Input (b) 750 K

(c) 1500 K (d) 2250 K

Figure 8.26: Lattice containing 14.3% helium and a cluster of three Schottky trios in the centre. (a) Displays the input configuration, (b), (c) and (d) are the configurations after molecular dynamics was run at 750, 1500 and 2250 K respectively.

8.4.6.1 1500 K, Trajectories

The helium atoms occupying the vacancy cluster after 1 ns at 1500 K are displayed in Figure 8.27. Again it can be seen that despite the lattice being saturated with

helium atoms, only those which were within 2 or 3 nearest neighbour positions migrated to become sequestered in the vacancies.



(a) 1500 K, cluster (b) 1500 K, helium trajectories

Figure 8.27: Lattice containing 14.3% helium and a cluster of three Schottky trios in the centre, only the helium atoms and vacancies clustered are displayed. The simulation was run for 1 ns at 1500 K. (a) Displays the cluster. (b) Displays the helium atoms initial positions and the migration pathways taken to the cluster (orange).

8.4.6.2 2250 K, Cluster Analysis

Figure 8.28 displays the configuration of helium atoms after the system was evolved for 1 ns at 2250 K. Only helium atoms are displayed (the lattice atoms and defects are hidden for clarity). It can be seen that the helium atoms have migrated to form clusters, which are colour coded according to size. The largest 12 clusters are labelled.

The breakdown of how many helium atoms and vacancies are in each cluster is detailed in Table 8.4. Unlike in the lattice with 7.7% He, some of the clusters have He:Vacancy ratios above 1:1. However, all ratios are still well below the maximum of 3.5:1 predicted from the earlier calculations.

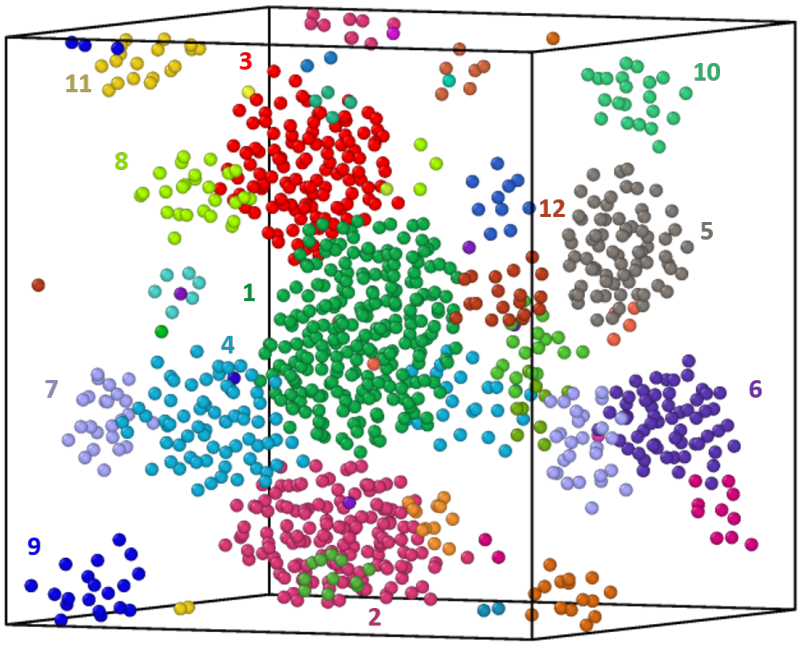


Figure 8.28: Lattice containing 14.3% helium after molecular dynamics has been run for 1 ns at 2250 K. Only helium atoms are displayed. Cluster analysis has been performed and the helium atoms coloured according to which cluster they occupy. The 12 largest clusters are labelled.

Table 8.4: Detailing the number of helium atoms and vacancies in each cluster displayed in Figure 8.28 and the He:Vacancy ratio calculated for each

Cluster Identifier		Number of		Ratio (:1)
Number	Colour	Helium	Vacancies	
1	Green	240	264	0.91
2	Pink	149	175	0.85
3	Red	119	130	0.92
4	Baby Blue	92	85	1.08
5	Grey	72	71	1.01
6	Purple	60	63	0.95
7	Lilac	52	56	0.93
8	Lime Green	29	34	0.85
9	Blue	22	30	0.73
10	Pale Green	21	19	1.11
11	Yellow	20	16	1.25
12	Brown	20	24	0.83

8.5 Molecular Dynamics, Defect-Free PuO_2

Lattices with a range of helium concentrations but no initial defects were generated. Each lattice was evolved at 2250 K for 5 ns, as at this temperature clusters began to form in the above simulations (Section 8.4). Cluster analysis was performed at 1 and 5 ns. For reference, the legend for helium atoms and oxygen and plutonium vacancy colours is displayed again in Figure 8.29.

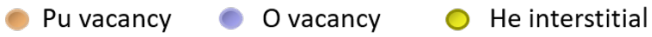


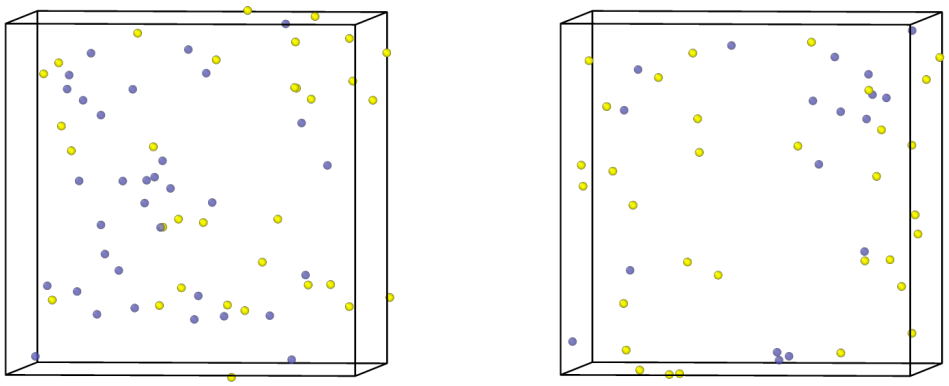
Figure 8.29: Legend of the colours of Pu vacancies (pink), O vacancies (blue), and He interstitials (yellow).

8.5.1 *Configurations*

The configurations of the oxygen and plutonium vacancies and helium atoms at 1 and 5 ns are displayed in this section for each helium concentration. The clusters identified are then analysed.

8.5.1.1 0.5% Helium

As can be seen in Figure 8.30, no He clusters form during 5 ns. As the temperature of the simulation was 2250 K, oxygen is mobile and so O vacancies are present in the lattice. Thus, whilst the He atoms have not clustered, they are mobile. From compariason of Figures 8.30a and 8.30b it can be seen that the He atoms have migrated to occupy different OISs.

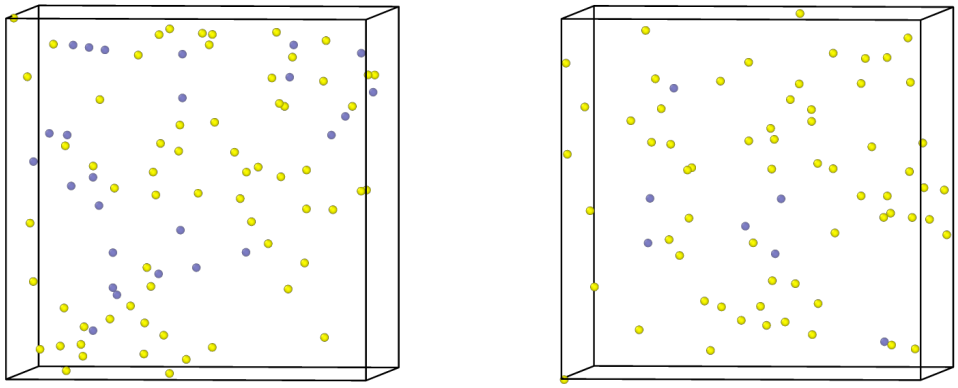


(a) 1 ns (b) 5 ns

Figure 8.30: Lattice containing 0.5% helium evolved at 2250 K for 5 ns.

8.5.1.2 1% Helium

No helium clusters were observed to form during the 5 ns simulation with a 1% helium concentration. The helium atoms were mobile and have migrated between OISs, likely via the oxygen vacancies.

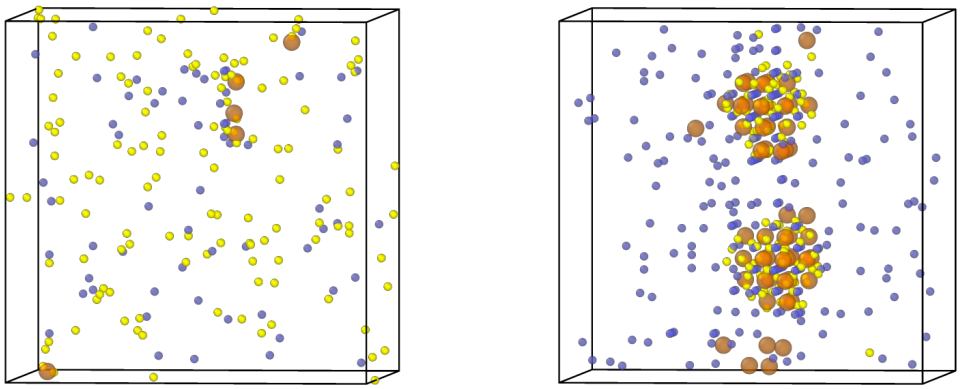


(a) 1 ns (b) 5 ns

Figure 8.31: Lattice containing 1% helium evolved at 2250 K for 5 ns.

8.5.1.3 2% Helium

As can be seen in Figure 8.32a, one small helium cluster has begun to form after 1 ns at 2250 K. After 5 ns (Figure 8.32b) two large helium clusters have formed. It is of interest to note that whilst there are many oxygen vacancies throughout the lattice and within the helium clusters, the majority of plutonium vacancies are within the helium clusters.

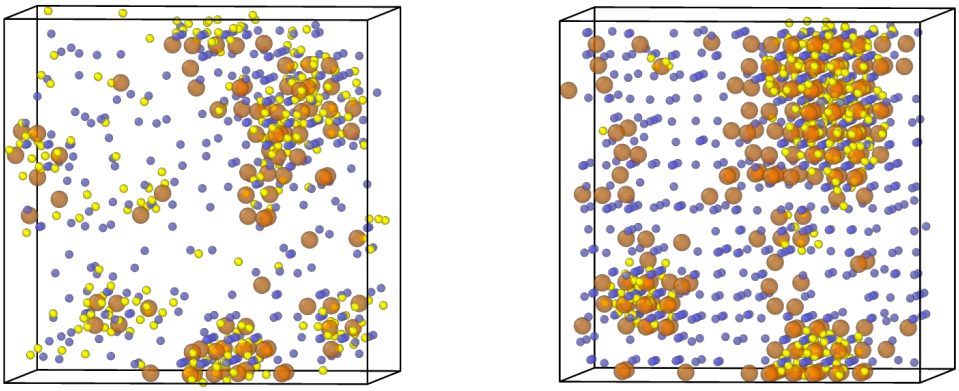


(a) 1 ns (b) 5 ns

Figure 8.32: Lattice containing 2% helium evolved at 2250 K for 5 ns.

8.5.1.4 4% Helium

As displayed in Figure 8.33, multiple helium clusters have formed after 1 ns, but some helium atoms remain in interstitial positions. After 5 ns, there are no isolated helium atoms, all of the helium atoms occupy clusters.

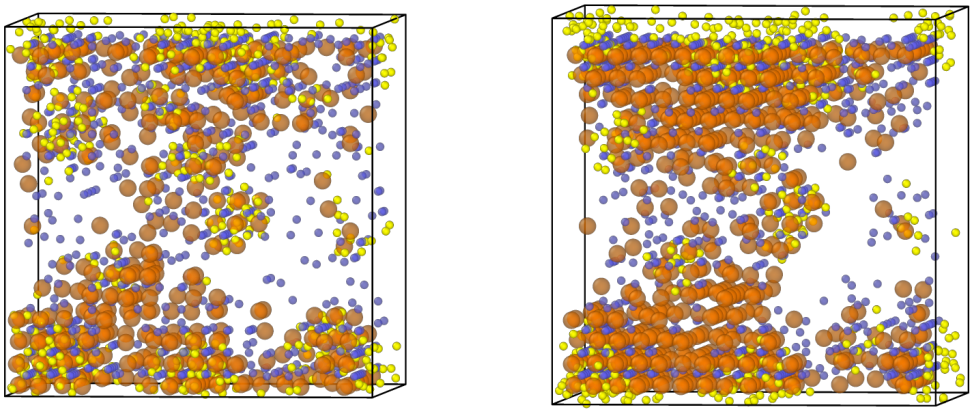


(a) 1 ns (b) 5 ns

Figure 8.33: Lattice containing 4% helium evolved at 2250 K for 5 ns.

8.5.1.5 7.7% Helium

As can be seen in Figure 8.34a, large helium clusters have formed after 1 ns. It appears that during the next 4 ns, these clusters merge to form fewer, larger clusters (Figure 8.34b).

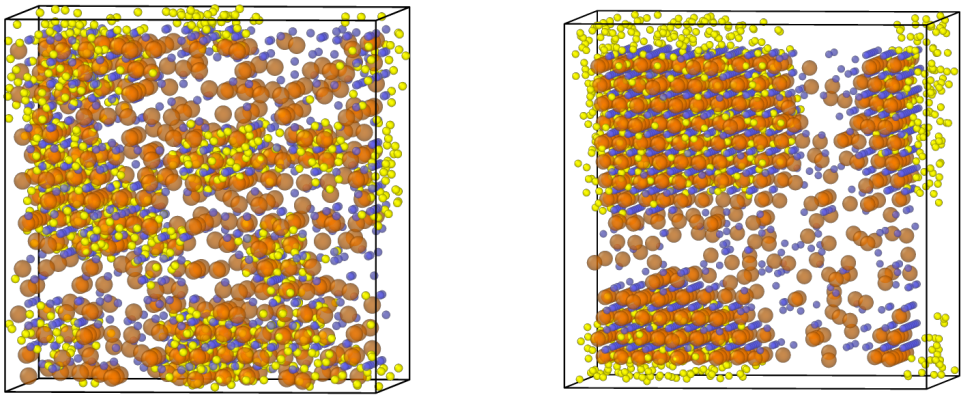


(a) 1 ns (b) 5 ns

Figure 8.34: Lattice containing 7.7% helium evolved at 2250 K for 5 ns.

8.5.1.6 14.3% Helium

From Figure 8.35a it can be seen that after 1 ns the helium atoms are distributed in clusters throughout the lattice. In Figure 8.35b, the clusters have merged to form one giant cluster. There are a significant number of vacancies present in Figure 8.35b, comprised of 788 plutonium vacancies and 1422 oxygen vacancies. As such, there are more vacancies in the lattice than helium atoms (1024), which has been the case for all simulations upon inspection. The specific He:Vacancy ratios will be calculated in the following section.



(a) 1 ns (b) 5 ns

Figure 8.35: Lattice containing 14.3% helium evolved at 2250 K for 5 ns.

8.5.2 *Cluster Analysis*

Table 8.5 displays analysis of how many large clusters were present in the above simulations. A large cluster was defined as one containing more than 9 helium atoms. From Table 8.5, it can be seen that no large clusters were formed within the simulation time until the helium concentration was 2%. For the lattice containing 2% He, at 1 ns one large cluster had formed (containing 10 He), this cluster grew dramatically over the next 4 ns so that at 5 ns it contained 68 He atoms. For He concentrations above 2%, the number of clusters decreased during the 1 ns to 5 ns time period, this is because the clusters were merging to form fewer, larger clusters.

Figure 8.36 plots the evolution of the lattice containing 4% He as a function of the number of helium clusters and number of vacancies present in the lattice. The number of clusters at t=0 was 250. This is because there are 250 He atoms in the simulation sufficiently separated that they count as isolated clusters. As the number of clusters decreases this is due to helium atoms occupying shared spaces. It can be

Table 8.5: The number of large helium clusters ($\geq$ 9 He) formed after 1 ns and 5 ns in PuO_2 at 2250 K and the number of helium atoms in the largest clusters

He at.%	No. large clusters		Max cluster size (No. He)	
	1 ns	5 ns	1 ns	5 ns
0.5	0	0	1	1
1	0	0	1	1
2	1	2	10	68
4	7	3	40	202
7.7	12	7	101	342
14.3	19	1	240	1015

observed that the number of vacancies in the lattice increases whilst the number of clusters decreases, reinforcing the finding that helium clustering requires vacancies to act as seed locations. At roughly 3 ns, it can be seen that the number of helium clusters plateaus, indicating that whilst helium atoms are still joining and leaving clusters, a steady state has been reached. The initial 500 ps corresponds to the equilibration period.

Next, the He:Vacancy ratios of the large He clusters identified in Table 8.5 were calculated. Figure 8.37 displays a histogram of the cluster ratios for each helium concentration. As seen in Figure 8.37a the most frequent He:Vacancy ratio formed after 1 ns is 0.7:1 and the maximum is 2:1. After 5 ns (Figure 8.37b) the mode is lower, at 0.5:1. There are fewer clusters in total, with overall lower He:Vacancy ratios, indicating that helium clusters have merged to form clusters with a more stable (lower) He:Vacancy ratio. As was evident from Figure 8.36, the number of clusters becomes stable after approximately 3 ns, so it is likely that this is the point at which the clusters with lower He:Vacancy ratios have formed.

The systems studied in this Section initially contained no defects which is not a true representation of PuO_2. As such, it is suggested that physical PuO_2 helium clusters will form in lattices with lower helium concentrations. This is predicted because intrinsic defects will be present in the lattice resulting from radiation damage, which can act as seed locations for He clusters.

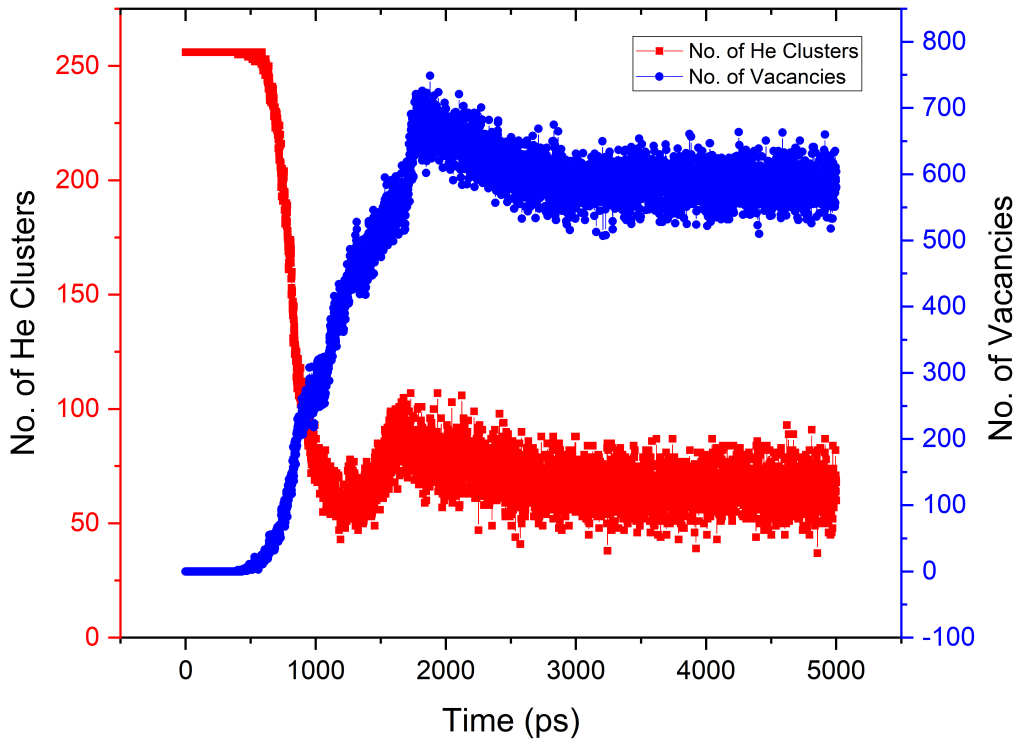
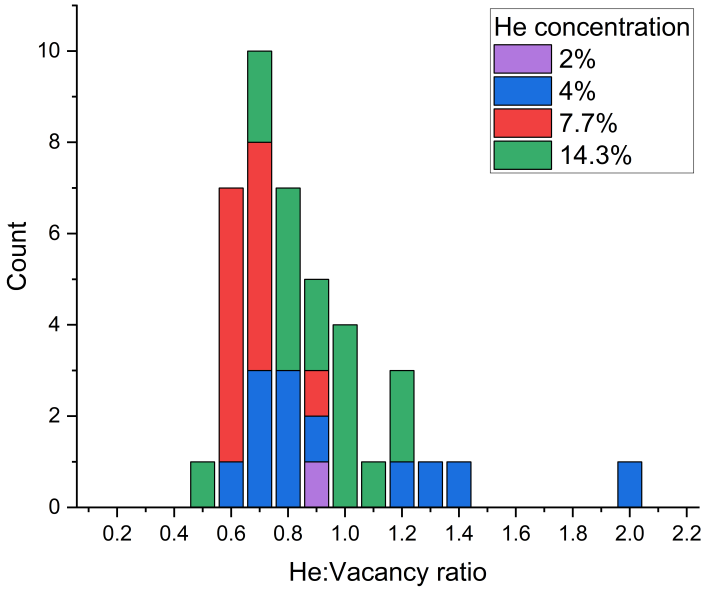
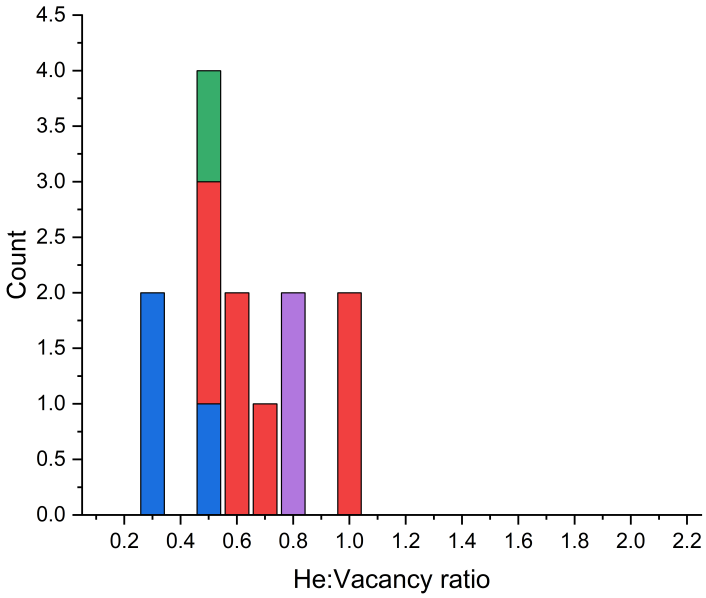


Figure 8.36: The number of helium clusters (left y-axis, red) and the number of vacancies (right y-axis, blue) as a function of time. The simulation was of PuO_2 at 2250 K with a 4% He concentration. As the number of vacancies increases, the number of clusters decreases, as more helium atoms are joining clusters so the overall number decreases as there are fewer, bigger helium clusters. After 3000 ps a stable state of the number of He clusters and lattice vacancies is established.



(a) 1 ns



(b) 5 ns

Figure 8.37: Histogram of the He:Vacancy ratio of large ($\geq$9 He) clusters formed after (a) 1 ns and (b) 5 ns for different helium concentrations in PuO_2 with 2% Schottky concentration. (a) After 1 ns at the mode He:Vacancy ratio was 0.7:1. (b) After the system was evolved for 5 ns, large clusters had formed for all helium concentrations. The mode He:Vacancy ratio was 0.5:1. The number of clusters is significantly reduced as smaller clusters have merged together.

8.5.2.1 0.5% Helium

In the simulations discussed above, no helium clusters were formed in the 0.5% helium lattice after 5 ns at 2250 K. However, in Section 7.4 molecular dynamics calculations were run on the same lattice at higher temperatures to study helium diffusion. Cluster analysis was performed on the output files from these simulations. It was found that all helium atoms remained in their isolated OISs until 2400 K, at which temperature two helium atoms occupied a Schottky trio as displayed by Figure 8.38.

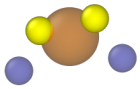


Figure 8.38: Configuration of a He_2V_3 cluster formed after 5 ns at 2400 K.

For each temperature, the percentage of helium atoms occupying clusters was calculated after 5 ns and the results are plotted in Figure 8.39. It was found that in each simulation one helium cluster would form, with the number of helium atoms occupying the cluster increasing with temperature.

The diffusivity calculated in Section 7.4 is also plotted in Figure 8.39. From this it can be seen that there is a correspondence between the plateau in helium diffusivity and the growth of helium clusters. In Section 7.4.2 the same correspondence was found. Thus, it is suggested that helium clustering is the key factor attributing to the high temperature plateau in helium diffusivity.

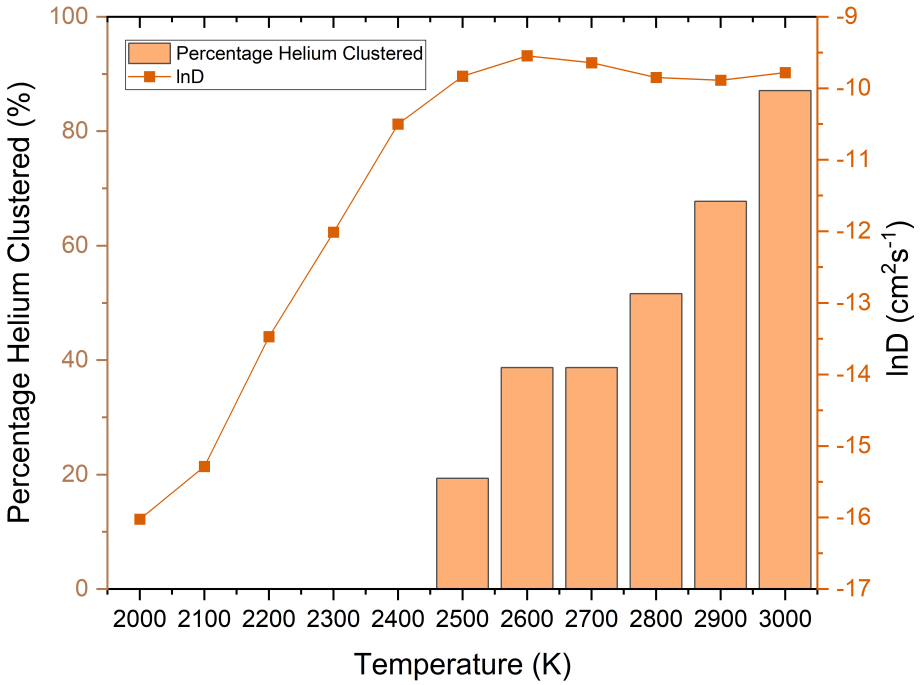
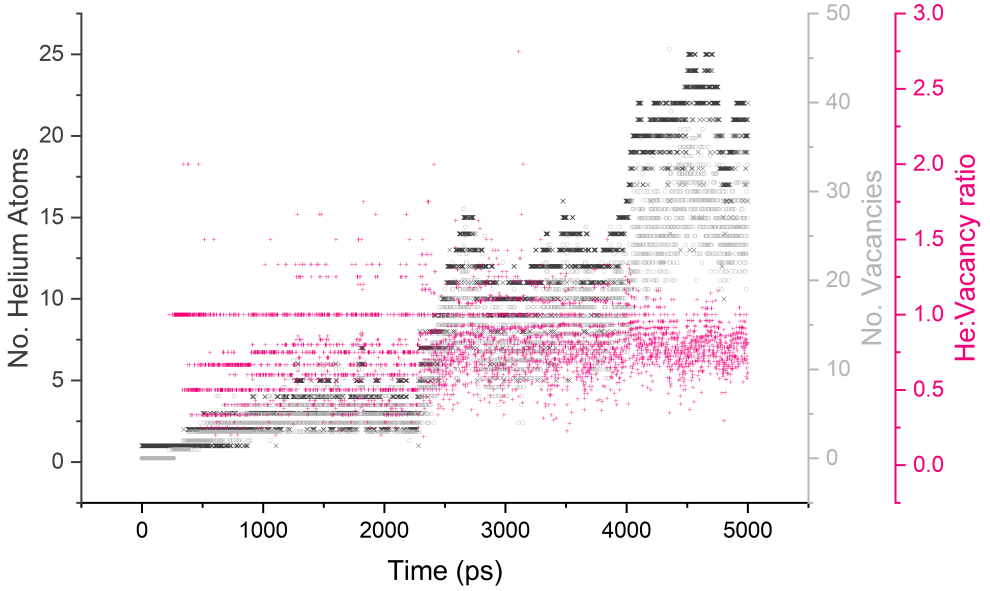


Figure 8.39: Bar and line chart showing the percentage of helium atoms occupying a cluster (left-axis bar chart) and the helium diffusivity (right-axis line chart) over a range of temperatures.

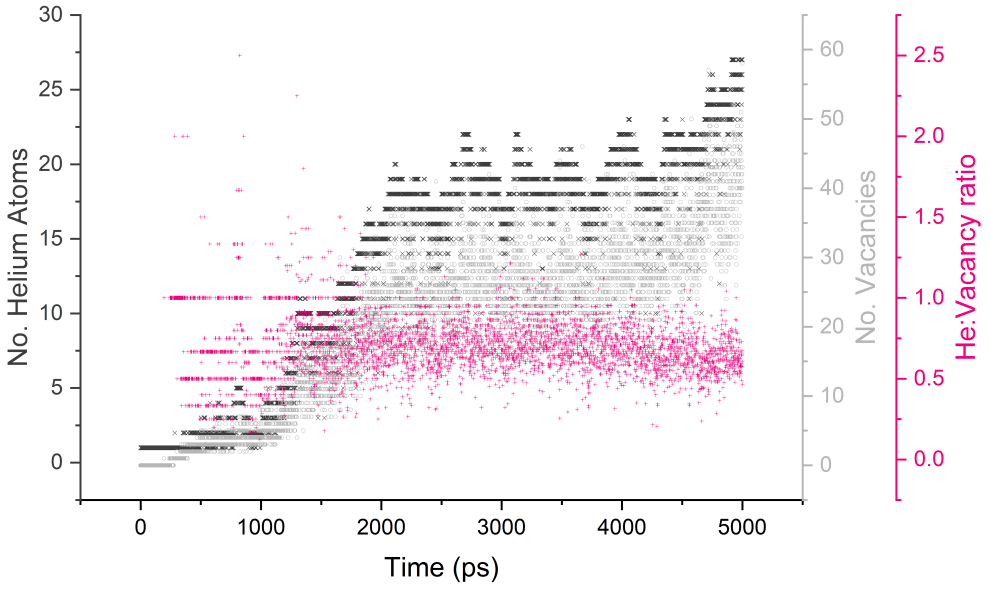
It was found that at each temperature (> 2500 K) one large helium cluster had formed. Figure 8.40 plots the number of helium atoms and vacancies in the evolving cluster at each time step at: (a) 2900 K, and (b) 3000 K. The He:Vacancy ratio was calculated and is also plotted in Figure 8.40.

At both temperatures plotted in Figure 8.40 it can be seen that the number of helium atoms and vacancies in the cluster follow a similar trend. Both increase and decrease concurrently suggesting they are interdependent in the evolution of a cluster.

From Figure 8.40 it can be observed that at higher temperatures, larger clusters form quicker. The time taken for a large cluster to form (≥ 9 He) can be determined from Figure 8.40a as approximately 2.5 ns. At 3000 K (Figure 8.40b) a large helium cluster formed approximately 1 ns quicker than at 2900 K. This may be due to the higher temperatures resulting in the atoms having higher kinetic energies and therefore migrating from lattice sites more rapidly. As such, more oxygen vacancies are available for helium migration and more plutonium vacancies may be available to trap helium. In both plots, once a large cluster is established, there is a convergence



(a) 2900 K



(b) 3000 K

Figure 8.40: Scatter plot with three y-axes detailing the evolution of the largest He cluster as a function of time. The left y-axis (dark grey) plots the No. of He atoms and the right y-axis (grey) plots the No. of vacancies in the largest cluster. The far right y-axis (pink) plots the He:Vacancy ratio for the largest cluster.

in the He:Vacancy ratio with a mean value of 0.78:1 at 2900 K and 0.71:1 at 3000 K.

In Figure 8.40a, there is a rapid increase in total helium atoms and vacancies in the cluster. Despite this, the average He:Vacancy ratio remains roughly constant. This could imply that maintaining a stable He:Vacancy ratio is a key factor in cluster evolution. In Figure 8.40b the number of helium atoms and vacancies displays a more gradual increase.

Cluster analysis was performed for all lattices in which a large cluster had formed. Figure 8.41 displays a box plot of the results. The range of the mean He:Vacancy ratios is narrow, between 0.88-0.71:1. It was found that the mean He:Vacancy ratio decreases with increasing temperature. It is suggested that this trend may be due to the convergence in He:Vacancy ratio values being established earlier at higher temperatures (Figure 8.40) and as such the mean value is closer to the ideal value.

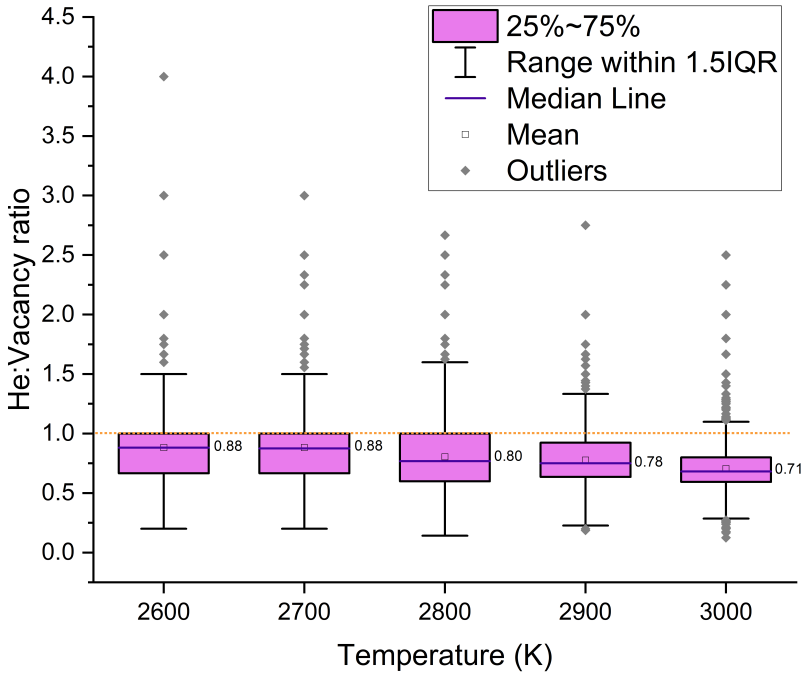


Figure 8.41: Box plot of the He:Vacancy ratio of the largest cluster at each temperature in which clustering was observed during 5 ns. Dashed orange line through y=1. The mean values are displayed.

From Figure 8.41 it can be seen that at each temperature the interquartile range is below a He:Vacancy ratio of 1:1, with the upper quartile being equal to 1 for the three lowest temperatures. Therefore, though clusters with ratios greater than 1:1

were found to be energetically feasible in Sections 8.2 and 8.3, they are predicted to be rare. This is in agreement with the results of Section 8.5.2 in which it was found that the mean He:Vacancy ratio of clusters in lattices with higher helium concentrations run at 2250 K was 0.7:1 after 1 ns. However, as displayed in Figure 8.37, when the lattices were evolved for a further 4 ns, the mean He:Vacancy ratio reduced to 0.5:1.

8.5.3 *Comparison*

The number of clusters formed after 1 ns at 2250 K in the initially defect-free lattice can be compared to the number of clusters formed in the lattice which contained three Schottky trios discussed in Section 8.4. Figure 8.42 displays the results of this comparison. It can be seen that there is no difference in the number of clusters formed after 1 ns in either lattice. For both initial lattices, no large helium clusters form during 1 ns until the helium concentration was 2%. In both lattices at this concentration one helium cluster forms.

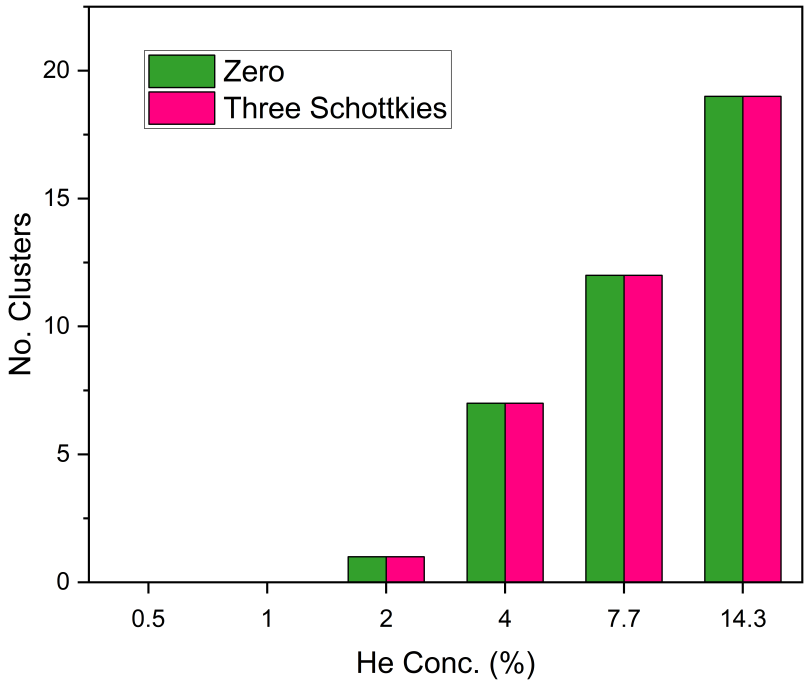


Figure 8.42: Bar chart displaying the number of helium clusters formed after 1 ns in initially defect-free PuO_2 (green) and a lattice containing three Schottky trios (pink) at 2250 K.

It is suggested that the identical number of clusters formed may be due to the high temperature at which the simulations were run (2250 K). At such a high temperature, many oxygen vacancies are present in the lattice due to oxygen being mobile above 1500 K. As helium has been found to be mobile via oxygen vacancies, helium will be mobile within the lattice regardless of whether the initial lattice contained zero defects, or three Schottky trios.

The lattices containing three Schottky trios and 1, 2 and 4% helium were run for an additional 4 ns. Figure 8.43 displays the number of clusters formed after the 5 ns simulation for both the lattices initially containing zero defects and three Schottky trios.

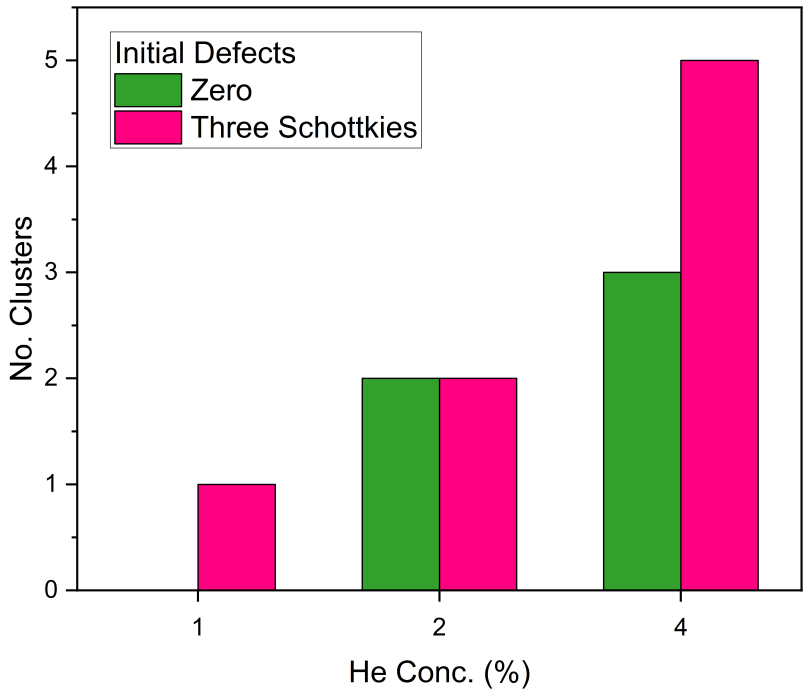


Figure 8.43: Bar chart displaying the number of helium clusters formed after 5 ns in initially defect-free PuO_2 (green) and a lattice containing three Schottky trios (pink) at 2250 K.

As can be seen from Figure 8.43, after 5 ns there are some differences in the cluster formation in the different lattices. Notably, after 5 ns, one cluster has formed in the 1% helium lattice which contained three Schottky trios (displayed in Figure 8.18). After 5 ns the cluster which initially contained three Schottky trios contains seven plutonium vacancies. In contrast, the cluster which was initially defect-free still contained zero plutonium vacancies. Both lattices contained oxygen vacancies.

Thus, it is suggested that it is the presence of plutonium vacancies that is key for enabling helium nucleation.

In Section 8.5.2.1 it was found that for the lattice containing 0.5% helium and no initial defects, clustering was observed when the temperature exceeded 2500 K. Figure 8.44 displays the number plutonium vacancies present in the lattice after 5 ns over a range of temperatures. Oxygen vacancies were present at all temperatures displayed. It can be seen that no plutonium vacancies are present until 2400 K, at which there is one V_{Pu}. This plutonium vacancy forms a Schottky trio which accommodates two helium atoms as identified in Figure 8.38. As detailed in Section 7.4, in the high temperature region of diffusion (R3), plutonium is mobile and as such plutonium vacancies are being generated via temporary plutonium Frenkel pairs. However, PuFPs are energetically unstable and therefore often quickly recombine. Stable plutonium vacancies can be found in Schottky trio defects.

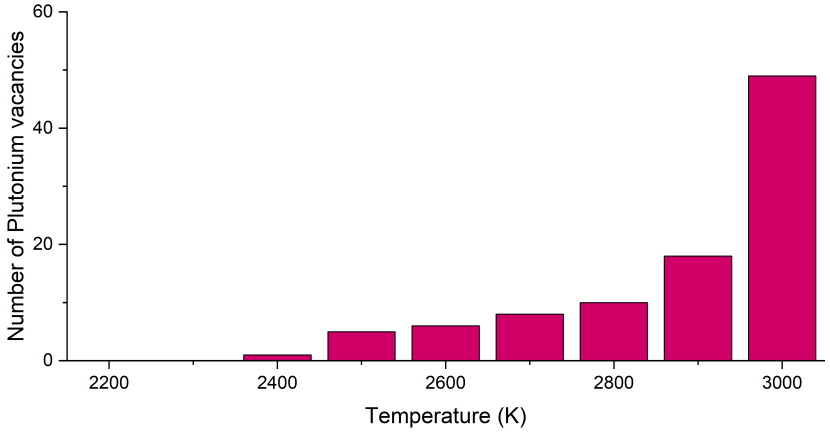


Figure 8.44: Bar chart displaying the number of plutonium vacancies in a PuO_2 lattice containing 0.5% helium after 5 ns at a range of temperatures.

Above 2400 K, the number of plutonium vacancies increases and in turn so does the percentage of helium atoms occupying a cluster as displayed by Figure 8.39.

It can therefore be concluded that helium clustering depends primarily on vacancies. Oxygen vacancies must be present for helium to migrate to a cluster and plutonium vacancies must be present to trap helium at a cluster. Additionally, oxygen vacancies frequently need to be present to stabilise plutonium vacancies, preventing the ejection of helium via PuFP recombination.

8.6 Conclusions

Multiple computational methods have been used to investigate helium clustering behaviour in PuO_2 using LAMMPS. OVITO has been used to inspect the output clusters and calculate the He:Vacancy ratios.

From following an iterative energy minimisation procedure, many helium clusters have been relaxed and the minimum energy configurations determined. From this, it was found that the largest energetically stable helium cluster had a He:Vacancy ratio of $\sim$ 3.5:1. This was determined from the calculation of the successive incorporation energies of clusters with increasing numbers of helium. When the energy for an additional helium atom to join the cluster exceeded that of helium incorporation in an OIS (1.7 eV), then it was no longer energetically favourable for the cluster to grow.

In addition, NEB calculations were performed to determine the energy barriers for successive helium addition and removal from a cluster. By calculating the difference in energy barriers for the addition and removal of a helium atom, the maximum energetically stable cluster was determined. For all three vacancy cluster sizes (1, 2 and 4 Schottky trios), the maximum energetically stable He:Vacancy ratio was found to be $\sim$ 3.5:1, in agreement with the energy minimisation calculations.

Long molecular dynamics simulations were run at high temperatures to determine if clusters would nucleate at Schottky trios, and how they would form in an initially defect-free lattice. From such simulations it was found that whilst the maximum energetically stable cluster is predicted to have a He:Vacancy ratio of 3.5:1, the majority of clusters which form have much lower helium densities, with He:Vacancy ratios averaging 1:1. This finding is comparable to the maximum He:Vacancy ratio of 1.6:1 which was calculated by Van Brutzel *et al.* [217] from their molecular dynamics simulations of helium clusters in UO_2.

Cluster analysis of the diffusion simulations presented in Chapter 7 has also been performed. It was found that the plateau in helium diffusivity corresponds to temperatures at which helium clusters have formed. The clusters were found to have an average He:Vacancy ratio below 1:1. Finally, it was found that the temperatures corresponded to those at which plutonium vacancies were present and stable (i.e. as Schottky trios). As such, it is predicted that Schottky trios are a likely seed location for helium bubble nucleation. Therefore, in agreement with the findings of Liu *et al.* [218] of xenon behaviour in UO_2, it is predicted that a key factor in helium bubble nucleation rates in PuO_2 is the low mobility of plutonium ions.

Chapter 9

Conclusions

A range of atomistic simulation techniques have been used to investigate helium diffusion and clustering behaviour in PuO_2. Via multiple computational methods it has been found that helium accommodation is most favourable in plutonium vacancies. It is predicted that Schottky trio defects are likely helium bubble nucleation sites as they accommodate a stable plutonium vacancy. The key helium migration mechanism was determined to be oxygen vacancy assisted interstitial hops. It is suggested that helium will migrate via this mechanism to become sequestered in a Schottky trio at which a helium bubble can nucleate. This research has shown that helium diffusion depends primarily on oxygen vacancies, whilst helium clustering depends on both oxygen and plutonium vacancies. As defects will be present in stored PuO_2 due to both thermodynamic and decay events, it is predicted that both helium diffusion and clustering are possible under storage conditions.

The stability of intrinsic defects in PuO_2 was determined via energy minimisation calculations using GULP. First, a range of interatomic potentials were evaluated to ensure they accurately reproduced experimental data and could therefore be used as a predictive tool. The Read potential was determined to be the most suitable potential for describing PuO_2. Using this model it was found that Schottky trio defects and oxygen Frenkel pairs are the most energetically stable defects in PuO_2, in agreement with the available literature. Plutonium Frenkel pairs were found to be energetically unfavourable. Thus, after collision cascade events in PuO_2 it is predicted that unless stabilised by oxygen vacancies, plutonium vacancies will rapidly recombine with interstitials to be annihilated.

The Read potential was then employed in METADISE to investigate the surfaces of PuO_2. It was found that the (111) surface was the most energetically stable surface for pure PuO_2. The same order of energetic stability for defects was found at the

surface as in the bulk. However, the defect energy for plutonium Frenkel pairs was much lower at the surface resulting in a strongly exothermic segmentation energy. As such, there is an energetic drive for plutonium Frenkel pairs to form at the surface of PuO_2 rather than in the bulk. It was hoped that the surface simulations would be extended to grain boundaries as these are predicted to be important in the transmission of helium through the lattice [223]. Due to time constraints this was not possible but would be a natural progression of this work.

Whilst many interatomic potentials are available for PuO_2 interactions, extremely limited data is available for modelling the interaction of He with PuO_2. From the literature, one Pu—He interatomic potential was identified and has been shown to be a good fit to a standard Buckingham potential. This potential was implemented in GULP and it was found that the octahedral interstitial site is the most stable site for helium to occupy in defect-free PuO_2. This finding was in agreement with the more extensive studies available of helium incorporation in UO_2.

Helium clusters were then built up at defect sites in PuO_2. It was found that clusters formed surrounding defects which contained a plutonium vacancy. The maximum energetically favourable size of the cluster was determined to be $6m + n$ where m and n are number of V_{Pu} and V_O respectively. As the Schottky trio defect is the most energetically stable defect containing a V_{Pu}, it is predicted that these will be seed locations for helium nucleation.

Whilst the Read potential performed successfully for the static calculations in GULP, it is widely documented that core-shell models such as the Read potential do not perform well in molecular dynamics simulations. As such, it was required to perform a potential evaluation for use in LAMMPS. From this, the Cooper potential was determined to be the most robust for use in molecular dynamics. From modelling diffusion in PuO_2 over a range of temperatures it was found that oxygen has a much higher mobility than plutonium. Additionally, it was determined that when defects are in the lattice, oxygen diffusivity greatly increases at low temperatures. The diffusivity data calculated was in agreement with experimental data giving confidence in the accuracy of simulations.

Helium incorporation was modelled in LAMMPS and the energetic stability of helium incorporation was in agreement with the earlier GULP simulations, i.e. helium is most stable in plutonium vacancy sites. Helium diffusion was then investigated and it was found that helium migrates via oxygen vacancy assisted interstitial hops. As such, helium diffusivity corresponds to oxygen diffusivity and was found to be limited below 1500 K in a defect-free lattice. It was determined that when

defects are present within the lattice, helium is mobile at lower temperatures. As radiogenic defects will be present within the stored PuO_2, it is predicted that helium will be mobile under the temperature storage conditions. These simulations were repeated for larger supercell sizes with no discernible change in results found. Thus, the 8x8x8 supercell lattices was used throughout the molecular dynamics work was suitable.

The modelling results predict that helium behaves similarly in PuO_2 to UO_2. As such, existing experimental findings from UO_2 are of relevance in developing an understanding of stored PuO_2. The key factor determining helium diffusivity has been found to be the concentration of defects within the lattice. As PuO_2 has a higher radioactivty than UO_2, more defects will be present within the lattice. Therefore, it is predicted that helium diffusion may be higher in PuO_2 than in UO_2.

At high temperatures a plateau in helium diffusivity was observed. It has been shown that this plateau corresponds to the formation of helium clusters, in which helium is less mobile.

The nucleation of such helium clusters was studied. From analysis of high temperature molecular dynamics simulations it was determined that it is possible for helium clustering to occur in PuO_2 if both oxygen and plutonium vacancies are available. The oxygen vacancies enable the helium to migrate whilst stable plutonium vacancies trap helium atoms. The presence of such vacancies is possible either at high temperatures (at which oxygen and plutonium are mobile), or from radiogenic defects resulting from decay events in PuO_2. Although it was found via static calculations that plutonium Frenkel pairs are energetically favourable for helium occupation, they are unlikely to act as seed sites for helium clusters. This is due to PuFPs in the bulk having a high defect energy and so are likely to rapidly recombine. It has been found that occupation of a PuFP by a single helium atom does not prevent recombination. Thus, the presence of oxygen vacancies to stabilise plutonium vacancies (i.e. Schottky trios) are frequently required for helium bubble nucleation.

The growth of large helium clusters in PuO_2 has been demonstrated. The maximum He:Vacancy ratio of an energetically stable cluster was calculated via multiple methods to be $\sim$ 3.5:1. Above this value it requires more energy for helium to join a cluster than to leave it. Finally, from the average He:Vacancy ratio of the clusters generated and examined in this work, it is suggested that helium clusters with He:Vacancy ratios less than 1:1 will form in PuO_2 during storage, due to the presence of radiogenic defects.

9.1 Future Work

The next step in this research would be to study helium incorporation at the surfaces of PuO_2. The importance of such work is to determine if there is an energetic drive for helium to migrate to surfaces. If so, for the UK's plutonium inventory this could lead to the sequestered helium migrating to surfaces and result in the pressurisation of the head space inside storage canisters. A possible first step in such work would be static surface simulations such as those of Palmer [93]. By determining incorporation energies of helium at surface interstitial and defect sites the segmentation energy could be calculated. In Chapter 4 it was found that there is an energetic drive for PuFPs to form at surfaces rather than in the bulk. As it has been found that there is an energetic drive for helium to accommodate plutonium vacancies, if stable plutonium vacancies are present at PuO_2 surfaces, it is possible that helium will migrate to surface defects.

Molecular dynamics could then be used to study helium diffusion behaviour in the surface region. In UO_2 it has been found that there is an enhancement of helium diffusivity near to dislocations or grain boundaries [223]. Lattices containing such dislocations and grain boundaries could be generated for PuO_2 and helium diffusivity in their vicinity investigated.

It has been predicted that helium release may be dependent on the original specific surface area of PuO_2 powders rather than temperature and age. The development of models studying PuO_2 nanoparticles could therefore prove an important area of research to determine if helium diffusivity is surface area dependant.

Whilst the research comprising this thesis has focused much on the nucleation and growth of helium clusters, future research could examine the resolution of helium clusters. Such work has been performed for helium in UO_2 [46]. This work could deepen the understanding of any events which could cause a helium bubble to rapidly leave the lattice, which could lead to pressurisation of the storage canisters. For example, collision cascades in the vicinity of a cluster could be generated to determine if a helium cluster remains stable during such events.

Helium clustering behaviour was not exhibited in many of the 1 ns simulations presented in this work. However, when select simulations were extended to 5 ns, clustering was sometimes observed. As such, it would be pertinent for future research to extend the timescale of all the 1 ns diffusion and cluster calculations presented in this work. Furthermore, statistical analysis to predict how the high temperature, nanosecond timescale simulations performed in this research could be translated to

the low temperature, extended time scales of real world scenarios would be advantageous to develop.

Further study of helium diffusion in lattices containing extended defects and different concentrations of Frenkel pairs, Schottky trios, and divacancies could yield significant findings. Additionally, the fission product americium could be accommodated in the models. Recent work by Neilson *et al.* [132] has found americium to alter the energetic stability of helium incorporation at different sites. Thus, a difference in helium diffusivity behaviour may be found in a lattice containing other fission products. Multitudes of lattices containing radiation damage could be constructed to investigate this. A suggested method of pursuing such research would be to use collision cascades. Such work may correspond with the helium resolution simulations discussed above.

Finally, as more experimental data from the repacking of plutonium becomes available, it would be advantageous to incorporate such data into computational models. Example data obtained could include: defect concentrations, helium concentrations, pressures, and observed bubble sizes. Experimental studies could consist of calculating thermal release rates from PuO_2 powders using the Knudsen method combined with TEM and XRD characterisation. Such data could enable validation of the computational calculations presented in this thesis, and would prove a valuable tool in the continued development of more rigorous computational models to study the behaviour of helium in PuO_2.

Appendix A

Static Helium Build-up Simulations

This Appendix contains details of the static helium in defective PuO_2 calculations performed in GULP as discussed in Chapter 5. The helium atoms are input in different configurations surrounding each defect and the input and relaxed configurations are displayed alongside the defect energy in units of eV/He. Each configuration is named according to the number of helium atoms and their location, for example: '2_OIS_1_Pu' refers to a configuration with 2 helium atoms in separate OIS and 1 in a plutonium vacancy.

Shorthand used in configuration names:

DB: Dumbbell

EC: Edge-Centered

Adj: Adjacent OIS site

Diag: Diagonal configuration

Dist: In an OIS more than one nearest neighbour position away (distant)

Cent: Located at midpoint of two vacancy sites

Pu: Plutonium vacancy site

O: Oxygen vacancy site

The atoms and vacancies are coloured in accordance with the legend displayed by Figure A.1.



Figure A.1: Legend of colours used to represent atoms. Yellow spheres: He, red spheres: oxygen, blue spheres: plutonium, blue x: plutonium vacancy, red x: oxygen vacancy.

A.1 Plutonium Vacancy

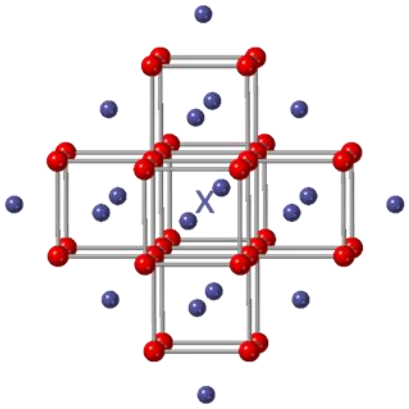
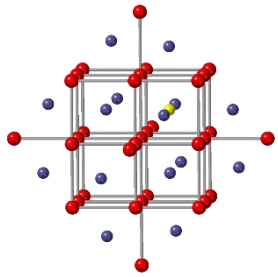
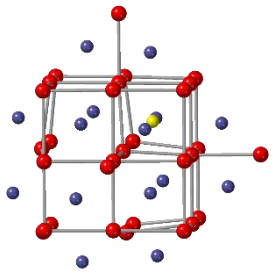
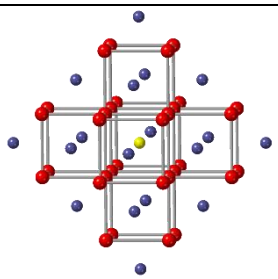
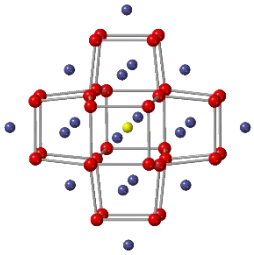
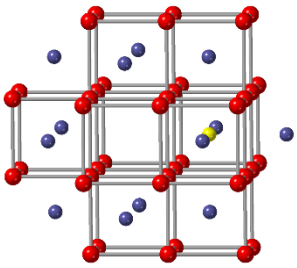
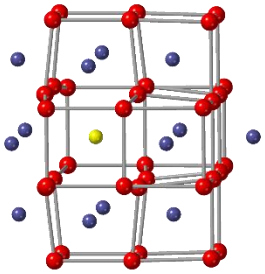
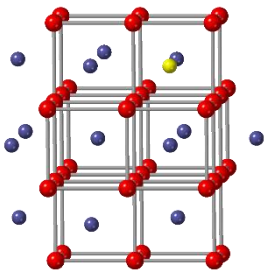
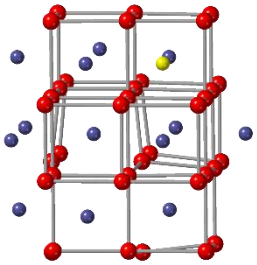
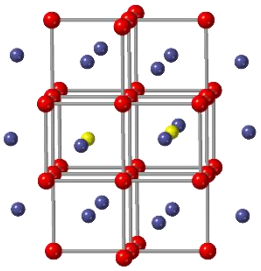
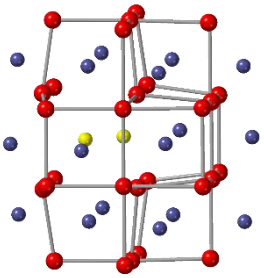
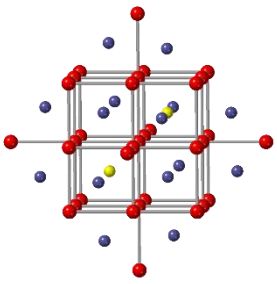
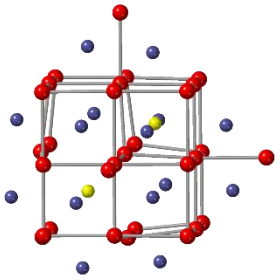
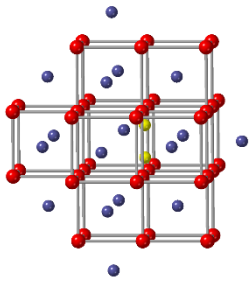
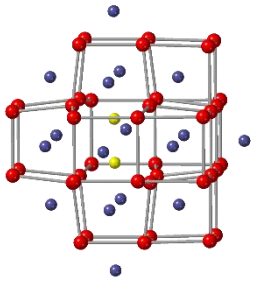
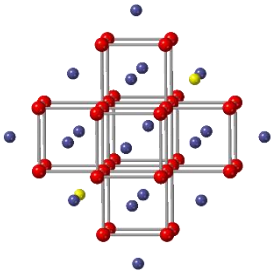
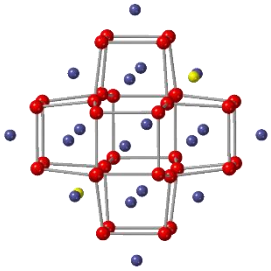
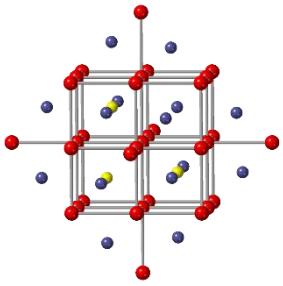
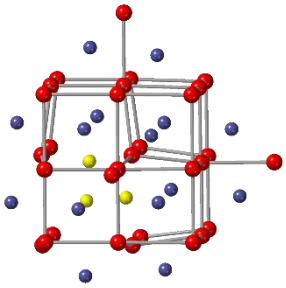
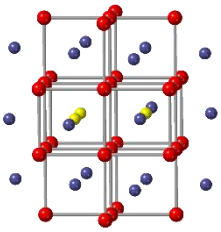
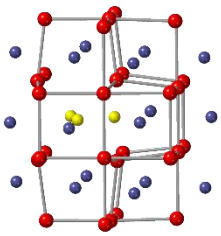
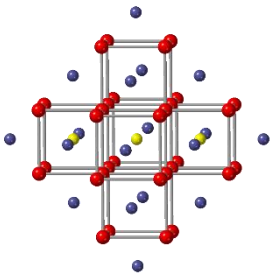
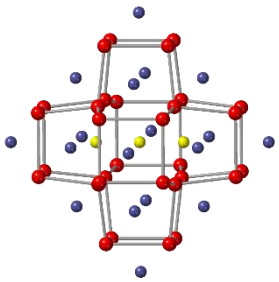
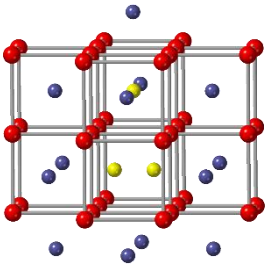
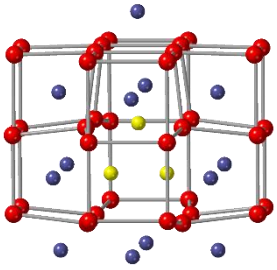
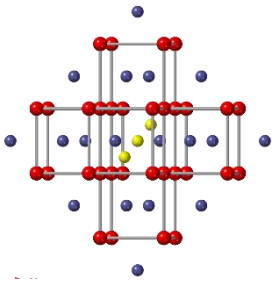
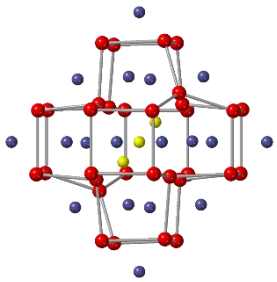
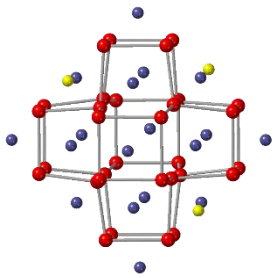
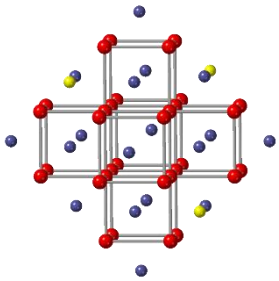
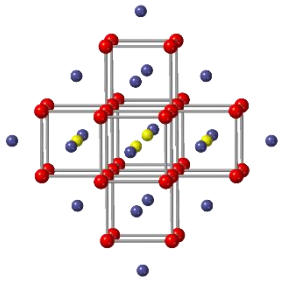
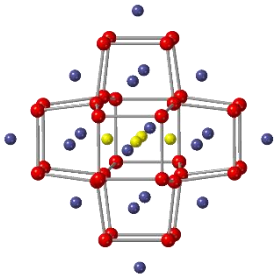
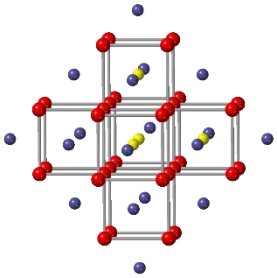
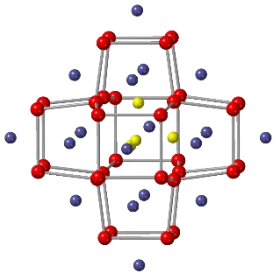
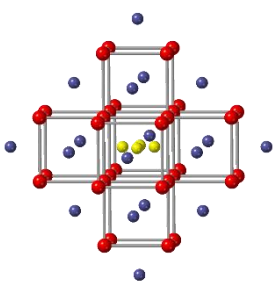
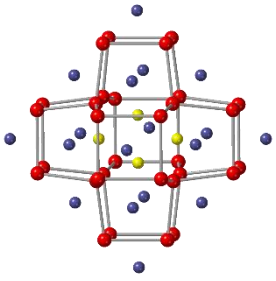
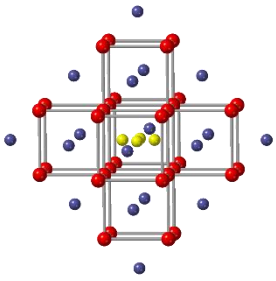
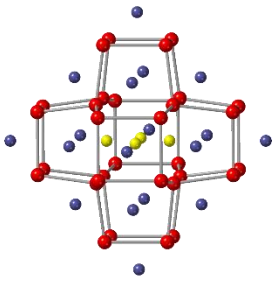
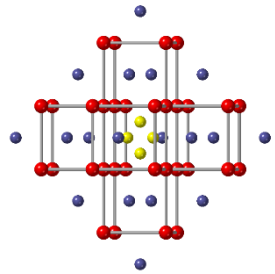
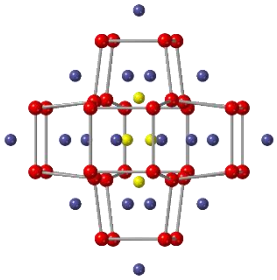
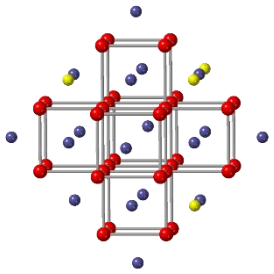
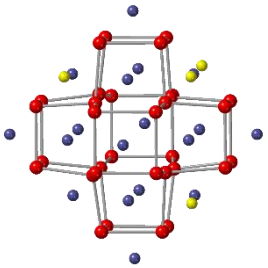
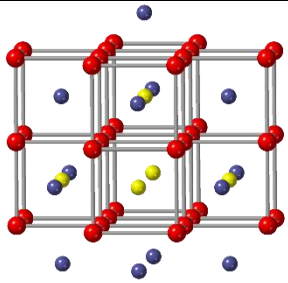
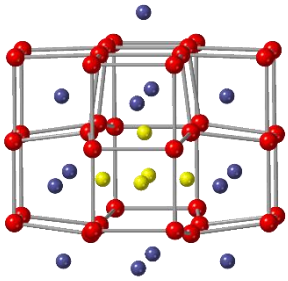
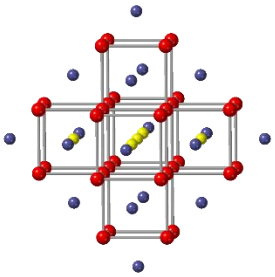
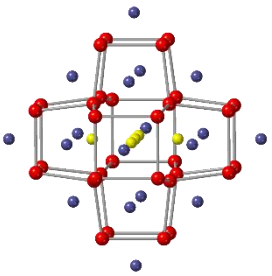
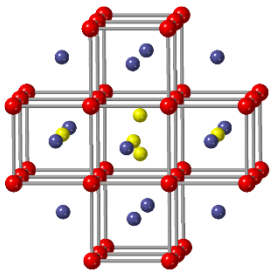
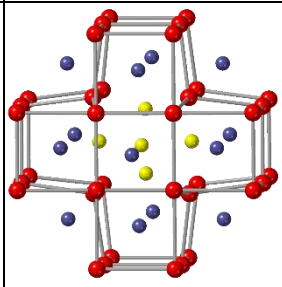
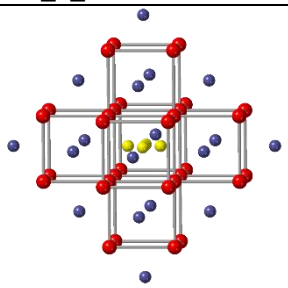
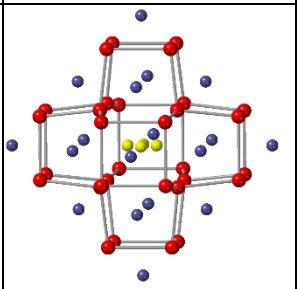
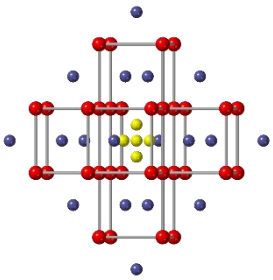
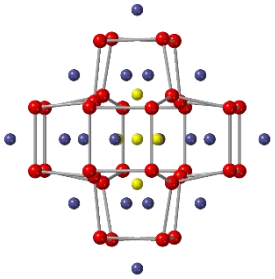
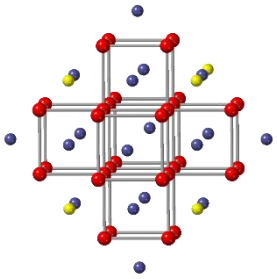
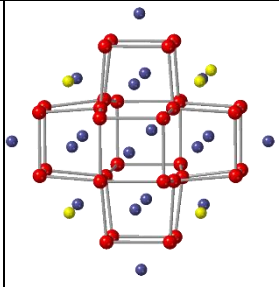
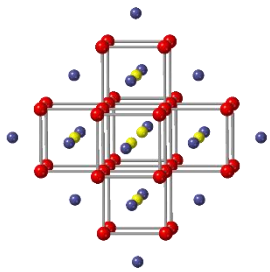
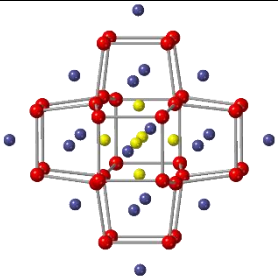
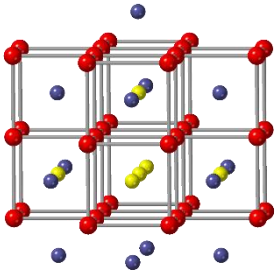
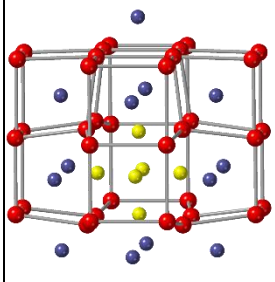


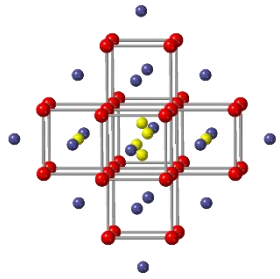
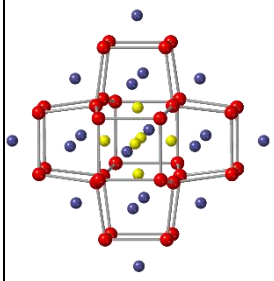
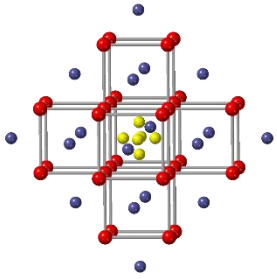
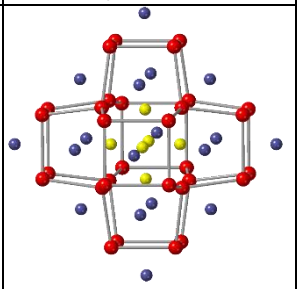
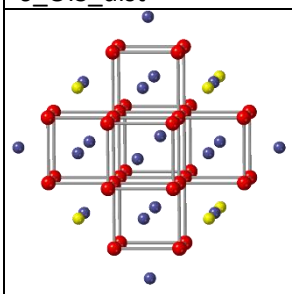
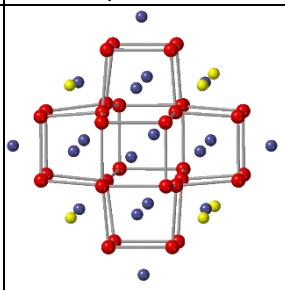
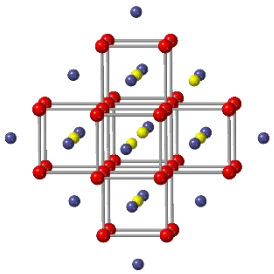
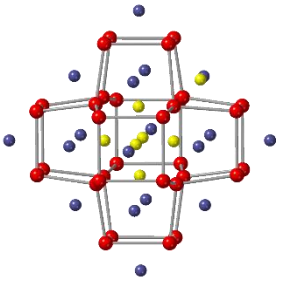
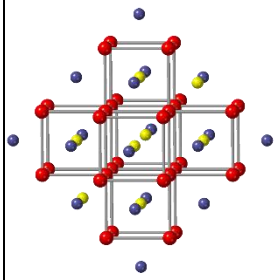
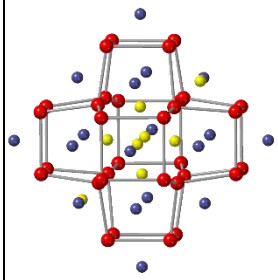
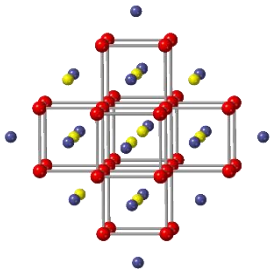
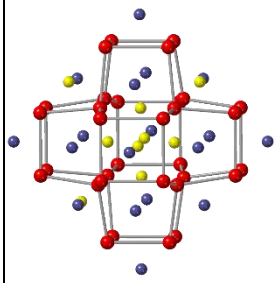
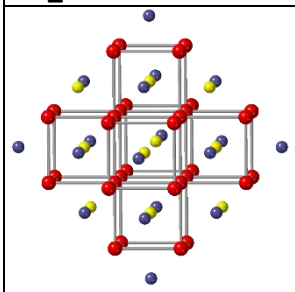
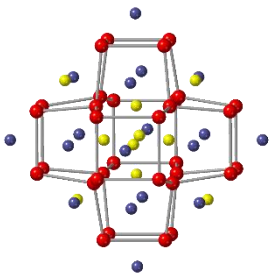
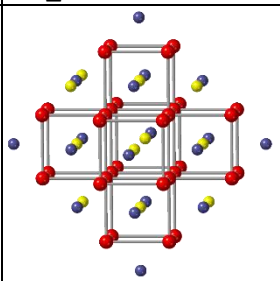
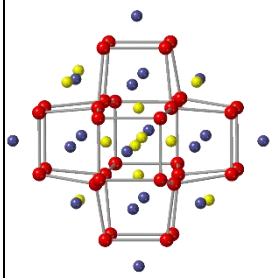
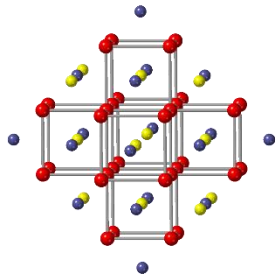
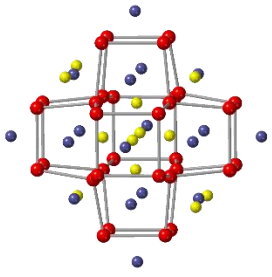
Figure A.1.1: Plutonium vacancy in PuO_2. Blue x displays the plutonium vacancy site.

Table A.1.1: Details of helium build up calculations surrounding a plutonium vacancy. For each configuration the unrelaxed and relaxed configurations are displayed alongside the defect energy. For 1-6 He surrounding the Pu vacancy multiple configurations are shown. For 7-12 He only the configuration of all He in isolated OIS is included.

Configuration	**E_d (eV/He)**	**Configuration**	**E_d (eV/He)**
Before Relaxation	*After Relaxation*	*Before Relaxation*	*After Relaxation*
1 He			
1_OIS	1.24 eV/He	Pu	-0.23 eV/He
			
adjHe	-0.23 eV/He	1_dist	1.08 eV/He
			
2 He			
2_OIS	0.18 eV/He	Pu_OIS	0.50 eV/He
			
DB_adj	0.05 eV/He	2_dist	1.23 eV/He
			
3 He			
3_OIS	0.26 eV/He	Pu_2_OIS	0.20 eV/He

			
Pu_2_OIS_Para	0.28 eV/He	DB_OIS	0.18 eV/He
			
3_Diag	1.14 eV/He	3_OIS_dist	1.24 eV/He
			
4 He			
4_OIS	0.28 eV/He	Pu_3_OIS	0.25 eV/He
			
DB_2_OIS	0.25 eV/He	2_DB	0.28 eV/He
			

Diamond	0.34 eV/He	4_OIS_dist	0.34 eV/He
			
5 He			
5_OIS	0.30 eV/He	Pu_4_OIS	0.37 eV/He
			
DB_3_OIS	0.29 eV/He	Pu_2_DB	18.35 eV/He
			
5_Diamond	0.85 eV/He	5_OIS_dist	1.26 eV/He
			
6 He			
6_OIS	0.30 eV/He	Pu_5_OIS	0.30 eV/He
			

DB_4_OIS	0.30 eV/He	3_DB	0.30 eV/He
			
6_OIS_dist	1.26 eV/He	**7_OIS**	0.44 eV/He
			
8_OIS	0.55 eV/He	**9_OIS**	0.64 eV/He
			
10_OIS	0.71 eV/He	**11_He**	0.77 eV/He
			
12_He	0.82 eV/He		
			

A.2 Oxygen Vacancy

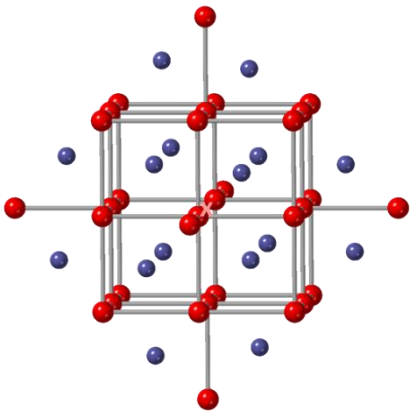
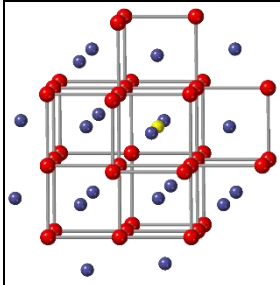
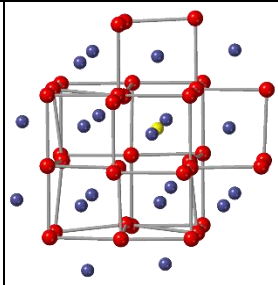
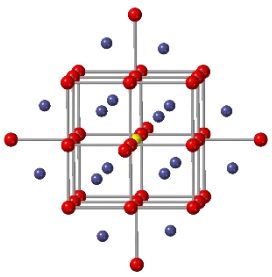
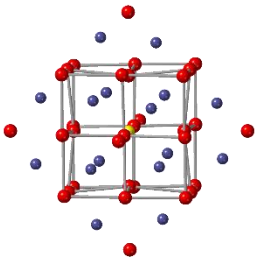
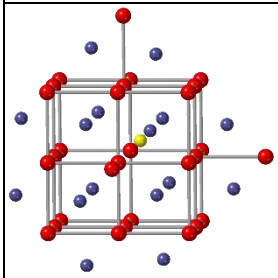
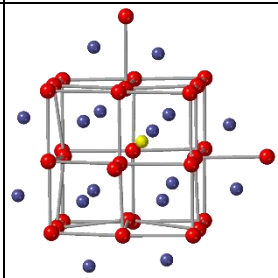
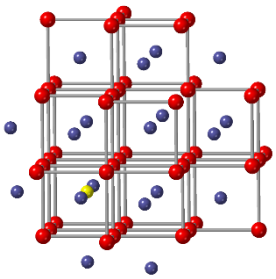
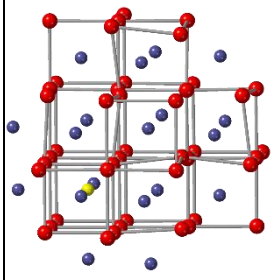
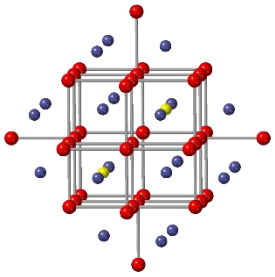
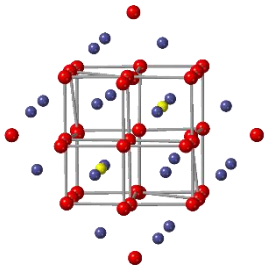
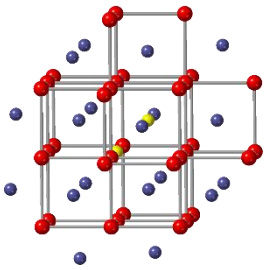
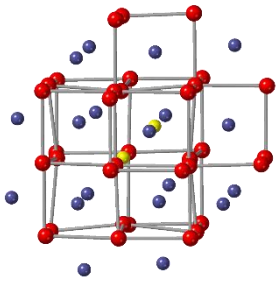
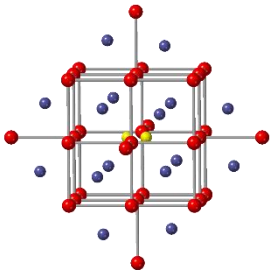
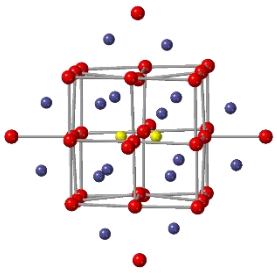
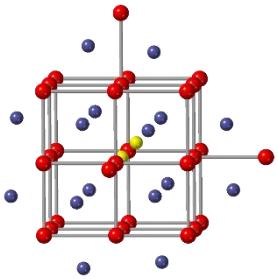
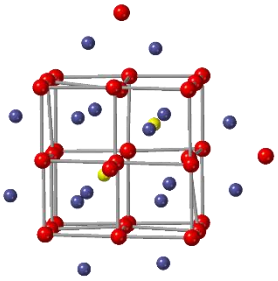
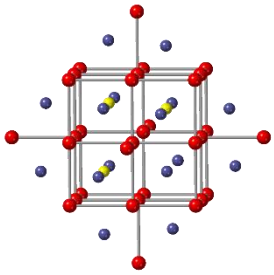
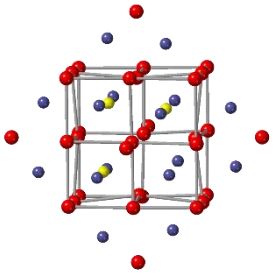
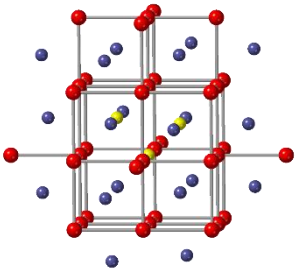
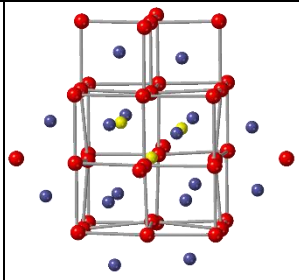
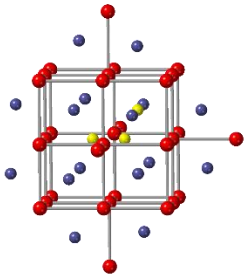
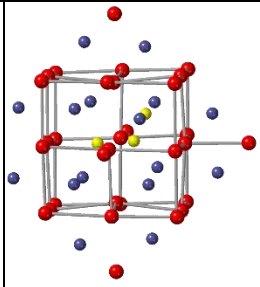
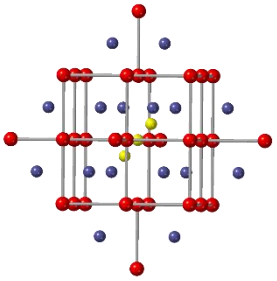
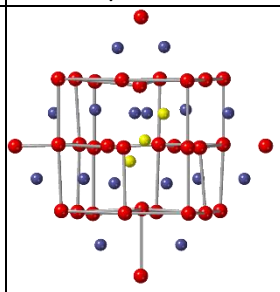
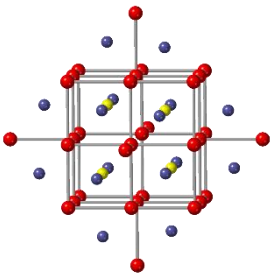
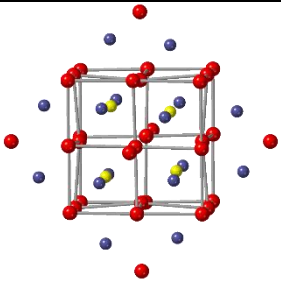
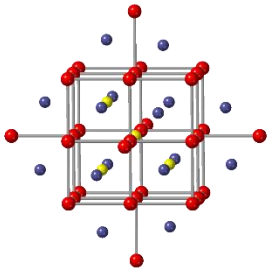
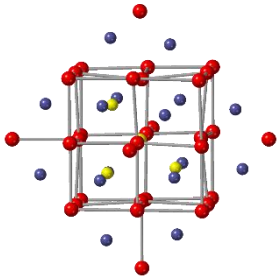
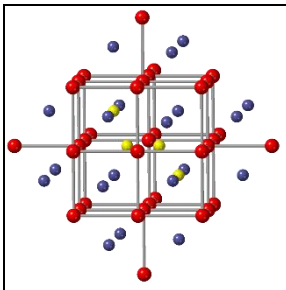
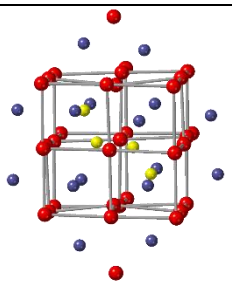
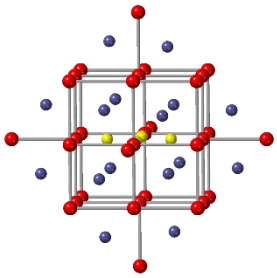
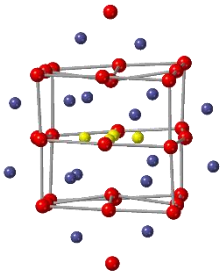
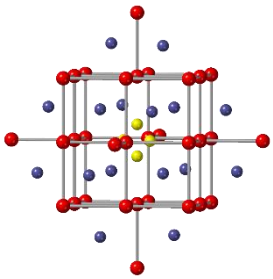
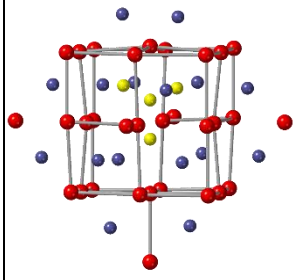
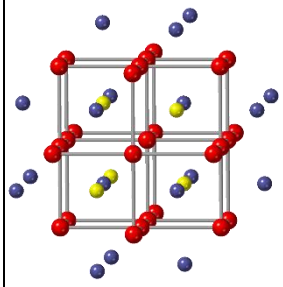
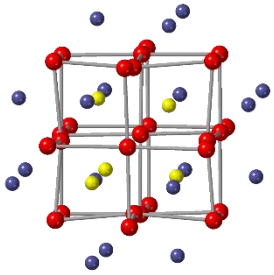
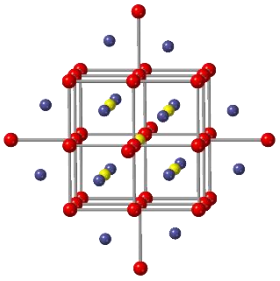
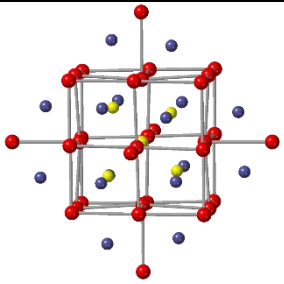
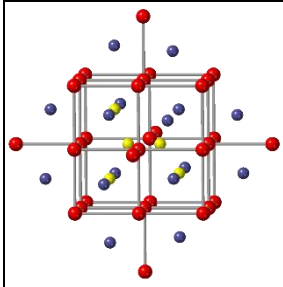
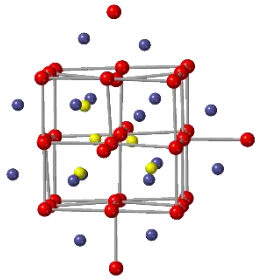
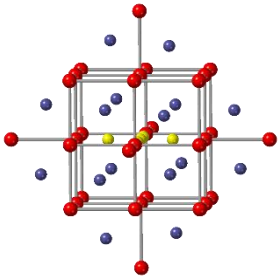
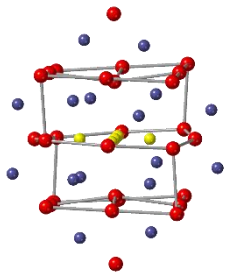
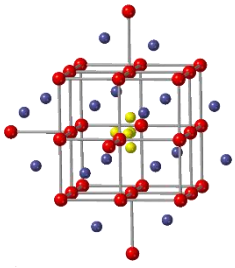
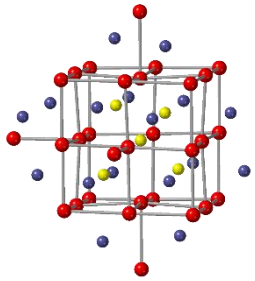
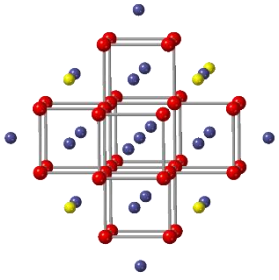
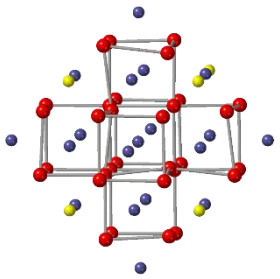


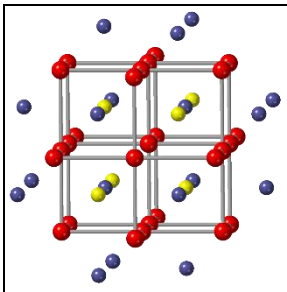
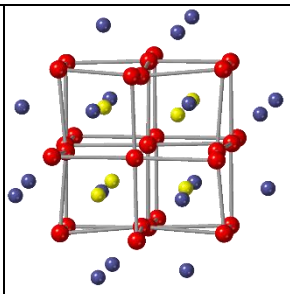
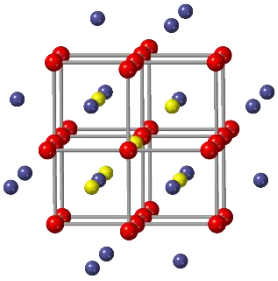
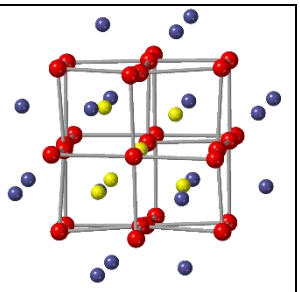
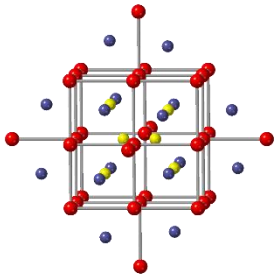
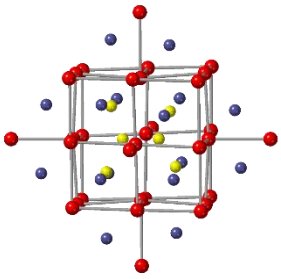
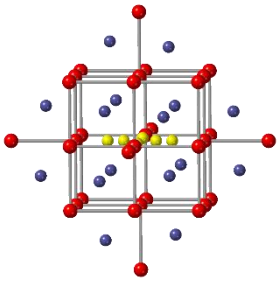
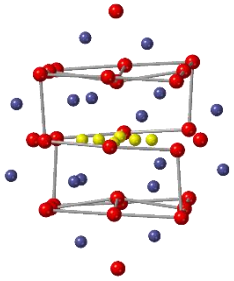
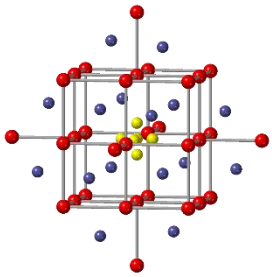
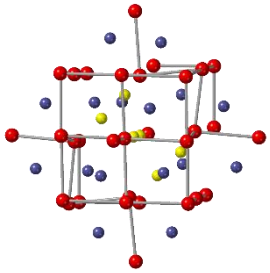
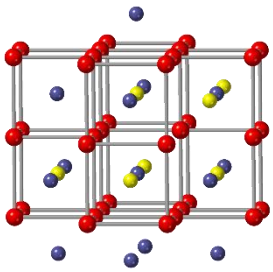
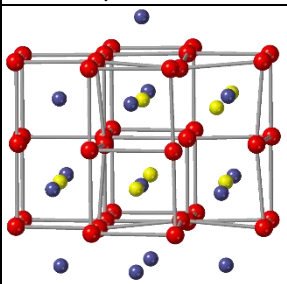
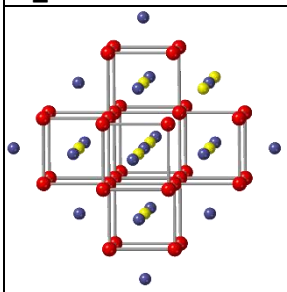
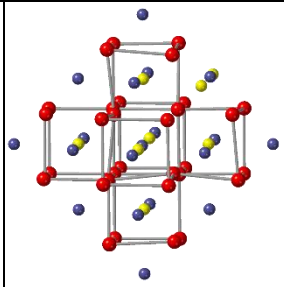
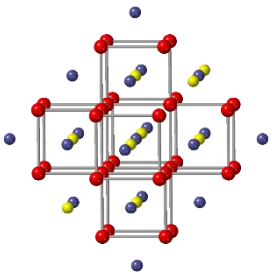
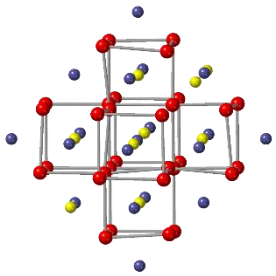
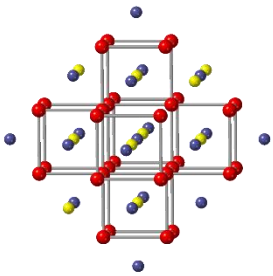
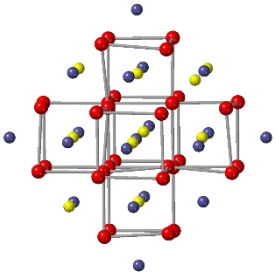
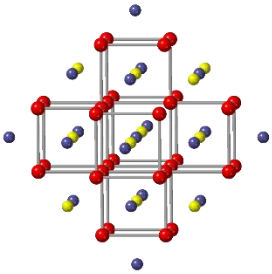
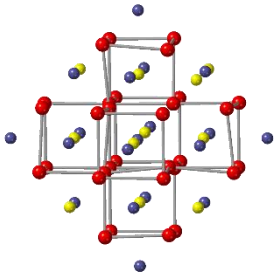
Figure A.2.1: Oxygen vacancy in PuO_2. Oxygen vacancy site illustrated by the pale red x.

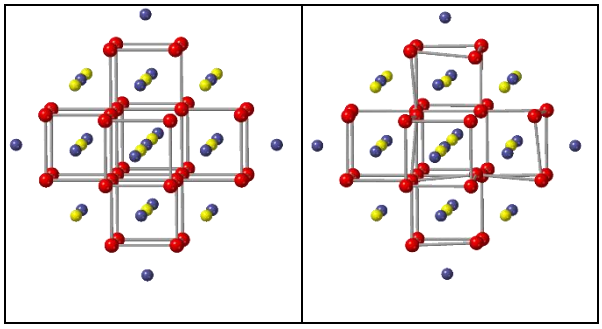
Table A.2.1: Helium build up simulations surrounding an oxygen vacancy. For each configuration the unrelaxed and relaxed configurations are displayed alongside the defect energy. For 1-6 He surrounding the O vacancy multiple configurations are shown. For 7-12 He only the configuration of all He in isolated OIS is included.

Configuration	**E_d (eV/He)**	**Configuration**	**E_d (eV/He)**
Before Relaxation	*After Relaxation*	*Before Relaxation*	*After Relaxation*
1 He			
1_OIS	1.03 eV/He	O	1.28 eV/He
			
Centre_OIS_O	1.73 eV/He	1_Dist	1.04 eV/He
			
2 He			
2_OIS	1.04 eV/He	O_OIS	1.11 eV/He

			
DB_O	2.36 eV/He	O_adj	1.34 eV/He
			
3 He			
3_OIS	1.05 eV/He	O_2_OIS	1.06 eV/He
			
DB_1_OIS	1.85 eV/He	3_Diag	3.05 eV/He
			
4 He			
4_OIS	1.05 eV/He	O_3_OIS	1.03 eV/He
			
DB_2_OIS	1.60 eV/He	4_EC	3.05 eV/He

			
4_Diamond	1.59 eV/He		
			
5 He			
5_OIS	1.06 eV/He	O_4_OIS	1.02 eV/He
			
DB_3_OIS	1.44 eV/He	O_4_EC	3.65 eV/He
			
5_Octahedral	1.02 eV/He	5_Dist	1.08 eV/He
			
6 He			
6_OIS	1.06 eV/He	O_5_OIS	1.04 eV/He

			
DB_4_OIS	1.34 eV/He	DB_4_EC	7.85 eV/He
			
6_Octahedral	2.33 eV/He	**7_OIS**	1.07 eV/He
			
8_OIS	1.07 eV/He	**9_OIS**	1.03 eV/He
			
10_OIS	1.05 eV/He	**11_OIS**	1.08 eV/He
			
12_OIS	1.10 eV/He		



A.3 Divacancy

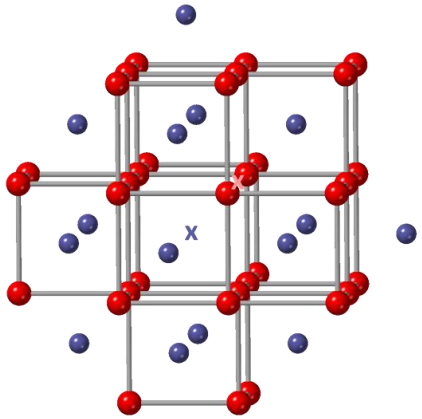
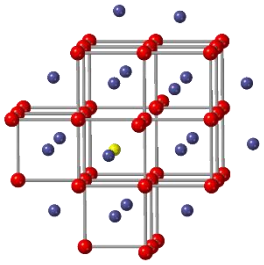
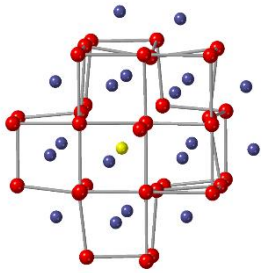
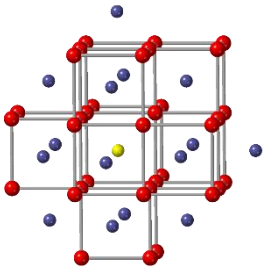
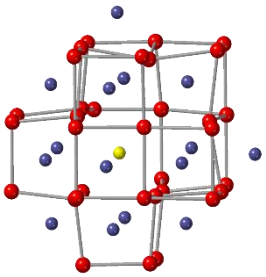
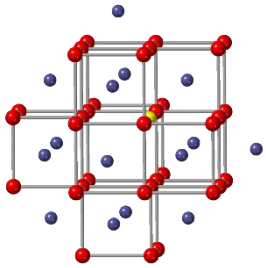
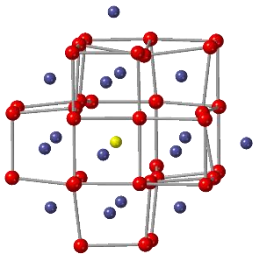
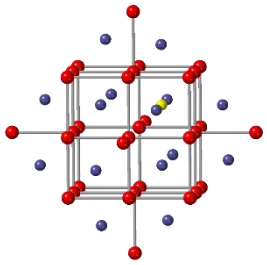
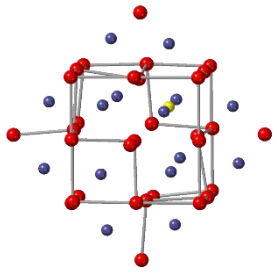
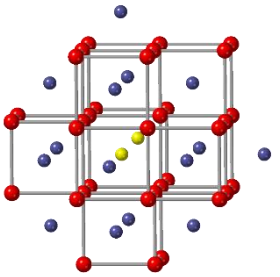
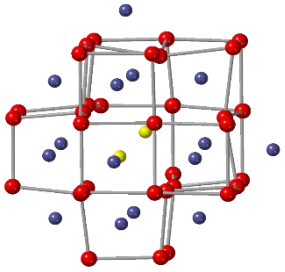
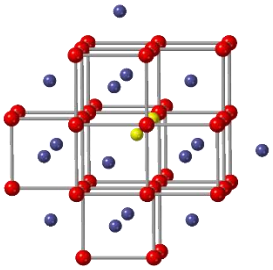
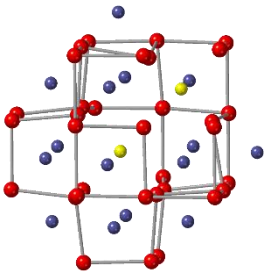
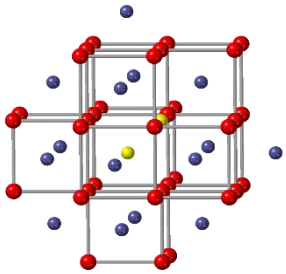
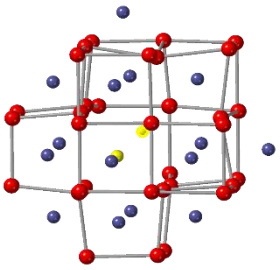
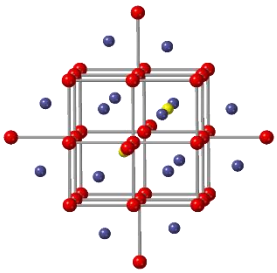
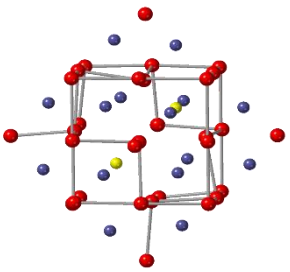
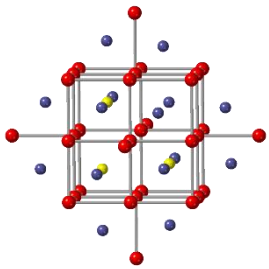
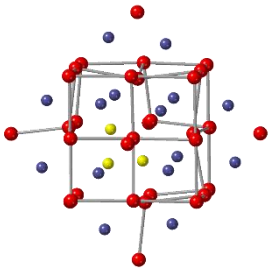
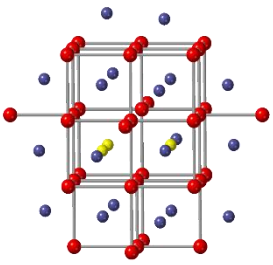
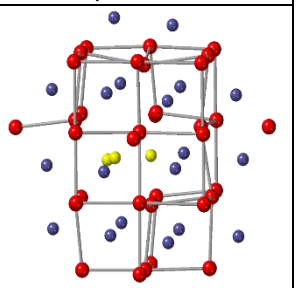
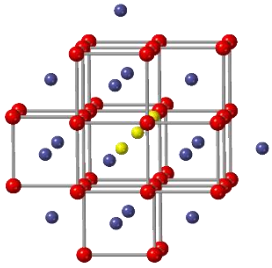
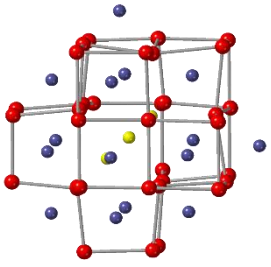
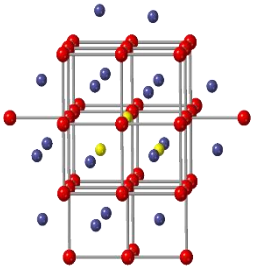
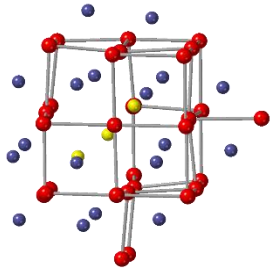
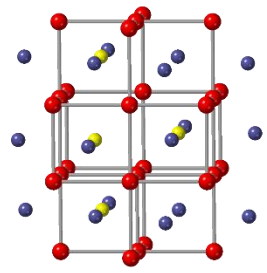
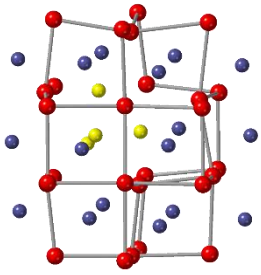
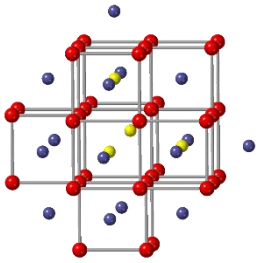
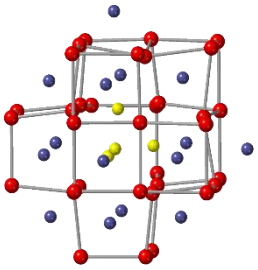
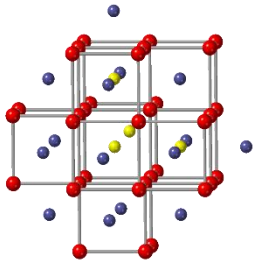
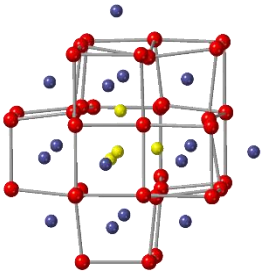
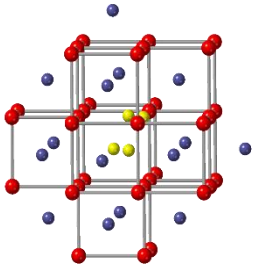
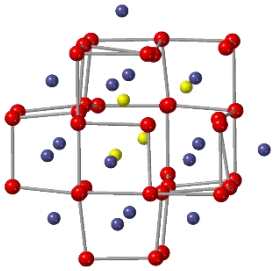
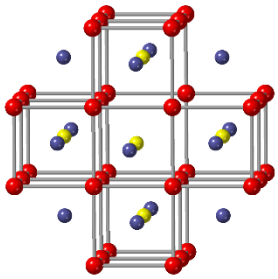
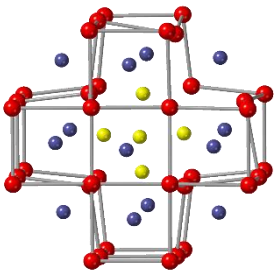
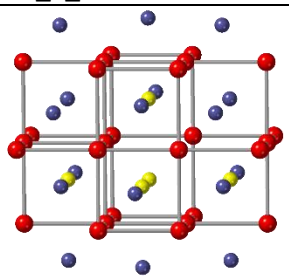
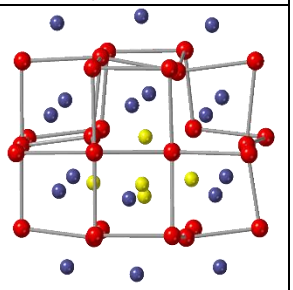
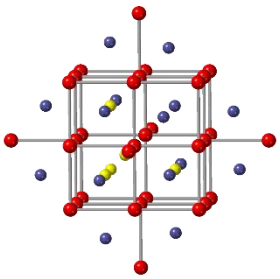
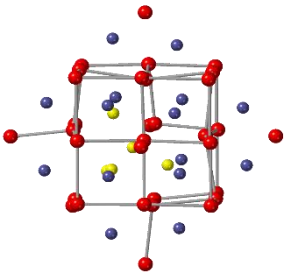
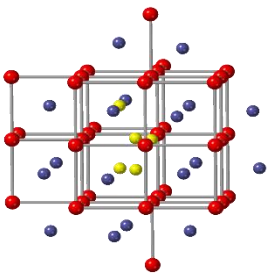
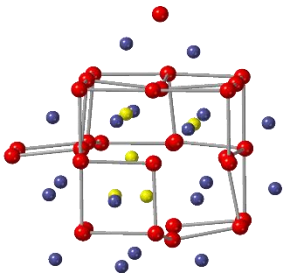
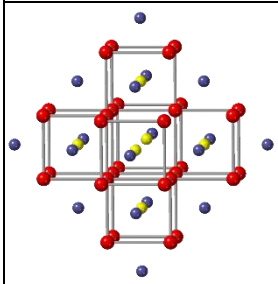
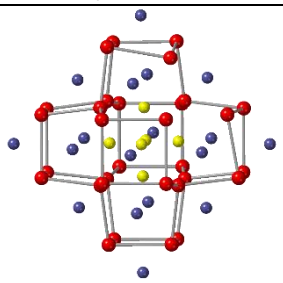
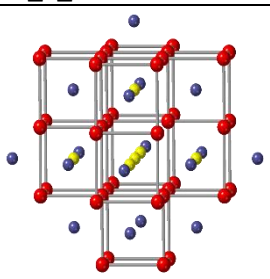
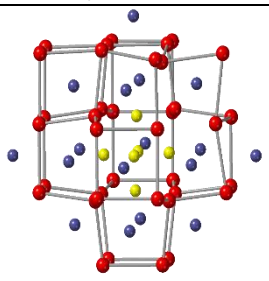


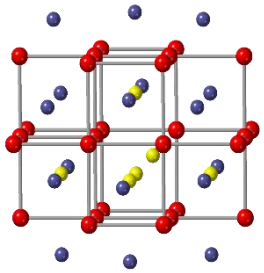
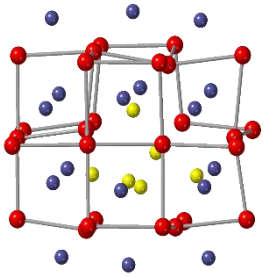
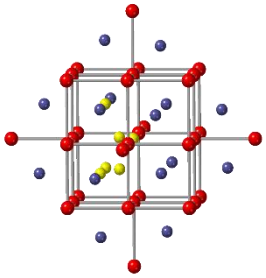
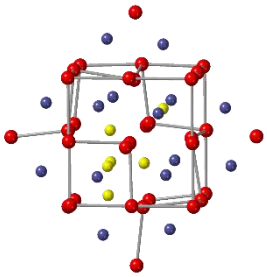
Figure A.3.1: Divacancy in PuO_2. Blue x illustrates plutonium vacancy, pale red x illustrates oxygen vacancy.

Table A.3.1: Helium build up simulations for 1-6 He surrounding a divacancy. For each configuration the unrelaxed and relaxed configurations are displayed alongside the defect energy.

Configuration	**E_d (eV/He)**	**Configuration**	**E_d (eV/He)**
Before Relaxation	*After Relaxation*	*Before Relaxation*	*After Relaxation*
1 He			
1_OIS	-0.23 eV/He	Pu	-0.23 eV/He
			
O	-0.23 eV/He	1_OIS_Dist	1.05 eV/He

			
2 He			
Pu_Cent	-0.05 eV/He	O_Cent	0.41 eV/He
			
Pu_O	-0.05 eV/He	Cent_OIS	0.41 eV/He
			
3 He			
3_OIS	0.22 eV/He	Pu_2_OIS	0.14 eV/He
			
Pu_Cent_O	0.49 eV/He	Pu_O_OIS	0.55 eV/He
			
4 He			

4_OIS	0.18 eV/He	Pu_3_OIS	0.18 eV/He
			
Pu_Cent_2_OIS	0.18 eV/He	Pu_DB_O	0.38 eV/He
			
5 He			
5_OIS	0.25 eV/He	Pu_4_OIS	0.25 eV/He
			
Pu_Cent_3_OIS	0.37 eV/He	Pu_DB_O_OIS	0.63 eV/He
			
6 He			
6_OIS	0.27 eV/He	Pu_5_OIS	0.27 eV/He
			

Pu_Cent_4_OIS	0.38 eV/He	Pu_DB_O_2_OIS	0.38 eV/He
			

A.4 Schottky Trio

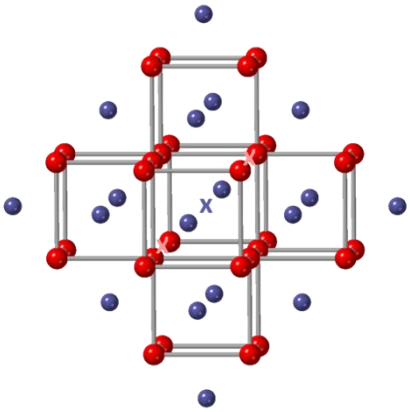
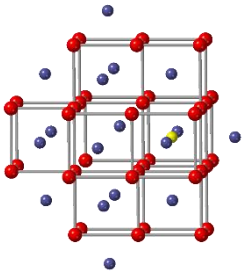
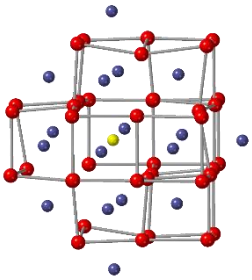
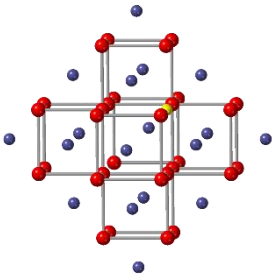
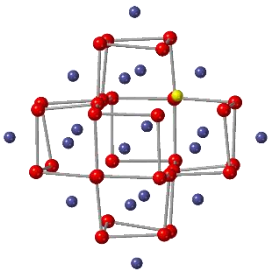
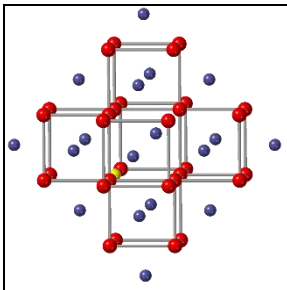
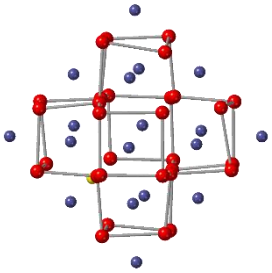
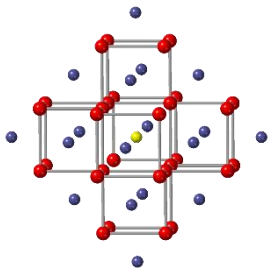
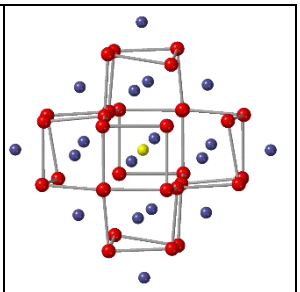
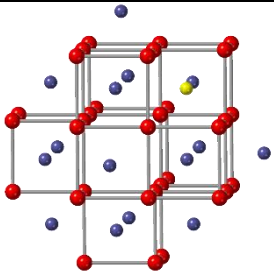
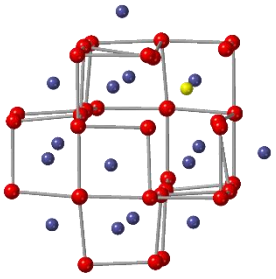
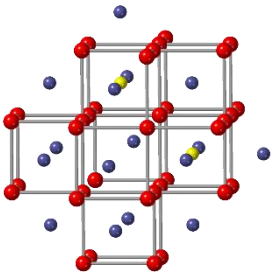
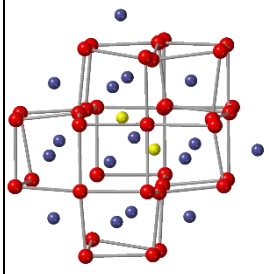
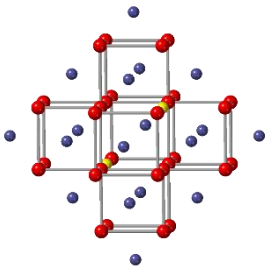
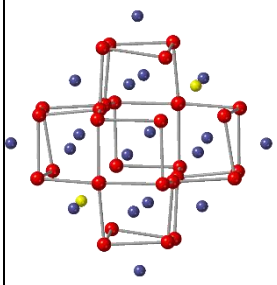
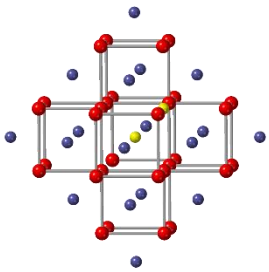
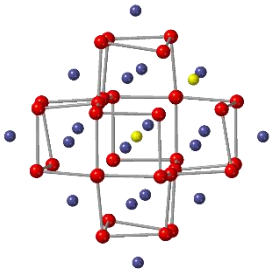
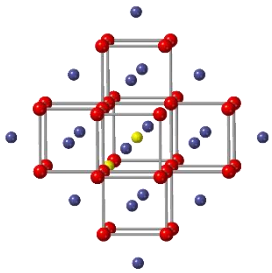
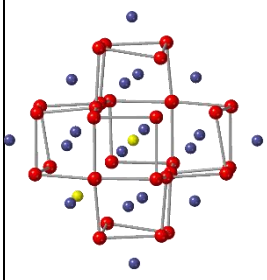
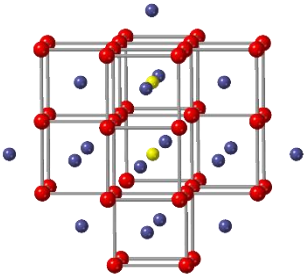
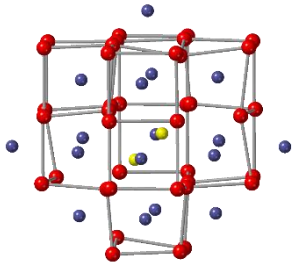
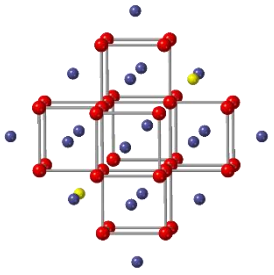
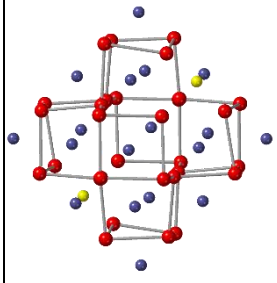
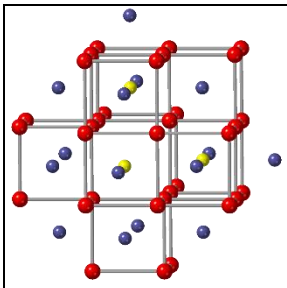
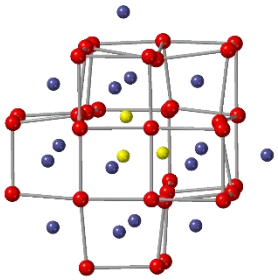
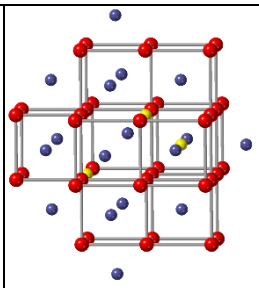
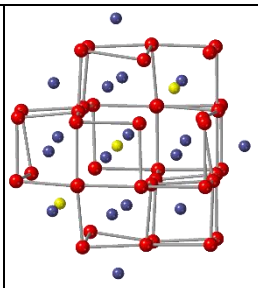
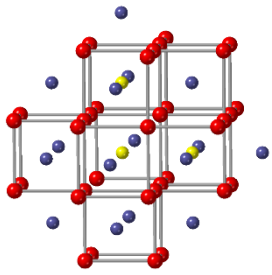
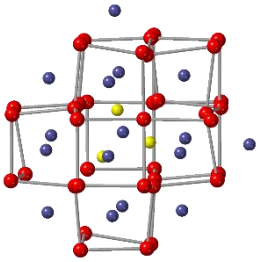
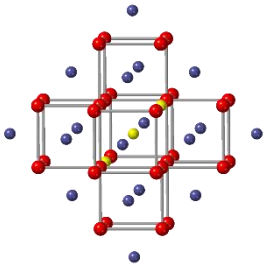
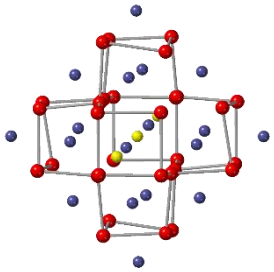
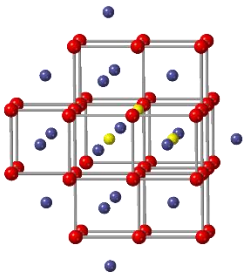
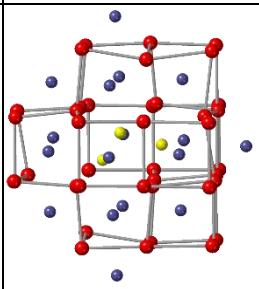
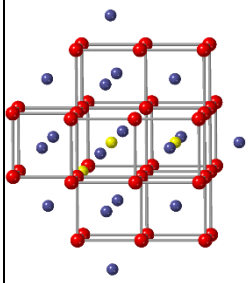
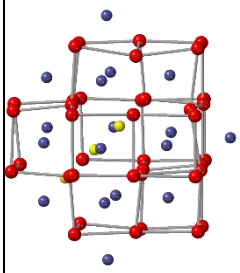
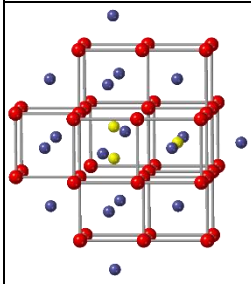
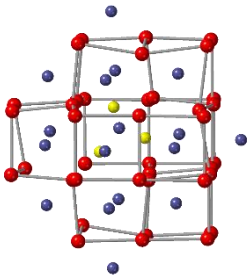
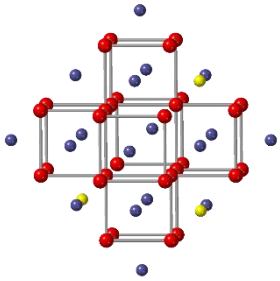
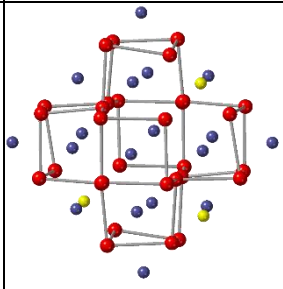
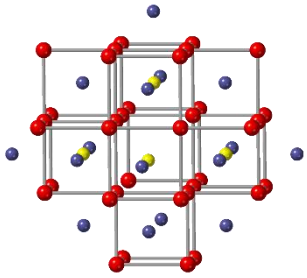
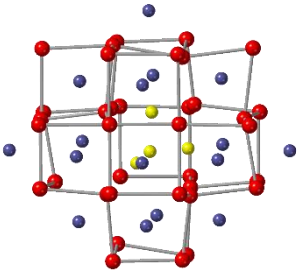
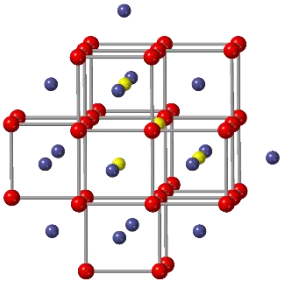
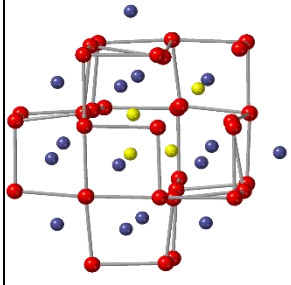


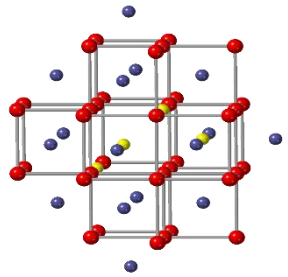
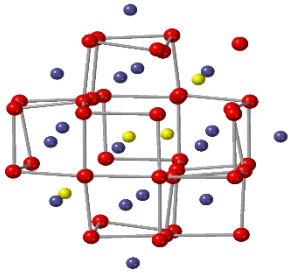
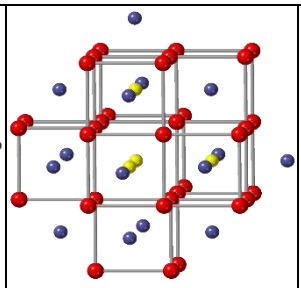
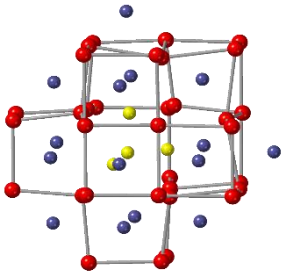
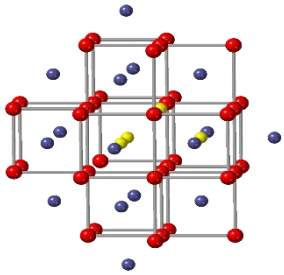
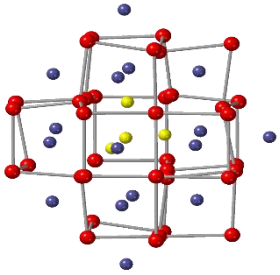
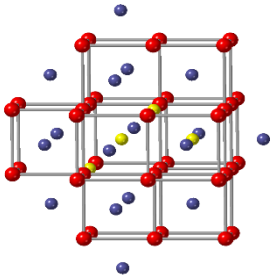
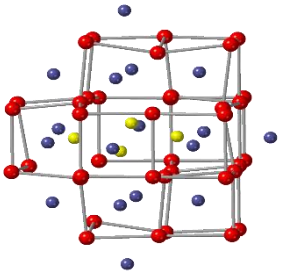
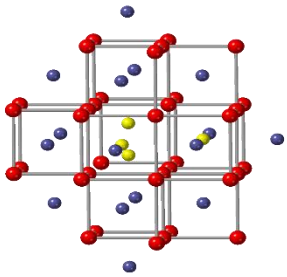
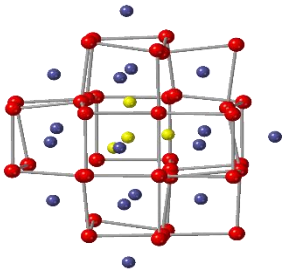
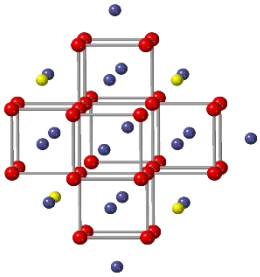
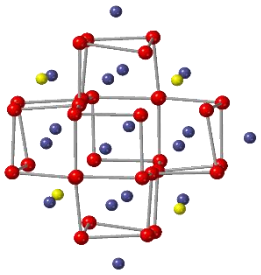
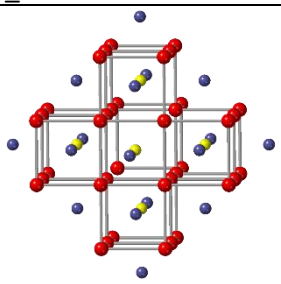
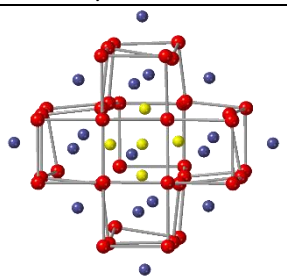
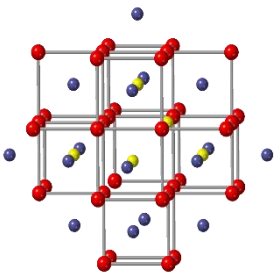
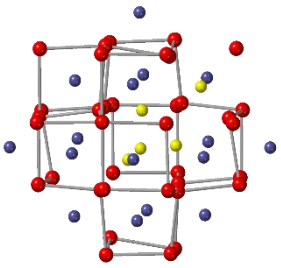
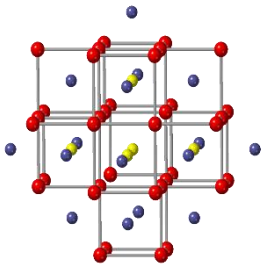
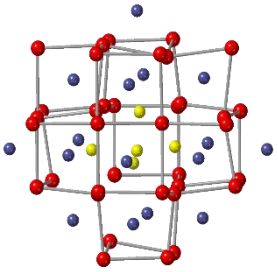
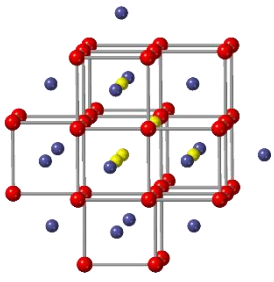
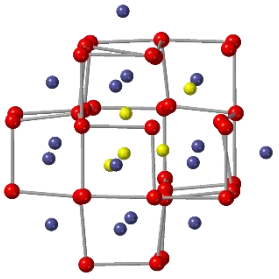
Figure A.4.1: Schottky trio in PuO_2, red x's display the oxygen vacancies, blue x displays the plutonium vacancy.

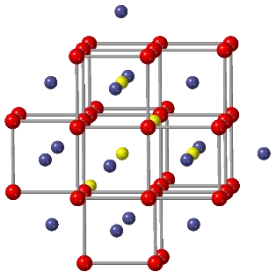
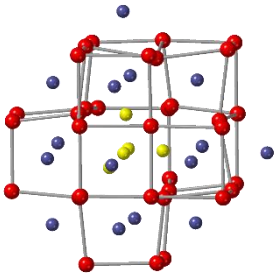
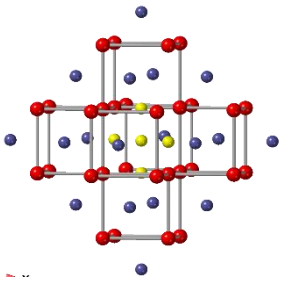
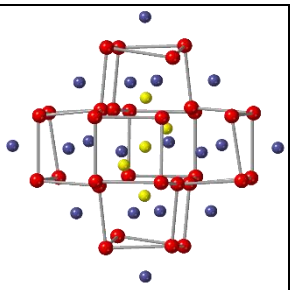
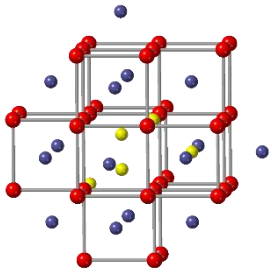
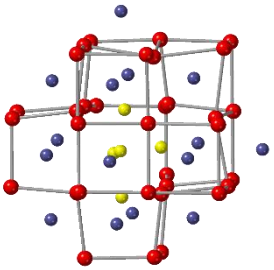
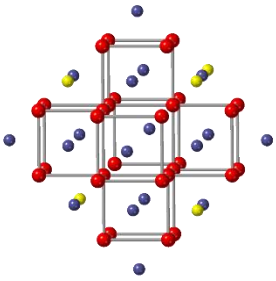
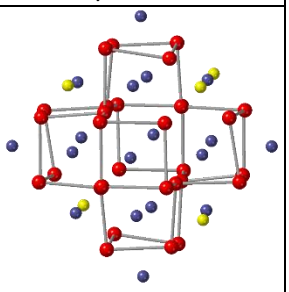
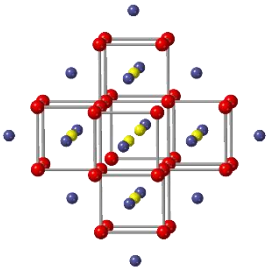
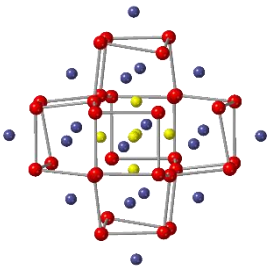
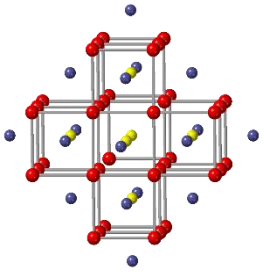
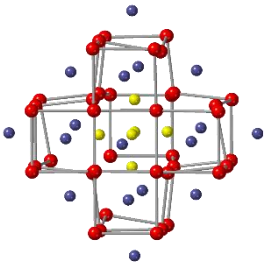
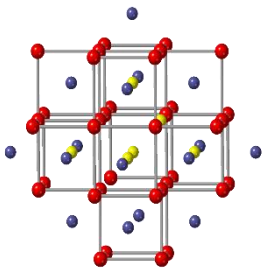
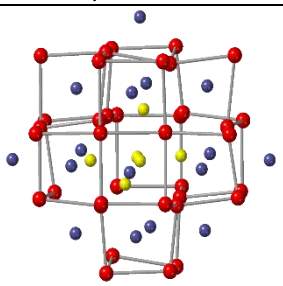
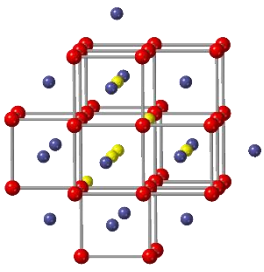
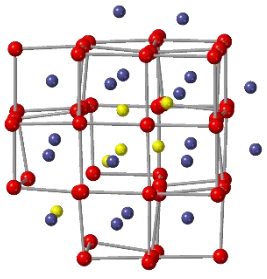
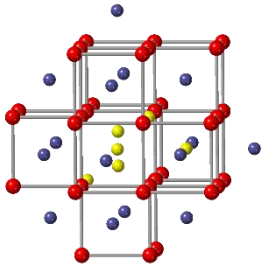
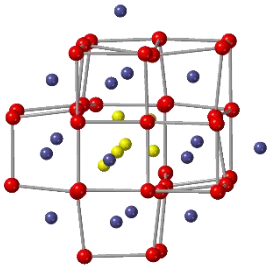
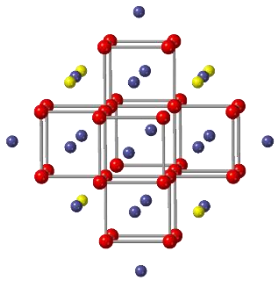
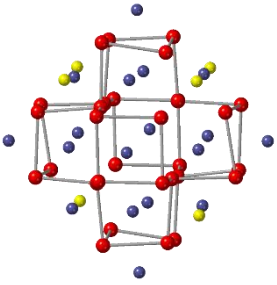
Table A.4.1: Helium build up simulations surrounding a Schottky defect. For each configuration the unrelaxed and relaxed configurations are displayed alongside the defect energy. For 1-6 He surrounding the Schottky trio multiple configurations are shown. For 7-12 He only the configuration of all He in isolated OIS is included.

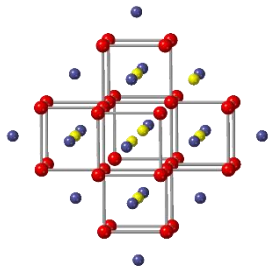
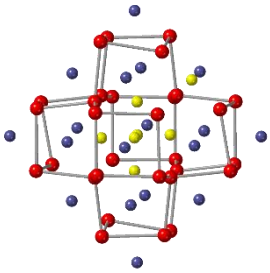
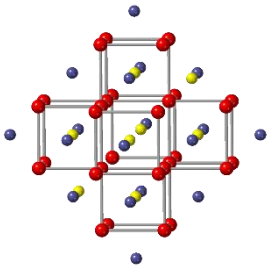
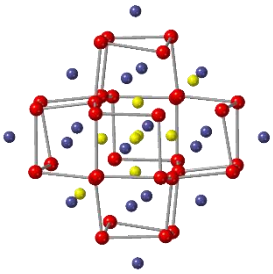
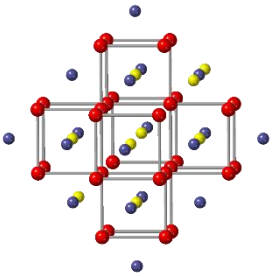
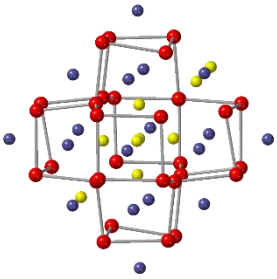
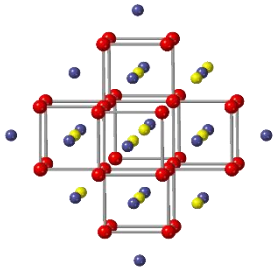
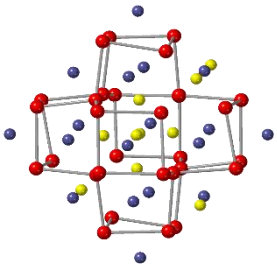
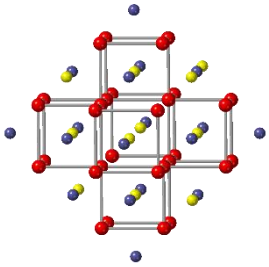
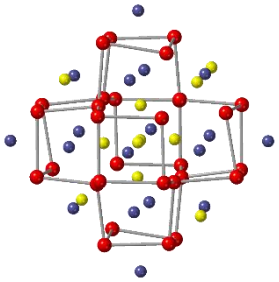
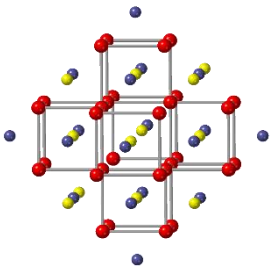
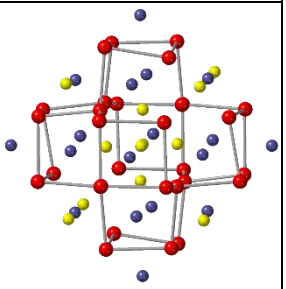
Configuration	**E_d (eV/He)**	**Configuration**	**E_d (eV/He)**
Before Relaxation	*After Relaxation*	*Before Relaxation*	*After Relaxation*
1 He			
1_OIS	-0.22 eV/He	O1	1.77 eV/He
			
O2	1.77 eV/He	Pu	-0.22 eV/He

			
1_OIS_Dist	1.05 eV/He		
			
2 He			
2_OIS	0.20 eV/He	O1_O2	1.04 eV/He
			
Pu_O1	0.41 eV/He	Pu_O2	0.41 eV/He
			
Pu_OIS	-0.12 eV/He	2_OIS_Dist	1.04 eV/He
			
3 He			
3_OIS	0.24 eV/He	O1_O2_OIS	0.62 eV/He

			
Pu_2_OIS	0.10 eV/He	Pu_O1_O2	0.19 eV/He
			
Pu_O1_OIS	0.11 eV/He	Pu_O2_OIS	0.51 eV/He
			
DB_OIS	0.10 eV/He	3_OIS_Dist	1.10 eV/He
			
4 He			
4_OIS	0.15 eV/He	O1_3_OIS	0.43 eV/He
			
O1_O2_2_OIS	0.61 eV/He	Pu_3_OIS	0.16 eV/He

			
Pu_O1_2_OIS	0.15 eV/He	Pu_O1_O2_1_OIS	0.23 eV/He
			
DB_2_OIS	0.15 eV/He	4_OIS_Dist	1.13 eV/He
			
5 He			
5_OIS	0.24 eV/He	O1_4_OIS	0.33 eV/He
			
Pu_4_OIS	0.24 eV/He	Pu_O1_3_OIS	0.33 eV/He
			
Pu_O1_O2_2_OIS	0.24 eV/He	5_Diamond	0.34 eV/He

			
DB_O1_O2_1_OIS	0.24 eV/He	5_OIS_Dist	1.16 eV/He
			
6 He			
6_OIS	0.25 eV/He	Pu_5_OIS	0.25 eV/He
			
Pu_O1_4_OIS	0.34 eV/He	Pu_O1_O2_3_OIS	0.55 eV/He
			
DB_O1_O2_2_OIS	0.38 eV/He	6_OIS_Dist	1.17 eV/He
			
7_OIS	0.35 eV/He	**8_OIS**	0.43 eV/He

			
9_OIS	0.53 eV/He	**10_OIS**	0.61 eV/He
			
11_OIS	0.67 eV/He eV/He	**12_OIS**	0.73 eV/He
			

A.5 Plutonium Frenkel Pair

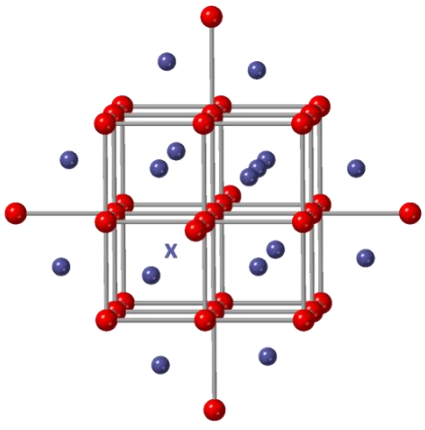
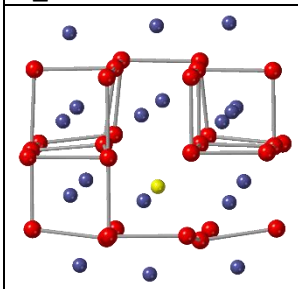
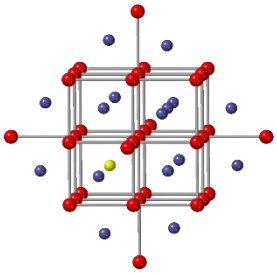
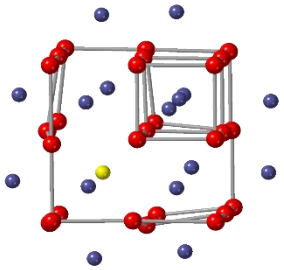
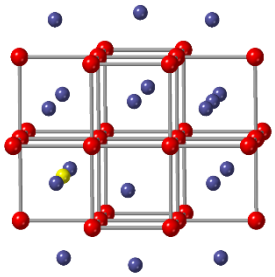
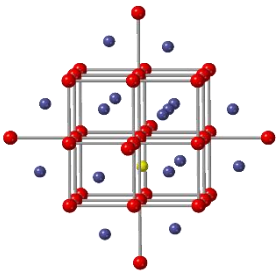
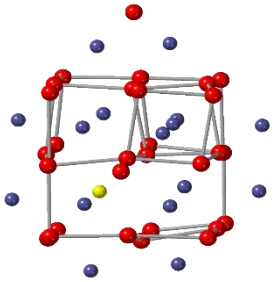
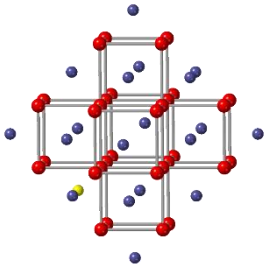
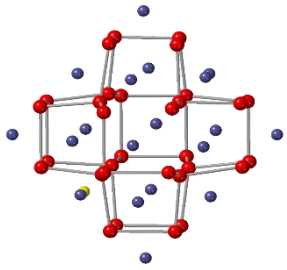
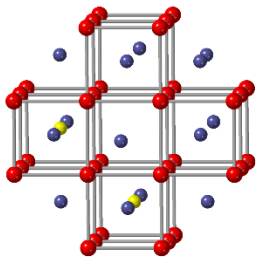
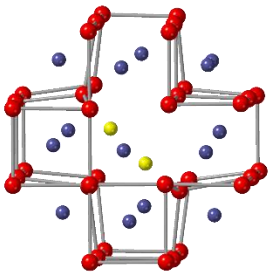
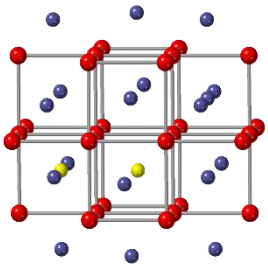
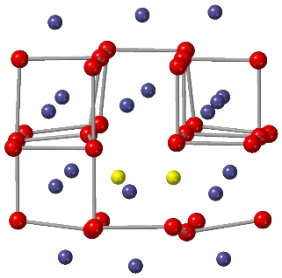
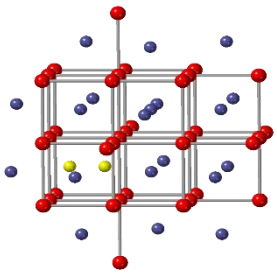
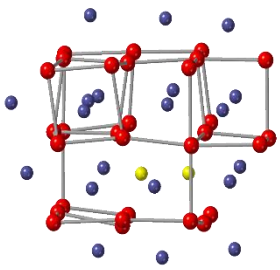
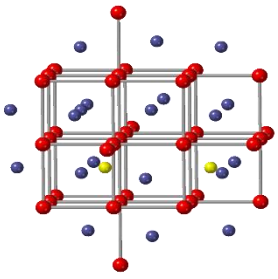
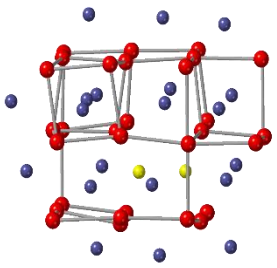
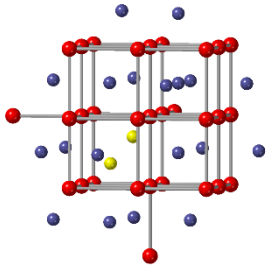
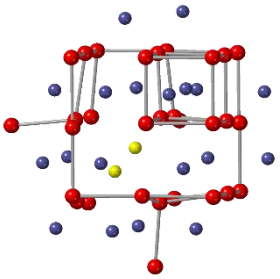
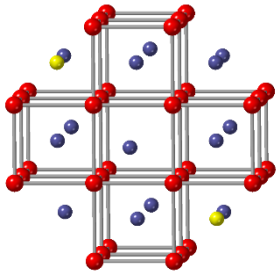
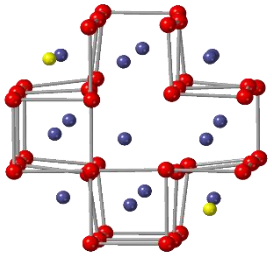
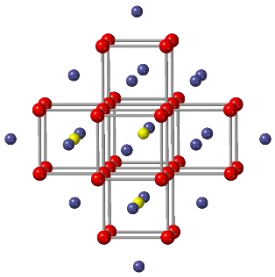
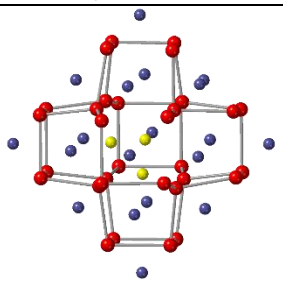
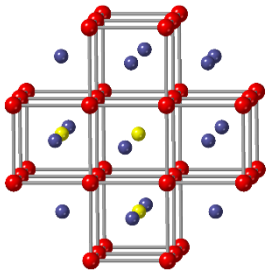
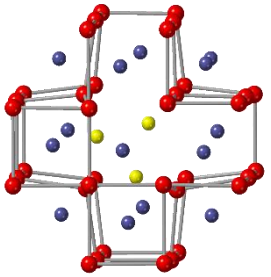
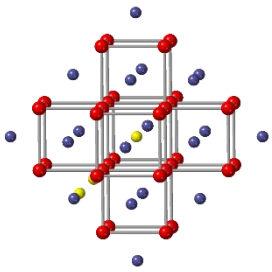
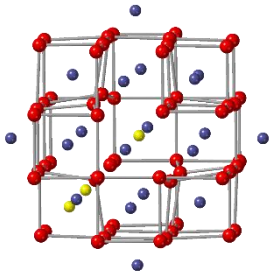
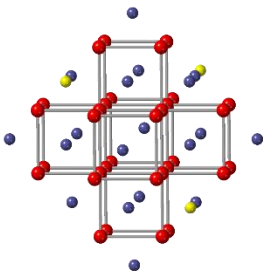
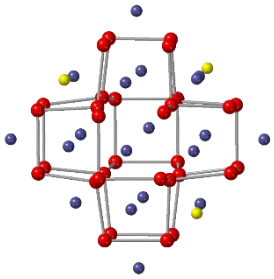
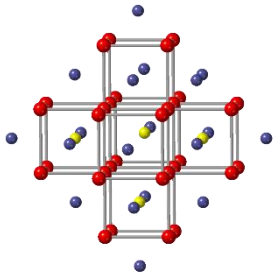
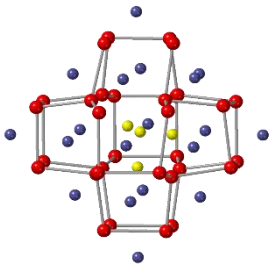
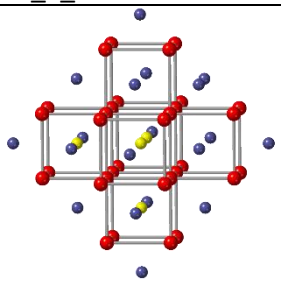
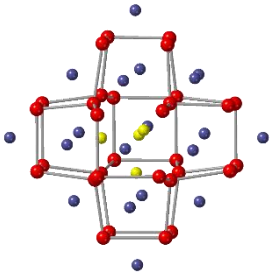
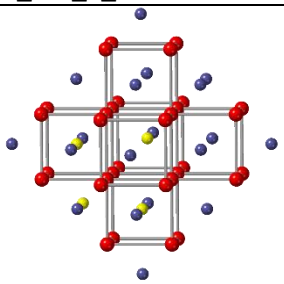
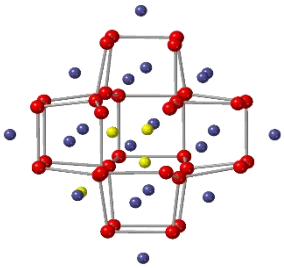
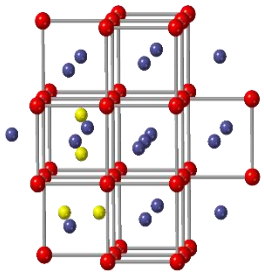
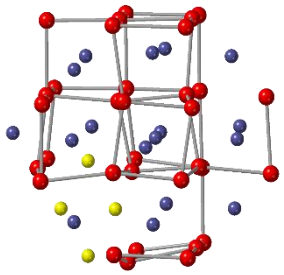


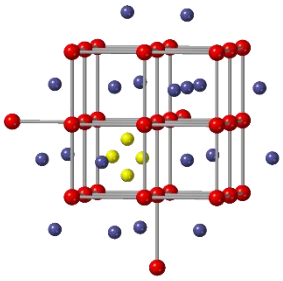
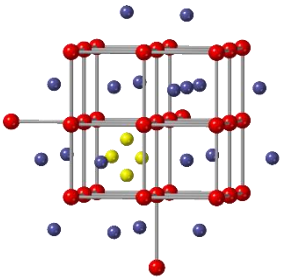
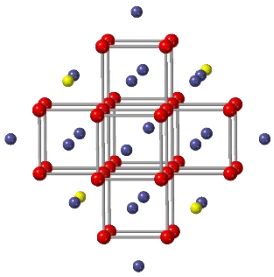
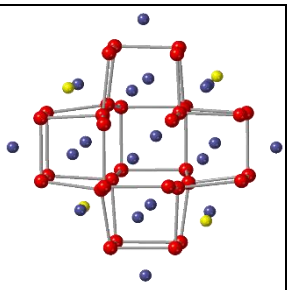
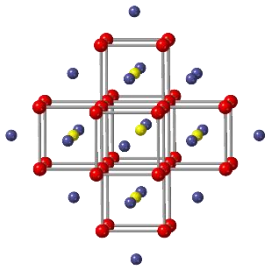
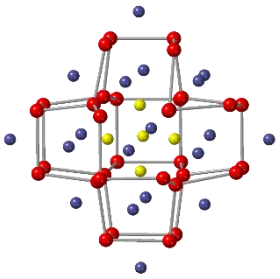
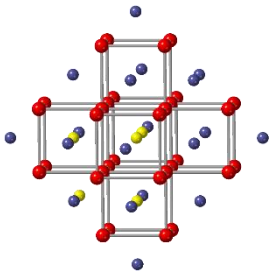
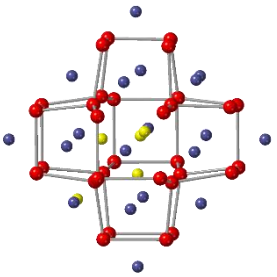
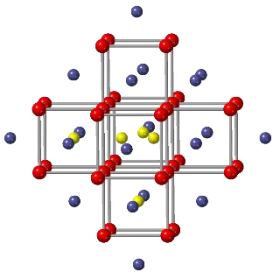
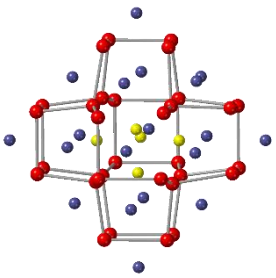
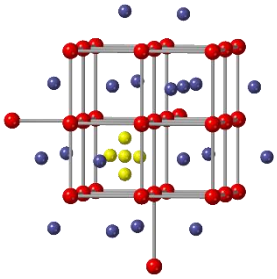
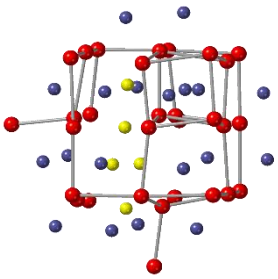
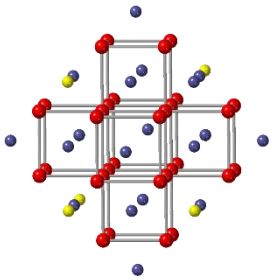
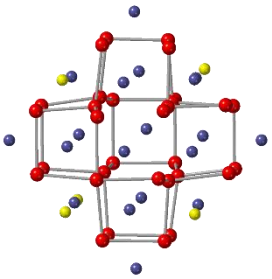
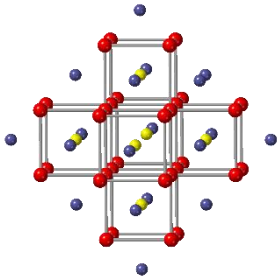
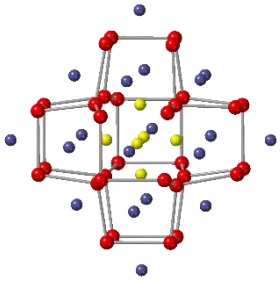
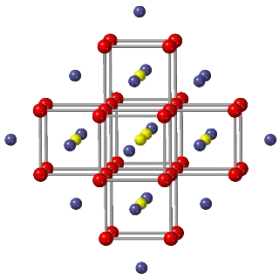
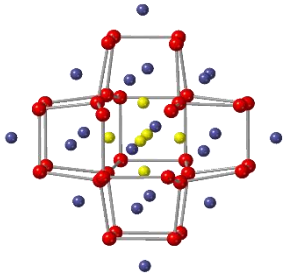
Figure A.5.1: Plutonium Frenkel pair in PuO_2, the plutonium vacancy is illustrated by the blue x.

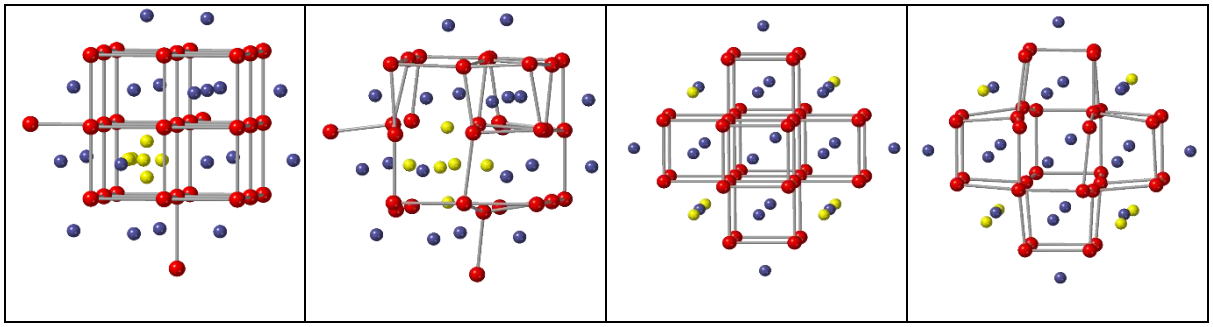
Table A.5.1: Helium build up simulations surrounding a Plutonium Frenkel pair. For each configuration the unrelaxed and relaxed configurations are displayed alongside the defect energy. For 1-6 He surrounding the PuFP multiple configurations are shown.

Configuration	**E_d (eV/He)**	**Configuration**	**E_d (eV/He)**

Before Relaxation	*After Relaxation*	*Before Relaxation*	*After Relaxation*
1 He			
1_OIS	-0.29 eV/He	Pu	-0.24 eV/He
			
Cent_OIS_Pu	-0.29 eV/He	1_OIS_Dist	1.23 eV/He
			
2 He			
2_OIS	0.10 eV/He	Pu_OIS	-0.02 eV/He
			
DB_Pu	-0.04 eV/He	DB_OIS	-0.02 eV/He
			
2_Diag	0.20 eV/He	2_OIS_Dist	1.29 eV/He

			
3 He			
3_OIS	0.23 eV/He	Pu_2_OIS	0.14 eV/He
			
Pu_OIS_Cent	2.10 eV/He	3_OIS_Dist	1.35 eV/He
			
4 He			
4_OIS	0.18 eV/He	Pu_3_OIS	0.22 eV/He
			
4_OIS_1_Dist	0.49 eV/He	DBPu_DBOIS	0.17 eV/He
			
4_Diamond	0.19 eV/He	4_OIS_Dist	1.32 eV/He

			
5 He			
5_OIS	0.22 eV/He	Pu_4_OIS	0.44 eV/He
			
3_OIS_DB_Pu	0.26 eV/He	5_Diamond	0.73 eV/He
			
5_OIS_Dist	1.31 eV/He		
			
6 He			
6_OIS_1_Dist	0.25 eV/He	Pu_5_OIS	0.25 eV/He
			
6_Diamond	0.44 eV/He	6_OIS_Dist	1.32 eV/He



A.6 Oxygen Frenkel Pair

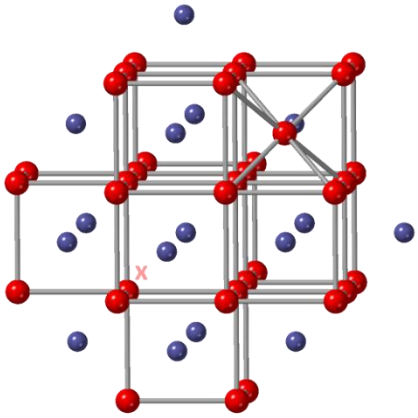
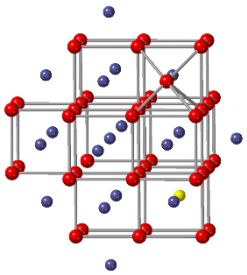
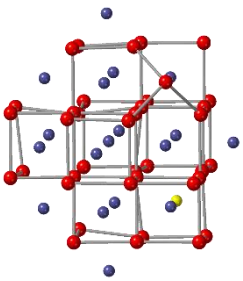
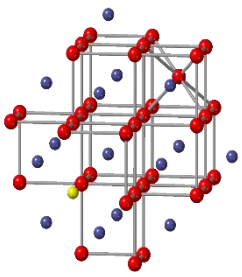
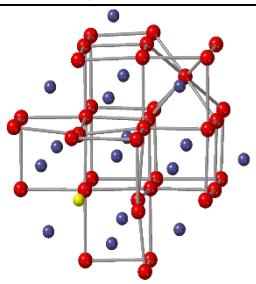
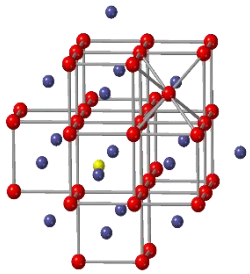
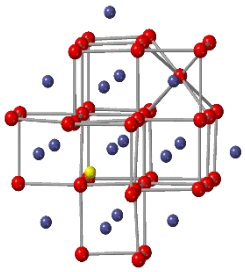
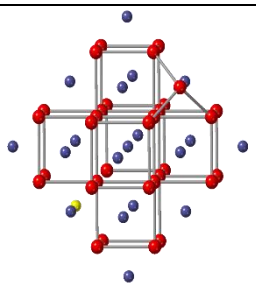
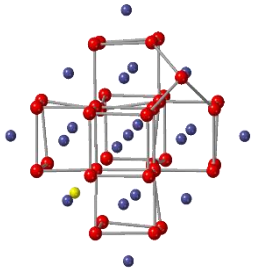
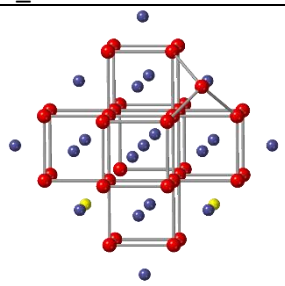
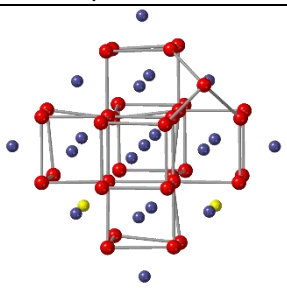
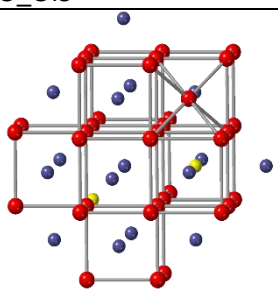
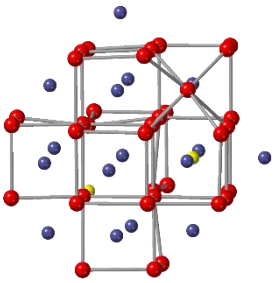
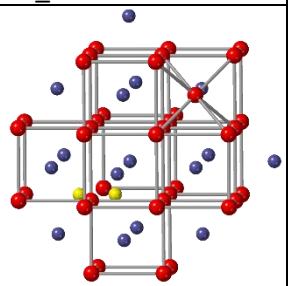
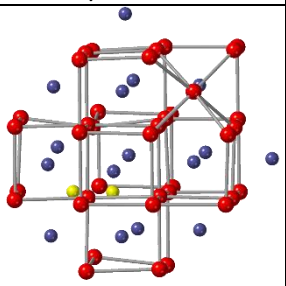
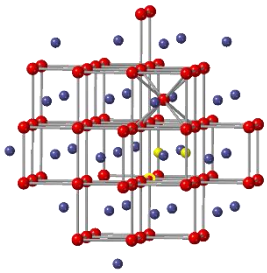
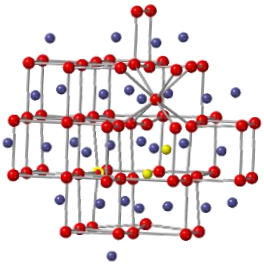
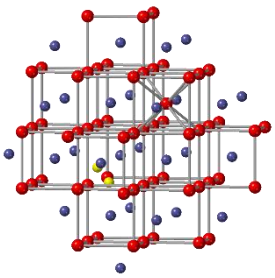
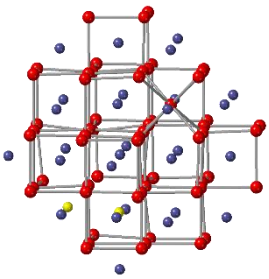
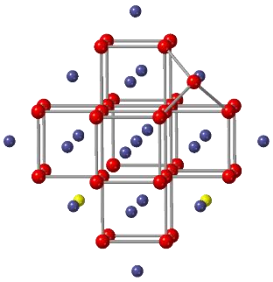
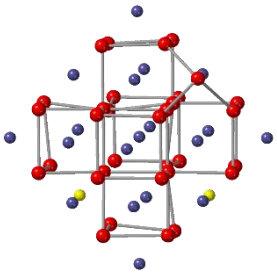
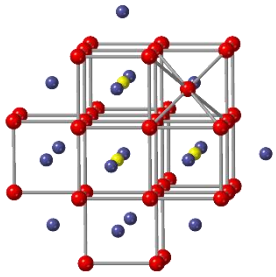
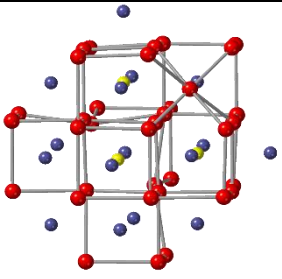
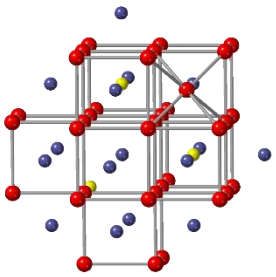
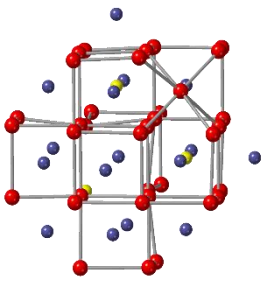
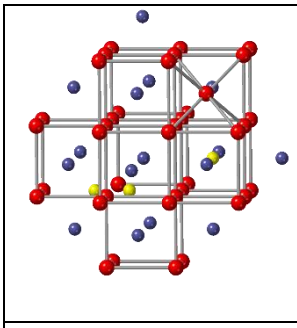
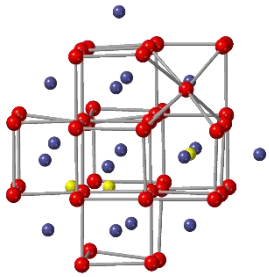
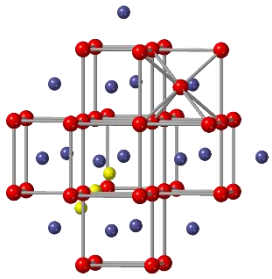
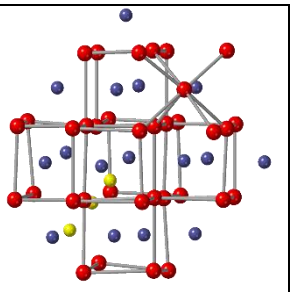
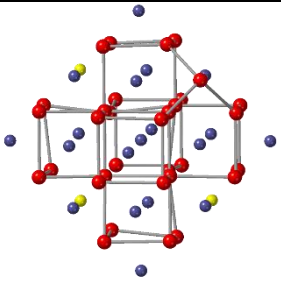
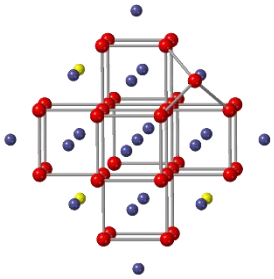
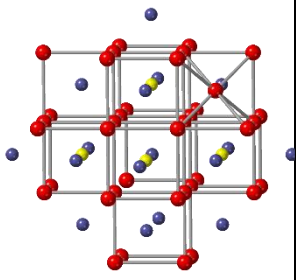
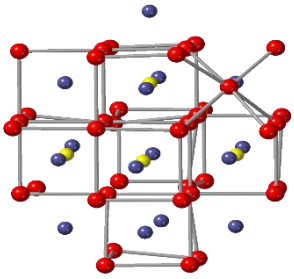
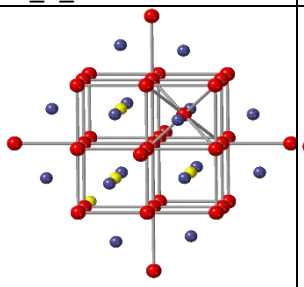
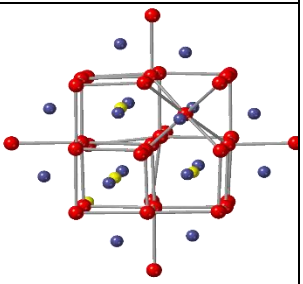
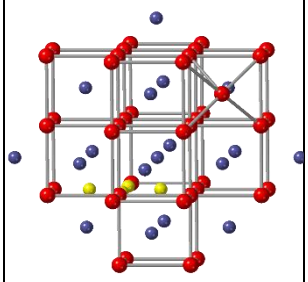
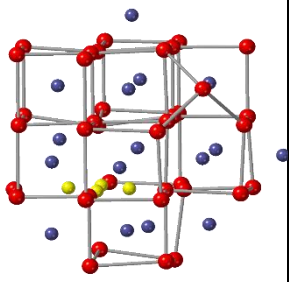
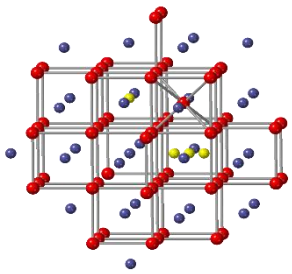
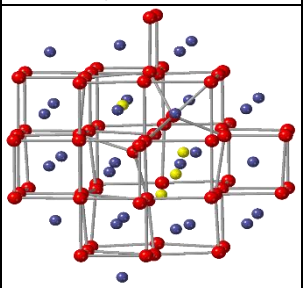
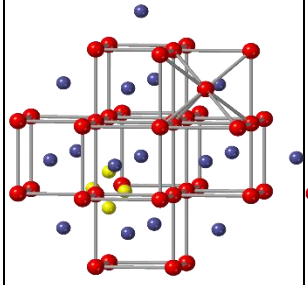
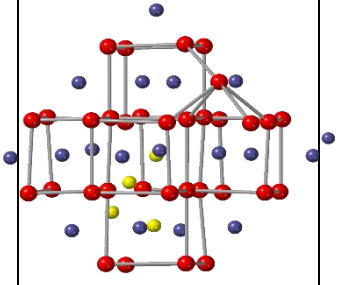
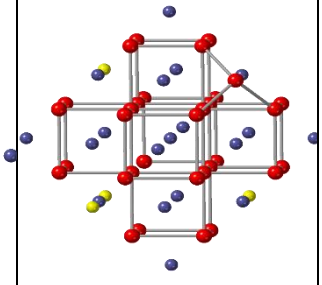
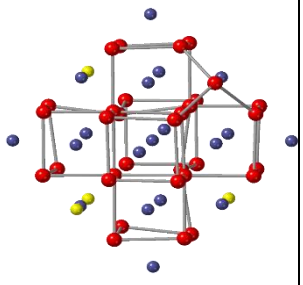


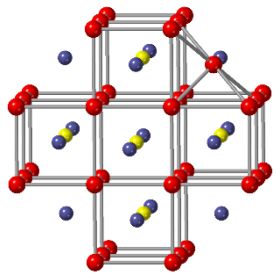
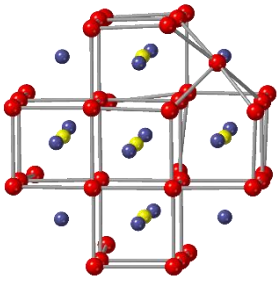
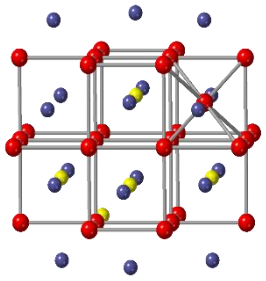
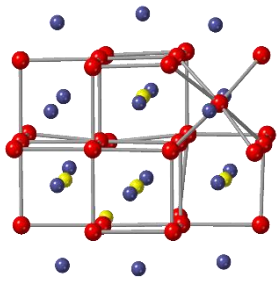
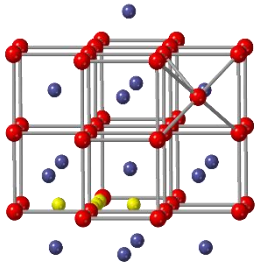
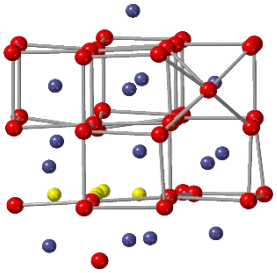
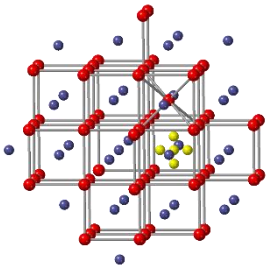
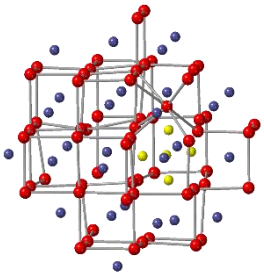
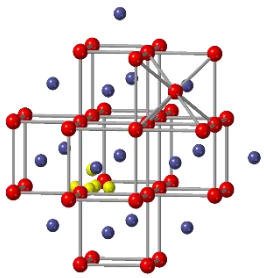
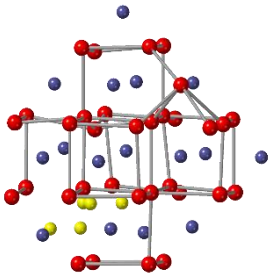
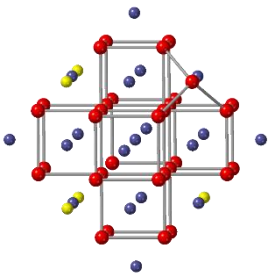
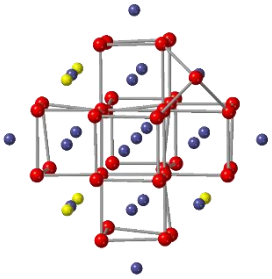
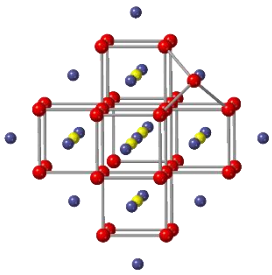
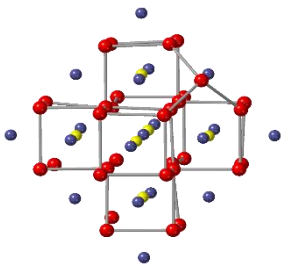
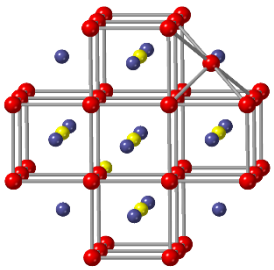
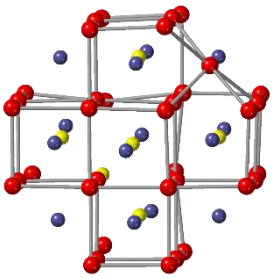
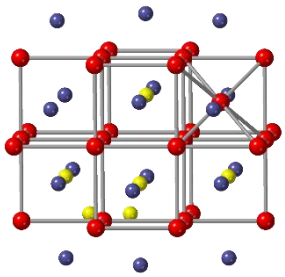
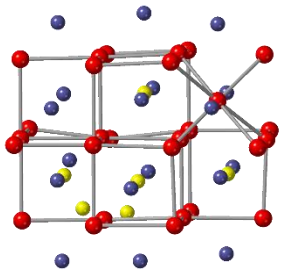
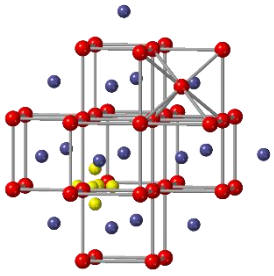
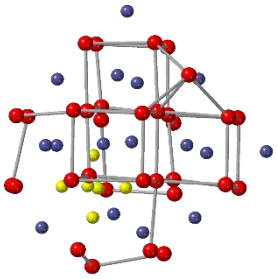
Figure A.6.1: Oxygen Frenkel pair in PuO_2 with the oxygen vacancy represented by a red x.

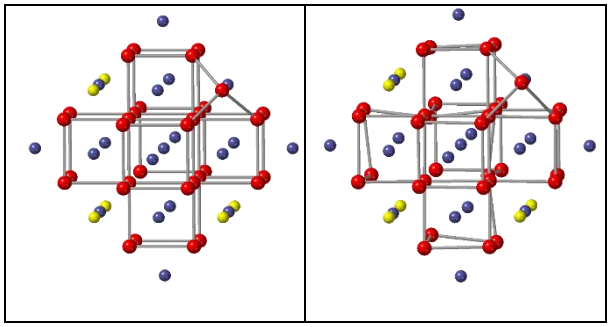
Table A.6.1: Helium build up simulations surrounding an Oxygen Frenkel pair. For each configuration the unrelaxed and relaxed configurations are displayed alongside the defect energy. For 1-6 He surrounding the OFP multiple configurations are shown.

Configuration	**E_d (eV/He)**	**Configuration**	**E_d (eV/He)**
Before Relaxation	*After Relaxation*	*Before Relaxation*	*After Relaxation*
1 He			
1_OIS	1.03 eV/He	O	1.41 eV/He
			
Cent_OIS_O	6.75 eV/He	1_OIS_Dist	5.25 eV/He

			
2 He			
2_OIS	1.05 eV/He	O_OIS	1.19 eV/He
			
DB_O	2.40 eV/He	DB_OIS	1.17 eV/He
			
2_Diag	1.09 eV/He	2_OIS_Dist	1.07 eV/He
			
3 He			
3_OIS	1.07 eV/He	O_2_OIS	1.16 eV/He
			
DB_1_OIS	1.97 eV/He	3_Diag	3.10 eV/He

			
3_OIS_Dist	1.07 eV/He		
			
4 He			
4_OIS	1.05 eV/He	O_3_OIS	1.16 eV/He
			
4_EC	3.11 eV/He	DB_2_OIS	1.68 eV/He
			
4_Diamond	1.57 eV/He	4_OIS_Dist	1.09 eV/He
			
5 He			
5_OIS	1.05 eV/He	O_4_OIS	1.10 eV/He

			
O_4_EC	3.70 eV/He	5_Oct_OIS	5.16 eV/He
			
5_Oct_O	2.55 eV/He	5_OIS_Dist	1.08 eV/He
			
6 He			
6_OIS	1.09 eV/He	O_5_OIS	1.11 eV/He
			
DB_4_OIS	1.52 eV/He	6_Oct	3.12 eV/He
			
6_OIS_Dist	1.08 eV/He		



A.7 Oxygen Frenkel Pair 3

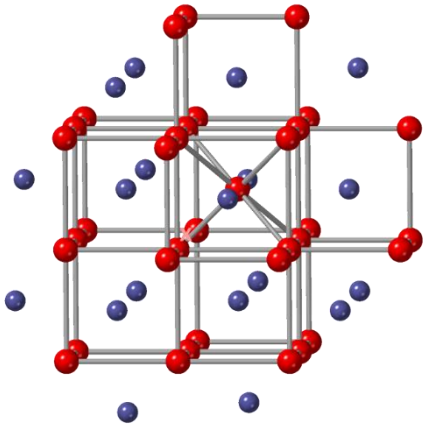
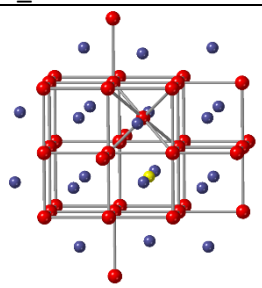
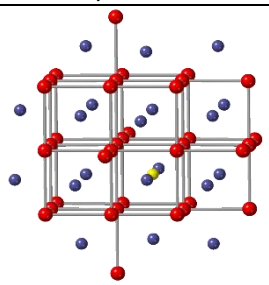
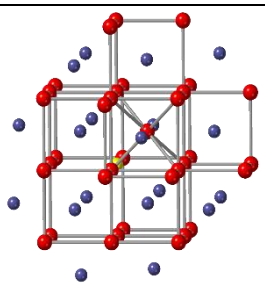
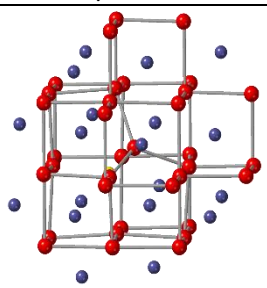
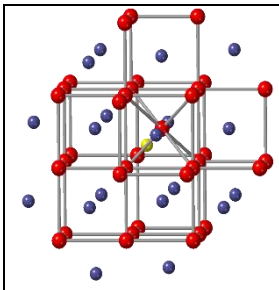
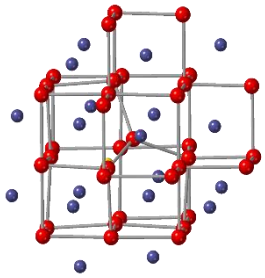
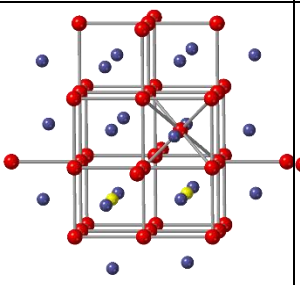
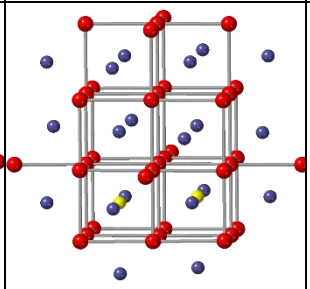
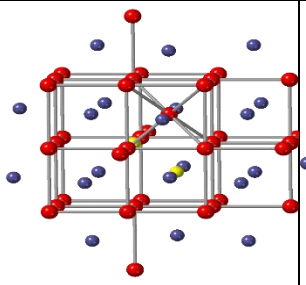
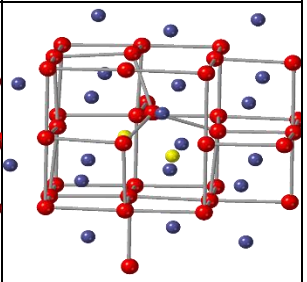
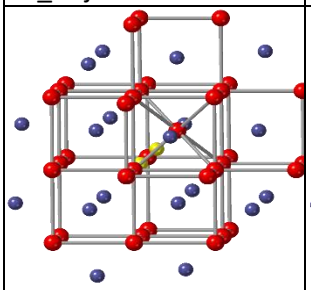
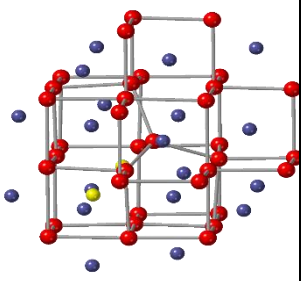
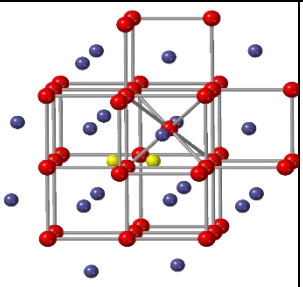
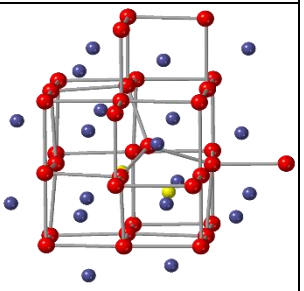
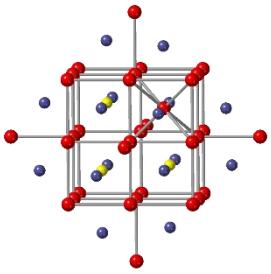
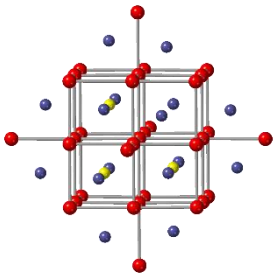
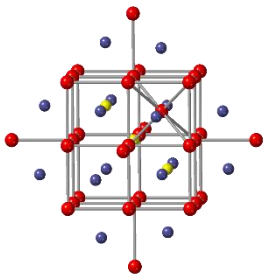
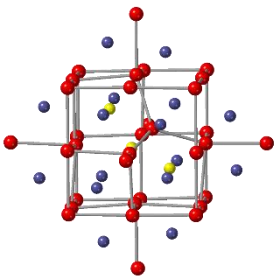
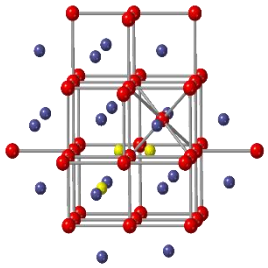
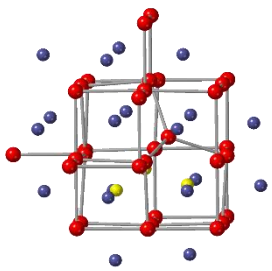
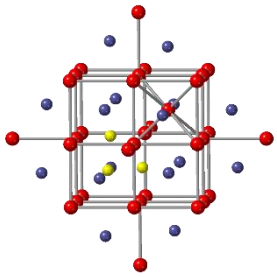
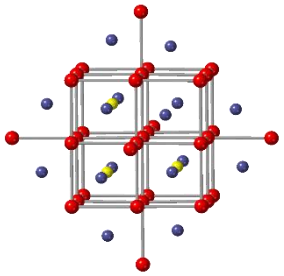
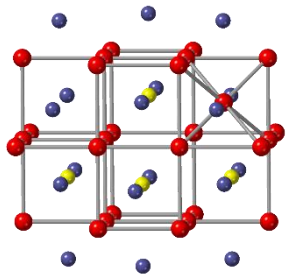
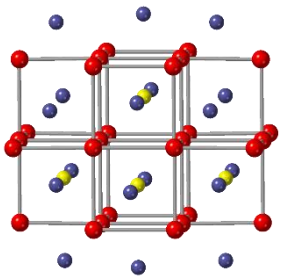
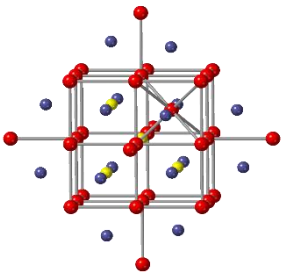
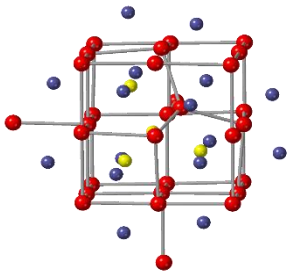
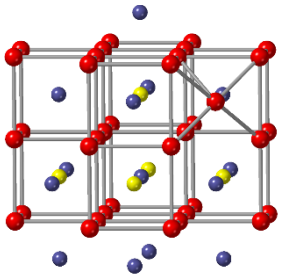
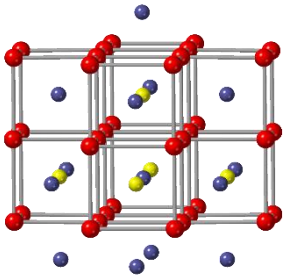
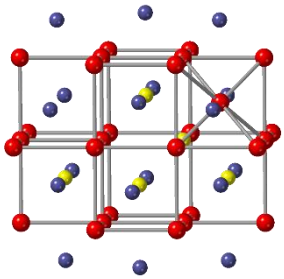
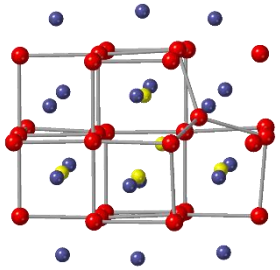
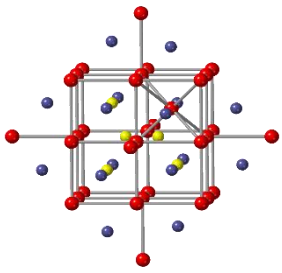
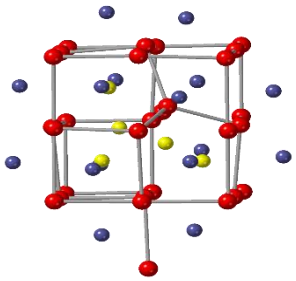
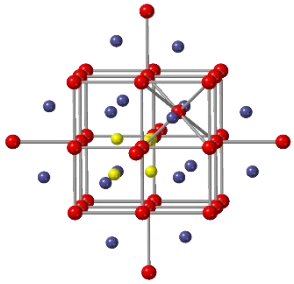
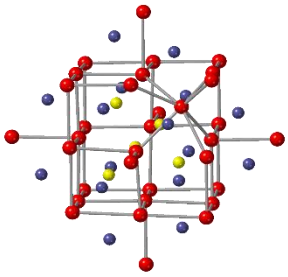
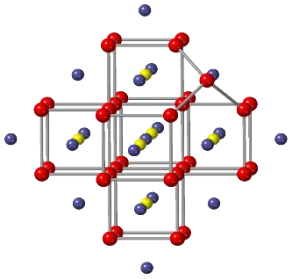
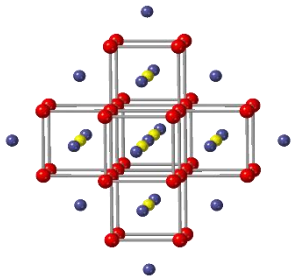
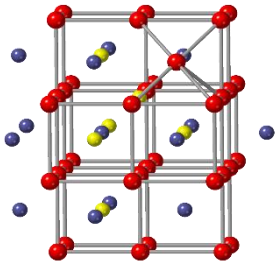
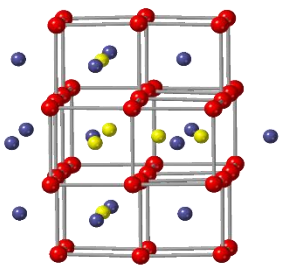


Figure A.7.1: Oxygen Frenkel pair 3 configuration in PuO_2 with the oxygen vacancy represented by a red x. Note that the oxygen interstitial and vacancy are not separated by any lattice atoms.

Table A.7.1: Helium build up simulations surrounding an Oxygen Frenkel pair (configuration 3). For each configuration the unrelaxed and relaxed configurations are displayed alongside the defect energy. For 1-6 He surrounding the OFP3 multiple configurations are shown.

Configuration	**E_d (eV/He)**	**Configuration**	**E_d (eV/He)**
Before Relaxation	*After Relaxation*	*Before Relaxation*	*After Relaxation*
1 He			
1_OIS	1.06 eV/He	O	4.83 eV/He
			
Cent	4.83 eV/He		

			
2 He			
2_OIS	1.05 eV/He	O_OIS	2.83 eV/He
			
O_Adj	2.83 eV/He	DB_O	2.83 eV/He
			
3 He			
3_OIS	1.05 eV/He	O_2_OIS	2.15
			
DB_OIS	2.15 eV/He	O_2_EC	1.05 eV/He
			
4 He			

4_OIS	1.05 eV/He	O_3_OIS	1.82 eV/He
			
5 He			
5_OIS	1.05 eV/He	O_4_OIS	1.68 eV/He
			
DB_3_OIS	2.03 eV/He	O_4_EC	2.29 eV/He
			
6 He			
6_OIS	1.06 eV/He	O_5_OIS	1.54 eV/He
			

Appendix B

MSD Plots of Larger Supercells

This Appendix contains mean squared displacement plots of oxygen, plutonium and helium diffusion in larger supercell sizes (10x10x10 and 12x12x12) at three temperatures.

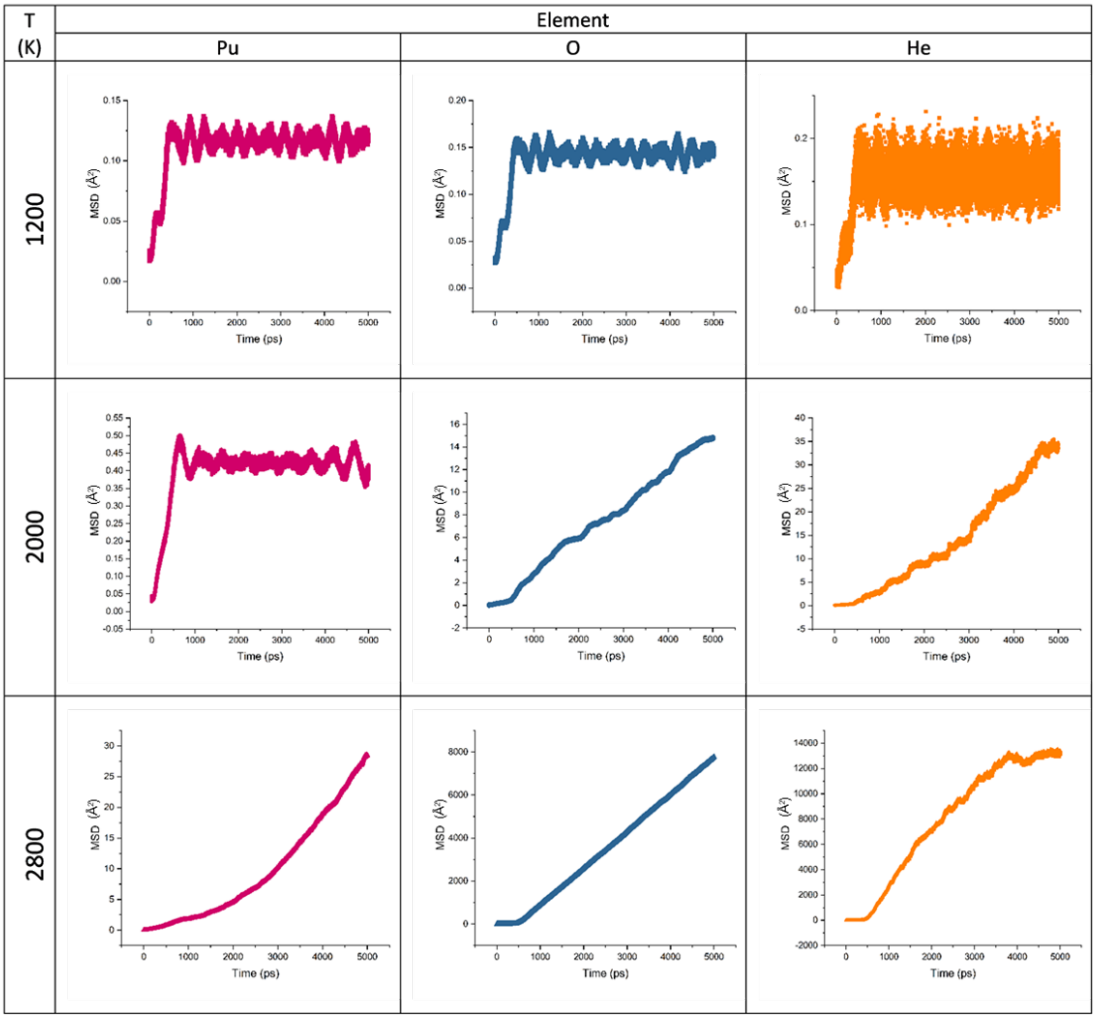


Figure 1: MSD of Pu, O and He in an 10x10x10 supercell at 1200, 2000 and 2800 K including the initial 1 ns equilibriation period.

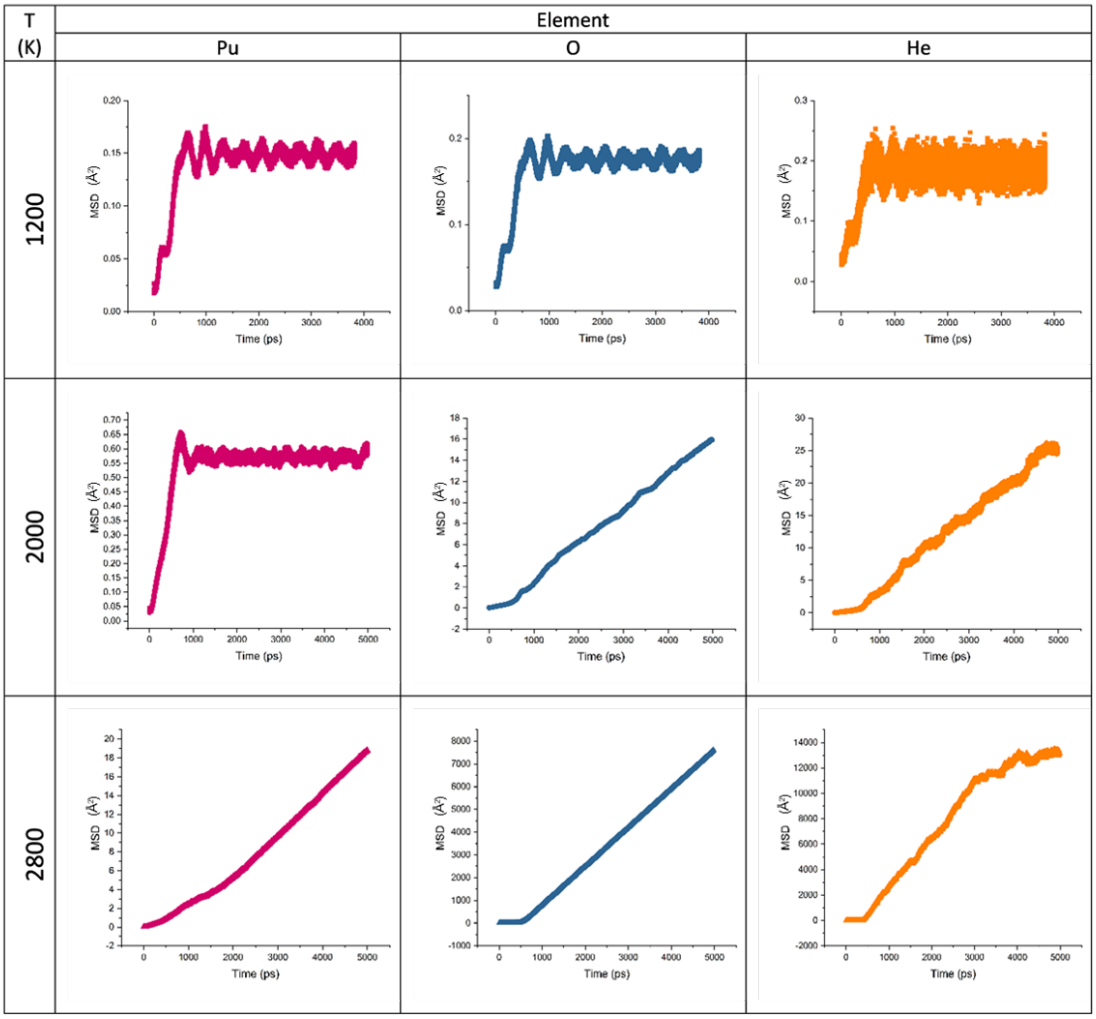


Figure 2: MSD of Pu, O and He in an 12x12x12 supercell at 1200, 2000 and 2800 K including the initial 1 ns equilibriation period.

References

[1] IAEA, "The potential role of nuclear energy in national climate change mitigation strategies," Vienna, Tech. Rep. 1984, 2021.

[2] BEIS, "Net zero strategy: Build back greener," Tech. Rep., 2021.

[3] NDA, "Progress on Plutonium Consolidation, Storage and Disposition," Tech. Rep., 2019.

[4] N. C. Hyatt, "Plutonium management policy in the United Kingdom: The need for a dual track strategy," *Energy Policy*, vol. 101, pp. 303–309, 2017, ISSN: 0301-4215. DOI: https://doi.org/10.1016/j.enpol.2016.08.033.

[5] N. C. Hyatt, "Safe management of the UK separated plutonium inventory: a challenge of materials degradation," *npj Materials Degradation*, vol. 4, p. 28, 2020, ISSN: 2397-2106. DOI: 10.1038/s41529-020-00132-7.

[6] H. E. Sims, K. J. Webb, J. Brown, D. Morris, and R. J. Taylor, "Hydrogen yields from water on the surface of plutonium dioxide," *Journal of Nuclear Materials*, vol. 437, no. 1, pp. 359–364, 2013, ISSN: 0022-3115. DOI: https://doi.org/10.1016/j.jnucmat.2013.02.040.

[7] "Small Modular Nuclear Reactors," *POST Note*, no. 580, 2018.

[8] "Trends in Energy," *POST Note*, no. 503, 2015.

[9] "New Nuclear Power Technologies," *POST Note*, no. 457, 2014.

[10] S. S. Hecker, "Plutonium in use - from single atoms to multiton amounts," *Los Alamos Science*, no. 26, pp. 10–15, 2000.

[11] P. McPherson, *Principles of Nuclear Chemistry*, ser. Essential Textbooks in Chemistry. 2016, ISBN: 9781786340535.

[12] P. Atkins and J. de Paula, *Atkins' Physical Chemistry*. OUP Oxford, 2010, pp. 401–404, ISBN: 9780199543373.

[13] S. S. Hecker, "Plutonium - an element at odds with itself," *Los Alamos Science*, no. 26, pp. 16–23, 2000.

[14] Z. Lovasic, "Nuclear management of spent fuel from power reactors," in *Nuclear Fuel Cycle Science and Engineering*, I. Crossland, Ed., Woodhead Publishing, 2012, pp. 427–458, ISBN: 978-0-85709-073-7. DOI: https://doi.org/10.1533/9780857096388.4.427.

[15] NDA, "NDA 5-year R&D Plan 2019 to 2024," Tech. Rep., Apr. 2019.

[16] J. W. Dawson and M. Phillips, "Gas-cooled nuclear reactor designs, operation and fuel cycle," in *Nuclear Fuel Cycle Science and Engineering*, I. Crossland, Ed., Woodhead Publishing, 2012, pp. 300–332, ISBN: 978-0-85709-073-7. DOI: https://doi.org/10.1533/9780857096388.3.300.

[17] T. Wiss, J.-P. Hiernaut, D. Roudil, *et al.*, "Evolution of spent nuclear fuel in dry storage conditions for millennia and beyond," *Journal of Nuclear Materials*, vol. 451, no. 1, pp. 198–206, 2014, ISSN: 0022-3115. DOI: https://doi.org/10.1016/j.jnucmat.2014.03.055.

[18] W. Schulz and E. Horwitz, "Recent progress in the extraction chemistry of actinide ions," *Journal of the Less Common Metals*, vol. 122, no. C, pp. 125–138, 1986, ISSN: 0022-5088.

[19] A. Clark, P. Yang, and J. Shafer, "Coordination of Actinides and the Chemistry Behind Solvent Extraction," in *Experimental and Theoretical Approaches to Actinide Chemistry*. Jan. 2018, ISBN: 9781119115526. DOI: 10.1002/9781119115557.ch5.

[20] J. Laidler, "Nuclear Fuel Reprocessing," in *Encyclopedia of Materials: Science and Technology*, K. J. Buschow, R. W. Cahn, M. C. Flemings, *et al.*, Eds., Oxford: Elsevier, 2001, pp. 6303–6309, ISBN: 978-0-08-043152-9. DOI: https://doi.org/10.1016/B0-08-043152-6/01119-0.

[21] "Jone done sellafield plant safely completes its mission," *gov.uk*, Jul. 2022.

[22] "Managing the UK Plutonium Stockpile," *POST Note*, no. 531, 2016.

[23] W. Walker and M. Lonnroth, *Nuclear Power Struggles: Industrial Competition and Proliferation Control*. London: Allen & Unwin, 1983, ISBN: 0043381049.

[24] OECD Nuclear Energy Agency and Organisation for Economic Co-operation and Development, *Plutonium Fuel: An Assessment*, ser. Nuclear Energy Agency v. 1. Organisation for Economic Co-operation and Development, 1989, ISBN: 978-92-64-13265-1.

[25] NDA, "NDA: Annual Report and Accounts 2021 to 2022," Tech. Rep., Jul. 2022.

[26] IAEA, "Status and Advances in MOX Fuel Technology," Tech. Rep., 2003.

[27] S. Morrison and G. Parks, "The effect of ^{241}Am on UK plutonium recycle options in thorium-plutonium fuelled LWRs – Part I: PWRs," *Annals of Nuclear Energy*, vol. 135, p. 106 952, 2020, ISSN: 0306-4549. DOI: https://doi.org/10.1016/j.anucene.2019.106952.

[28] S. Morrison and G. Parks, "The effect of ^{241}Am on UK plutonium recycle options in thorium-plutonium fuelled LWRs – Part II: BWRs," *Annals of Nuclear Energy*, vol. 135, p. 106 974, 2020, ISSN: 0306-4549. DOI: https://doi.org/10.1016/j.anucene.2019.106974.

[29] A. J. Kuperman, "Challenges of plutonium fuel fabrication: explaining the decline of spent fuel recycling," *International Journal of Nuclear Governance,*

Economy and Ecology, vol. 4, pp. 302–316, Jan. 2019, ISSN: 1742-4186. DOI: 10.1504/IJNGEE.2019.106023.

[30] T. Cochran, H. Feiveson, W. Patterson, *et al.*, "Fast Breeder Reactor Programs: History and Status, Report 8 in the International Panel on Fissile Material (IPFM)," Princeton University, Princeton, NJ, USA, Tech. Rep., 2010.

[31] M. Stennett, L. Casey, C. Corkhill, *et al.*, "Advanced ceramic wasteforms for the immobilisation of radwastes," in *Advances in Materials Science for Environmental and Energy Technologies II*. John Wiley & Sons, Ltd, 2013, pp. 11–22, ISBN: 9781118751176. DOI: https://doi.org/10.1002/9781118751176.ch2. eprint: https://ceramics.onlinelibrary.wiley.com/doi/pdf/10.1002/9781118751176.ch2.

[32] M.-X. Zhong, B. Walkley, D. J. Bailey, *et al.*, "Synthesis of $Ca_{1-x}Ce_xZrTi_{2-2x}Al_{2x}O_7$ zirconolite ceramics for plutonium disposition," *Journal of Nuclear Materials*, vol. 556, p. 153 198, 2021, ISSN: 0022-3115. DOI: https://doi.org/10.1016/j.jnucmat.2021.153198.

[33] S. Dimosthenous, C. M. Handley, L. R. Blackburn, C. L. Freeman, and N. C. Hyatt, "A high throughput computational investigation of the solid solution mechanisms of actinides and lanthanides in zirconolite," *RSC Adv.*, vol. 11, pp. 25 179–25 186, 41 2021. DOI: 10.1039/D1RA02914B.

[34] L. R. Blackburn, S.-K. Sun, S. M. Lawson, *et al.*, "Synthesis and characterisation of $Ca_{1-x}Ce_xZrTi_{2-2x}Cr_{2x}O_7$: Analogue zirconolite wasteform for the immobilisation of stockpiled UK plutonium," *Journal of the European Ceramic Society*, vol. 40, no. 15, pp. 5909–5919, 2020, ISSN: 0955-2219. DOI: https://doi.org/10.1016/j.jeurceramsoc.2020.05.066.

[35] P. A. Bingham, R. J. Hand, M. C. Stennett, N. C. Hyatt, and M. T. Harrison, "The use of surrogates in waste immobilization studies: A case study of plutonium," vol. 1107, 2008, pp. 421–428. DOI: 10.1557/proc-1107-421.

[36] S. S. Hecker, "The plutonium challenge - stockpile stewardship," *Los Alamos Science*, no. 26, pp. 24–26, 2000.

[37] K. Hesketh, G. Schlosser, D. Porsch, *et al.*, "Plutonium management in the medium term," *Nuclear Technology*, vol. 148, Dec. 2004. DOI: 10.13182/NT04-A3564.

[38] B. D. Wirth, A. J. Schwartz, M. J. Fluss, M. J. Caturla, M. A. Wall, and W. G. Wolfer, "Fundamental studies of plutonium aging," *MRS Bulletin*, vol. 26, no. 9, pp. 679–683, 2001. DOI: 10.1557/mrs2001.177.

[39] D. Clark, S. Hecker, G. Jarvinen, and M. Neu, "Plutonium," in Jan. 2006, vol. 191, pp. 813–1264, ISBN: 978-94-007-0210-3. DOI: 10.1007/1-4020-3598-5_7.

[40] C. Anderson, L. Blackburn, C. Boxall, *et al.*, "The TRANSCEND University Consortium: Theme 4: Nuclear Materials – 22092," (Phoenix, Arizona), Mar. 2022.

[41] G. Bailey, E. Bluhm, J. Lyman, *et al.*, "Gas Generation from Actinide Oxide Materials," Los Alamos National Laboratory, Los Alamos, NM, Tech. Rep. LA-13781-MS, 2000, p. 72.

[42] K. Webb, R. Taylor, C. Campbell, *et al.*, "Thermal processing of chloride-contaminated plutonium dioxide," *ACS Omega*, vol. 4, no. 7, pp. 12 524–12 536, 2019, PMID: 31460372. DOI: 10.1021/acsomega.9b00719. eprint: https://doi.org/10.1021/acsomega.9b00719.

[43] C. Ferry, C. Poinssot, C. Cappelaere, *et al.*, "Specific outcomes of the research on the spent fuel long-term evolution in interim dry storage and deep geological disposal," *Journal of Nuclear Materials*, vol. 352, no. 1, pp. 246–253, 2006, Proceedings of the E-MRS 2005 Spring Meeting Symposium N on Nuclear Materials (including the 10th Inert Matrix Fuel Workshop), ISSN: 0022-3115. DOI: https://doi.org/10.1016/j.jnucmat.2006.02.061.

[44] V. Dremov, P. Sapozhnikov, A. Kutepov, *et al.*, "Atomistic simulations of helium dynamics in a plutonium lattice," *Physical Review B*, vol. 77, p. 224 306, 22 Jun. 2008. DOI: 10.1103/PhysRevB.77.224306.

[45] W. G. Wolfer, "Radiation Effects In Plutonium. What is known? Where should we go from here?" *Los Alamos Science*, no. 26, pp. 274–285, 2000.

[46] D. C. Parfitt and R. W. Grimes, "Predicted mechanisms for radiation enhanced helium resolution in uranium dioxide," *Journal of Nuclear Materials*, vol. 381, no. 3, pp. 216–222, 2008, ISSN: 0022-3115. DOI: https://doi.org/10.1016/j.jnucmat.2008.06.038.

[47] J. L. Chen and N. Kaltsoyannis, "Computational Study of Plutonium-Americium Mixed Oxides ($Pu_{0.92}Am_{0.08}O_{2-x}$); Water Adsorption on {111}, {110}, and {100} Surfaces," *Journal of Physical Chemistry C*, vol. 124, pp. 6646–6658, 2020, ISSN: 19327455. DOI: 10.1021/acs.jpcc.9b11601.

[48] D. Laventine, C. Boxall, R. Orr, and R. Taylor, "Direct mass analysis of water absorption onto thoria thin films," *Progress in Nuclear Science and Technology*, vol. 5, pp. 136–139, Nov. 2018. DOI: 10.15669/pnst.5.136.

[49] M. S. Read, S. R. Walker, and R. A. Jackson, "Derivation of enhanced potentials for plutonium dioxide and the calculation of lattice and intrinsic defect properties," *Journal of Nuclear Materials*, vol. 448, no. 1, pp. 20–25, 2014, ISSN: 0022-3115. DOI: https://doi.org/10.1016/j.jnucmat.2014.01.020.

[50] B. L. Scott, A. L. Pugmire, J. T. Stritzinger, D. Veirs, L. E. Wolfsberg, and M. P. Wilkerson, "Relationships between experimental signatures and processing history for a variety of PuO_2 materials," *Journal of Nuclear Materials*, 2019.

[51] G. Jomard and F. Bottin, "Thermodynamic stability of PuO_2 surfaces: Influence of electronic correlations," *Physical Review B*, vol. 84, p. 195 469, 19 Nov. 2011. DOI: 10.1103/PhysRevB.84.195469.

[52] J. Emsley, *Nature's Building Blocks: An A-Z Guide to the Elements*. OUP Oxford, 2011, "405–411", ISBN: 9780192570468.

[53] S. S. Hecker and J. C. Martz, "Aging of plutonium and its alloys," *Los Alamos Science*, no. 26, pp. 238–243, 2000.

[54] J. Haschke, T. Allen, L. Morales, "Surface and Corrosion Chemistry of Plutonium," *Los Alamos Science*, no. 26, 2000.

[55] M. S. Read and R. A. Jackson, "Derivation of enhanced potentials for uranium dioxide and the calculation of lattice and intrinsic defect properties," *Journal of Nuclear Materials*, vol. 406, no. 3, pp. 293–303, 2010, ISSN: 0022-3115. DOI: https://doi.org/10.1016/j.jnucmat.2010.08.044.

[56] B. Ao, P. Chen, P. Shi, X. Wang, W. Hu, and L. Wang, "Computer simulation of helium effects in plutonium during the aging process of self-radiation damage," *Communications in Computational Physics*, vol. 11, no. 4, pp. 1205–1225, 2012. DOI: 10.4208/cicp.290610.210111s.

[57] D. Wheeler and P. Bayer, "Evaluation of the nucleation and growth of helium bubbles in aged plutonium," *Journal of Alloys and Compounds*, vol. 444-445, pp. 212–216, 2007, Proceedings of the Plutonium Futures - The Science 2006 Conference, ISSN: 0925-8388. DOI: https://doi.org/10.1016/j.jallcom.2007.01.038.

[58] H. Ullmaier, P. Ehrhart, P. Jung, and H. Schultz, *Atomic Defects in Metals / Atomare Fehlstellen in Metallen*, ser. Landolt-Börnstein: Numerical Data and Functional Relationships in Science and Technology - New Series / Condensed Matter. Springer Berlin Heidelberg, 1991, ISBN: 9783540514350.

[59] M. Stan, J. Ramirez, P. Cristea, *et al.*, "Models and simulations of nuclear fuel materials properties," *Journal of Alloys and Compounds*, vol. 444-445, pp. 415–423, 2007, Proceedings of the Plutonium Futures - The Science 2006 Conference, ISSN: 0925-8388. DOI: https://doi.org/10.1016/j.jallcom.2007.01.102.

[60] B. P. Uberuaga, D. A. Andersson, and C. R. Stanek, "Defect behavior in oxides: Insights from modern atomistic simulation methods," *Current Opinion in Solid State and Materials Science*, vol. 17, no. 6, pp. 249–256, 2013, Frontiers in Methods for Materials Simulations, ISSN: 1359-0286. DOI: https://doi.org/10.1016/j.cossms.2013.07.003.

[61] C. Micheau, M. Virot, S. Dourdain, *et al.*, "Relevance of formation conditions to the size, morphology and local structure of intrinsic plutonium colloids," *Environmental Science: Nano*, vol. 7, no. 8, pp. 2252–2266, 2020, ISSN: 2051-8153. DOI: 10.1039/D0EN00457J.

[62] A. Walsh, A. A. Sokol, and R. Catlow, *Computational Approaches to Energy Materials*. Wiley, Apr. 2013, p. 314, ISBN: 9781119950936. DOI: 10.1002/9781118551462.

[63] J. D. Gale and A. L. Rohl, "The General Utility Lattice Program (GULP)," *Molecular Simulation*, vol. 29, no. 5, pp. 291–341, 2003. DOI: 10.1080/0892702031000104887.

[64] G. Lu and E. Kaxiras, "An overview of multiscale simulations of materials," *Handbook of Theoretical and Computational Nanotechnology, American Scientific Publishers*, vol. 10, Feb. 2004.

[65] D. S. Sholl and J. A. Steckel, *Density Functional Theory: A Practical Introduction*. John Wiley & Sons, Inc, 2009.

[66] J. A. Martinez, D. E. Yilmaz, T. Liang, S. B. Sinnott, and S. R. Phillpot, "Fitting empirical potentials: Challenges and methodologies," *Current Opinion in Solid State and Materials Science*, vol. 17, no. 6, pp. 263–270, 2013, Frontiers in Methods for Materials Simulations, ISSN: 1359-0286. DOI: https://doi.org/10.1016/j.cossms.2013.09.001.

[67] C. R. A. Catlow and G. D. Price, "Computer modelling of solid-state inorganic materials," *Nature*, vol. 347, 1990.

[68] J. D. Gale, "Empirical potential derivation for ionic materials," *Philosophical Magazine B*, vol. 73, pp. 3–19, Jan. 1996. DOI: 10.1080/13642819608239107.

[69] F. Vesely, *Introduction to Computational Physics, 6.5: Particles and Fields*, Accessed: 30/09/2022.

[70] F. Vesely, "Computational Physics," in Springer New York, 1994, ISBN: 978-1-4757-2307-6. DOI: https://doi.org/10.1007/978-1-4757-2307-6.

[71] G. Grant and W. Richards, *Computational Chemistry*, ser. Computational Chemistry. Oxford University Press, 1995, ISBN: 9780198557418.

[72] R. W. Hockney and J. W. Eastwood, *Computer simulation using particles*. CRC Press, 1988, ISBN: 9780852743928.

[73] A. P. Thompson, H. M. Aktulga, R. Berger, *et al.*, "LAMMPS - a flexible simulation tool for particle-based materials modeling at the atomic, meso, and continuum scales," *Computer Physics Communications*, vol. 271, p. 108 171, 2022. DOI: 10.1016/j.cpc.2021.108171.

[74] J. F. Ziegler and J. P. Biersack, "The stopping and range of ions in matter," in *Treatise on Heavy-Ion Science: Volume 6: Astrophysics, Chemistry, and Condensed Matter*. Boston, MA: Springer US, 1985, pp. 93–129, ISBN: 978-1-4615-8103-1. DOI: 10.1007/978-1-4615-8103-1_3.

[75] A. B. Lidiard, "The Mott-Littleton method: An introductory survey," *Journal of The Chemical Society, Faraday Transactions 2*, vol. 85, May 1989. DOI: 10.1039/f29898500341.

[76] B. G. Dick and A. W. Overhauser, "Theory of the dielectric constants of alkali halide crystals," *Physical Review*, vol. 112, pp. 90–103, 1 Oct. 1958. DOI: 10.1103/PhysRev.112.90.

[77] A. Dwivedi and A. N. Cormack, "A computer simulation study of the defect structure of calcia-stabilized zirconia," *Philosophical Magazine A*, vol. 61, no. 1, pp. 1–22, 1990. DOI: 10.1080/01418619008235554. eprint: https://doi.org/10.1080/01418619008235554.

[78] M. W. Cooper, "Atomic scale simulation of irradiated nuclear fuel," Imperial College London, 2015.

[79] P. J. D. Lindan and M. J. Gillan, "Shell-model molecular dynamics simulation of superionic conduction in CaF_2," *Journal of Physics: Condensed Matter*, vol. 5, no. 8, pp. 1019–1030, Feb. 1993. DOI: 10.1088/0953-8984/5/8/005.

[80] P. J. Mitchell and D. Fincham, "Shell model simulations by adiabatic dynamics," *Journal of Physics: Condensed Matter*, vol. 5, no. 8, pp. 1031–1038, Feb. 1993. DOI: 10.1088/0953-8984/5/8/006.

[81] R. Fletcher, "Conjugate Direction Methods," in *Practical Methods of Optimization*. John Wiley & Sons, Ltd, 2000, ch. 4, pp. 80–94, ISBN: 9781118723203. DOI: https://doi.org/10.1002/9781118723203.ch4. eprint: https://onlinelibrary.wiley.com/doi/pdf/10.1002/9781118723203.ch4.

[82] J. Christensen and C. Bastien, "Introduction to General Optimization Principles and Methods," in *Nonlinear Optimization of Vehicle Safety Structures*, J. Christensen and C. Bastien, Eds., Oxford: Butterworth-Heinemann, 2016, ch. 3, pp. 107–168, ISBN: 978-0-12-804424-7. DOI: https://doi.org/10.1016/B978-0-12-417297-5.00003-1.

[83] R. Fletcher, "Newton-Like Methods," in *Practical Methods of Optimization*. John Wiley & Sons, Ltd, 2000, ch. 3, pp. 44–79, ISBN: 9781118723203. DOI: https://doi.org/10.1002/9781118723203.ch3. eprint: https://onlinelibrary.wiley.com/doi/pdf/10.1002/9781118723203.ch3.

[84] E. Bitzek, P. Koskinen, F. Gähler, M. Moseler, and P. Gumbsch, "Structural relaxation made simple," *Physical Review Letters*, vol. 97, p. 170 201, 17 Oct. 2006. DOI: 10.1103/PhysRevLett.97.170201.

[85] N. A. Zarkevich and D. D. Johnson, "Nudged-elastic band method with two climbing images: Finding transition states in complex energy landscapes," *The Journal of Chemical Physics*, vol. 142, no. 2, p. 024 106, 2015. DOI: 10.1063/1.4905209.

[86] J. D. Gale, "GULP: A computer program for the symmetry-adapted simulation of solids," *J. Chem. Soc., Faraday Trans.*, vol. 93, pp. 629–637, 4 1997. DOI: 10.1039/A606455H.

[87] J. S. Blakemore, "Dielectric and Magnetic Properties of Solids," in *Solid State Physics*, 2nd ed. Cambridge University Press, 1985, pp. 405–489. DOI: 10.1017/CBO9781139167871.007.

[88] N. F. Mott and M. J. Littleton, "Conduction in polar crystals. I. Electrolytic conduction in solid salts," *Trans. Faraday Soc.*, vol. 34, pp. 485–499, 0 1938. DOI: 10.1039/TF9383400485.

[89] R. A. Jackson, A. D. Murray, J. H. Harding, and C. R. A. Catlow, "The calculation of defect parameters in UO_2," *Philosophical Magazine A*, vol. 53, no. 1, pp. 27–50, 1986. DOI: 10.1080/01418618608242805. eprint: https://doi.org/10.1080/01418618608242805.

[90] CrystalMaker Software Ltd, *CrystalMaker*, version 10.6.2.

[91] F. Kröger and H. Vink, "Relations between the concentrations of imperfections in crystalline solids," in ser. Solid State Physics, F. Seitz and D. Turnbull, Eds., vol. 3, Academic Press, 1956, pp. 307–435. DOI: https://doi.org/10.1016/S0081-1947(08)60135-6.

[92] G. W. Watson, E. T. Kelsey, N. H. de Leeuw, D. J. Harris, and S. C. Parker, "Atomistic simulation of dislocations, surfaces and interfaces in MgO," *J. Chem. Soc., Faraday Trans.*, vol. 92, pp. 433–438, 3 1996. DOI: 10.1039/FT9969200433.

[93] N. A. Palmer, "Atomistic simulation studies of storage and ageing behaviour of plutonium dioxide and mixed oxide fuel," University of Birmingham, 2019.

[94] T. E. Littleford, R. A. Jackson, and M. S. Read, "An atomistic surface simulation study predicting morphologies and segregation in yttrium lithium fluoride," *Surface Science*, vol. 606, no. 19, pp. 1550–1555, 2012, ISSN: 0039-6028. DOI: https://doi.org/10.1016/j.susc.2012.06.002.

[95] D. E. Parry, "The electrostatic potential in the surface region of an ionic crystal," *Surface Science*, vol. 49, no. 2, pp. 433–440, Apr. 1975. DOI: 10.1016/0039-6028(75)90362-3.

[96] M. Abramowski, R. Grimes, and S. Owens, "Morphology of UO_2," *Journal of Nuclear Materials*, vol. 275, no. 1, pp. 12–18, 1999, ISSN: 0022-3115. DOI: https://doi.org/10.1016/S0022-3115(99)00110-5.

[97] Y. Liu, S. Niu, W. Lai, *et al.*, "Crystal morphology prediction of energetic materials grown from solution: Insights into the accurate calculation of attachment energies," *CrystEngComm*, vol. 21, pp. 4910–4917, 33 2019. DOI: 10.1039/C9CE00848A.

[98] G. Wulff, "XXV. Zur Frage der Geschwindigkeit des Wachsthums und der Auflösung der Krystallflächen," *Zeitschrift für Kristallographie - Crystalline Materials*, vol. 34, pp. 449–530,

[99] D. M. Duffy and P. W. Tasker, "A calculation of the formation energies of intrinsic defects near grain boundaries in NiO," *Philosophical Magazine A*, vol. 50, no. 2, pp. 143–154, 1985. DOI: 10.1080/01418618408244218.

[100] A. Stukowski, "Visualization and analysis of atomistic simulation data with OVITO - the Open Visualization Tool," *Modelling and Simulation in Materials Science and Engineering*, vol. 18, no. 1, Jan. 2010, ISSN: 0965-0393. DOI: 10.1088/0965-0393/18/1/015012.

[101] L. Verlet, "Computer 'Experiments' on Classical Fluids. I. Thermodynamical Properties of Lennard-Jones Molecules," *Physical Review*, vol. 159, pp. 98–103, 1 Jul. 1967. DOI: 10.1103/PhysRev.159.98.

[102] F. Jensen, *Introduction to Computational Chemistry*. Hoboken, NJ, USA: John Wiley & Sons, Inc., 2006, ISBN: 0470011874.

[103] J. P. Eckmann and D. Ruelle, "Ergodic theory of chaos and strange attractors," *Reviews of Modern Physics*, vol. 57, pp. 617–656, 3 Jul. 1985. DOI: 10.1103/RevModPhys.57.617.

[104] B. D. Todd and P. J. Daivis, *Nonequilibrium Molecular Dynamics: Theory, Algorithms and Applications*. Cambridge University Press, 2017, pp. 150–202. DOI: 10.1017/9781139017848.

[105] "The mean square displacement," *Democritus: A Molecular Dynamics simulation, UCL (Online)*, https://www.ucl.ac.uk/~ucfbasc/Theory/msd.html.

[106] D. Frenkel and B. Smit, "Chapter 4 - molecular dynamics simulations," in *Understanding Molecular Simulation (Second Edition)*, D. Frenkel and B. Smit, Eds., Second Edition, San Diego: Academic Press, 2002, pp. 63–107, ISBN: 978-0-12-267351-1. DOI: https://doi.org/10.1016/B978-012267351-1/50006-7.

[107] OriginLab Corporation, *OriginPro*, version 2021.

[108] The MathWorks Inc., *MATLAB*, version 2020a.

[109] D. S. Aidhy, Y. Zhang, and W. J. Weber, ""radiation damage in cubic zro_2 and yttria-stabilized zirconia from molecular dynamics simulations"," *Scripta Materialia*, vol. 98, pp. 16–19, 2015, ISSN: 1359-6462. DOI: https://doi.org/10.1016/j.scriptamat.2014.10.036.

[110] C. Meis and J. Gale, "Computatonal study of tetravalent uranium and plutonium lattice diffusion in zircon," *Materials Science and Engineering: B*, vol. 57, pp. 52–61, Dec. 1998. DOI: 10.1016/S0921-5107(98)00253-0.

[111] T. Arima, S. Yamasaki, Y. Inagaki, and K. Idemitsu, "Evaluation of thermal properties of UO_2 and PuO_2 by equilibrium molecular dynamics simulations from 300 to 2000 K," *Journal of Alloys and Compounds*, vol. 400, no. 1-2, pp. 43–50, Sep. 2005, ISSN: 0925-8388. DOI: 10.1016/j.jallcom.2005.04.003.

[112] H. Yu, D. Meng, H. Huang, and G. Li, "First results on oxygen self-diffusion in α-Pu_2O_3 investigated by molecular dynamics," *Journal of Nuclear Materials*, vol. 452, pp. 6–9, Sep. 2014. DOI: 10.1016/j.jnucmat.2014.04.044.

[113] M. W. D. Cooper, M. J. D. Rushton, and R. W. Grimes, "A many-body potential approach to modelling the thermomechanical properties of actinide oxides," *Journal of Physics: Condensed Matter*, vol. 26, p. 105 401, Mar. 2014, ISSN: 0953-8984. DOI: 10.1088/0953-8984/26/10/105401.

[114] T. Diaz de la Rubia, R. S. Averback, R. Benedek, and W. King, "Role of thermal spikes in energetic displacement cascades," *Physical Review Letters*, vol. 59, pp. 1930–1933, Nov. 1987. DOI: 10.1103/PhysRevLett.59.1930.

[115] L. Mallinson, *Ageing Studies and Lifetime Extension of Materials*, 1st ed. New York: Springer, 2001, ISBN: 0-306-46477-2.

[116] T. D. Chikalla and R. P. Turcotte, "Self-radiation damage ingrowth in $^{238}PuO_2$," *Radiation Effects and Defects in Solids*, vol. 19, pp. 93–98, 1973.

[117] M. Kato, A. Komeno, H. Uno, *et al.*, "Self-radiation damage in plutonium and uranium mixed dioxide," *Journal of Nuclear Materials*, vol. 393, no. 1, pp. 134–140, 2009, ISSN: 0022-3115. DOI: https://doi.org/10.1016/j.jnucmat.2009.05.020.

[118] B. Chung, K. Lema, and P. Allen, "Effects of self-irradiation in plutonium alloys," *Journal of Nuclear Materials*, vol. 471, pp. 239–242, 2016, ISSN: 0022-3115. DOI: https://doi.org/10.1016/j.jnucmat.2015.09.028.

[119] Y. Lu, Y. Yang, and P. Zhang, "Charge states of point defects in plutonium oxide: A first-principles study," *Journal of Alloys and Compounds*, vol. 649, pp. 544–552, Aug. 2015. DOI: 10.1016/j.jallcom.2015.07.219.

[120] H. Nakamura, M. Machida, and M. Kato, "LDA+U Study on Plutonium Dioxide with Spin-Orbit Couplings," *Progress in Nuclear Science and Technology*, vol. 2, pp. 16–19, 2011, ISSN: 2185-4823. DOI: 10.15669/pnst.2.16.

[121] L.-F. Wang, B. Sun, H.-F. Liu, D.-Y. Lin, and H.-F. Song, "Thermodynamics and kinetics of intrinsic point defects in plutonium dioxides," *Journal of Nuclear Materials*, vol. 526, p. 151 762, 2019, ISSN: 0022-3115. DOI: https://doi.org/10.1016/j.jnucmat.2019.151762.

[122] M. W. D. Cooper, S. T. Murphy, M. J. D. Rushton, and R. W. Grimes, "Thermophysical properties and oxygen transport in the $(U_x,Pu_{1-x})O_2$ lattice," *Journal of Nuclear Materials*, vol. 461, pp. 206–214, 2015, ISSN: 0022-3115. DOI: https://doi.org/10.1016/j.jnucmat.2015.03.024.

[123] M. Chu, D. Meng, S. Xiao, W. Wang, and Q. Chen, "Evaluation of thermal properties of PuO_2 and α-Pu_2O_3 by atomic simulation," *Journal of Alloys and Compounds*, vol. 539, pp. 7–11, Oct. 2012. DOI: 10.1016/j.jallcom.2012.05.094.

[124] R. C. Belin, P. J. Valenza, M. A. Reynaud, and P. E. Raison, "New hermetic sample holder for radioactive materials fitting to Siemens D5000 and Bruker D8 X-ray diffractometers: application to the Rietveld analysis of plutonium dioxide," *Journal of Applied Crystallography*, vol. 37, no. 6, pp. 1034–1037, Dec. 2004. DOI: 10.1107/S0021889804022885.

[125] M. Idiri, T. Le Bihan, S. Heathman, and J. Rebizant, "Behavior of actinide dioxides under pressure: UO_2 and ThO_2," *Physical Review B*, vol. 70, p. 014 113, 1 Jul. 2004. DOI: 10.1103/PhysRevB.70.014113.

[126] V. Sobolev, "Modelling thermal properties of actinide dioxide fuels," *Journal of Nuclear Materials*, vol. 344, no. 1, pp. 198–205, 2005, Proceedings of the 11th International Symposium on Thermodynamics of Nuclear Materials, ISSN: 0022-3115. DOI: https://doi.org/10.1016/j.jnucmat.2005.04.042.

[127] R. G. Haire, "Advance in plutonium chemistry 1967 - 2000," *American Nuclear Society*, 2000.

[128] S. R. Walker, R. A. Jackson, and M. S. D. Read, "Atomistic modelling of actinide oxides for nuclear fuel applications," *physica status solidi (c)*, vol. 10, no. 2, pp. 197–201, 2013. DOI: 10.1002/pssc.201200513. eprint: https://onlinelibrary.wiley.com/doi/pdf/10.1002/pssc.201200513.

[129] Y. Dong, L. Qi, J. Li, and I.-W. Chen, ""a computational study of yttria-stabilized zirconia: Ii. cation diffusion"," *Acta Materialia*, vol. 126, pp. 438–450, 2017, ISSN: 1359-6454. DOI: https://doi.org/10.1016/j.actamat.2017.01.008.

[130] M. Freyss, N. Vergnet, and T. Petit, "Ab initio modeling of the behavior of helium and xenon in actinide dioxide nuclear fuels," *Journal of Nuclear Materials*, vol. 352, no. 1, pp. 144–150, 2006, Proceedings of the E-MRS 2005 Spring Meeting Symposium N on Nuclear Materials (including the 10th Inert Matrix Fuel Workshop), ISSN: 0022-3115. DOI: https://doi.org/10.1016/j.jnucmat.2006.02.048.

[131] X. Tian, T. Gao, C. Lu, J. Shang, and H. Xiao, "First principle study of the behavior of helium in plutonium dioxide," *The European Physical Journal B*, vol. 86, no. 4, p. 179, 2013, ISSN: 1434-6036. DOI: 10.1140/epjb/e2013-31047-y.

[132] W. D. Neilson, H. Steele, N. Kaltsoyannis, and S. T. Murphy, "Accommodation of helium in $PuO_{2\pm x}$ and the role of americium," *Physical Chemistry Chemical Physics*, vol. 24, pp. 8245–8250, 14 2022. DOI: 10.1039/D1CP05570D.

[133] P. Tiwary, A. van de Walle, B. Jeon, and N. Grønbech-Jensen, "Interatomic potentials for mixed oxide and advanced nuclear fuels," *Physical Review B*, vol. 83, p. 094 104, 9 Mar. 2011. DOI: 10.1103/PhysRevB.83.094104.

[134] A. Tan, M. Abramowski, R. Grimes, and S. Owens, "Surface defect configurations on the (100) dipolar surface of UO_2," *Physical Review B*, vol. 72, Jul. 2005. DOI: 10.1103/PhysRevB.72.035457.

[135] P. Tasker, "The surface properties of uranium dioxide," *Surface Science*, vol. 87, no. 2, pp. 315–324, 1979, ISSN: 0039-6028. DOI: https://doi.org/10.1016/0039-6028(79)90531-4.

[136] Y. Jiang, J. B. Adams, and M. van Schilfgaarde, "Density-functional calculation of CeO_2 surfaces and prediction of effects of oxygen partial pressure and temperature on stabilities," *The Journal of Chemical Physics*, vol. 123, no. 6, p. 064 701, 2005. DOI: 10.1063/1.1949189. eprint: https://doi.org/10.1063/1.1949189.

[137] B. Sun, H. Liu, H. Song, *et al.*, "First-principles study of surface properties of PuO_2: Effects of thickness and O-vacancy on surface stability and chemical activity," *Journal of Nuclear Materials*, vol. 426, no. 1-3, pp. 139–147, Jul. 2012, ISSN: 0022-3115. DOI: 10.1016/j.jnucmat.2012.02.029.

[138] S. Moxon, A. R. Symington, J. S. Tse, *et al.*, "The energetics of carbonated PuO_2 surfaces affects nanoparticle morphology: a DFT+U study," *Physical Chemistry Chemical Physics*, vol. 22, no. 15, pp. 7728–7737, 2020, ISSN: 1463-9076. DOI: 10.1039/D0CP00021C.

[139] K. A. Nekrasov, A. S. Boyarchenkov, D. D. Seitov, S. K. Gupta, and A. Y. Kupryazhkin, "The equilibrium shapes of plutonium dioxide nanocrystals: A molecular dynamics simulation," *AIP Conference Proceedings*, vol. 2220, no. 1, p. 130 002, 2020. DOI: 10.1063/5.0001606.

[140] J. Wellington, B. Tegner, J. Collard, A. Kerridge, and N. Kaltsoyannis, "Oxygen Vacancy Formation and Water Adsorption on Reduced AnO_2 {111}, {110} and {100} Surfaces (An = U, Pu); A Computational Study," *The Journal of Physical Chemistry C*, vol. 122, Mar. 2018. DOI: 10.1021/acs.jpcc.7b11512.

[141] A. H. Tan, R. W. Grimes, and S. Owens, "Structures of UO_2 and PuO_2 surfaces with hydroxide coverage," *Journal of Nuclear Materials*, vol. 344, no. 1, pp. 13–16, 2005, Proceedings of the 11th International Symposium on Thermodynamics of Nuclear Materials, ISSN: 0022-3115. DOI: https://doi.org/10.1016/j.jnucmat.2005.04.008.

[142] J. Pegg, A. Shields, M. Storr, D. Scanlon, and N. Leeuw, "Interaction of hydrogen with actinide dioxide (111) surfaces," *The Journal of Chemical Physics*, vol. 150, p. 134 701, Apr. 2019. DOI: 10.1063/1.5087577.

[143] L. Venault, A. Deroche, J. Gaillard, *et al.*, "Dihydrogen H_2 steady state in α-radiolysis of water adsorbed on PuO_2 surface," *Radiation Physics and Chemistry*, vol. 162, pp. 136–145, 2019, ISSN: 0969-806X. DOI: https://doi.org/10.1016/j.radphyschem.2018.09.022.

[144] C. R. Stanek, M. R. Bradford, and R. W. Grimes, "Segregation of Ba^{2+}, Sr^{2+}, Ce^{4+} and Zr^{4+} to UO_2 surfaces," *Journal of Physics: Condensed Matter*, vol. 16, no. 27, S2699–S2714, Jun. 2004. DOI: 10.1088/0953-8984/16/27/008.

[145] N. R. Williams, M. Molinari, S. C. Parker, and M. T. Storr, "Atomistic investigation of the structure and transport properties of tilt grain boundaries of UO_2," *Journal of Nuclear Materials*, vol. 458, pp. 45–55, 2015, ISSN: 0022-3115. DOI: https://doi.org/10.1016/j.jnucmat.2014.11.120.

[146] G. Watson, "Atomistic and electronic structure calculation of defects at the surfaces of oxides," *Radiation Effects and Defects in Solids*, vol. 157, no. 6-12, pp. 773–781, 2002. DOI: 10.1080/10420150215767. eprint: https://doi.org/10.1080/10420150215767.

[147] S. Vyas, R. W. Grimes, D. H. Gay, and A. L. Rohl, "Structure, stability and morphology of stoichiometric ceria crystallites," *J. Chem. Soc., Faraday Trans.*, vol. 94, pp. 427–434, 3 1998. DOI: 10.1039/A707052G.

[148] P. Hartman and P. Bennema, "The attachment energy as a habit controlling factor: I. theoretical considerations," *Journal of Crystal Growth*, vol. 49, no. 1, pp. 145–156, 1980, ISSN: 0022-0248. DOI: https://doi.org/10.1016/0022-0248(80)90075-5.

[149] T. Taylor and W. Ellis, "A LEED study of UO_2(∼100) vicinal surfaces," *Surface Science*, vol. 77, no. 2, pp. 321–336, 1978, ISSN: 0039-6028. DOI: https://doi.org/10.1016/0039-6028(78)90009-2.

[150] C. Muggelberg, M. Castell, G. Briggs, and D. Goddard, "An STM study of the UO_2(001) surface," *Applied Surface Science*, vol. 142, no. 1, pp. 124–128, 1999, ISSN: 0169-4332. DOI: https://doi.org/10.1016/S0169-4332(98)00664-3.

[151] T. Bo, J.-H. Lan, C.-Z. Wang, *et al.*, "First-Principles Study of Water Reaction and H_2 Formation on UO_2 (111) and (110) Single Crystal Surfaces," *The Journal of Physical Chemistry C*, vol. 118, no. 38, pp. 21 935–21 944, 2014. DOI: 10.1021/jp503614f. eprint: https://doi.org/10.1021/jp503614f.

[152] E. Murray, N. Palmer, W. Neilson, *et al.*, "Atomistic Simulation of Helium Incorporation in PuO_2," *Proceedings of the WM Symposia*, Mar. 2022.

[153] M. Freyss and T. Petit, "Ab initio modelling of the behaviour of helium in americium and plutonium oxides," CEA-Cadarache, 13108 Saint-Paul-lez-Durance, France, Tech. Rep. INIS-FR–3001, 2004, p. 6.

[154] D. Gryaznov, S. Rashkeev, E. Kotomin, E. Heifets, and Y. Zhukovskii, "Helium behavior in oxide nuclear fuels: First principles modeling," *Nuclear Instruments and Methods in Physics Research Section B: Beam Interactions with Materials and Atoms*, vol. 268, no. 19, pp. 3090–3094, 2010, Radiation Effects in Insulators, ISSN: 0168-583X. DOI: https://doi.org/10.1016/j.nimb.2010.05.054.

[155] N. Kuganathan, P. Ghosh, A. Arya, and R. Grimes, "Helium trapping and clustering in ThO_2," *Journal of Nuclear Materials*, vol. 507, pp. 288–296, 2018, ISSN: 0022-3115. DOI: https://doi.org/10.1016/j.jnucmat.2018.05.006.

[156] Y. Yun, O. Eriksson, and P. M. Oppeneer, "Theory of He trapping, diffusion, and clustering in UO_2," *Journal of Nuclear Materials*, vol. 385, no. 3, pp. 510–516, 2009, ISSN: 0022-3115. DOI: https://doi.org/10.1016/j.jnucmat.2008.12.311.

[157] J.-P. Crocombette, "Ab initio energetics of some fission products (Kr, I, Cs, Sr and He) in uranium dioxide," *Journal of Nuclear Materials*, vol. 305, no. 1, pp. 29–36, 2002, ISSN: 0022-3115. DOI: https://doi.org/10.1016/S0022-3115(02)00907-8.

[158] R. W. Grimes, R. H. Miller, and C. R. A. Catlow, "The behaviour of helium in UO_2: Solution and migration energies," *Journal of Nuclear Materials*, vol. 172, pp. 123–125, 1990.

[159] B. Ao, X. Wang, W. Hu, J. Yang, and J. Xia, "Atomistic study of small helium bubbles in plutonium," *Journal of Alloys and Compounds*, vol. 444-445, pp. 300–304, 2007, Proceedings of the Plutonium Futures - The Science 2006 Conference, ISSN: 0925-8388. DOI: https://doi.org/10.1016/j.jallcom.2006.11.077.

[160] F. H. Ree, "A statistical mechanical theory of chemically reacting multiphase mixtures: Application to the detonation properties of PETN," *The Journal of Chemical Physics*, vol. 81, no. 3, pp. 1251–1263, 1984. DOI: 10.1063/1.447811. eprint: https://doi.org/10.1063/1.447811.

[161] R. A. Aziz, V. P. S. Nain, J. S. Carley, W. L. Taylor, and G. T. McConville, "An accurate intermolecular potential for helium," *The Journal of Chemical Physics*, vol. 70, no. 9, pp. 4330–4342, 1979. DOI: 10.1063/1.438007. eprint: https://doi.org/10.1063/1.438007.

[162] F. Garrido, L. Nowicki, G. Sattonnay, T. Sauvage, and L. Thomé, "Lattice location of helium in uranium dioxide single crystals," *Nuclear Instruments and Methods in Physics Research Section B: Beam Interactions with Materials and Atoms*, vol. 219-220, pp. 196–199, 2004, Proceedings of the Sixteenth International Conference on Ion Beam Analysis, ISSN: 0168-583X. DOI: https://doi.org/10.1016/j.nimb.2004.01.053.

[163] T. Petit, M. Freyss, P. Garcia, *et al.*, "Molecular modelling of transmutation fuels and targets," *Journal of Nuclear Materials*, vol. 320, no. 1, pp. 133–137, 2003, Proceedings of the 2nd Seminar on European Research on Materials for Transmutation, ISSN: 0022-3115. DOI: https://doi.org/10.1016/S0022-3115(03)00179-X.

[164] W. D. Neilson, J. T. Pegg, H. Steele, and S. T. Murphy, "The defect chemistry of non-stoichiometric $PuO_{2\pm x}$," *Physical Chemistry Chemical Physics*, vol. 23, no. 8, pp. 4544–4554, 2021, ISSN: 1463-9076. DOI: 10.1039/D0CP06497A.

[165] K. Yamada, K. Kurosaki, M. Uno, and S. Yamanaka, "Evaluation of thermal properties of uranium dioxide by molecular dynamics," *Journal of Alloys and Compounds*, vol. 307, no. 1, pp. 10–16, 2000, ISSN: 0925-8388. DOI: https://doi.org/10.1016/S0925-8388(00)00806-9.

[166] H. Balboa, L. Van Brutzel, A. Chartier, and Y. Le Bouar, "Damage characterization of (U,Pu)O_2 under irradiation by molecular dynamics simulations," *Journal of Nuclear Materials*, vol. 512, pp. 440–449, Dec. 2018. DOI: 10.1016/j.jnucmat.2018.07.056.

[167] W. Mingjie, Z. Li, D. Jiguang, H. Duohui, W. Lili, and J. Gang, "The MD simulation of thermal properties of plutonium dioxide," *Physica B: Condensed Matter*, vol. 407, no. 23, pp. 4595–4599, 2012, ISSN: 0921-4526. DOI: https://doi.org/10.1016/j.physb.2012.08.010.

[168] M. J. Rahman, B. Szpunar, and J. A. Szpunar, "Molecular dynamics study of primary radiation damage in PuO_2 and $(U_{0.5}Pu_{0.5})O_2$," *Computational*

Materials Science, vol. 166, Aug. 2019. DOI: 10.1016/j.commatsci.2019.05.013.

[169] V. Saltas, A. Chroneos, M. W. D. Cooper, M. E. Fitzpatrick, and F. Vallianatos, "Investigation of oxygen self-diffusion in PuO_2 by combining molecular dynamics with thermodynamic calculations," *RSC Adv.*, vol. 6, pp. 103 641–103 649, 105 2016. DOI: 10.1039/C6RA24575G.

[170] Y. Dong, L. Qi, J. Li, and I.-W. Chen, ""a computational study of yttria-stabilized zirconia: I. using crystal chemistry to search for the ground state on a glassy energy landscape"," eng, *Acta Materialia*, vol. 127, no. C, pp. 73–84, 2017, ISSN: 1359-6454.

[171] K. C. Lau and B. I. Dunlap, ""molecular dynamics simulation of yttria-stabilized zirconia (ysz) crystalline and amorphous solids"," *Journal of Physics: Condensed Matter*, vol. 23, no. 3, p. 035 401, Jan. 2011. DOI: 10.1088/0953-8984/23/3/035401.

[172] M. Kilo, C. Argirusis, G. Borchardt, and R. A. Jackson, "Oxygen diffusion in yttria stabilised zirconia—experimental results and molecular dynamics calculations," *Physical Chemistry Chemical Physics*, vol. 5, pp. 2219–2224, 11 2003. DOI: 10.1039/B300151M.

[173] M. Kato, H. Nakamura, M. Watanabe, T. Matsumoto, and M. Machida, "Defect Chemistry and Basic Properties of Non-Stoichiometric PuO_2," *Defect and Diffusion Forum*, vol. 375, pp. 57–70, May 2017. DOI: 10.4028/www.scientific.net/DDF.375.57.

[174] R. Deaton and C. Wiedenheft, "Self-diffusion of oxygen in $^{238}PuO_2$," *Journal of Inorganic and Nuclear Chemistry*, vol. 35, no. 2, pp. 649–650, 1973, ISSN: 0022-1902. DOI: https://doi.org/10.1016/0022-1902(73)80579-2.

[175] A. Bayoglu, A. Giordano, and R. Lorenzelli, "Mesure de l'autodiffusion de l'oxygene dans $PuO_{2.00}$ par echange isotopique," *Journal of Nuclear Materials*, vol. 113, no. 1, pp. 71–74, 1983, ISSN: 0022-3115. DOI: https://doi.org/10.1016/0022-3115(83)90168-X.

[176] G. E. Murch and C. R. A. Catlow, "Oxygen diffusion in UO_2, ThO_2 and PuO_2. A review," *J. Chem. Soc., Faraday Trans. 2*, vol. 83, pp. 1157–1169, 7 1987. DOI: 10.1039/F29878301157.

[177] H. Matzke, "Atomic transport properties in UO_2 and mixed oxides (U,Pu)O_2," *J. Chem. Soc., Faraday Trans. 2*, vol. 83, pp. 1121–1142, 7 1987. DOI: 10.1039/F29878301121.

[178] T. Yamashita, N. Nitani, T. Tsuji, and H. Inagaki, "Thermal expansions of NpO_2 and some other actinide dioxides," *Journal of Nuclear Materials*, vol. 245, no. 1, pp. 72–78, 1997. DOI: 10.1016/S0022-3115(96)00750-7.

[179] H. Mehrer, *Diffusion in Solids*, ser. Springer Series in Solid-State Sciences. Springer, 2007, ISBN: 978-3-540-71488-0. DOI: https://doi.org/10.1007/978-3-540-71488-0.

[180] S. Günay, B. Akgenç, and Ç. Taşseven, "Modeling superionic behavior of plutonium dioxide," *High Temperature Materials and Processes*, vol. 35, no. 10, pp. 999–1004, 2016. DOI: doi:10.1515/htmp-2015-0133.

[181] G. Riemer and H. Scherff, "Plutonium diffusion in hyperstoichiometric mixed uranium-plutonium dioxides," *Journal of Nuclear Materials*, vol. 39, no. 2, pp. 183–188, 1971, ISSN: 0022-3115. DOI: https://doi.org/10.1016/0022-3115(71)90023-7.

[182] H. Matzke, "Lattice disorder and metal self-diffusion in non-stoichiometric UO_2 and (U,Pu)O_2," *Journal de Physique Colloques*, vol. 34, no. C9, pp. C9-317-C9–325, 1973. DOI: 10.1051/jphyscol:1973956.

[183] A. Boyarchenkov, S. Potashnikov, K. Nekrasov, and A. Kupryazhkin, "Investigation of cation self-diffusion mechanisms in $UO_{2\pm x}$ using molecular dynamics," *Journal of Nuclear Materials*, vol. 442, no. 1, pp. 148–161, 2013, ISSN: 0022-3115. DOI: https://doi.org/10.1016/j.jnucmat.2013.08.030.

[184] M. Kato, T. Uchida, and T. Sunaoshi, "Measurement of oxygen chemical diffusion in PuO_{2-x} and analysis of oxygen diffusion in PuO_{2-x} and (Pu,U)O_{2-x}," *physica status solidi (c)*, vol. 10, no. 2, pp. 189–192, 2013. DOI: https://doi.org/10.1002/pssc.201200454. eprint: https://onlinelibrary.wiley.com/doi/pdf/10.1002/pssc.201200454.

[185] S. Potashnikov, A. Boyarchenkov, K. Nekrasov, and A. Kupryazhkin, "High-precision molecular dynamics simulation of UO_2–PuO_2: Anion self-diffusion in UO_2," *Journal of Nuclear Materials*, vol. 433, no. 1, pp. 215–226, 2013, ISSN: 0022-3115. DOI: https://doi.org/10.1016/j.jnucmat.2012.08.033.

[186] E. Murray, Y. Zhou, P. Slater, R. Smith, P. Goddard, and H. Steele, "Atomistic simulation of helium diffusion and clustering in plutonium dioxide," *Physical Chemistry Chemical Physics*, vol. 24, pp. 20 709–20 720, 35 2022. DOI: 10.1039/D2CP02244C.

[187] L. Luzzi, L. Cognini, D. Pizzocri, *et al.*, "Helium diffusivity in oxide nuclear fuel: Critical data analysis and new correlations," *Nuclear Engineering and Design*, vol. 330, pp. 265–271, 2018, ISSN: 0029-5493. DOI: https://doi.org/10.1016/j.nucengdes.2018.01.044.

[188] D. Roudil, X. Deschanels, P. Trocellier, C. Jégou, S. Peuget, and J.-M. Bart, "Helium thermal diffusion in a uranium dioxide matrix," *Journal of Nuclear Materials*, vol. 325, pp. 148–158, Feb. 2004. DOI: 10.1016/j.jnucmat.2003.11.012.

[189] Z. Talip, T. Wiss, V. Di Marcello, *et al.*, "Thermal diffusion of helium in ^{238}Pu-doped UO_2," *Journal of Nuclear Materials*, vol. 445, no. 1, pp. 117–127, 2014, ISSN: 0022-3115. DOI: https://doi.org/10.1016/j.jnucmat.2013.10.066.

[190] S. Guilbert, T. Sauvage, P. Garcia, *et al.*, "He migration in implanted UO_2 sintered disks," *Journal of Nuclear Materials*, vol. 327, no. 2, pp. 88–96, 2004, ISSN: 0022-3115. DOI: https://doi.org/10.1016/j.jnucmat.2004.01.024.

[191] P. Garcia, G. Martin, P. Desgardin, *et al.*, "A study of helium mobility in polycrystalline uranium dioxide," *Journal of Nuclear Materials*, vol. 430, no. 1, pp. 156–165, 2012, ISSN: 0022-3115. DOI: https://doi.org/10.1016/j.jnucmat.2012.06.001.

[192] M. S. El-Genk and J.-M. Tournier, "Estimates of helium gas release in $^{238}PuO_2$ fuel particles for radioisotope heat sources and heater units," *Journal of Nuclear Materials*, vol. 280, no. 1, pp. 1–17, 2000, ISSN: 0022-3115. DOI: https://doi.org/10.1016/S0022-3115(00)00036-2.

[193] G. Martin, P. Garcia, H. Labrim, *et al.*, "A NRA study of temperature and heavy ion irradiation effects on helium migration in sintered uranium dioxide," *Journal of Nuclear Materials*, vol. 357, no. 1, pp. 198–205, 2006, ISSN: 0022-3115. DOI: https://doi.org/10.1016/j.jnucmat.2006.06.021.

[194] P. Trocellier, D. Gosset, D. Simeone, *et al.*, "Application of nuclear reaction geometry for ^{3}He depth profiling in nuclear ceramics," *Nuclear Instruments and Methods in Physics Research. Section B, Beam Interactions with Materials and Atoms*, vol. 206, 1-4 May 2003. DOI: 10.1016/S0168-583X(03)00914-5.

[195] J. Belle, *Uranium Dioxide: Properties and Nuclear Applications*. Naval Reactors, Division of Reactor Development, U. S. Atomic Energy Commission, 1961, vol. 7.

[196] P. Sung, "Equilibrium solubility and diffusivity of helium in single-crystal uranium dioxide," University of Washington, 1967.

[197] F. Rufeh, D. R. Olander, and T. H. Pigford, "The solubility of helium in uranium dioxide," *Nuclear Science and Engineering*, vol. 23, no. 4, pp. 335–338, 1965. DOI: 10.13182/NSE65-A21069.

[198] K. Nakajima, H. Serizawa, N. Shirasu, Y. Haga, and Y. Arai, "The solubility and diffusion coefficient of helium in uranium dioxide," *Journal of Nuclear Materials*, vol. 419, no. 1, pp. 272–280, 2011, ISSN: 0022-3115. DOI: https://doi.org/10.1016/j.jnucmat.2011.08.045.

[199] Y. Pipon, C. Raepsaet, D. Roudil, and H. Khodja, "The use of NRA to study thermal diffusion of helium in $(U,Pu)O_2$," *Nuclear Instruments and Methods in Physics Research Section B: Beam Interactions with Materials and Atoms*, vol. 267, no. 12, pp. 2250–2254, 2009, Proceedings of the 11th International Conference on Nuclear Microprobe Technology and Applications and the 3rd International Workshop on Proton Beam Writing, ISSN: 0168-583X. DOI: https://doi.org/10.1016/j.nimb.2009.03.025.

[200] C. Ronchi and J. P. Hiernaut, "Helium diffusion in uranium and plutonium oxides," *Journal of Nuclear Materials*, vol. 325, no. 1, pp. 1–12, 2004, ISSN: 0022-3115. DOI: https://doi.org/10.1016/j.jnucmat.2003.10.006.

[201] X.-Y. Liu and D. Andersson, "Revisiting the diffusion mechanism of helium in UO_2: A DFT+U study," *Journal of Nuclear Materials*, vol. 498, pp. 373–

377, 2018, ISSN: 0022-3115. DOI: https://doi.org/10.1016/j.jnucmat.2017.10.066.

[202] E. Yakub, C. Ronchi, and D. Staicu, "Diffusion of helium in non-stoichiometric uranium dioxide," *Journal of Nuclear Materials*, vol. 400, no. 3, pp. 189–195, 2010, ISSN: 0022-3115. DOI: https://doi.org/10.1016/j.jnucmat.2010.03.002.

[203] K. Govers, S. Lemehov, M. Hou, and M. Verwerft, "Molecular dynamics simulation of helium and oxygen diffusion in $UO_{2\pm x}$," *Journal of Nuclear Materials*, vol. 395, no. 1, pp. 131–139, 2009, ISSN: 0022-3115. DOI: https://doi.org/10.1016/j.jnucmat.2009.10.043.

[204] J. Biersack and J. Ziegler, "Refined universal potentials in atomic collisions," *Nuclear Instruments and Methods in Physics Research*, vol. 194, no. 1, pp. 93–100, 1982, ISSN: 0167-5087. DOI: https://doi.org/10.1016/0029-554X(82)90496-7.

[205] S. Corporation, *pair$_s$tylezblcommand*, Accessed: 21/09/2022.

[206] R. A. Aziz, A. R. Janzen, and M. R. Moldover, "Ab initio calculations for helium: A standard for transport property measurements," *Physical Review Letters*, vol. 74, pp. 1586–1589, 9 Feb. 1995. DOI: 10.1103/PhysRevLett.74.1586.

[207] X. Gai, T. Lazauskas, R. Smith, and S. D. Kenny, "Helium bubbles in bcc Fe and their interactions with irradiation," *Journal of Nuclear Materials*, vol. 462, pp. 382–390, 2015, ISSN: 0022-3115. DOI: https://doi.org/10.1016/j.jnucmat.2014.10.027.

[208] R. A. Aziz and M. J. Slaman, "An Analysis of the ITS-90 Relations for the Non-Ideality of ^{3}He and ^{4}He: Recommended Relations Based on a New Interatomic Potential for Helium," *Metrologia*, vol. 27, no. 4, pp. 211–219, Jan. 1990. DOI: 10.1088/0026-1394/27/4/005.

[209] M. Paffett, D. Kelly, S. Joyce, J. Morris, and K. Veirs, "A critical examination of the thermodynamics of water adsorption on actinide oxide surfaces," *Journal of Nuclear Materials*, vol. 322, no. 1, pp. 45–56, 2003, ISSN: 0022-3115. DOI: https://doi.org/10.1016/S0022-3115(03)00315-5.

[210] E. Yakub and L. Yakub, "Helium in uranium dioxide: Computer simulation (Review Article)," *Low Temperature Physics*, vol. 48, no. 8, pp. 634–644, 2022. DOI: 10.1063/10.0012651. eprint: https://doi.org/10.1063/10.0012651.

[211] M. Stan and P. Cristea, "Defects and oxygen diffusion in PuO_2," *Journal of Nuclear Materials*, vol. 344, no. 1, pp. 213–218, 2005, Proceedings of the 11th International Symposium on Thermodynamics of Nuclear Materials, ISSN: 0022-3115. DOI: https://doi.org/10.1016/j.jnucmat.2005.04.044.

[212] H. Sims, H. Steele, R. Taylor and D. Woodhead, *A literature review of pressurisation mechanisms in cans of PuO_2*. NNL and Sellafield Ltd, 2010.

[213] T. Ichinomiya, B. P. Uberuaga, K. E. Sickafus, *et al.*, "Temperature accelerated dynamics study of migration process of oxygen defects in UO_2," *Journal of Nuclear Materials*, vol. 384, no. 3, pp. 315–321, 2009, ISSN: 0022-3115. DOI: https://doi.org/10.1016/j.jnucmat.2008.12.040.

[214] S. D. Günay, "Investigation of Oxygen Diffusion in Irradiated UO_2 with MD Simulation," *High Temperature Materials and Processes*, vol. 35, no. 10, pp. 981–987, 2016. DOI: doi:10.1515/htmp-2015-0137.

[215] T. G. Zocco, "Transmission electron microscopy of plutonium alloys," *Los Alamos Science*, no. 26, pp. 286–289, 2000.

[216] K. Katsuyama, A. Ishimi, K. Maeda, T. Nagamine, and T. Asaga, "Helium release from the uranium–plutonium mixed oxide (MOX) fuel irradiated to high burn-up in a fast breeder reactor (FBR)," *Journal of Nuclear Materials*, vol. 401, no. 1, pp. 86–90, 2010, ISSN: 0022-3115. DOI: https://doi.org/10.1016/j.jnucmat.2010.04.002.

[217] L. Van Brutzel and A. Chartier, "A new equation of state for helium nanobubbles embedded in UO_2 matrix calculated via molecular dynamics simulations," *Journal of Nuclear Materials*, vol. 518, pp. 431–439, 2019, ISSN: 0022-3115. DOI: https://doi.org/10.1016/j.jnucmat.2019.02.015.

[218] X.-Y. Liu and D. Andersson, "Molecular dynamics study of fission gas bubble nucleation in UO_2," *Journal of Nuclear Materials*, vol. 462, p. 8, 2015, ISSN: 0022-3115.

[219] B. Ao, X. Wang, W. Hu, and J. Yang, "Molecular dynamics simulation of helium–vacancy interaction in plutonium," *Journal of Nuclear Materials*, vol. 385, pp. 75–78, Mar. 2009. DOI: 10.1016/j.jnucmat.2008.09.034.

[220] M. Robinson, S. Kenny, R. Smith, and M. Storr, "He migration and bubble formation in Ga stabilised δ-Pu," *Journal of Nuclear Materials*, vol. 444, no. 1, pp. 493–500, 2014, ISSN: 0022-3115. DOI: https://doi.org/10.1016/j.jnucmat.2013.10.017.

[221] J. Shi, L. Li, L. Peng, F. Gao, and J. Huang, "Atomistic study on helium-to-vacancy ratio of neutron irradiation induced helium bubbles during nucleation and growth in α-Fe," *Nuclear Materials and Energy*, vol. 26, p. 100 940, 2021, ISSN: 2352-1791.

[222] B. Ao, P. Chen, P. Shi, X. Wang, W. Hu, and L. Wang, "Computer simulation of helium effects in plutonium during the aging process of self-radiation damage," *Communications in Computational Physics*, vol. 11, no. 4, pp. 1205–1225, 2012. DOI: 10.4208/cicp.290610.210111s.

[223] C. Galvin, M. Cooper, P. Fossati, C. Stanek, R. Grimes, and D. Andersson, "Pipe and grain boundary diffusion of He in UO_2," *Journal of Physics: Condensed Matter*, vol. 28, p. 405 002, Aug. 2016. DOI: 10.1088/0953-8984/28/40/405002.